



Pilkington Library

Author/Filing Title SHAH EEDULLAH

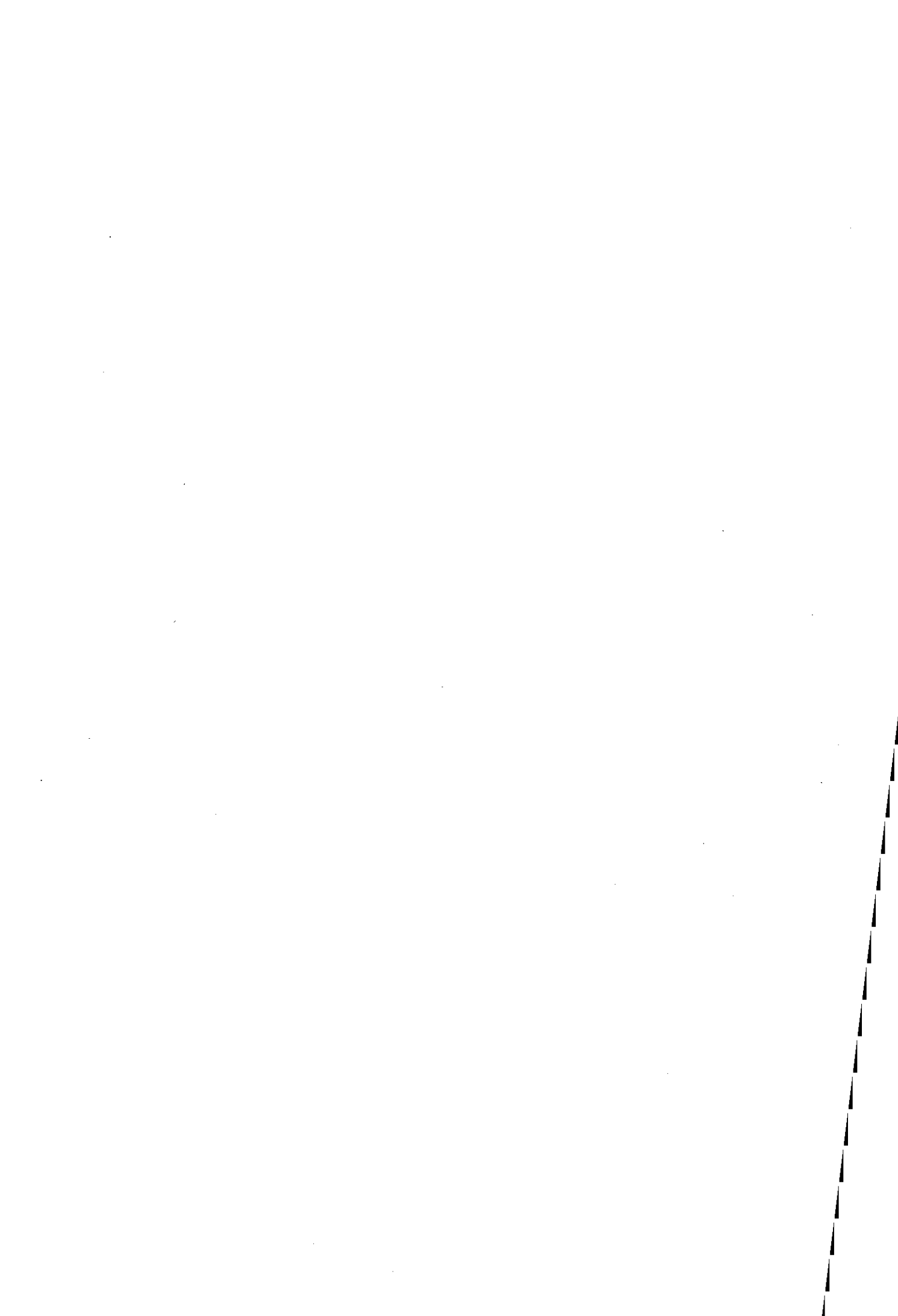
Vol. No. Class Mark T

**Please note that fines are charged on ALL
overdue items.**

FOR REFERENCE ONLY

0402509277





The Use of Microstructural Evolution in a Coated Nickel Base Superalloy, IN738, as a Time-Temperature Recorder


by

Mohamed Rafiullah SHAHEEDULLAH
B.Sc. (CNA), M.Sc. (UMIST)
Associate, Institute of Materials

Submitted in partial fulfilment for the requirements of
the award of Doctor of Philosophy
at Loughborough University

December 2000

Supervisor : Dr. R. C. Thomson
Institute of Polymer Technology and Materials Engineering
Loughborough University

 Loughborough University Public Library
Date Apr 02
Class
Acc No. 040250927

Acknowledgements

The usual thanks should go to my academic supervisor Dr Rachel Thomson, director of research Professor D.R.Gabe and industrial contacts, Dr Birendra Nath and Dr David Gooch of Innogy for their guidance and feedback on technical matters. Innogy is thanked for funding this research.

Mr Frank Page taught me how to use the SEM, projected many honest opinions and gave assistance beyond the call of duty.

It is welcome to find someone who is interested in science, Dr David Ross and I have had many interesting (and sometimes very useful) conversations.

Dr David Hitt knows as much about the IPTME as anyone, and his accessibility over the years is much appreciated. Andy Baker deserves credit for keeping me informed on the progress of my national cricket team.

Shenhua Song and his wife Xiaolin.

Good luck to Neil, Gareth and Wendy with their research, thanks go to them and others who have made the lab a happier place.

Dr David Hall is deservedly mentioned for some emergency Auger sessions (and free food).

All technicians and experimental officers are appreciated for their willingness to help.

My nephew, Shakeel Rashid, is ever cheerful.

There were people who made me feel welcome in Loughborough when I first came, students and residents, I won't name them all but I have not forgotten them.

A mention must be made of William Cartledge, whom I have known on and off since my early days as a metallurgist in Altrincham.

Abstract

Nickel base superalloys are used for turbine blades in gas turbine engines, and are required to operate at very high temperatures (~900°C) for long periods of time in an aggressive environment. A particular problem is that although the operating times of such blades are generally well known, their effective operating temperatures are less well defined due to variations in position and metal-gas temperature. The microstructure of this material is known to evolve as a function of time and temperature. The aim of this research is to develop a model that will enable the microstructure to act as a time temperature recorder for IN738LC industrial gas turbine blades.

The effect of thermal exposure on IN738LC alloy has been investigated experimentally using a variety of techniques. Typically, the microstructure prior to service exposure consists of γ/γ' matrix with primary MC carbides throughout and small amounts of $M_{23}C_6$ carbides mainly at grain boundaries. A number of microstructural features were seen to change with temperature and time. A transformation of MC to $M_{23}C_6$ carbide was found to occur with time and temperature, up to the $M_{23}C_6$ solution temperature of approximately 1000°C. A model to predict the effective temperature experienced, given a known operating time, was developed based on precipitation theory and the ratio of these two carbides. The solution temperature of the $M_{23}C_6$ carbide limits the temperature range in which this model could be used. A second parameter has therefore been considered for use at higher temperatures - the width of the γ' envelope surrounding the grain boundaries

Two external coatings of the MCrAlY type have been studied in detail; a NiCrAlYRe and a CoCrAlY coating. The NiCrAlYRe coating consists of a number of phases, some of which undergo transformations on thermal exposure. However, the CoCrAlY coating was a simpler system characterised by a change in proportions of its two main phases on thermal exposure. The extent of the interdiffusion zone generally increased with time and temperature, this feature is therefore a potentially useful parameter in a model to enable prediction of service temperature.

Table of Contents

1	INTRODUCTION	1
2	REVIEW OF GAMMA PRIME (γ) STRENGTHENED NICKEL BASE SUPERALLOYS	5
2.1	INTRODUCTION	5
2.2	MICROSTRUCTURAL CONSTITUENTS	6
2.3	STRENGTHENING MECHANISMS	12
2.4	PROPERTIES	15
2.5	IN738LC	19
2.6	REJUVENATION	23
2.7	HIGH TEMPERATURE OXIDATION	25
2.8	COATINGS	27
3	EXPERIMENTAL METHODS	39
3.1	INTRODUCTION	39
3.2	TEST PROGRAMME	39
3.3	MATERIAL	45
3.4	X- RAY DIFFRACTION	47
3.5	OPTICAL MICROSCOPY	52
3.6	SCANNING ELECTRON MICROSCOPY (SEM)	53
3.7	ENERGY DISPERSIVE X-RAY (EDX) ANALYSIS	53
3.8	AUGER SPECTROSCOPY	65
3.9	THERMODYNAMIC MODELLING	69
	APPENDIX 3A ANALYSIS OF EDX DATA	79
	APPENDIX 3B EXTRACTION AND XRD PROCEDURES	82
	APPENDIX 3C INTERPLANAR SPACINGS OF CARBIDES, BORIDES AND INTERMETALLICS	87
4	CHARACTERISATION OF ALLOY IN738LC	90
4.1	INTRODUCTION	90
4.2	EFFECT OF THERMAL EXPOSURE ON MICROSTRUCTURE	91
4.3	EFFECT OF VERY HIGH TEMPERATURE EXPOSURE ON CARBIDES	126
5	CHARACTERISATION OF COATINGS	131
5.1	INTRODUCTION	131
5.2	FORMAT FOR DATA AND RESULTS	132
5.3	APPEARANCE AND COMPOSITION OF PHASES	134
5.4	COATING RT122	138
5.5	COATING SC2453	177
	APPENDIX 5A COMPREHENSIVE EDX DATA FOR RT122 (ATOM%)	229
	APPENDIX 5B COMPREHENSIVE EDX DATA FOR SC2453 (ATOM%)	231
6	MODELLING OF MICROSTRUCTURAL TRANSFORMATION IN IN738LC	234
6.1	INTRODUCTION	234
6.2	JOHNSON MEHL AVRAMI KOLMOGOROV (JMAK) EQUATION	234
6.3	MODELS FOR DIFFUSION CONTROLLED PRECIPITATION REACTIONS	237
6.4	A MODEL FOR PRECIPITATION OF CARBIDES IN SUPERALLOYS	239
6.5	A MODEL FOR IN738LC	243

1.2 DISCUSSION	247
APPENDIX 6A: DIFFUSION COEFFICIENTS OF SOME ELEMENTS IN NI AND NI-BASED ALLOYS.....	250
7 CONCLUSIONS AND FURTHER WORK.....	251
7.1 INTRODUCTION	251
7.2 CHARACTERISATION OF IN738LC.....	251
7.3 COATING CHARACTERISATION	252
7.4 INDICATORS OF REMAINING SERVICE LIFE	254
7.5 FURTHER WORK	254
REFERENCE LIST	256

Table of Figures

Figure 2.1 The structure of γ	7
Figure 2.2 The flow stress of Ni_3Al as a function of temperature ⁴	7
Figure 3.1 Thermal exposure experienced by creep test samples	40
Figure 3.2 Thermal exposure of coated IPTME samples	41
Figure 3.3 Thermal exposure of both creep and IPTME samples	41
Figure 3.4 Schematic of incident and diffracted X-ray beams	47
Figure 3.5 Effect of rotating a crystal on the diffracted beam.....	50
Figure 3.6 Schematic of an X-ray diffractometer ⁶¹	50
Figure 3.7 Example XRD trace, red - raw data, green - deconvoluted.....	51
Figure 3.8 Sample / beam electron interactions ⁶⁴	55
Figure 3.9 Electron shells	57
Figure 3.10 Schematic of a SEM/EDX system ⁶⁴	58
Figure 3.11 Example EDX spectrum.....	60
Figure 3.12 Processes resulting in Auger electron emission	66
Figure 3.13 An Auger spectrum for pure nickel ⁶⁵	67
Figure 3.14 Peak shapes for carbon.....	68
Figure 3.15 Comparison of as-received and cleaned samples of pure nickel ⁶⁵	68
Figure 4.1 Example trace for X-ray diffraction of extracted carbides from IN738LC 915°C for 2448 hours.....	96
Figure 4.2 Layout for substrate data	96
Figure 4.3 IN738LC Equilibrium bar 1 composition (G1).....	99
Figure 4.4 IN738LC – sensitivity of equilibrium to Al content (bar 1 composition).....	100
Figure 4.5 IN738LC – sensitivity of equilibrium to increasing Cr content (bar 1 composition)	101
Figure 4.6 Effect of thermal exposure on width of γ envelope at 950°C	107
Figure 4.7 Equilibrium prediction of effect of temperature on weight% of elements in MC	109
Figure 4.8 G0 Virgin Bar –microscopy data	112
Figure 4.9 G10 Commercial heat treatment 1120°C for 2 hours, 845°C for 24 hours – microscopy data.....	114
Figure 4.10 G1/3 exposed at 850°C for 283 hours (fatigue test) – microscopy data	116
Figure 4.11 G2/2 sample exposed at 950°C for 1025 hours.....	118
Figure 4.12 G12/5-X exposed at 950°C for 12000 hours.....	120
Figure 4.13 XRD slides G7/A20 and G11/4-Z.....	122
Figure 4.14 Summary of EDX data for MC carbides.....	123
Figure 4.15 Graph of experimentally determined M_{23}C_6 : MC ratios, with simple trendlines (exponential first order fit)	125
Figure 4.16 Unexposed sample.....	129
Figure 4.17 Exposed at 1190°C for 20 hours.....	129
Figure 5.3.1 Data layout for composition profile and general micrographs.....	136
Figure 5.3.2 Data layout for thermally exposed samples	137
Figure 5.4.1 As-coated composition.....	139
Figure 5.4.2 Composition modified – Al depletion.....	140
Figure 5.4.3 Composition modified – Cr depletion.....	141
Figure 5.4.4 G12/6-Z unexposed, coating – interdiffusion – substrate profile.....	143
Figure 5.4.5 G12/6-Z unexposed –coating characteristics	144
Figure 5.4.6 G12/6-Z interdiffusion zone characteristics	145

Figure 5.4.7 G12/2-W exposed at 850°C for 4800 hours, coating – interdiffusion – substrate profile.....	149
Figure 5.4.8 G12/2-W exposed at 850°C for 4800 hours – coating characteristics	150
Figure 5.4.9 G12/2-W exposed at 850°C for 4800 hours – interdiffusion characteristics ...	151
Figure 5.4.10 G12/2-X exposed at 850°C for 9600 hours, coating – interdiffusion – substrate profile.....	152
Figure 5.4.11 G12/2-X exposed at 850°C for 9600 hours – coating characteristics	153
Figure 5.4.12 G12/2-X exposed at 850°C for 9600 hours – interdiffusion characteristics ..	154
Figure 5.4.13 G12/4-Y exposed at 950°C for 4800 hours – coating – interdiffusion – substrate profile	155
Figure 5.4.14 G12/4-Y exposed at 950°C for 4800 hours – coating characteristics	156
Figure 5.4.15 G12/4-Y exposed at 950°C for 4800 hours – interdiffusion characteristics ..	157
Figure 5.4.16 G12/5-W exposed at 950°C for 9600 hours – coating – interdiffusion – substrate profile	158
Figure 5.4.17 G12/5W exposed at 950°C for 9600 hours – coating characteristics.....	159
Figure 5.4.18 G12/5W exposed at 950°C for 9600 hours – interdiffusion characteristics...	160
Figure 5.4.19 G12/5-X exposed at 950°C 12000 –coating – interdiffusion – substrate profile	161
Figure 5.4.20 G12/5-X exposed at 950°C for 12000 hours – coating characteristics	162
Figure 5.4.21 G12/5-X exposed at 950°C for 12000 hours – interdiffusion layer characteristics	163
Figure 5.4.22 Effect of thermal exposure on coating, optical micrographs	166
Figure 5.4.23 Effect of thermal exposure on core coating, optical micrographs (β -bright, γ -dark).....	167
Figure 5.4.24 Phase map for coating experimentally determined at 850°C and 950°C, 4800 to 1200 hours,	168
Figure 5.4.25 Effect of thermal exposure on interdiffusion zone, secondary electron micrographs (magnification varies).....	170
Figure 5.4.26 Phase map for interdiffusion phases, experimentally determined.....	171
Figure 5.5.1 As-coated composition.....	179
Figure 5.5.2 Composition modified – Al depletion.....	180
Figure 5.5.3 Composition modified – Cr depletion.....	181
Figure 5.5.4 G13/6-Z unexposed coating – interdiffusion – substrate profile.....	183
Figure 5.5.5 G13/6-Z as-coated coating characteristics	184
Figure 5.5.6 G13/6-Z unexposed, backscattered electron micrograph, annotated for EDX points on coating.....	185
Figure 5.5.7 G13/6-Z as-coated interdiffusion zone characteristics.....	186
Figure 5.5.8 G13/6-Z unexposed, backscattered electron micrograph, annotated for EDX points on interdiffusion zone	187
Figure 5.5.9 G13/2-W exposed at 850°C for 4800 hours – coating - interdiffusion - substrate	195
Figure 5.5.10 G13/2-W exposed at 850°C for 4800 hours – coating characteristics	196
Figure 5.5.11 Auger spectroscopy on G13/2-W coating particles ‘note 1’	197
Figure 5.5.12 G13/2-W exposed at 850°C for 4800 hours – interdiffusion characteristics .	198
Figure 5.5.13 G13/2-X exposed at 850°C for 9600 hours – coating - interdiffusion - substrate	199
Figure 5.5.14 G13/2-X exposed at 850°C for 9600 hours – coating characteristics	200
Figure 5.5.15 G13/2-X exposed at 850°C for 9600 hours – interdiffusion characteristics ..	201

Figure 5.5.16 G13/4-Y exposed at 950°C for 4800 hours – coating - interdiffusion - substrate	202
Figure 5.5.17 G13/4-Y exposed at 950°C for 4800 hours – coating characteristics	203
Figure 5.5.18 G13/4-Y exposed at 950°C for 4800 hours – interdiffusion characteristics ..	204
Figure 5.5.19 G13/4-Y wavelength dispersive analysis for carbon.....	205
Figure 5.5.20 G13/4-Y exposed at 950°C for 4800 hours – Auger analysis for carbon	206
Figure 5.5.21 G13/4-Y exposed at 950°C for 4800 hours – Auger analysis for carbon	207
Figure 5.5.22 G13/5-W exposed at 950°C for 9600 hours – coating - interdiffusion - substrate.....	208
Figure 5.5.23 G13/5-W exposed at 950°C for 9600 hours – coating characteristics	209
Figure 5.5.24 G13/5-W exposed at 950°C for 9600 hours – interdiffusion characteristics .	210
Figure 5.5.25 G13/5-X exposed at 950°C for 12000 hours – coating - interdiffusion - substrate.....	211
Figure 5.5.26 G13/5-X exposed at 950°C for 12000 hours – coating characteristics	212
Figure 5.5.27 G13/5-X exposed at 950°C for 12000 hours –interdiffusion characteristics .	213
Figure 5.5.28 Effect of thermal exposure on coating microstructure – optical micrographs	216
Figure 5.5.29 Effect of thermal exposure on coating microstructure – backscattered electron micrographs (magnification varies).....	217
Figure 5.5.30 Effect of thermal exposure on core coating microstructure – backscattered electron micrographs (magnification varies).....	218
Figure 5.5.31 Phase map for SC2453 coating, experimentally determined at 850°C and 950°C, 4800 to 1200 hours,.....	219
Figure 5.5.32 Effect of thermal exposure on interdiffusion layer- backscattered electron micrographs (magnification varies).....	221
Figure 5.5.33 Phase map SC2453 interdiffusion layer, experimentally determined.....	222
Figure 5.5.34 Schematic of diffusion processes at 950°C.....	228
Figure 6.1 Concept of extended volume.....	237
Figure 6.2 Experimental data (averaged) and calculated curve for $M_{23}C_6$ / MC ratio versus exposure time.....	248
Figure 6.3 Long term calculated values of R'	249

1 Introduction

A particular problem in the power generation industry is that in order to predict the remaining life of components both the temperatures and the stresses which they have experienced during service are required. The stresses can be readily calculated using finite elements methods, however the temperatures are more difficult to determine due to differences in location of components and fluid flow variations around them. The focus of this research is to establish the effective operating temperature of conventionally cast nickel base superalloy turbine blades using the microstructure as a time-temperature recorder.

The specific alloy investigated is IN738LC which comes from the γ strengthened group of alloys, a review of which is presented in Chapter 2. Particular attention has been paid to microstructural features. The bulk of the substrate comprises the FCC γ nickel base matrix, strengthened by a distribution of $L1_2$ γ , $Ni_3(Al,Ti)$ precipitates. The small lattice mismatch imparts mechanical strength to the alloy. Additionally, two types of carbide are present in IN738LC, MC and $M_{23}C_6$. Thermal exposure at typical service temperatures have been found to result in a transformation of MC to $M_{23}C_6$. This reaction has been used to create time temperature recorders for other nickel base superalloys, and is investigated in detail in this research for IN738LC.

In practice blades are often used with a protective coating to provide additional resistance to effects such as oxidation and hot corrosion. Coatings generally have high aluminium and chromium concentrations and a popular type is now based on MCrAlY coatings.

Two MCrAlY coatings on IN738LC substrates have been investigated in some detail in this research, denoted SC2453 and RT122. RT122 is fairly common, however SC2453 contains much less cobalt but has rhenium additions and has not been characterised extensively in the open literature. In particular a systematic study of the effect of thermal exposure (temperature and time) on the interaction between both coatings and the substrate has been carried out in this research.

The materials, test programme and experimental techniques used are described in Chapter 3. In parallel with this research, other investigations are underway, one of which is a programme of creep testing using coated IN738LC material. These creep specimens were to be made available for this research programme, primarily for quantitative examination of the substrate feature used in a time / temperature prediction model. A further, controlled thermal exposure

programme was implemented at IPTME, to complement the samples that would be available from the creep test programme, and to provide a standard set of samples for examination of the effect of thermal exposure on the two coating systems.

Experimental analysis techniques that have been used include optical microscopy, scanning electron microscopy (SEM), Energy dispersive X-ray analysis (EDX), X-ray diffraction (XRD), and Auger analysis and these have been discussed in some detail in Chapter 3. Growing use is being made of computer software and thermodynamic database systems to predict equilibrium conditions for materials and a section in this chapter is devoted to thermodynamic modelling. Equilibrium predictions can be made for IN738LC and MCrAlY coating systems using currently available software/database combinations, and an insight can be gained into the likely microstructural changes during service.

The first experimental analysis undertaken is the characterisation of the effect of thermal exposure on the IN738LC base alloy. With the benefit of information available from work done on similar systems, interest was focussed on carbide transformations. The extent of the MC to $M_{23}C_6$ transformation was found to increase with thermal exposure, both time and temperature (up to the solvus of $M_{23}C_6$, thermodynamic calculations predicted the $M_{23}C_6$ solvus to be approximately 1010°C.). This was considered a suitable feature to be used in a time temperature recorder model. A full programme was undertaken to quantitatively analyse the $M_{23}C_6$: MC ratio from the creep test programme and thermal exposure specimens. The extracted carbides were additionally examined by SEM and their morphology studied. The MC carbides (often termed Chinese script carbides) exhibit tetrahedral heads with bone like appendages. The $M_{23}C_6$ particles are simple cuboids that can interconnect at grain boundaries and form a mesh like structure. During the carbide transformation MC combines with γ resulting in $M_{23}C_6$ and γ' , which surrounds the $M_{23}C_6$ particles. The width of the γ' envelope has been examined qualitatively and was also found to increase on thermal exposure, but the magnitude is small (up to a few microns width). Further quantitative work would be required to properly evaluate this feature for potential use in a time temperature recorder model.

Having identified a microstructural feature, the carbide ratio, that varied with thermal exposure, the next requirement was to create a model that could predict a temperature for a given time based on measurement of this feature. Kinetic models are often based on Avrami relationships between phase volume fraction and time, in particular the Johnson-Mehl-

Avrami-Kolmogorov type equations. An existing model for another superalloy was adapted for carbide transformations appropriate for IN738LC in this research and was used to calculate the amount of $M_{23}C_6$ precipitated over time. Experimental data are required to determine the value of constants in the model. The fit of model predictions to experimental data in the temperature and time ranges applied was found to be reasonable. The simple adaptation of the model represents experimental data well in the temperature range appropriate for service conditions, i.e. up to 950°C. However, the model does not take into account $M_{23}C_6$ dissolution as its solvus is approached and is therefore limited in application to temperatures below the solvus of $M_{23}C_6$. Typical service temperatures are 800°C to 950°C, the thermodynamically predicted solvus of $M_{23}C_6$ is 1010°C, hence the model is suitable for practical applications.

The second experimental investigation was that of the effect of thermal exposure on the coating/substrate systems. A detailed study was carried out at two temperatures 850°C and 950°C. The simpler of the two coatings was found to be RT122. This coating consists of the commonly found γ and β phases. Thermal exposure has the effect of depleting β (the most aluminium rich phase) at outer and inner layers of the coating. β depletion at the outer layer is the result of formation of aluminium oxide (Al_2O_3). However, β depletion at the inner surface is the result of the aluminium concentration being higher in the coating than the substrate, and aluminium therefore diffusing from the coating towards the substrate. The interdiffusion zone consists mostly of γ , with occasional β particles. The width of the interdiffusion zone increased with thermal exposure. A recrystallised region was evident in the substrate below the interdiffusion zone, exhibiting a change in morphology of γ/γ' and small grains. The amount of γ' in this recrystallised region seemed to increase with thermal exposure.

Coating SC2453 was found to be more complex, as indicated by the thermodynamic calculations. At 850°C the phases in the coating are γ' , β , σ (equiaxed, rhenium containing) and small amounts of γ . Over the time investigated, β depletion at outer and inner layers begins to occur. The interdiffusion layer at 850°C consists of γ' and σ needles. There is a thin layer of rhenium containing σ particles at the interface between the interdiffusion layer and the coating. At 950°C, the phases in the coating are γ , β , α and σ . Thermal exposure results in outer and inner β depleted layers, and additionally depletion of σ at the core in inner layers of the coating. At the higher temperature, chromium diffusion (towards the

substrate) appears to become more apparent, in addition to the often found diffusion of aluminium. The interdiffusion layer at 950°C consists of γ and α (rhenium containing). The rhenium content of the α was found to vary. There is a thin layer of rhenium containing α particles at the interface between the interdiffusion layer and the coating. Thermal exposure results in an increase in volume fraction of the interdiffusion zone, with phases penetrating from the interdiffusion zone into the substrate.

2 Review of Gamma Prime (γ) Strengthened Nickel Base Superalloys

2.1 Introduction

In power and aerospace turbines, the material requirements include resistance to high temperature (above 700°C) effects, including;

- oxidation
- erosion
- corrosion (including 'hot corrosion')
- creep.

Superalloys were developed to meet these needs. Superalloys are usually based on Group VIIIA elements such as iron, nickel or cobalt. Typical alloying additions include chromium, aluminium, tungsten, molybdenum and tantalum amongst others. Superalloys are manufactured as both wrought and cast products. Early superalloys were iron-rich and used carbon to achieve sufficient yield stresses. However, for certain applications chromium carbides could be deleterious to corrosion resistance. In order to enable the use of lower carbon levels, the precipitation strengthening mechanism (already applied to light alloys at the time) was developed for austenitic Fe-Ni-Cr superalloys with a wide range of nickel contents. Aluminium and titanium additions were found to have a hardening effect by this mechanism. The hardening phase was later identified as $\text{Ni}_3(\text{Al,Ti})$, known as γ' , hence the title of this chapter.

The major groups of iron and nickel base superalloys are;

1. Iron base and iron rich alloys

These alloys have the advantage of relatively low cost. The disadvantages include that the composition can favour the formation of brittle phases, and the γ' hardening phase is metastable, limiting life at long-term thermal exposure at higher temperatures

2. Wrought nickel base superalloys

These typically contain 15-20 mass% Cr and Co with other alloying elements including molybdenum and sometimes tungsten. These alloys are precipitation hardened by the γ' as described above. The high temperature capability of these alloys is affected by the

volume fraction of γ' , commonly around 45%, which is more limited than in cast alloys due to the possibility of incipient melting on hot working, Durand-Charre¹ chapter 1.5.3.

3. Cast nickel base superalloys

Castings have a higher volume fraction of the γ' than wrought alloys, typically 50-60%. A balance is sought between the volume fraction of γ' , which is rich in aluminium (required for oxidation resistance), and the remaining matrix, which is rich in chromium (required for hot corrosion resistance). Alloy IN738 was designed to achieve such a balance.

The focus for the research described here is on nickel-base superalloys. For turbine blades there are two main reasons for the use of cast rather than wrought nickel base alloys. The first is that increasing titanium and aluminium content improves the stress rupture properties. The second is that forging superalloys with a high volume fraction of γ' is more problematic, as the material is worked at a temperature above the γ' solvus.

The particular superalloy under consideration is the conventionally cast form of IN738LC (low carbon). This belongs to the gamma prime (γ') precipitation hardening class of nickel-base superalloys, which is described in the following sections.

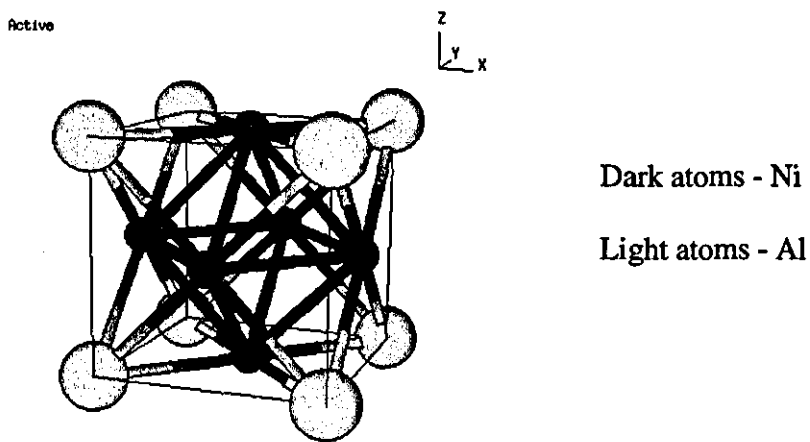
2.2 Microstructural Constituents

2.2.1 Gamma, γ

The alloy matrix consists of close packed face centred cubic (FCC) austenite. This phase is made up of nickel with elements in solution, some of which provide strengthening (see section 2.3.2) or form oxide films (section 2.7.2). The volume fraction of the matrix in later generations of this group of alloys is in the region of 30%, due to the high volume fraction of the precipitating phase (see next section). Both solid solution hardening and precipitation hardening can strengthen the austenitic matrix. However the FCC γ matrix can be destabilised by the presence of BCC stabilising solutes such as Cr, Mo, Ta, Nb and W, Jena and Chaturvedi².

2.2.2 Gamma Prime, γ'

Typically γ' is Ni_3Al or Ni_3Ti although other elements can be substituted for Al, Ti or Ni. γ' is coherent with the γ matrix. γ' has an $L1_2$ type structure, shown below in Figure 2.1 that exhibits long-range order

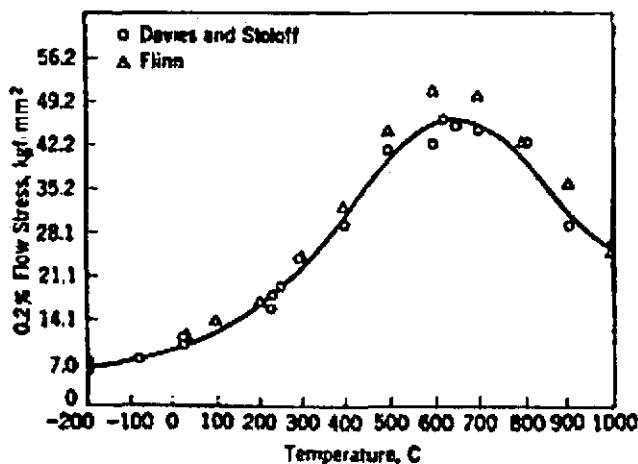
Figure 2.1 The structure of γ 

Substitution of other elements for aluminium can affect the degree of long range order. For example substitution of niobium can result in a decrease of 25% in the long range order, Jena and Chaturvedi². γ can exist in two forms. The coarse form, referred to as primary γ and the hyperfine form, termed secondary γ . Secondary γ is sometimes referred to as cooling γ . Primary γ can be blocky or spheroidal.

The interface between γ and γ is coherent. The lattice size of γ varies slightly compared to that of the γ matrix. This mismatch (termed δ) causes lattice distortion which impedes dislocation motion. The shape of primary γ is said by Sims *et al*³ to be related to matrix-lattice mismatch. This magnitude of misfit can be assigned a positive or negative value. The mismatch was found to affect γ morphology. At 0-0.2% mismatch γ occurs as spheres, around 0.5%-1.0% cubes and at mismatches above about 1.25% γ occurs as plates.

The strength of γ is low at low temperatures but unusually, increases with temperature up to a maximum at about 700-750°C. This is thought to be due to the formation and interaction of complex faults.

Figure 2.2 The flow stress of Ni₃Al as a function of temperature⁴



Durand-Charre¹ has reviewed the changes in morphology of γ' on thermal exposure. The cuboidal precipitates tend to group together in short chains that subsequently coalesce. On standard heat treatments, zones with the appearance of γ' rafted structure can exist, although there is actually no applied load. These zones disappear when the homogenising treatment is prolonged to 50 hours or more.

To assist in the study of γ' , Krieger and Baris⁵ investigated the chemical partitioning of elements in γ' separated from precipitation hardened nickel base alloys. The authors aim in particular was to be able to measure the composition and quantity of the γ' phase. Their basic technique is anodic dissolution of the sample matrix in a 1% solution of ammonium sulphate and citric acid. This was modified to enable a comprehensive study of the separation of γ' from 15 nickel base superalloys. They were able to determine composition of γ' , calculate lattice parameters of γ' and determine partitioning of elements between γ and γ' .

The partitioning of alloying elements to the γ and γ' phases can influence particle coarsening kinetics, antiphase boundary energy and misfit. Titanium and niobium partition to γ' and increase its lattice parameter. Molybdenum, iron and to a lesser extent chromium tend to partition to and expand γ . Tantalum and tungsten are reported to behave similarly to niobium and molybdenum respectively².

2.2.3 Carbides

Carbides appear in conventionally cast and directionally solidified nickel base alloys in a number of different compositions and stoichiometries. The most common are:

1. MC

2. $M_{23}C_6$

3. M_6C

4. M_7C_3

2.2.3.1 MC

MC carbides form during freezing. They occur as discrete particles, often with so-called 'Chinese-script' morphology, distributed throughout the alloy in both matrix and intergranular positions. The distribution is often interdendritic. MC carbides result from combination of reactive and refractory metals. The FCC structure is a dense, closely packed structure. Pure MC carbides are extremely stable. The preferred order of formation in superalloys is HfC, TaC, NbC, and TiC in order of decreasing stability. Thermodynamics would predict the following order HfC, TiC, TaC, and NbC. The reasoning for this change in stability order is as follows. It is known that M atoms can substitute for each other, e.g. (Ti,Nb)C. However, the less reactive elements such as Mo and W can also substitute in these carbides. The change in stability order is said to be due to the molybdenum or tungsten substitution, which weakens the binding forces in MC carbides resulting in degeneration, see Equation 2.1. This typically leads to formation of $M_{23}C_6$ and M_6C type carbides as the more stable compounds in the alloys after heat treatments and/or service. Additions of niobium or tantalum tend to counteract this effect. It should be noted that thermodynamics only takes into account Gibbs free energy, interfacial energy may also have an effect on nucleation and growth.

Superalloys that contain hafnium and titanium were found to contain two or more MC carbides with different compositions, by Starink, Cama and Thomson⁶. Typical compositions ranged from Hf-lean ($Ti_{0.4}Ta_{0.35}W_{0.2}Hf_{0.05}C$) to Hf rich ($Ti_{0.07}Ta_{0.12}W_{0.06}Hf_{0.75}C$). The wide range of compositions is said to be caused by a miscibility gap in the MC carbide phase, which causes the formation of MC carbides to shift from Hf lean in the initial stages of solidification to Hf rich in the later stages.

MC carbides are categorised in Sims *et al*³ to be of two types. MC(I), single monatomic low parameter FCC compound characterising those commonly found in most cast or wrought superalloys can be and usually is readily decomposed, Equation 2.2 and Equation 2.3, section 2.2.3.5. If an alloy contains hafnium and is held at high temperature for considerable time, FCC MC(3) can form. This phase is very finely divided and has not been observed to decompose.

2.2.3.2 $M_{23}C_6$

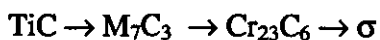
$M_{23}C_6$ carbides are profuse in alloys with moderate to high chromium content. They can result from lower temperature heat treatment and service (760-980°C) and soluble carbon residual in the alloy matrix. These carbides can occur at grain boundaries, twin lines, stacking faults and at twin ends. $M_{23}C_6$ carbides have the complex cubic structure, which, if the carbon atoms were removed, would closely approximate the structure of the topologically close packed (TCP) δ phase (see section 2.2.4). Coherency between $M_{23}C_6$ and δ is high. When tungsten or molybdenum are present the approximate composition is $Cr_{21}(Mo,W)_2C_6$, (ref.³). $M_{23}C_6$ carbides have a significant effect on nickel alloy properties. Their critical location at grain boundaries promotes a significant effect on rupture strength, apparently through inhibition of grain boundary sliding. However, eventually rupture can initiate either by fracture of these same grain boundary $M_{23}C_6$ particles or by decohesion of the $M_{23}C_6$ interface. Cellular $M_{23}C_6$ can initiate in certain alloys but can be avoided by heat treatment and chemistry control, as it can be deleterious.

2.2.3.3 M_6C

M_6C carbides have a complex cubic structure and form at slightly higher temperatures than $M_{23}C_6$, 815°C - 980°C. They are similar to $M_{23}C_6$ but formed when the molybdenum and/or tungsten content is high. M_6C carbides are therefore formed when molybdenum or tungsten acts to replace chromium in other carbides. Typical formulae are $(Ni,Co)_3Mo_3C$ and $(Ni,Co)_2W_4C$. A wide range of composition for M_6C is possible with formulae ranging from approximately M_3C to $M_{13}C$, depending on alloy matrix content. For example, in Hastelloy X³, $M_{2.48}C = (Mo_{0.91}Ni_{0.90}Cr_{0.50}Fe_{0.17})C$ and $M_{13.25}C = (Mo_{6.34}Ni_{5.73}Cr_{0.69}Fe_{0.49})C$.

2.2.3.4 M_7C_3

M_7C_3 is usually Cr_7C_3 and can be involved in the formation of σ in some superalloys, Sims *et al*³



2.2.3.5 Carbide Reactions

The majority of carbon in most as-cast nickel-base superalloys is contained in the high temperature carbide MC. Jena and Chaturvedi² have summarised the effect of alloying elements on the stability of MC carbide. Ti, Ta, Nb, V (and Hf³) tend to stabilise MC carbides, other elements tend to destabilise MC carbides. Increasing addition of strong

carbide-formers results in the formation of carbides in the general order $M_7C_3 \rightarrow M_{23}C_6 \rightarrow M_6C \rightarrow MC$. The presence of strong carbide forming elements results in MC carbides on solidification.

During heat treatment and service, MC decomposes slowly yielding carbon, which permeates the alloy and activates a number of important reactions. The dominating carbide reaction in many alloys is believed to be the formation of $M_{23}C_6$ by the following reaction:



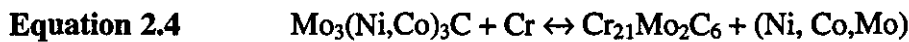
or



Also, M_6C and $M_{23}C_6$ interact, forming from one another



or



depending on the alloy.

The Hf-rich and Hf-lean MC carbides in MarM002, discussed in section 2.2.3.1 (Starink, Cama and Thomson⁶) were thermally exposed at 700-1000°C and for up to 250 days. The shapes, distribution and compositions of the MC carbides did not vary significantly with exposure at 700°C and 800°C. Exposure at the higher temperatures 900°C and 1000°C resulted in increases in the relative proportions of Hf-rich MC, implying that the carbides are transforming to a more thermodynamically stable composition.

In a subsequent study the above authors⁷ state that in MarM002, above about 800°C $M_{23}C_6$ forms via decomposition of the Hf-lean MC carbide:



For temperatures in excess of 900°C M_6C forms by the following reaction



2.2.4 Topologically Close Packed Phases (TCP)

Topologically close packed phases include sigma, laves and mu. These phases are generally thought to be deleterious and can form in service. They can occur after long times at elevated temperatures, possibly exacerbated by poor compositional control. The sigma phase in the iron chromium system has a composition of CrFe. In superalloys, a typical composition for sigma may be $(\text{Cr,Mo})_x(\text{Ni,Co})_y$, where x and y can vary between 1 and 7 but are often approximately equal, Sims *et al*³, chapter 8. Excessive amounts of chromium, molybdenum and tungsten are said to promote the formation of TCP phase¹. These phases usually precipitate near grain boundaries where concentrations of some of the aforementioned elements may be high. They can appear as thin linear plates. Sigma in particular is a brittle phase, which can lead to lower fracture resistance and elevated temperature rupture resistance. Additionally, they can denude the matrix from elements such as chromium, which reduces corrosion resistance.

2.3 Strengthening Mechanisms

2.3.1 Precipitation Strengthening

The contribution to the yield strength of Ni-base superalloys is far larger from precipitation hardening than from solid solution hardening. The most common precipitating phase is γ' , although γ'' can precipitate in Nb containing alloys. A controlled solution / ageing heat treatment is required to optimise the γ' distribution. The nature of the γ' phase has been discussed in detail in section 2.2.2. The interaction of the γ' precipitate with dislocations is of major significance with respect to the yield strength of precipitation strengthened superalloys. Dislocations either bow around precipitates or cut through them. Optimum strength is obtained when the interparticle spacing is just small enough to prevent the dislocations from bowing.

2.3.1.1 Mechanism

Three types of stacking fault exist in the $L1_2$ type structure;

1. Superlattice (intrinsic or extrinsic) faults
2. Antiphase boundary faults
3. Complex faults.

The large numbers of faults produced in nickel base alloys hardened by coherent precipitation play a dominant role in deformation. Some models suggest that the critical resolved shear stress (CRSS) is very dependent on fault energy of γ' . A number of possible hardening mechanisms are proposed. The two primary mechanisms are coherency strains and the presence of order in the particles. Strengthening by γ' is related to a number of compositional / microstructural factors. The most direct correlation can be made with volume fraction of γ' and γ' particle size

a. Effect of Volume Fraction:

Strength will increase with an increase in volume fraction of γ' but this is interdependent with the nature of the γ' precipitate. In cast alloys the character of the γ' precipitate developed can be extremely variable because of the effects of segregation and cooling rate, γ - γ' eutectic and coarse γ' may be developed. Subsequent heat treatments can modify the structure. The volume fraction of the γ' phase in cast alloys is typically 50% or greater.

b. Effect of Size:

The effect of γ' size on strength is dependent on the heat treatment of the alloy. Before the age strengthening peak, for a constant γ' volume fraction, the strengthening mechanism involves particle cutting and strength increases with γ' size. After the age strengthening peak, for a constant γ' volume fraction, γ' particles become large, dislocations no longer cut but bypass particles and strength now decreases.

2.3.1.2 Effect of Alloying

The effect various alloying elements have on γ' volume fraction has been summarised by Durand-Charre¹. Titanium and aluminium have a very large effect, niobium large and chromium, molybdenum and tungsten moderate. The substitution of tantalum and niobium for titanium and aluminium has been investigated by Chang and Hall⁸ in a series of nickel base superalloys. The aged strength increased proportionately with the substitution percentage of tantalum and niobium. The strength enhancement associated with the Ta + Nb substitution was observed in the temperature range up to 650°C. They state that prolonged ageing at high temperature of high Ta and Nb content alloys results in formation of large plate-like orthorhombic phase. This is caused by dissolution of the strengthening precipitates γ' and γ'' .

2.3.1.3 Precipitate Coarsening

The precipitation hardened system consists of γ precipitates of different sizes distributed in the matrix. When normal precipitation involving nucleation and growth is completed, the volume fraction has attained its thermodynamic equilibrium value. However, the average particle size continues to increase to competitive coarsening. Larger precipitates grow at expense of smaller ones. The driving force for this process is the minimisation of interfacial energy. Coarsening rate is reduced by substitution of aluminium by other elements such as Ti (higher melting point), Jena and Chaturvedi².

2.3.2 Solid Solution Strengthening

A solid solution is a solid, homogenous mixture of two or more elements. The solute atoms are present as either substitutional or interstitial sites in the matrix. Their presence can influence the mechanical properties of the metal by affecting the lattice parameter such that dislocations are impeded. The properties that can be changed by solute atoms include lattice parameter, modulus, stacking fault energy and electron density of the alloy.

The common solid solution elements in γ are iron, chromium, molybdenum, tungsten, titanium, and aluminium. These elements differ from nickel by 1-13% in atomic diameter. Aluminium, in addition to its contribution of precipitation strengthening, is an effective solid solution strengthener. Tungsten, molybdenum and chromium also contribute strongly, whereas iron, titanium, cobalt and vanadium are relatively weak solid solution strengtheners. Above about 0.6 T_M (melting temperature), the range of high temperature creep, γ strengthening is diffusion dependent. Slow diffusing elements such as molybdenum and tungsten would be expected to be the most effective hardeners². High melting point solutes are preferred for creep resistance. Examples of solid solution hardened superalloys include Inconel 625. These are generally used in the annealed temper.

2.3.3 Grain Size

Grain size refinement is expected to have an effect on strengthening. The grain size of IN738 subsequent to a typical industrial heat treatment is very large (in the order of mm), so this is not usually a factor in conventionally cast alloys.

Directional solidification produces components with columnar grain structures. This structure can significantly enhance creep strength, provided that the grain boundaries are parallel to the principal stress axis.

Solidifying a single crystal can enhance mechanical strength. This eliminates grain boundaries, which represent weak points in the microstructure.

2.4 Properties

2.4.1 Creep

2.4.1.1 Introduction

Creep is the dominant failure mechanism for industrial gas turbines, whereas in aero engines fatigue dominates.

The three classical stages of creep are;

1. Primary creep - begins fairly rapidly then decreases with time due to strain hardening
2. Secondary creep - steady state creep, strain is fairly uniform and at its lowest value
3. Tertiary creep - strain rate increases rapidly leading to fracture.

In superalloys creep generally occurs slightly above the recrystallisation temperature of the metal involved. Creep often begins with nucleation and growth of cavities on grain boundaries oriented perpendicular to the load axis. Nucleation is sensitive to interfacial energy. Growth of cavities is controlled by stress and grain boundary/surface diffusion. Studies have shown that diffusion should dominate at small size cavities and stress control at larger sizes.

2.4.1.2 Effect of Microstructure

Creep in superalloys is dependent on a number of microstructural parameters;

- γ precipitate volume fraction
- lattice mismatch
- morphology.

Creep strength increases approximately linearly with γ precipitate volume fraction. Creep strength can be increased by optimising lattice mismatch (and hence coherency strains). For better creep strength the γ particles should be very small but this can cause a loss in ductility. Carbides can pin grain boundaries preventing slide or migration. Carbide particles however, can also be sites for cavity formation during creep. There is usually an optimum carbon content of 0.5%- 0.15%. Cellular carbides or continuous carbide networks are deleterious to

creep rupture resistance. Phase instabilities during creep can cause progressive deterioration in properties;

- coarsening of grain boundary carbides
- coarsening of γ particles
- decomposition of metastable phases
- formation of deleterious TCP phases
- grain size and shape are also important variables. At higher temperatures, a coarser grain size will help minimise grain boundary sliding at lower stresses and is beneficial to creep strength.
- improvement in creep strength has been achieved by
- minimising segregation of alloying and impurity elements during solidification
- use of PHACOMP alloying guidelines (and more recently packages such as MTDATA⁹ with a suitable nickel alloy database) to minimise formation of deleterious phases
- use of directional solidification to avoid grain boundaries lying perpendicular to tensile axis (weak link)
- oxide dispersion strengthening (manufactured by powder technology).

Jensen and Tien¹⁰ investigated the relationship between microstructure and creep behaviour in Udimet 115, a γ strengthened superalloy. The alloy was heat treated to produce a bimodal distribution of hyperfine and coarse γ precipitates. They state that yield behaviour is controlled primarily by dislocation pair cutting of the hyperfine precipitates. Stage II work hardening is evidently governed mainly by the dislocation networks generated on coarse precipitates as they are bypassed by the Orowan mechanism. Stage III work hardening is said to exhibit a steady state for the stress strain deformation of the system. Extremely strong serrated flow occurs in this alloy at moderately elevated temperatures, and a stress-strain ductility minimum occurs at elevated temperatures. These appear to correlate with a change in fracture mechanism, from intergranular fracture to glide plane decohesion

2.4.1.3 Modelling of Creep

There are a number of classical theories for dislocation creep. Generally, a steady state (secondary) creep is said to arise from the balance between strain hardening and recovery. Another theory is that creep in complex alloys takes place under an effective stress, which differs from the applied stress by an amount σ_0 , the friction stress. The magnitude of this may be dependent on applied stress, temperature, solute/dislocation interactions and the presence of second phase particles. Stevens and Flewitt¹¹ studied creep theories with particular emphasis on the contribution of precipitates to the friction stress. They state that at high stress, dislocations may overcome γ' precipitates by cutting whereas at low stress bypass of precipitates involves diffusion-controlled climb. They developed a model, which considers the contribution of the back stress (resulting from the climb process) to the friction stress. This model is used to explain the decrease in creep resistance of this alloy as a consequence of precipitate coarsening at the operating temperature.

Design for creep life has been carried out by application of parametric methods. Heilmaier and Reppich¹² argue that these methods lack a physically based theory for creep and creep rupture. They aimed to extend a micro-mechanical model (Haaseen-Alexander-Ilschner) in order to predict creep rupture behaviour of two ODS nickel base superalloys. The effective stress model takes into account the hardening contribution σ_p , caused by the presence of second phase particles, in addition to the back-stress σ_p caused by dislocations. The modelled strain rate-stress dependence is transferred directly into creep-rupture stress lifetime diagrams using a modified Monkman-Grant relationship. The authors study included comparison of measured creep-rupture data to the model and they conclude that reliable lifetime predictions can be drawn at an early stage of creep.

Creep crack growth parameters have also been used to characterise behaviour for design purposes. Examples of these parameters include the stress intensity factor K_I and the path independent integral C^* . Nazmy and Wuthrich¹³ investigated the creep crack growth (CCG) in IN738 and IN939 nickel base superalloys. The authors aim was to generate data on the CCG behaviour of these alloys for analysis and determination of which parameter is most suitable for characterising behaviour for design purposes. Tests were carried out at various temperatures but mainly 850°C. The authors found that the stress intensity factor K_I was more appropriate to use for data correlation. Evidently, microstructural investigations indicated that in these alloys creep crack propagation took place by the nucleation and growth of grain boundary cavities. In their investigation the authors concluded that grain boundary

cavities were easily formed by various mechanisms and nucleation was therefore not the rate-controlling step. They concluded that the cavity growth process controls the rate of CCG.

2.4.2 Fatigue

2.4.2.1 Introduction

Fatigue can occur in a number of forms. In superalloys, relevant forms include high temperature low cycle fatigue (HTLCF), which can be due to cyclic stresses resulting from start up and shut down, isothermal low cycle fatigue and thermomechanical fatigue (TMF). Fatigue fractures can be transgranular (lower temperature) or intergranular (higher temperatures). Strengthening by solid solution or precipitation will increase fatigue strength. Precipitates can have deleterious effects in the case of lack of uniformity or instability. Fatigue at elevated temperatures shows many of the characteristics of creep rupture. As temperature is increased slip band cracking is suppressed in favour of intergranular fracture. High temperature fatigue can be described as a cyclic creep-rupture process. In γ strengthened nickel base superalloys, special attributes of γ mean that the fatigue behaviour has some unique aspects. These include hardening and softening cycles and effects due to dislocation interaction with γ particles.

2.4.2.2 Modelling of Fatigue Life

Techniques such as the strain range partitioning method (SRP) have been used for life prediction. The effect of strain rate and strain wave shape on fatigue life of IN738 has been studied by Nazmy¹⁴. Various strain rates and strain wave shapes were applied on HTLCF testing. Intergranular crack initiation and mixed crack propagation were observed mainly in slow-fast saw tooth wave, slow-slow and triangular wave. A reduction in the fatigue life of the specimens tested under these wave shapes, compared to those under fast-fast type of triangular wave shape, correspond with a variation in the fracture mode. The strain range partitioning method was applied, on the basis of a defined crack initiation criterion. The author observed that the wave shape effect on life was very sensitive when examined from the elastic strain range viewpoint. He proposes that a life prediction method that involves stresses may therefore also be worthy of consideration.

2.4.2.3 Effect of Thermal Exposure

Prior thermal exposure is a factor which may affect fatigue life, as found by Nazmy¹⁵. Prior exposure of IN738 at 1000°C for 240 hours in air resulted in an intergranular crack initiation.

This is atypical for fatigue. This was attributed to intergranular oxide penetration during service exposure. Overall, different thermal conditions were found to have different effects on fatigue life. He concluded that a Coffin-Manson plot could represent the HTLCF behaviour of IN738 alloy that had undergone different thermal exposure conditions. The Coffin-Manson equation relates plastic strain range to number of cycles to failure.

The temperature dependence of the cyclic behaviour of IN738 has been studied by Frenz, Meersmann, Ziebs, Kuhn, Sievert, and Olschewski¹⁶. Their mathematical treatment is said to show that maximum and minimum stress values measured in isothermal strain controlled tests correspond quite well with the results of non-isothermal tests. They used thermal mechanical constitutive equations based on the viscoplastic Chaboche model to describe the non-isothermal stress-strain behaviour. Their findings are said to show that IN738LC does not exhibit extra hardening or softening under the performed isothermal as well as non-isothermal cyclic non-proportional tension/torsion straining.

Hoffelner, Kny, Stickler and McCall¹⁷, studied a number of samples of IN738LC (low C and low Zr) and IN738HC (high C and high Zr). These were thermally exposed temperatures between 788°C and 982°C for times up to 20035 hours. The microstructures and phases were examined. They found;

1. TCP- σ in long term aged sample (788°C / 20000 hours)
2. Zr rich particles associated with γ/γ' islands were detected
3. Planar crystallographic defects in some γ' particles in long term aged samples were evident
4. Increase in time and temperature resulted in an increase in the mean particle diameter of primary and secondary γ' . The morphology of primary γ' changed from blocky to spherical
5. The amount of $M_{23}C_6$ particles increases with increasing ageing time and ageing temperature.

2.5 IN738LC

2.5.1 Chemical Composition

Cast nickel base superalloys have a higher volume fraction of γ than wrought superalloys, resulting in a relatively low volume fraction of matrix. This limits the maximum overall

amounts of alloying elements that partition preferentially to the matrix. The reduction in oxidation resistance due to lower chromium levels is compensated for by higher aluminium contents. However, chromium is a major source of hot corrosion resistance. Alloys 738LC and 939LC were designed to overcome this problem by having higher chromium content and correspondingly a lower γ' volume fraction.

A typical composition for IN738 is as follows (mass%):

C	Si	Cr	Co	Mo	W	Ti	Al	Zr
0.14	-	15.5	8	1.5	2.3	3.25	3.25	0.05
Ta	Nb	B	Fe	Cu	S	Ni		
1.5	0.60	0.005	-	-	-	Bal		

2.5.2 Microstructure

IN738 is a classic γ' precipitation hardened superalloy with standard alloying elements. The common heat treatment given is solution at 1120°C for 2 hours and subsequent ageing at 845°C for 24 hours. This results in the following microstructure;

- Ni-rich austenite matrix
- bimodal γ' particles - blocky particles plus fine precipitates in background
- MC distributed throughout the alloy
- $M_{23}C_6$ carbides, mainly at grain boundaries
- TCP phases (not usually present).

Various factors including melt temperature, thermal exposure and mechanical deformation can affect the microstructure.

2.5.2.1 γ'

A key characteristic of the γ' precipitate is the magnitude of the lattice mismatch with respect to the γ matrix. This has been experimentally determined by Li and Wahi¹⁸ for IN738 after various heat treatments. Creep deformed samples were also examined. The authors found a decrease in δ (varying between +0.04% and +0.08%) with increasing ageing temperature from 850°C to 950°C. They stated that heat treatment affected δ by a change in chemical composition of γ matrix and γ' phase, related to Al and Ti. Creep deformation leads to tetragonal distortion of the initially cubic γ' phase, and considerable changes in the misfit.

The effect of thermal exposure on γ in IN738 has been studied with respect to solutioning, ageing and long term exposure. A typical solution temperature applied to IN738 is 1120°C, for a soak time of two hours. It is known that this does not completely dissolve the γ phase. After investigating various combinations of solution temperatures and soak times for IN738 Balıkcı, Raman and Mirshams¹⁹ suggest a solution treatment of 1235°C for 4 hours. They found this to result in complete γ dissolution, giving a single phase solid solution. An investigation into temperatures that cause incipient melting would probably be a good complement to their work.

On isothermal ageing of IN738 at 755-850°C both primary (in cuboidal form) and secondary (spheroidal) γ precipitates obey diffusion controlled coarsening kinetics but the primary cuboids coarsen at the expense of the secondary spheroids until the spheroids disappear, Steven and Flewitt²⁰. This was found to result in a change to room temperature hardness and a loss of creep resistance.

The effect of exposure to service temperatures on γ will have an effect on mechanical strength. Stevens and Flewitt²¹ found that ageing IN738 at approximately 827°C resulted in a large volume fraction of γ , so achieving peak hardness. Ageing at 827 -1042°C (for 16 hours), however, causes a decrease in volume fraction of γ spheroids and an increase in their size, resulting in a rapid decrease in hardness. They measured an increase in hardness on exposure to 1042°C to 1194°C. Stevens and Flewitt attributed the effect they observed to dissolution of the coarse γ degenerate cuboids that bring about a redistribution of solid solution hardening elements, particularly aluminium.

2.5.2.2 Carbides

Grain refinement of conventionally cast IN738 can be affected by melt homogenisation temperature. According to Liu, Zhen, Banerji and Reif²² a low melt homogenisation temperature restrains the growth of columnar grains and produces a significant refinement of equiaxed grains. Stable, primary MC carbides can serve as nucleation substrata for the crystallisation of the γ matrix as the alloy is solidified.

The MC carbides themselves can become finer at high cooling rates, as investigated by Liu and Sommer²³ in IN738. At high cooling rates, small blocky carbides formed at superfine cell boundaries. Within the cooling rate range 10^{-2} to 10^5 °C/s, there exists a maximum value of

carbide size and volume percentage. This is evidently consistent with the variation of microsegregation level of carbide forming elements.

There is a tendency for the formation of $M_{23}C_6$ as a function of temperature and time. Swaminathan *et al*²⁴ reported that IN738 buckets exposed to service temperature for 81000 hours exhibited a continuous $M_{23}C_6$ carbide and γ network at the grain boundaries.

2.5.2.3 Topologically Close-Packed Phases (TCP)

TCP phases are intermetallic compounds involving transition elements. The atoms are more closely spaced than in normal geometrically close packed structures. These phases are often brittle and in modern superalloys are generally avoided by control of composition. Three families of TCP phases are described in the literature¹, the sigma (σ), the laves and a third that includes delta. Elements known to promote the formation of TCP phases include rhenium, molybdenum and tungsten. The most common is the σ phase, typical compositions being $Cr_{46}Fe_{54}$ and $\{(Ni)_8(Cr,Mo)_4(Cr,Mo,Ni)_{18}\}$. This phase can occur in a number of morphologies including a plate-like structure and a nodular form. Each morphology corresponds to a different orientation relationship, each with a high degree of coherency.

2.5.2.4 Dislocations and Faults

Microstructural features such as dislocations and related faults are at the root of the relationship between temperature and yield strength. According to Bettge, Osterle and Ziebs²⁵ study of IN738, the sequence of features with increasing temperature starting from 20 °C is faulted loops, APB-coupled dislocation pairs, high temperature stacking faults and Orowan loops within matrix channels. In their investigation, a drop in yield strength occurred at 450 °C and it was attributed to a change in deformation mechanism. Ductility minima were evident at certain temperatures the authors attributed these to strain localisation in single slip bands. Primary carbides cracked after a few percent of plastic strain.

The interaction between faults and γ in IN738 has been investigated by Mukherji, Jiao, Chen and Wahi²⁶. They state that the Burgers vector of a perfect dislocation in ordered $L1_2$ γ precipitates is twice that of the corresponding FCC matrix. Shearing of γ precipitates by matrix dislocations leads to various types of planar defects such as superlattice intrinsic or extrinsic stacking fault (SISF or SESF), antiphase boundary (APB) and complex stacking fault (CF). On investigation, they found three different mechanisms of interaction between

dislocations and γ precipitates. They state that the occurrence of a given mechanism depends on the particle size and test conditions of temperature, stress and strain rate.

2.5.3 Heat Treatment

Strengthening of γ containing superalloys usually requires solution treating and ageing. The solution temperature can vary from 1000°C to 1230°C. The purpose of solution treatment is to dissolve γ phase (and any other similar precipitates). Some carbides, for example lower carbides such as $M_{23}C_6$ and M_7C_3 may also be dissolved. In cast alloys the original dendritic freezing pattern is often visibly maintained. Ageing is then carried out in order to precipitate γ and strengthen the alloy. The ageing temperature range is about 760 - 1100°C and can consist of multiple stages. A typical solution temperature for IN738 is 1120°C. It is known that this does not fully solution the γ in this alloy. Hence, in addition to the hyperfine γ generated by ageing (and quenching), large irregular particles of γ exist in the background.

2.6 Rejuvenation

Rejuvenation is a term used for methods of recovering the properties (particularly creep rupture life) of a component once it has been in service. The component will have suffered a deterioration of creep properties with service exposure. This deterioration could involve one or more microstructural changes, the formation of creep voids, and cavitation. Typical rejuvenation techniques include hot isostatic pressing and re-heat treatment.

There is some debate as to whether creep rupture life is governed primarily by microstructural changes or the nucleation and growth of voids. Stevens and Flewitt¹¹ investigated the effect of reheat treatment and sintering on extending the creep life of IN738. They attributed the reduction in creep life to microstructural degradation. In particular, coarsening of γ phase precipitates was considered to be an important life-limiting factor. A possible explanation is that the ripening reduces the effectiveness of γ precipitates as barriers to dislocation motion through the friction stress concept of creep in multiphase alloys. The ultimate creep failure mode of IN738 at 750°C to 850°C was found to be growth and interlinkage of grain boundary creep cavities which assist the propagation of pre-existing oxidised grain boundary surface cracks. Successful recovery of creep properties was achieved by microstructural regeneration (reheat treatment). The heat treatment programme used was solution at 1120°C for 2 hours and 845°C for 16 hours. The authors suggested that significant cavity growth does not occur until the very late stages of rupture life. Hence, they

concluded that sintering the component, the aim of which is to eliminate the cavities, would not have significant advantages over conventional reheat treatment in IN738.

McLean and Tipler²⁷ suggest that whilst HIP treatment does heal cracks and cavities, this does not have a restoring effect on creep properties. They conducted an investigation into the rejuvenation of IN738LC turbine blades and samples undergoing creep testing and concentrated on examination of cavities and cracks rather than microstructure. They conclude that creep fracture of IN738LC occurs by the development of internal grain boundary damage largely in the final 10% of life, and not by the growth of surface cracks (for their test conditions). They state that HIP gives no greater restoration of creep strength than has been reported for simple reheat treatment.

Van Drunen and Liburdi²⁸ attributed service damage (in Inconel X-750) to a combination of surface damage and microstructural changes. Although cavities were not observed, their presence was assumed. In their study HIP reheat treated samples achieved superior creep rupture life and they recommend HIP as part of the rejuvenation treatment. Their study compared the creep rupture life of service exposed, conventional reheat treated and HIP reheat treated samples. The restoration of creep properties was achieved, according to the authors, by microstructural restoration and elimination of cavities by HIP reheat treatment.

Van Drunen and Liburdi²⁹ have also studied the effect of HIP treatments with respect to casting defects in IN738 turbine blades. Investment casting defects include shrinkage cavities, hot tears, microporosity and inhomogeneity. HIP processing can eliminate some of these. The authors carried out HIP processing and post HIP heat treatment. The samples were then tested for stress rupture strength, tensile strength and fatigue strength. They conclude that the HIP process yielded significant improvements in the mechanical properties of IN738 rotating turbine hardware. They explain that some undesirable effects can occur on HIPping, for example oxidation and nitriding. They also state that beneficial microstructural features can be destroyed during HIP processing, hence care should be taken.

Service-exposed buckets of IN738 were rejuvenated after 81000 hours²⁴. The details of the rejuvenation treatment were not available but a standard HIP treatment at 1204°C and 103.4 MPa for 2 to 4 hours is mentioned. Coating and re-heat treatment would have taken place subsequently. In this instance the authors found the rejuvenated microstructure to be unusual, being cellular. γ particles inside the cells were finer than those outside the cells. Most mechanical properties, including stress-rupture life, were not recovered.

2.7 High Temperature Oxidation

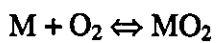
Resistance to degradation at high temperatures is often a primary requirement for superalloys, hence it is necessary to have a basic understanding of the mechanisms involved. The temperatures and atmospheres involved can vary considerably. An appreciation of the nature of alloy oxidation is important because this process is involved in degradation and protection.

2.7.1 Principles of Metal Oxidation

A reaction occurs between metal and gas at high temperature. Thermodynamics can predict the relative stability of oxides with respect to the base metal but do not predict how protective they will be. The rate of growth of an oxide scale (kinetic) depends on the specific physical crystallographic and morphological nature of the corrosion products. The basis for development of oxidation-resistant alloys is the formation of a protective oxide barrier between the metal and the environment. The principles of high temperature metal oxidation are described in Birks and Meier³⁰.

2.7.1.1 Thermodynamics

The study of thermodynamics including Ellingham diagrams can predict whether spontaneous oxidation will occur. Consider the reaction:



The oxygen partial pressure at which the metal and oxide coexist is effectively the dissociation pressure of the oxide, $P_{O_2}(M / MO_2)_{eq}$. This is given by

$$P_{O_2}(M / MO_2)_{eq} = \exp \frac{(\Delta G^0)}{RT}$$

ΔG^0 is the Gibbs free energy

T is temperature

R is the universal gas constant

For alloy oxidation the activity of the metal a_m is not unity, hence

$$(P_{O_2})_{eq} = \frac{a_{MO_2} \cdot \exp \left(\frac{\Delta G^0}{RT} \right)}{a_M} = \frac{a_{MO_2}}{a_M} \cdot P_{O_2}(M / MO_2)_{eq}$$

P_{O_2} is partial pressure of oxygen

thus, if metal M is exposed to O₂ (with partial pressure of O₂ being $P_{O_2}^*$), spontaneous oxidation will occur if

$$P_{O_2}^* > P_{O_2}(M / MO_2)_{eq}$$

2.7.1.2 Kinetics

Two possible oxidation rate laws are parabolic (growth rate is dependent on scale thickness and hence diffusion) and linear (growth rate is controlled by a surface reaction and is independent of scale thickness). The parabolic rate law is the more common and the reaction kinetics are often controlled by rates of transport of metal ions or oxidant across the barrier oxide scale.

2.7.2 Oxidation of Alloys

Oxidation of alloys is more complex than that of pure metals because the constituent elements may have different affinities for oxygen, the oxides may have different diffusion rates, tertiary oxides may form and other factors. Nickel base alloys generally rely on protective Cr₂O₃ and Al₂O₃ scales for oxidation resistance. Cr₂O₃ oxide is protective up to about 900°C, above this temperature Al₂O₃ is more effective. The precise minimum concentration needed to form an external healing layer depends on various factors such as temperature, oxygen partial pressure but is about 15%Cr for nickel base alloys (a greater concentration is required for a purely Cr₂O₃ external layer). As stated in section 2.5.1, IN738 contains a relatively high chromium content for superior resistance to hot corrosion.

Al₂O₃ is thermodynamically very stable. In binary Ni-Al alloys, an approximate minimum of 17wt% Al is required to form protective Al₂O₃. This relatively large figure is dictated by reaction kinetics. Nickel base alloys (and others) containing both chromium (at about 10 %) and aluminium benefit from a synergistic effect which allows Al₂O₃ to form at low levels of aluminium, about 5% Al. Smaller amounts of aluminium may enable a partial Al₂O₃ layer to develop at the base of the Cr₂O₃ scale, which is more protective than Cr₂O₃ alone. This allows more flexibility in the composition of substrates and MCrAl type coatings.

Failure of the protective scale can occur under conditions where it grows excessively. As the Cr₂O₃ or Al₂O₃ scale thickens, depletion of chromium or aluminium in the alloy at the alloy/scale interface occurs. Mechanical disruption of the layer can expose the substrate, which does not contain enough Cr/Al to form a protective layer. Breakaway oxidation of NiO could then occur. Another problem associated with these scales is that they are prone to

spalling, particularly on cooling. Small amounts of reactive elements such as yttrium result in a considerable improvement in mechanical integrity and adhesion of the protective scale, hence MCrAlY coatings.

The number of alloying elements in superalloys can result in complex oxidation behaviour. The oxidation performance of IN738X has been investigated in comparison with that of IN713C and two other alloys. The work by NASA has been summarised in Sims *et al*³. The test conditions included isothermal and cyclic oxidation at 900°C to 1100°C. The performance of IN738X was found to be relatively poor under these test conditions. The compositions of the scales of these materials at high temperatures can be quite complex. Titanium enrichment is associated with outer scales in IN713C and IN738X. In IN738X the Cr₂O₃ content of the scale was found to reach a maximum in time and was then overtaken by substantial NiO and NiCr₂O₃ scales that ultimately cause breakaway cyclic behaviour.

2.8 Coatings

Coatings provide protection against both high temperature oxidation/corrosion and reduction of mechanical properties due to diffusion of harmful species into the substrate. Generally, coatings on superalloys protect by forming adherent oxide scales using elements such as Al, Cr and Si, as previously discussed. The coating is rich in these elements as thermal cycling and mechanical damage cause the scale to spall, necessitating the formation of new scale.

There are numerous types of coating. The most relevant for superalloys are diffusion coatings and overlay coatings. The most common methods of implementing diffusion coatings are pack cementation and vapour deposition. Aluminising of nickel base alloys is an example. Overlay coatings are commonly applied by plasma spraying or electron beam physical vapour deposition (EBPVD). NiCrAlY coatings on superalloys are examples. The coating types are described in more detail in the following sections.

2.8.1 Diffusion Coatings

This method relies on the occurrence of diffusion between the coating and the substrate. Aluminium, chromium and silicon can be used to create coatings. The aluminide coating is of primary interest here. A number of processes are available, two of which (pack aluminising and chemical vapour deposition) are detailed below.

2.8.1.1 Pack Aluminising

The component is placed in a pack that consists of aluminium containing powder, a halide chemical activator and an inert filler such as alumina. On heating in an inert atmosphere the metal powder and activator react to form a vapour. This vapour in turn reacts with the surface of the component, enriching it with aluminium. In a nickel base alloy, the phases which form are Ni_3Al , NiAl , and Ni_2Al_3 . The aluminide can diffuse inward or outward with respect to the surface. This depends on the activity of aluminium with respect to the nickel.

Thermal treatments used for pack aluminising IN738 can affect the γ' morphology and creep rupture strength, McColvin³¹. A typical thermal cycle for pack aluminising is 1060°C for 90 minutes, then cooling to 850°C in 10 minutes and finally to room temperature in 2 hours. In thin sections, a significant decrease in volume fraction of primary γ' precipitates as well as an increase in size of these particles was evident. These changes are said to result in a drop in creep rupture life under high stress, low temperature test conditions.

2.8.1.2 Chemical Vapour Deposition

A vapour of predetermined composition is introduced into the coating chamber where it reacts with the surface of the component. Internal passages can be coated in this manner.

2.8.1.3 Comments on Aluminising

The significant phase is β -NiAl. β -NiAl is a high melting point phase. The solubility of most other superalloy substrate elements in NiAl is small. They are therefore mostly rejected from the layer and precipitate in the forms of carbides, metals (e.g. α -Cr) and TCP phases. These phases are found in the interdiffusion zone between the coating and substrate.

Recently, the effect of platinum additions has been studied. Whilst adding platinum is known to enhance oxidation resistance, Newcomb and Stobbs³² study noted that relative to simple aluminide coatings, the platinum promotes formation of fine grained NiAl which in turn leads to higher rates of diffusion. Microstructures of Al and Pt-Al degraded coatings are dominated by transformation of the B2 phase to a modified structure. This occurs at an earlier stage in the Pt-Al coating than in an Al coating. It is proposed that platinum blocks the continued loss of aluminium into the alloy as well as the inward ingress of oxygen through the coating.

The isothermal oxidation kinetics of platinum modified aluminide coatings on IN738 was studied by Niu, Wu, Boone, Smith, Zhang and Zhen³³. The authors found that the oxidation

kinetics of four coatings followed a parabolic rate law up to about 400 hours. Pt modified coatings showed smaller oxidation rates than simple aluminide coatings. Oxidation was generally found to result in the formation of Al_2O_3 scales. Ni_3Al formed at the scale-coating interface and propagated across the whole NiAl layer. Scale spalling led to fast growth of poorly protective oxides across the whole coating resulting eventually in their complete degradation. The authors propose that the presence of Pt had significant beneficial effects by promoting the formation of purer and thinner Al_2O_3 scales during the early stages, lowering the rate of NiAl degradation and delaying the onset of spalling.

The nature of the interdiffusion layer may provide some insight into the environmental history of a coated component. It is therefore worth noting characterisations that have been carried out. Basuki, Crosky and Gleeson³⁴ studied the interdiffusion behaviour in aluminide coated Rene 80H at 1150°C. They point out that at elevated temperatures the stability of a diffusion aluminide coating is affected by selective oxidation and hot corrosion processes, and interdiffusion between coating and substrate. Overheating resulted in various microstructural changes from the as-coated structure. In particular they observed initial homogenisation and consequent thickening of the coating β layer, followed by recession of the layer. The authors say that the driving force for the coating / substrate interdiffusion is the difference in thermodynamic activities of elements in the coating and substrate. The coating enlarged until it had entirely homogenised to a β -NiAl composition of maximum nickel content. After this point the β layer began to recede. They conclude that the phase transformations are best explained through the application of diffusion paths in the Ni-Cr-Al phase diagram

2.8.2 Overlay Coatings

To manufacture an overlay coating, a pre-alloyed material containing elements necessary to form an adherent protective scale is applied to the surface. Interdiffusion is required only for bonding. This method is used to apply the MCrAlY type coatings described in section 2.7.2.

Mazars, Manesse and Lopvet³⁵ have summarized the use of different types of MCrAlY coatings as follows;

NiCrAlY	-	high temp. applications > 900°C
CoCrAlY	-	medium temp. (700°C to 900°C)
FeCrAlY	-	moderate temp. gasification atm. < 700°C

The two common methods are physical vapour deposition (PVD) and plasma spraying.

2.8.2.1 Electron Beam Physical Vapour Deposition (EBPVD)

EBPVD is the most common physical vapour deposition method for coating superalloys. An ingot of the appropriate composition is vaporised in a vacuum using a focused electron beam. The parts to be coated are manipulated within the vapour cloud with the metal condensing out on the preheated substrate surface.

The composition of the coating may change from that of the ingot. A typical coating would be CoCrAlY (Co -19Cr-12Al-0.3Y). Bonding is achieved by post coat heat treatment.

2.8.2.2 Plasma Spraying

The coating material is a pre-alloyed powder that is injected into a high temperature plasma gas stream that has been created inside a plasma gun. The powder particles are melted and accelerated towards the substrate, solidifying on contact. Adherence is again achieved by post-coat heat treatment.

2.8.2.3 Comments on Overlay Coatings

Both EBPVD and plasma spraying are line of sight processes and therefore can be problematic for complex shapes. These two processes cannot coat internal passages, in contrast to aluminising.

Nicoll *et al*³⁶ investigated the solubility ranges of individual additions of silicon and titanium to MCrAlY superalloys. The level of silicon was found to drop with increasing aluminium content, no dependence on aluminium content was found with titanium. Both silicon and titanium were found to promote the formation of thin tenacious Al₂O₃ scales that showed little spalling under cyclic conditions at 1000°C.

As stated previously in section 2.7.2, yttrium improves the adhesion between an MCrAlY coating and the Al₂O₃ scale. The role of yttrium in the MCrAlY coatings was investigated by Tawancy *et al*³⁷. They found that with such a coating on a Ni- based superalloy, the yttrium segregated within an 5µm external surface layer of the coating, as well as within the interdiffusion zone. After exposure at 1000°C and 1100°C in still air, preferential segregation of Y to grain boundaries within the Al₂O₃ scale was evident. A number of mechanisms are suggested for the manner in which yttrium modifies the behaviour of the scale. These include the presence of oxidised yttrium 'pegs' within the Al₂O₃ scale,

improving mechanical adherence to coating. The presence of Y in the scale in solid solution and at grain boundaries is said to reduce scale growth rate.

2.8.2.4 Microstructure of Coating

The microstructure of MCrAlY coatings is dependent on the composition. The β phase is normally present, this being the phase with high aluminium content.

Czech, Schmitz and Stamm³⁸ investigated MCrAlY coatings with small additions rhenium 1-3%. They tested three coatings with and without rhenium. Two coatings that contained Re had different aluminium contents. The authors found the bulk coating to consist of four phases which they determined to be $\text{Ni}_{13}\text{Co}_4\text{Cr}_{83}$ (α), $\text{Ni}_{13}\text{Co}_{17}\text{Cr}_{53}\text{Re}_{17}$ (α), $\text{Ni}_{47}\text{Co}_9\text{Cr}_7\text{Al}_{34}$ (β), $\text{Ni}_{39}\text{Co}_{22}\text{Cr}_{28}\text{Al}_9\text{Re}_2$ (γ).

With the higher aluminium coating, thermal exposure for 3000 hours at 1000°C caused the Cr-rich phase to go into solution near the surface. Thermal exposure resulted in β depletion in the two coatings containing 15%Al but not that containing 24%Al.

2.8.3 Coating Performance

Aluminide coatings provide a protective Al_2O_3 layer. Thermal cycling and spallation of the film results in diffusion of Al from the coating to reform the scale. When the Al in the coating falls below about 4-5 wt% Al, a continuous Al_2O_3 layer can no longer be formed, rapid degradation will then occur.

Cheruvu *et al*³⁹ report that in aluminide and platinum modified aluminide coatings the β phase is partly transformed to γ' phase as a result of thermal exposure. They suggest that longer term thermal exposure will lead to transformation of γ' to γ .

Overlay coatings (e.g. NiCoCrAlY) also provide a protective a Al_2O_3 layer. This is superior to the aluminide coating because:

1. The presence of chromium increases the activity of the aluminium
2. Yttrium improves spallation resistance of the Al_2O_3 layer

Cobalt improves coating ductility and imparts some extra environmental degradation resistance. MCrAlY coatings usually have higher melting points than aluminide coatings.

MCrAlY coatings generally include a high proportion of β phase. These act as Al reservoirs for formation of Al_2O_3 . In service, the outer Al_2O_3 layer tends to spall off and Al is used up to re-form the layer. Further, interdiffusion between the coating and the substrate can also deplete the β phase. Hence, β depleted zones can occur at the outer surface of the coating (outer depleted layer) and adjacent to the interdiffusion layer (inner depleted layer)^{39,40,41,42}. It should be noted that clearly defined zones of these types would not always be present⁴².

Failure of MCrAlY coatings can occur due to due to loss of oxide and β -phase recession at the interdiffusion zone by diffusion of Al and Cr into the substrate, Dayananda, Behnke, McCaslin⁴³. Diffusional and thermodynamic interactions among alloy and coating elements are identified from an analysis of concentration profiles on the basis of observed uphill diffusion or zero flux plane (ZFP) development for the components. The interdiffusion of chromium was found to be enhanced down the gradient of aluminium and vice versa. The loss of Al from the coatings is also enhanced by a negative Co gradient into the substrate. The authors conclude that in order to reduce Al and Cr diffusion (thereby reducing β phase depletion) control composition of coating and substrate to result in smaller negative gradients for both Cr and Co towards substrate

Researchers have found that rhenium can have a beneficial effect on the oxidation and corrosion resistance of MCrAlY coatings. Czech *et al*^{44,38} consider this improvement to be due to the formation of a CrRe-rich phase below the oxidation layer. This phase is also said to influence the activity of Al to produce a dense Al_2O_3 oxide layer.

2.8.4 Interdiffusion Zone

Reactions occur within the coating and between the coating and the substrate, resulting in an interdiffusion zone.

2.8.4.1 Microstructure

The most common phases to appear in the coatings are γ , β , and γ' . Meisenkothen and Morral⁴⁵ studied 21 couples; Metal A (9.0% Cr, 18.1% Al), Metal B (6-20% Cr, 19-28%Al) – 21 variations. At 1200°C they found various combinations of γ , β , and γ' . The microstructure depends on temperature, initial coating composition and changes that might occur in coating composition during service.

They constructed an interdiffusion microstructure map (IMM). The IMM map was considered to be divided into five regions, the boundaries of which meet at a five line node.

The result of this is that small changes in the initial coating composition can yield significantly different microstructures and presumably different rates of interdiffusion

Mazars, Manesse and Lopvet³⁵ mention a crossed invariant reaction at 1000°C.



They say that interdiffusion mechanisms depend upon nature of the two opponents of the diffusion couple / substrate. A NiCrAlY coating on nickel base substrate, results in limited interdiffusion at 1100°C. The structure consisted of a chromium enriched matrix with some islands of chromium carbides, and local penetration into substrate. Prolonged exposure leads to lakes of γ' forming at lower boundary of internal diffusion zone.

Enrichment at the interdiffusion zone in NiCoCrAlY is due to Al and Co diffusion from the coating into the base material.

NiCrAlY and NiCoCrAlY coatings on an unnamed substrate were investigated by Morra Sisson and Biedermann⁴⁶. The samples were heat treated at 1080°C for an unspecified length of time. The primary microstructural regions that developed were $\beta + \alpha$ and $\gamma + \gamma'$. This phase distribution can develop on cooling from 1080°C with the $\beta + \gamma$ or $\gamma + \beta + \alpha$ phases to 900°C or room temperature with the $\alpha + \gamma' + \beta$ phases. During cooling the β phase will start to decompose to α while γ' will form in the γ . The resulting microstructure is a mixture of $\beta + \alpha$ in the dark region with $\gamma + \gamma'$ in the light region. The authors claim to have observed $M_{23}C_6$ carbides, due to diffusion of C into coating and carburization of Cr.

Czech, Schmitz and Stamm³⁸ investigated MCrAlY coatings, some with small additions rhenium 1-3%. Higher Cr content was found at interdiffusion zone in all tested alloys. This is explained by partial dissolution of the β phase in this area, which allows Al to diffuse into base material. This would normally result in precipitation of γ' , but in the presence of Co only γ is observed. γ has a higher solubility for Cr, hence the higher driving force from Cr from coating and base material into interdiffusion zone.

In a CoCrAlY coating on a GTD-111 substrate Cheruvu *et al*³⁹ state that growth of the interdiffusion zone is due to outward (from the base metal) diffusion of nickel and inward diffusion of aluminium, chromium and cobalt. Ellison, Daleo and Boone⁴⁷ specifically studied interdiffusion zones in DS GTD-111 alloy, with a CoCrAlY coating thermally exposed at 850, 950, 1000 and 1050 °C. They found interdiffusion between the coating and

the substrate to result in $\gamma + \beta$ growth zones below the original interface. The Al diffusion at the interdiffusion layer is said to be due to a $\gamma + \beta / \gamma + \gamma'$ diffusion couple.

Mathematical modelling has been applied to interdiffusion of high temperature coatings, Morral, Jin and Hopfe⁴⁸. Modelling can be used to predict chemical changes due to interdiffusion between a coating and substrate. There are three steps in the modelling process, microstructure prediction, concentration profile modelling and interpretation of results. This was applied to both aluminide and MCrAlY coatings on superalloys. The authors concluded that by considering the phase diagram associated with MCrAlY coatings on superalloys it can be seen that numerous microstructures may occur depending on the initial coating and superalloy compositions.

Peichl and Johner studied a number of phenomena in the interdiffusion zone⁴⁹. They noted that interdiffusion between materials of different chemical composition can cause pronounced porosity near the interface because of the Kirkendall effect. This effect has been found on several MCrAlY coating-substrate combinations e.g. NiCrAlY / MA754 and can in its final stage lead to complete separation of coating and substrate.

They also investigated the precipitation of acicular phases at the interdiffusion zone. In W-containing MarM002 with certain MCrAlY coatings, W-rich plate-like and cubic phases have been observed, with precise 45° orientation of their longitudinal axis to the $\langle 100 \rangle$ orientation of the base metal. The authors note that there is a possibility of misinterpreting the nature of Cr rich acicular phases at the interdiffusion zone because of the considerable lattice coherency between σ and $M_{23}C_6$. They hence investigated in detail acicular phases at the interdiffusion zone in IN100 with a number of coatings. A high concentration of N, presumed to have diffused from the atmosphere, was associated with the needles. Analysis by techniques including Auger and XRD indicated the needles to be $M_{23}C_6$ carbides, composition $Cr_{21}Mo_2C_6$. The main orientation of their growth was on the 111 lattice into the substrate. Itoh and Tamura⁵⁰ have also reported chromium carbides at the interdiffusion layer.

2.8.4.2 Growth of Interdiffusion Zone

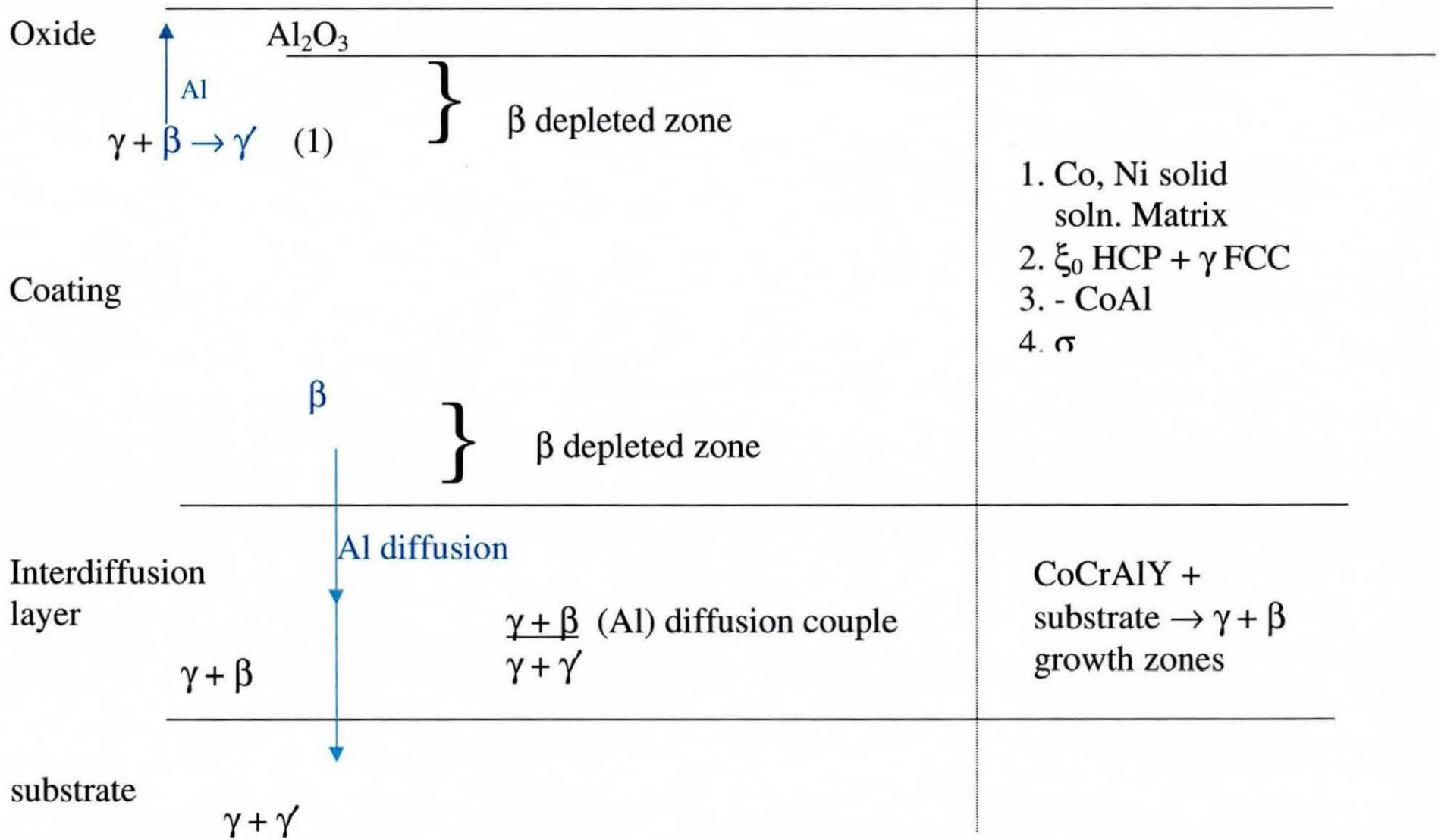
Itoh and Tamura⁵⁰ have investigated the kinetics of interdiffusion zone growth, studying three substrates including IN738LC and four types of MCrAlY coating. They describe the interdiffusion zone, in a general sense, to consist of an Al compound layer and an Al compound depleted layer. The growth of the interdiffusion zone was found to be parabolic.

For the four types of coating, they found the order of reaction diffusion rate to be NiCrAlY > CoCrAlY > CoNiCrAlY > NiCoCrAlY. They consider the growth of the interdiffusion zones to be controlled by mutual diffusion of Ni and Co elements through the reaction layer. A computer aided system for analysing interdiffusion zone growth was developed, enabling prediction of long term diffusion behaviours.

Coating substrate interdiffusion can shorten the life of a coating⁵¹. Diffusion barriers between overlay coatings and substrates have been examined to extend the protective life of the coating. A finite-difference diffusion model has been modified to predict the oxidative life enhancement due to use of a diffusion barrier. The original COSIM model simulates Al diffusion in the coating to the growing oxide scale as well as Al diffusion into the substrate. The modified model predicts the oxidative life of an overlay coating when a diffusion barrier is present eliminating diffusion of Al from the coating into the substrate.

The stress state can have a significant influence on the magnitude of the diffusion affected zones and the velocity of interdiffusing species, in a single crystal alloy, as studied by Sanz, Llanes, Bernadou, Anglada, and Lappaccini⁵². The nature of the zone beneath the coating (e.g. the γ rafting behaviour) is also said to affect the diffusion phenomena. However, two similarly rafted γ sub-coating microstructures do not necessarily lead to similar interdiffusion phenomena. Some microstructural transformation sequences are said to be influenced by the nature and frequency of the loading, and by the stress state. They mention the $\beta \rightarrow \gamma' \rightarrow \gamma$ transformation in particular. Pre-damage treatments were found to result in similar rafted microstructures under a NiCoCrAlYT_a coating even for different superalloys, by Sanz, Llanes, Bernadou, Anglada, and Lappaccini⁵³. They again state, however that similar rafted morphologies do not lead to similar creep behaviour.

2.8.5 Schematic of Surface Layers^{3,40,47}



Among the major life limiting factors of coatings are stresses arising from thermal cycling, and PtAl coatings can be resistant according to De Gaudezin, Colombo, Rocchin and Uberti⁵⁴. These can result from start up / shut down and changes in operational regime. Tests were carried out on coated and uncoated samples. They tested a PtAl coating and CoNiCrAlY coatings. The samples were tested in an atmosphere containing sodium sulphate under thermal cycling conditions. They found that PtAl coating succeeded in preventing corrosion attack. CoNiCrAlY coatings underwent damage to different extents as a consequence of oxide scale loss of integrity and / or spallation.

2.8.6 Coating Life Prediction

Chan⁵⁵ developed a mechanism (rather than empirical) based model, for coating life prediction. He adopted a fracture mechanics approach that results in explicit relationships between weight of oxide spalled and relevant physical and mechanical properties of the oxide. These include the process driving force (thermal stress), and the response parameters, weight of oxide spalled, oxide weight gain and weight loss of oxide forming element.

Chan *et al*⁵⁶ extended the above model to predict the usable life of a coating. The life prediction, methodology involved the consideration of loss of the oxide-forming element, Al. The volume fraction of the main Al containing phase, β , is calculated. The remaining life is defined based on the assumption that the useful life of the coating is zero when the volume fraction of the β phase is zero. At this stage the model assumes loss of Al is due to outward diffusion, to form the oxide. This model was extended to include the effect of inward diffusion of Al into the substrate⁵⁷. Coating life diagrams for GTD111 with MCrAlY, PtAl and aluminide coatings were constructed and compared with experimental data. The authors consider that the model shows promise as a predictive tool for forecasting useful life of combustion turbine coatings in service.

A further step in this model is examination under variable temperature conditions, as blades experience complex thermal histories. The model was used to predict the response of the coating under single step and multi step temperature conditions⁵⁸. Comparison of predicted and experimental data indicated, according to the authors, that the proposed life prediction methodology is applicable for thermal cycling involving variable temperatures.

Kartavova *et al*⁵⁹ propose a model for lifetime prediction of coatings by considering alloying element diffusion and oxide layer formation. They assume a critical oxide layer thickness of 4 μ m, stating that experiments show that spallation occurs after this thickness. Using

diffusion coefficients, concentrations of total Ni, Cr, Al and Co were computed as well as kinetic of Al_2O_3 growth. They develop an equation for outer boundary of oxide layer in terms of integrals of element concentrations w.r.t. distance from boundary (with constants and other factors). Numerical methods are used to determine parameters.

The prediction of concentration profiles in the coating has also been the subject of study. Lee *et al*⁶⁰ proposed a numerical based model, based on the finite difference method to develop the solutions to the various diffusion equations for aluminium diffusion in the coating. Previous, similar models, predicted concentration profiles in a single phase region. The authors model also predicts $\gamma(\gamma+\beta)$ interface motion and β phase life. The results of the model were compared with experimental results for the isothermal oxidation of a CoCrAlY coating on MM509. Good agreement was found where diffusion coefficients were known.

2.8.7 Time -Temperature Correlation

Properties of the turbine blade bulk and coating can be used to estimate exposure time and temperature. Srinivasan *et al*⁴⁰ suggest that the width of the Al depleted zones mentioned in section [2.8.3] grow as a function of temperature and time and can be used to estimate local service temperature. These authors compared use of these measurements with estimates based on γ coarsening and reported good correlation. Cheruvu *et al*⁴² investigated estimating time-temperature correlation by analysing γ size and the width of the interdiffusion zone. They came to the conclusion that for their subject material (GTD-111), time-temperature correlation would be easier and less time consuming by analysis of interdiffusion zone thickness.

Ellison *et al*⁴⁷ made a detailed study of producing temperature estimates based on interdiffusion zone thickness between a CoCrAlY overlay coating and a directionally solidified GTD-111 substrate. Their interdiffusion zone consisted mainly of $\gamma + \beta$ growth zones. They found the width of the interdiffusion zone to be proportional to $t^{1/2}$ (t representing time). The authors developed a temperature estimation model based on quantitative analysis of the $\gamma + \beta$ interdiffusion zone. This requires calibration for the system of interest.

3 Experimental Methods

3.1 Introduction

The experimental part of the test programme included characterisation of the effect of thermal exposure as a function of time, in air, on;

- IN738LC alloy substrate
- MCrAlY coatings SC2453 and RT122, and their interaction with IN738LC substrate.

Appropriate materials and analytical techniques were needed to achieve these characterisations. The objective of this chapter is to describe the materials investigated, the tests applied and the analytical methods used.

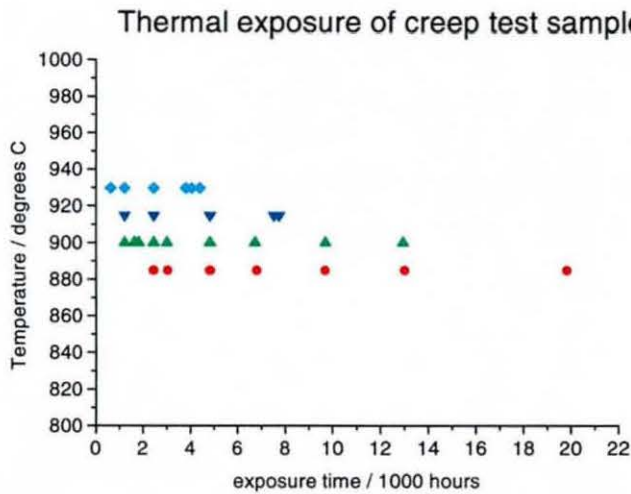
The bulk material is IN738LC, a conventionally cast nickel base superalloy as described in Chapter 2. The four coatings applied to these materials are denoted as SC2453, SC2231, SV20 and RT122

Techniques used to analyse these specimens include optical microscopy, X-ray diffraction, scanning electron microscopy, energy dispersive X-ray analysis and auger electron spectroscopy.

3.2 Test Programme

The purpose of the experimental test programme, as stated in the introduction, is to characterise the effect of thermal exposure in air on IN738LC and the coatings. This necessitates a test programme that will provide samples that have been subjected to thermal exposure at varying time and temperatures, corresponding to those imposed on turbine blades in service.

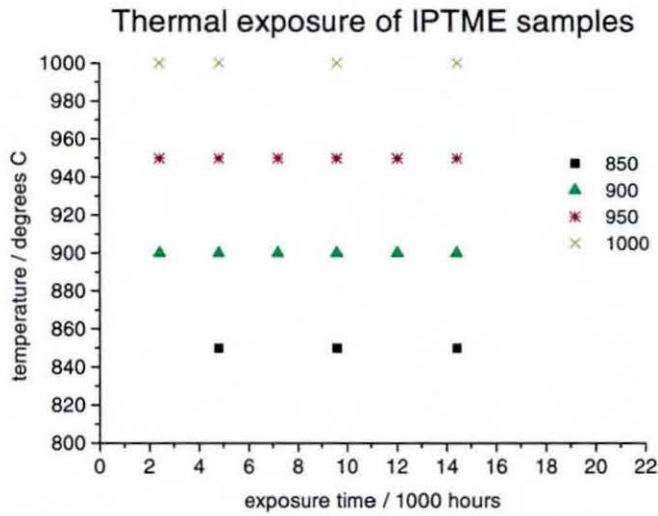
It was known that creep tests of coated IN738LC test bars were being carried out at a laboratory on behalf of Innogy, and that these samples would become available. Full details of these samples are shown in Table 3.2. The thermal exposure experienced by these samples is shown in Figure 3.1 below,

Figure 3.1 Thermal exposure experienced by creep test samples

Some smaller programmes of fatigue and rejuvenation evaluation were also being carried out. However, the time and temperature combinations in these test programmes were not deemed to provide sufficient data for a time temperature recorder. Further, late availability of the creep samples, particularly the long term tests, would hamper the investigation.

Additional (plate) material was therefore provided by Innogy. Coated and uncoated plate material would be supplied for additional tests considered appropriate by IPTME. The uncoated plate would be used to characterise any heat-treated state for IN738LC not supplied by other samples. The coated plate would be used in a separate IPTME thermal exposure programme. This was designed to facilitate investigation of the effect of thermal exposure on the coatings and bulk substrate. This programme would be used to provide a systematic sequence of time and temperature characterisation. With respect to the microstructure, consistent conditions are preferable when examining various times and temperatures. The IPTME sequence was thus required to provide a set of samples over a comprehensive range of temperatures and exposure times. The programme for heat treatment of the plate samples at IPTME is detailed in Table 3.3 and shown in Figure 3.2 below,

Figure 3.2 Thermal exposure of coated IPTME samples



The above sequence was to be used to characterise the microstructure of the coating, in addition to substrate.

The thermal exposure experienced by both creep tests and IPTME samples are summarised in Figure 3.3.

Figure 3.3 Thermal exposure of both creep and IPTME samples

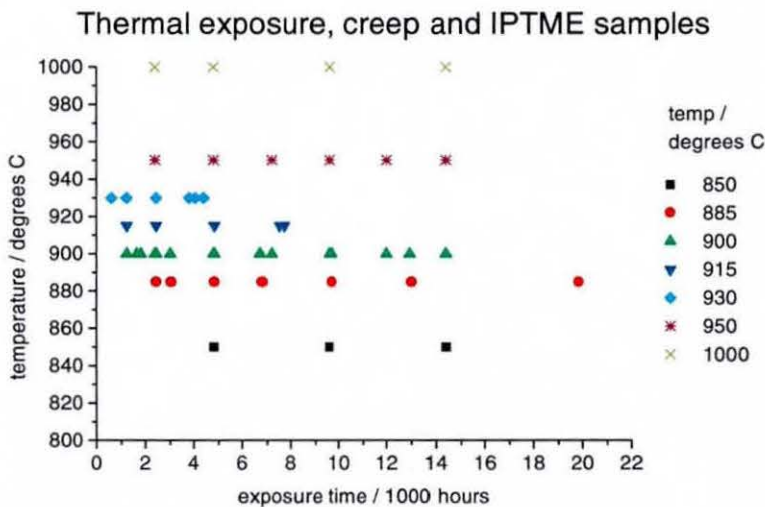


Table 3.1 Overview of test programme material

IPTME Lab ID	Base metal	Heat treatment and test cycle
G0	IN738LC bar 1	HIPped virgin material
G1	IN738 bar-1	HIPped, solution treated, aged, low cycle fatigue tested, various rejuvenation treatments and further testing
G2	IN738LC bar 1	HIPped, solution treated, aged, creep-fatigue tested, various rejuvenation treatments and further testing
G3	IN738 bar-2	As cast and solution treated
G4	IN738LC bar 2	HIPped and solution treated
G5	IN738 bar-2	HIPped, solution treated and aged
G6	IN738LC bar 2	As cast, solution treated and coated
G7	IN-738 bar-2	HIPped, solution treated, coated, solution treated and aged
		HIPped, solution treated, coated, solution treated, aged, creep tested to different life fractions
G8	IN738 Plate	HIPped
G9	IN738LC Plate	HIPped and solution treated
G10	IN738LC Plate	HIPped, solution treated and aged
		HIPped, solution treated and aged, thermally exposed at high temperatures
G11 to G13	IN738 Plate	HIPped, solution treated, aged, coated, solution treated and aged, thermally exposed at various temperature/time combinations
G14	IN738LC plate	Long term creep test programme at 850°C

'coated' here refers to all 4 coatings

'HIP' is hot isostatic pressing

Not all of the above groups were used; G3, G4, G5, G8, G9. Highlighted boxes indicate major parts of test programme. Samples from the G7 group comprise part of a large, separate, creep testing programme and analysed during the course of this research. Samples G11-13 comprise material heat treated isothermally at Loughborough and are described in detail in Table 3.3.

Table 3.2 G7 coated creep test samples

test ID	external coating	test type	test temp. / °C	life hours
D-01	RT-122	none		
D-06	RT-122	string	930	612.00
D-07	RT-122	string	930	1224.00
D-02	RT-122	string	930	2448.00
D-08	RT-122	string	915	1224.00
D-09	RT-122	string	915	2448.00
D-03	RT-122	string	915	4833.00
D-10	RT-122	string	900	1224.00
D-11	RT-122	string	900	2448.00
D-12	RT-122	string	900	4833.00
D-04	RT-122	string	900	9707.00
D-05	RT-122	string	885	19852.00
B-01	SC2231	none		
B-06	SC2231	string	930	612.00
B-07	SC2231	string	930	1224.00
B-02	SC2231	string	930	4056.00
B-08	SC2231	string	915	1224.00
B-09	SC2231	string	915	2448.00
B-03	SC2231	string	915	7743.00
B-10	SC2231	string	900	1224.00
B-11	SC2231	string	900	2448.00
B-12	SC2231	string	900	4833.00
B-04	SC2231	string	900	1816.00
B-05	SC2231	string	885	19852.00
A-01	SC2453	none		
A-12	SC2453	string	930	612.00
A-13	SC2453	string	930	1224.00
A-02	SC2453	creep	930	4408.00
A-14	SC2453	string	915	1224.00
A-15	SC2453	string	915	2448.00
A-03	SC2453	creep	915	7533.00
A-16	SC2453	string	900	1224.00
A-08	SC2453	creep	900	1637.00
A-07	SC2453	creep	900	3010.00
A-17	SC2453	string	900	2448.00
A-06	SC2453	creep	900	6719.00
A-18	SC2453	string	900	4833.00
A-04	SC2453	creep	900	12930.00
A-19	SC2453	string	885	2448.00
A-11	SC2453	creep	885	3045.00
A-10	SC2453	creep	885	6802.00
A-20	SC2453	string	885	4833.00
A-09	SC2453	creep	885	13010.00
A-21	SC2453	string	885	9707.00
A-05	SC2453	creep	885	19852.00
C-01	SV20	none		
C-06	SV20	string	930	612.00
C-07	SV20	string	930	1224.00
C-02	SV20	string	930	3802.00
C-08	SV20	string	915	1224.00
C-09	SV20	string	915	2448.00
C-03	SV20	string	915	4833.00
C-10	SV20	string	900	1224.00
C-11	SV20	string	900	2448.00
C-12	SV20	string	900	4833.00
C-04	SV20	string	900	9707.00
C-05	SV20	string	815	19852.00

Table 3.3 G11 to G13 Loughborough heat treatment samples

Exposure time / hours Date completed	SV-20	RT-122	SC2453	SC2231
	Temperature / °C			
14400 22/09/00	850	850	850	850
	900	900	900	900
	950	950	950	950
	1000	1000	1000	1000
12000 14/06/00	900	900	900	900
	950	950	950	950
9600 06/03/00	850	850	850	850
	900	900	900	900
	950	950	950	950
	1000	1000	1000	1000
7200 27/11/99	900	900	900	900
	950	950	950	950
4800 19/08/99	850	850	850	850
	900	900	900	900
	950	950	950	950
	1000	1000	1000	1000
2400 11/05/99	900	900	900	900
	950	950	950	950
	1000	1000	1000	1000

3.3 Material

The materials used include a number of casts of IN738LC, and MCrAlY coatings.

The IN738LC material used in this work came from three batches, denoted by;

- bar 1
- bar 2
- plate.

The four MCrAlY coating designations were SV20, SC2231, SC2453 and RT122. They were applied to;

- IN738LC bar 2 creep test samples
- IN738LC plate samples for thermal exposure.

Coatings SC2453 and RT122 were selected for detailed investigation.

Knowledge of the composition of these materials was essential to facilitate experimental analysis. Hence, chemical analyses were obtained for each of the materials. An analysis from an example of each cast is commonly used for quality control of bulk materials, such as IN738LC in 1-3 above. With respect to coatings, it is possible for compositions to vary between applications, but the extent of this is not known. It is assumed that quality control procedures would be in place to attempt to minimise variation. A single analysis was carried out on an example from each coating in order to provide a point of comparison for further work. The coating samples chosen had only been subjected to the coating treatment cycle. The measured compositions of the bar, plate material and the coatings, as supplied by Innogy, are given in Table 3.4.

Table 3.4 Compositions of samples used in this research (mass%)

Element	Specification N POW - IN738LC- rev3.0		Deritend analysis	Howmet Analysis	Plate Inco analysis	INCO analysis			
	Min.	Max.				Bar 1	Bar-2	Plate	Coatings
						SV20	SC2231	SC2453	RT122
Carbon	0.09	0.13	0.10	0.096	0.092				
Silicon		0.3	0.01	0.03	0.03	2.23	0.55	0.13	0.19
Manganese		0.2	0.01	0.01	<0.01	0.01	0.01	0.01	0.01
Phosphorus		0.015	0.004	<0.005	<0.01	<0.005	<0.005	<0.005	<0.005
Sulphur		0.004	0.001	0.0005	0.002				
Aluminium		3.2	3.47	3.59	3.55	4.77	6.67	10.4	6.96
Boron	0.007	0.012	0.01	0.01	0.011				
Bismuth			-	-					
Cobalt	8.0	9.0	8.75	8.21	8.46	1.17	31.4	10.6	35.2
Chromium	15.7	16.3	16.04	15.90	15.8	21.6	25.8	21.5	18.6
Copper		0.1	0.01	0.01	<0.01	<0.01	<0.01	0.01	<0.01
Iron		0.5	0.09	0.07	0.16	0.1	0.08	0.08	0.07
Hafnium			-	-	-				
Magnesium			-	-					
Molybdenum	1.5	2.0	1.76	1.67	1.73	0.19	0.14	0.06	0.1
Nickel	Bal.	Bal.	Bal.	Bal.	Bal.	Bal.	Bal.	Bal.	Bal.
Niobium	0.6	1.1	0.79	0.76	0.79	0.09	0.05	0.02	0.04
Lead			-	-					
Tantalum	1.5	2.0	1.72	1.78	1.71	1.0	0.12	0.05	0.06
Titanium	3.2	3.7	3.33	3.44	3.32	0.38	0.18	0.25	0.11
Vanadium			-	-		<0.01	<0.01	<0.01	<0.01
Tungsten	2.4	2.8	2.63	2.59	2.61	0.29	0.25	0.17	0.33
Zirconium	0.03	0.08	0.05	0.03	0.048				
Al + Ti	6.5	7.2	6.8	6.96					
Rhenium						0.06	<0.01	1.58	<0.01
Yttrium						0.53	0.53	0.64	0.33

3.4 X-Ray Diffraction

X-ray diffraction is a technique that can identify crystalline phases. It is possible to isolate the carbide particles in nickel alloys by the electrochemical dissolution of the matrix. X-ray diffraction of the extracted particles can give the interplanar spacings of the phases that can then be compared to reference data for identification. Lattice parameters and volume fractions of the phase can then be calculated.

3.4.1 Basic Theory

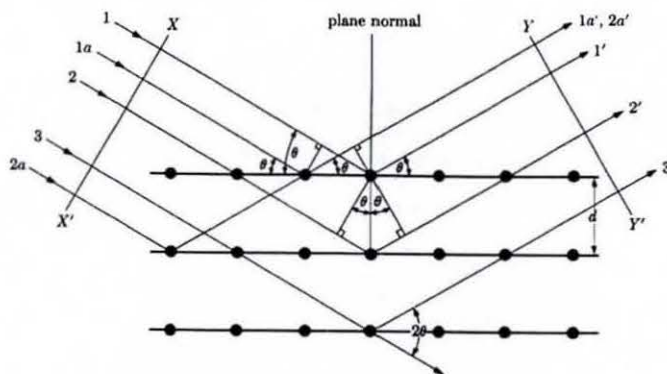
When X-rays are directed to materials, scattering of the X-rays can occur. The types of scattering are as follows;

- randomly spaced atoms, which scatter in all directions giving a weak signal
- periodically spaced atoms which give an intense signal (i.e. diffraction) in a few specific directions (angles) for which Bragg's Law is satisfied.

Most angles do not satisfy Bragg's Law, hence there is no scattering and the X-rays cancel each other out.

Bragg's Law states that diffraction of an incident beam on a crystalline material can occur when the wavelength of the wave motion is of the same order of magnitude as the repeat distance between the scattering centres. An example of how this can occur in a crystalline material is shown in Figure 3.4.

Figure 3.4 Schematic of incident and diffracted X-ray beams



Rays 1 and 1a in the plane X-X' strike two atoms in the top plane and are scattered in all directions. Only in the directions 1' and 1a' in plane Y - Y' are these scattered beams completely in phase and thus capable of reinforcing one another. In that instance the path difference is zero. This reinforcement can also occur with rays scattered by atoms in different planes. The conditions necessary for diffraction to occur are defined by Bragg's Law;

Equation 3.1
$$n\lambda = 2d \sin \theta$$

n is the order of the reflection. It may take on any integral value consistent with $\sin\theta$ not exceeding unity and is equal to the number of wavelengths in the path difference between rays scattered by adjacent planes.

d is interplanar distance

θ is the incident angle of the X-ray with respect to the plane in the sample

λ is the wavelength of the X-ray.

The factors that determine the possible angles 2θ , in which a given can diffract a beam of monochromatic X-rays are effectively, the *shape* and *size* of the unit cell.

X-rays are used because the typical wavelength range 0.05 nm to 0.25 nm is of similar order to interplanar distances in crystalline materials. The lattice parameter a is often used to describe a unit cell. For a cubic structure;

Equation 3.2
$$\frac{1}{d^2} = \frac{(h^2 + k^2 + l^2)}{a^2}$$

where

a is lattice parameter

h, k, l are Miller indices

Combining with Bragg's law, we have

Equation 3.3
$$\sin^2 \theta = \frac{\lambda^2}{4a^2} (h^2 + k^2 + l^2)$$

For a tetragonal structure

Equation 3.4
$$\sin^2 \theta = \frac{\lambda^2}{4} \left(\frac{h^2 + k^2}{a^2} + \frac{l^2}{c^2} \right)$$

Note 1: this is just for **direction**. Relative **Intensity** is determined by position of atoms within a cell.

Note 2: for many crystals, there are particular atomic arrangements, which reduce the intensities of some diffracted beams to zero, i.e. they cause systematic absences of the predicted peak.

3.4.2 Methods of Measurement

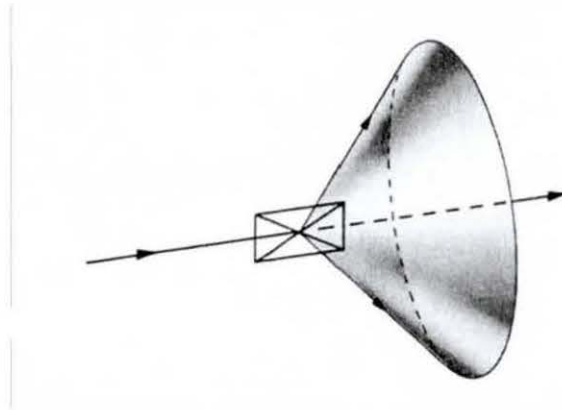
In order to find the Bragg angles for a crystal and determine the relative beam intensities,

either θ or λ must be varied. There are three main methods;

	λ	θ
Laue method	variable	fixed
Rotating crystal method	Fixed	variable
Powder method	Fixed	variable

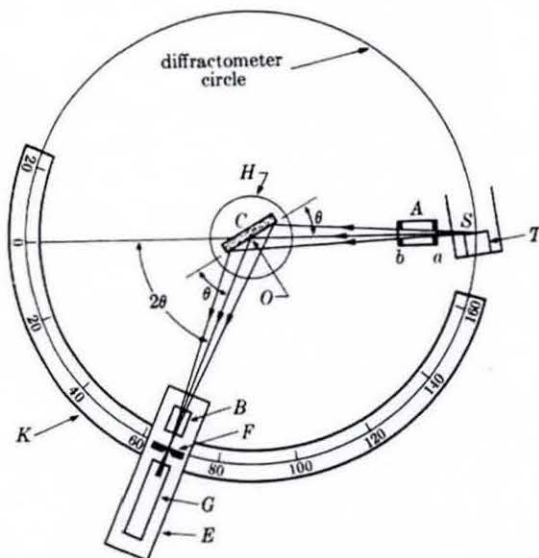
The powder method is that used in this research and will therefore be considered in more detail.

The crystal to be examined is reduced to a very fine powder and placed in a beam of monochromatic X-rays. Each particle of the powder is a tiny crystal oriented at random with respect to the incident beam. By chance, some of the crystals will be correctly aligned so that certain planes e.g. 100 can reflect the incident beam when it is at the appropriate angle. Other crystals will be correctly oriented for 110 reflections and so on. Note that for each suitable combination of crystal alignment and Bragg angle, the crystal may be aligned at the 12 O' clock position, 10' clock and so on, giving rise to diffracted beam in the form of a cone figure. This is equivalent to a beam incident at a Bragg angle on a single crystal, which is then rotated in the direction that does not affect the angle of the incident beam. The rotation does not actually occur in the powder method but the presence of a large number of crystal particles having all possible orientations is equivalent to orientation, Figure 3.5.

Figure 3.5 Effect of rotating a crystal on the diffracted beam

This method, then, generally gives 2θ values for the Bragg angle and a measure of the intensity of each.

3.4.3 Measurement Apparatus

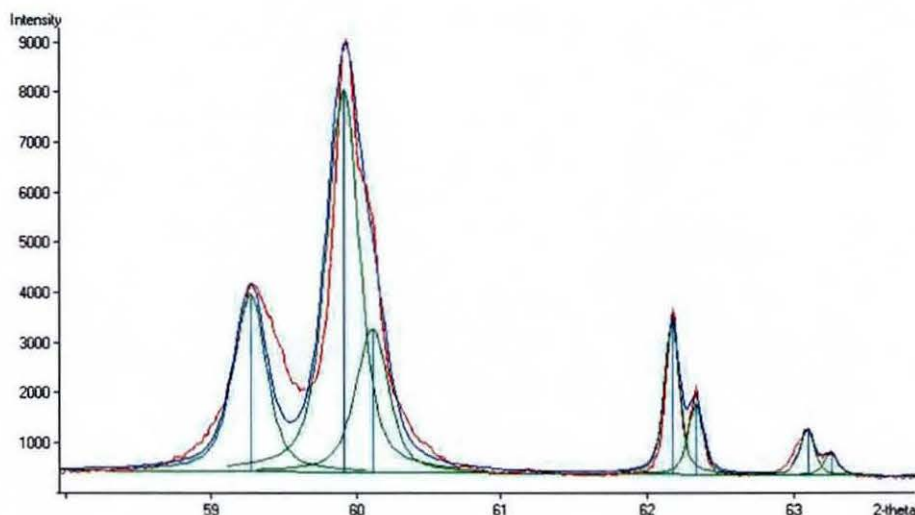
Figure 3.6 Schematic of an X-ray diffractometer⁶¹

C	powder specimen
H	Table which can rotated about axis O (perpendicular to plane of drawing)
S	X-ray source
T	line focal spot on target of X-ray tube
F	focus slit
G	Counter
A, B	Slits
E	carriage that can be rotated about axis O, angular position read on scale K

An X-ray diffractometer, Figure 3.6, can measure the intensity of a diffracted beam at various 2θ angles. The intensity can be measured by a camera, being proportional to the amount of blackening on the film, or by an electronic counter. In a counter, the incoming X-rays are converted to surges or pulses per unit time, this number being directly proportional to the intensity of the beam.

In a modern diffractometer, the powder specimen is supported on a table that can be rotated. X-rays diverge from the source and are diffracted by the specimen to form convergent diffracted beam, which comes to a focus at a slit and then enters the counter. The angle 2θ may be read from a graduated scale and on contemporary systems recorded on a computer. An example trace is shown in Figure 3.7 below. Intensity of the peaks increases with mass fraction of contributing material. Peaks for different planes from the same or different materials can overlap. There are methods for deconvoluting these peaks. For the purposes of this research a software package was available which carried out this deconvolution, Philips ProFit version 1. The green peaks in Figure 3.7 have been deconvoluted by ProFit. This software can identify Bragg angles and give their relative intensities.

Figure 3.7 Example XRD trace, red - raw data, green - deconvoluted



3.4.4 Analysis of Data

The Bragg angles can be used to calculate periodic interplanar distances, Equation 3.1. These distances can be used to characterise the material, by comparison with known data. The Powder Diffraction File⁶² holds data on many organic and inorganic compounds including;

- relative intensity of diffracted beam for different Miller indices
- lattice parameter

On identification of the Bragg angles, it is possible to calculate ratios of two different materials using peak intensities. Whilst a ratio based on peak intensities may not precisely correspond to the mass fraction ratio, it should be a function of the mass fraction ratio. This

is a technique used in this research to calculate a ratio for two carbides in IN738LC, MC and $M_{23}C_6$. The full details of the extraction procedure and calculation of the ratio are given in Appendix 3B.

3.4.5 Experimental Procedure

To extract the carbide particles, the samples were immersed in an electrolytic cell. The composition and strength of the electrolyte, along with the current density are selected so as to dissolve the matrix whilst leaving the carbides intact. High voltages (and associated current densities) will result in a large number of precipitates being released from the matrix in a shorter time but chemical dissolution of the carbides may also occur. A solution that has been used for nickel base superalloys is 10% hydrochloric acid, 1% tartaric acid, in methanol⁶³. This solution was designed to dissolve both γ and γ' , leaving the carbides.

The specimens were anodically polarised in the above mentioned solution at a voltage of 4-5V. After about two hours the extracted particles were collected on a glass fibre filter mesh of one-micron pore diameter by filtration. This filter is relatively resistant to the acid concentration used and from previous experience the size of the particles is expected to be greater than one micron, subsequently confirmed by scanning electron microscopy (SEM). The filter with the collected particles was examined in a Philips PW1316 diffractometer with a Hiltonbrooks EHT generator and automation system, and a graphite monochromator. The tube was a Cu X-ray tube at 40 kV and 30 mA. The samples were scanned over 2 theta values from 10 - 140 degrees. The divergence was one degree wide, the receiving slit was 0.2mm wide, with a scatterslit of one degree. The full extraction procedure is given detailed in Appendix 3B

3.5 Optical Microscopy

To enable examination by optical microscopy (and SEM), the samples were metallographically prepared to reveal microstructural features.

The metallographic preparation involved grinding on silicon carbide papers in a sequence of 240, 400, 800 and 1200 grit. Subsequent pre-polishing was performed on a silk napped cloth with three micron diamond, then final polishing was carried out on a short nap synthetic cloth with one micron diamond particles.

One of the following two etchants were used; either

- five seconds in Kalling's reagent (5 g CuCl_2 , 100 ml HCl and 100 ml methanol) – attacks γ

or

- 1% citric acid, 1% ammonium sulphate in H_2O , electrolytic 5 V for 5 sec – attacks γ .

Almost all of the etching was carried out using the citric acid/ammonium sulphate in water electrolytic etchant, however there was an example of fine grain boundary M_{23}C_6 , well delineated by Kalling's reagent.

Optical microscopy was used to;

- view the extent of MC carbides throughout the sample
- view the extent of M_{23}C_6 precipitation at the grain boundaries
- determine whether gamma prime envelopment was occurring at the grain boundaries
- give a preliminary indication of gamma prime morphology
- view phases in coating and interdiffusion layer.

3.6 Scanning Electron Microscopy (SEM)

Where the maximum magnification of optical microscopy is typically 1000 times (nominal), scanning electron microscopy (SEM) is capable of much higher magnifications and can be used to resolve features not observable optically. There are generally two imaging modes, secondary electron imaging, which gives good resolution (a few nanometres being possible) and depth of field, and backscattered imaging, which gives contrast that is dependent on atomic number of elements within the sample. The electron interactions that give rise to the two imaging modes are described in the following section on energy dispersive X-ray analysis.

A Cambridge Instruments Stereoscan 360 at 20 kV equipped with a backscatter detector was used to confirm features examined by optical microscopy. SEM was also used to select particles for energy dispersive X-ray (EDX) analysis (see section 3.7)

3.7 Energy Dispersive X-ray (EDX) Analysis

3.7.1 Introduction

Energy dispersive X-ray (EDX) analysis is a method of analysing microscopic particles for composition. The apparatus is usually linked to an electron microscope, enabling particles

viewed onscreen to be analysed. This technique uses a semiconductor detector to classify X-radiation according to energy. The detector converts the energy of incident X-ray photons into pulses of current proportional to the photon energy. These pulses are amplified, digitised and then analysed. A spectrum is produced in which the energy in electron volts can be related to elements in the material. Some of the limitations that apply are as follows;

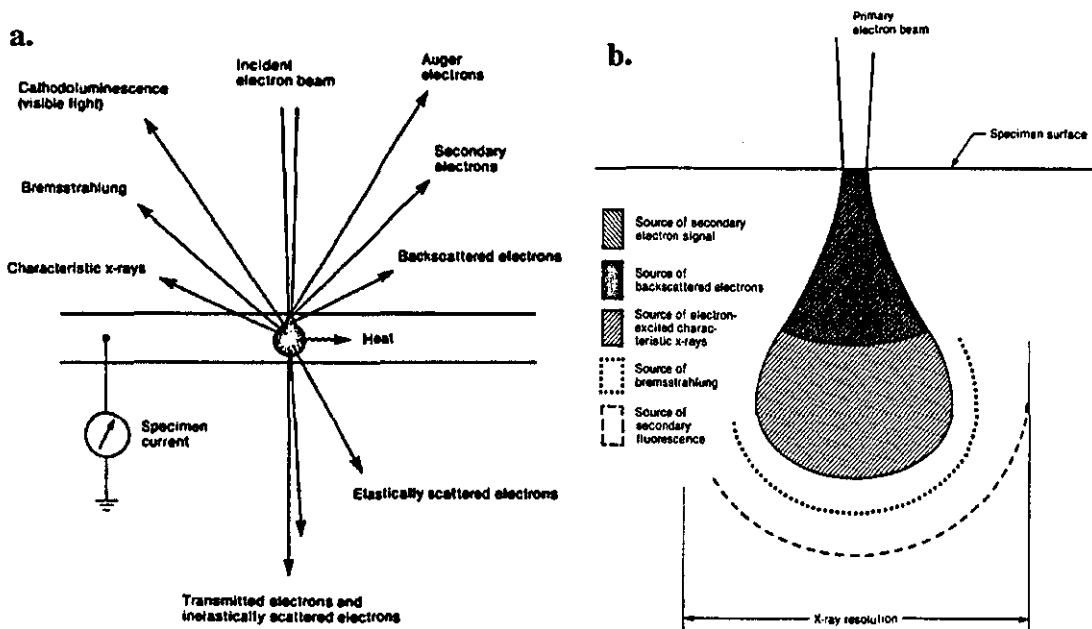
- the elements that can be detected are limited by the material used for the window of the detector
- the sample under analysis must be (or made to be) electrically conducting
- the minimum size of the particle is approximately one micron
- there is a possibility that the peaks for different elements may overlap.

The principle on which EDX analysis is based is that when excited by electrons of sufficient energy, every element in a sample will emit a unique and characteristic pattern of X-rays. Furthermore, under given analysis conditions, the number of X-rays emitted by each element bears a more or less direct relationship to the concentration of that element. The X-ray emissions can be converted to analysable data by a series of electronic components.

The system used was a Link AN10000 EDX system, linked to the above-mentioned scanning electron microscope.

3.7.2 Basic Theory

In an electron column, electrons are accelerated through an electric field, thus acquiring kinetic energy. This energy is transferred to the sample. The dissipation of this energy leads to a variety of emitted signals. The signals discussed here are the emitted secondary electrons, backscattered electrons, Bremsstrahlung and characteristic X-rays. Figure 3.8 describes the electron / beam interactions that can occur.

Figure 3.8 Sample / beam electron interactions⁶⁴

3.7.2.1 Secondary Electrons

The primary electron (from the column) may interact with an electron in the sample, which can then be ejected with some amount of kinetic energy. If the ejected electron is weakly bound, it typically emerges with only a few electron volts (eV) energy, and is called a secondary electron. Since they have little energy, secondary electrons can escape from the sample to be detected only if they are created relatively near the surface. For the same reason they are sensitive to topography. Secondary electrons carry little information about the elemental composition. However, the sensitivity to topography makes secondary electrons the most common choice for imaging.

3.7.2.2 Backscattered Electrons

If the primary electron interacts with the nucleus of a sample atom, it may be scattered in any direction with little loss of energy. Some of these scattered electrons will be directed back out of the sample, perhaps with more than one scattering event, allowing them to be detected. These are termed backscattered electrons and are much more energetic than secondary electrons and so may escape from a greater depth within the sample. The main influence on the strength of the backscattered electron (BSE) signal is the mean atomic number of the sample in the interaction volume. The higher the atomic number of an atom, the greater the positive charge of its nucleus, the greater the probability of a backscattered electron signal.

Particles with higher atomic number therefore generally appear brighter on backscattered electron imaging.

3.7.2.3 Bremsstrahlung (background)

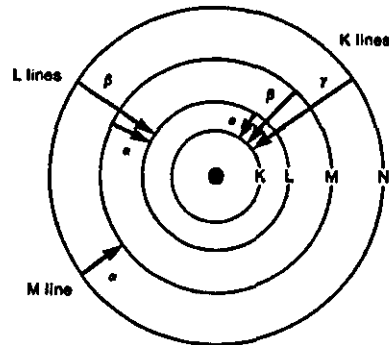
The primary electron may also be scattered inelastically by the Coulomb field of an atomic nucleus, thus giving up some or all of its energy. This may be emitted in the form of X-radiation called Bremsstrahlung (from the German 'braking radiation').

3.7.2.4 Characteristic X-rays

When an electron is ejected from an inner atomic shell by interaction with a high-energy electron beam, the result is an ion in an excited state. Through a relaxation (or de-excitation) process, this excited ion gives up energy to return to a normal (ground) state. The mechanics of the relaxation process are as follows;

- an electron in the excited ion drops from an outer shell into the vacant site
- each drop results in the loss of a specific amount of energy
- the magnitude of this energy is the difference between the vacant shell and the shell contributing the electron.
- this energy is given up in the form of X-rays
- the energy of the radiation uniquely indicates the element from which it came, hence the name characteristic X-rays.

The nomenclature of an emitted X-ray signal is dependent on the shell where the initial vacancy occurs, and how many shells the filling electron travels, pictured in Figure 3.9. For instance, if the initial vacancy occurs in the K shell and the filling electron drops from the adjacent shell, K_{α} radiation is emitted. If the filling electron drops from two shells way, K_{β} radiation is emitted.

Figure 3.9 Electron shells

The most useful property of X-ray emissions according to Vaughan⁶⁴ is Mosely's Law which relates their energy to atomic number;

Equation 3.5 $E = c_1(Z - c_2)^2$

E is the energy of the characteristic X-ray, Z is the atomic number c_1 and c_2 are constants for a given line type.

Thus, from the energy of an X-ray emission, the atomic number of the emitter can be determined if the line type is known.

The intensity of the characteristic X-ray is influenced by three factors;

- atomic number – of the emitting atom and average for bulk sample
- X-ray absorption
- secondary fluorescence.

With respect to the atomic number of the emitter, the ionisation cross section expresses the probability of ionisation under given conditions. The fluorescence yield is the probability that ionisation will produce a characteristic X-ray. The average atomic number of the sample affects the amount of energy lost to other scattering processes, energy that is therefore unavailable to ionise a sample atom.

As the X-ray travels through the sample it may be absorbed, giving up its energy entirely to an electron and ejecting the electron from its orbital. The probability of absorption increases as the X-ray energy approaches the binding energy (of the electron) from above and reaches a

maximum when the X-ray energy is just greater than the binding energy. Just beyond this maximum (from higher to lower energy, for each shell), there is a sudden drop in the probability of absorption. This is known as the absorption edge.

The probability of X-ray absorption as a function of path length through the sample is given by Beer's Law;

Equation 3.6
$$\frac{I}{I_0} = \exp(-\mu_m \rho d)$$

$\frac{I}{I_0}$ is the fraction of X-rays transmitted through the thickness d of a material of

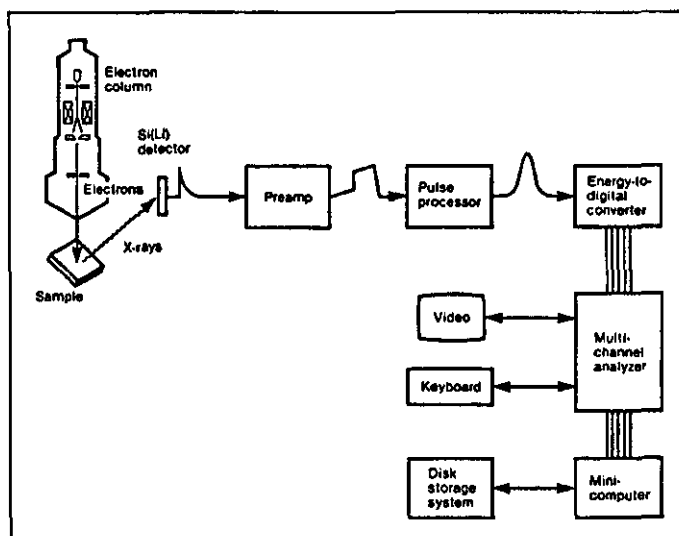
density ρ . μ_m is the mass absorption coefficient and is a function of the atomic number Z of the absorber and the X-ray energy E .

When an X-ray is absorbed by an atom in the sample, the absorbing atom is left in an excited state. It subsequently relaxes, emitting its own characteristic X-rays, a process known as secondary fluorescence.

3.7.3 Apparatus

The major components that make up a typical SEM/EDX system are pictured in Figure 3.10.

Figure 3.10 Schematic of a SEM/EDX system⁶⁴



3.7.3.1 Detector

The detector is almost always manufactured from a single crystal of silicon. Free charge carriers (electrons and holes) are created in the silicon crystal during the absorption of each X-ray. This charge is subsequently measured.

The detector operates in its own high purity vacuum. It is therefore sealed in a tube, which has a window at one end to allow transmission of X-rays. The most common window material is beryllium. X-rays from elements lighter than sodium are however absorbed by the beryllium window and cannot be detected. The detector needs to be at an optimum angle with respect to the sample, to minimise mass absorption of X-rays. This take-off angle is usually in excess of 30°.

A detector related phenomenon that can occur is the presence of escape peaks. An incoming X-ray can occasionally be absorbed by the silicon crystal, which can then emit an X-ray 1.74 keV less than that of the incoming X-ray (1.74 keV is the energy of the silicon $K\alpha$ X-ray). Usually the magnitude of escape peaks is at most a few percent of its parent peak and they are most likely to occur when the primary X-ray energy is above 1.84 keV (silicon shell binding energy). Hence, parent peaks above 1.84 keV may exhibit small associated peaks offset by 1.74 keV. These escape peaks can be removed by analysis software.

3.7.3.2 Preamplifier

The current conducted by the detector crystal is integrated and amplified.

3.7.3.3 Pulse Processor

The step increases generated by the preamplifier are conditioned for acceptance by an analogue to digital converter. Two methods are in common use. The first involves an initial differentiation and subsequent multiple integration of the step signal. A second method known as time-variant processing, is more time-efficient. However this latter method is sensitive to variations in count rate, which unavoidably occur during the raster scan of an inhomogeneous sample.

3.7.3.4 EDC and multi channel analyser

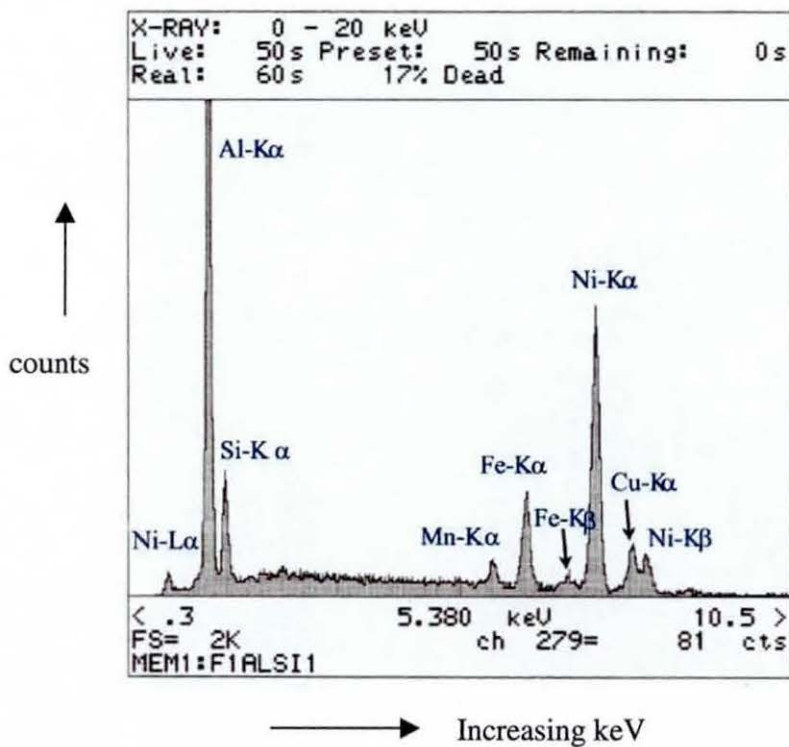
This is a means by which the signal information is accumulated and assembled into a spectrum. The energy to digital converter (EDC) measures the height of the voltage pulse (from the pulse processor, remembering that this is proportional to the X-ray energy) and

assigns a channel number. The number of counts in that channel of the multi channel analyser is increased by one. This process is then repeated to create the spectrum.

3.7.4 The Spectrum

The energy dispersive spectrum is usually displayed as a histogram with x-axis energy and y-axis counts (intensity). An example of part of a spectrum containing a number of elements is shown in Figure 3.11 below. For the elements nickel and copper, both $K\alpha$ and $K\beta$ can be seen. The roughness of the spectrum represents channel to channel statistical fluctuations.

Figure 3.11 Example EDX spectrum



3.7.5 Qualitative Analysis.

In its simplest form, qualitative analysis proceeds by comparing the energies of peaks in the spectrum with tables listing the known energies of X-ray emissions for each element. The peaks can then be labelled as in Figure 3.11. Escape peaks can be removed by computer algorithms. The accelerating voltage affects the relative peak heights and a consistent value is to be used. The greatest source of uncertainty is peak overlap. Whilst peaks that are close in energy can be separated by the pulse processor, there is a limit to this capability, and some peaks will directly overlap. For example, titanium K lines appear at 4.5 and 4.9 keV and the

two strongest barium L lines (in addition to the three K lines) occur at 4.5 and 4.8 keV. Hence a significant barium presence will obscure titanium peaks. However, the relative peak heights of the barium peaks alone will be different to the peak heights for barium and titanium. Thus, the presence of titanium can be inferred by analysis of the peak heights.

The results of qualitative analysis can also be presented in line profile and dot map formats, to highlight presence of individual elements. In a line profile a graph of the intensity (y-axis) of an X-ray signal can be superimposed on the electron image. In the dot map, the brightness of the SEM CRT beam at each point is modulated by the X-ray output of the element of interest.

3.7.6 Quantitative analysis

Quantitative analysis seeks to establish the concentrations as well as identities of each element. After a qualitative analysis has been carried out, quantitative analysis proceeds with the following steps;

- background removal
- deconvolution of overlapping peaks
- calculation of elemental concentration.

3.7.6.1 Background Removal

The background can be removed by filtering, among other methods. Filtering relies on the distinction between the slope of the spectrum in regions where only background is present, and the slope in the vicinity of the characteristic peaks. Three bands of information are present

- a) background, low rate of change
- b) characteristic peaks, medium rate of change
- c) statistical channel to channel fluctuations, high rate of change.

A digital filter attenuates a and c above whilst leaving characteristic peak information with minimum perturbation.

3.7.6.2 Deconvolution

Once escape peaks and background have been removed the remaining peaks are referred to as net peaks. The next step is to evaluate intensities. A region of interest (ROI) for each peak is

defined and can be integrated. However, this comes more complex when peaks overlap. The purpose of deconvolution is to separate overlapping peaks, deriving the contributions of each constituent peak to the composite peak. A number of methods are available;

- use of overlap coefficients
- reference deconvolution
- filtered least squares fitting.

If an X-ray peak overlaps the ROI (region of interest) of another element, the fraction of the peak that falls within the ROI depends only on the relative position and standard deviation of the peak, not on the composition. The fraction of the peak that falls within its own ROI is independent of composition. The ratio of the two fractions is called the overlap coefficient. Overlap coefficients are used to calculate the contributions of peaks to each other.

Reference deconvolution depends on subtracting a model for the interfering peak from the analysed composite peak. This uses pure-element standard peaks and fitting of peak models to data.

Filtered least squares fitting combines background filtering and reference deconvolution in a single operation. Peak models are first derived from acquired spectra, then the background is suppressed by filtering as described in 3.7.6.1. The unknown spectrum is also filtered. The filtered models are then fitted to the filtered unknown spectra by a statistical method.

3.7.7 Quantitative Calculations

The quantitative analysis in the previous section has resulted in determination of the number of net peak counts for each spectral peak obtained on analysis. However, these data must undergo further corrections to obtain elemental concentrations. A number of beam/sample interactions complicate the single process used to characterise the material - X-ray emission. These complications can be grouped into three categories the effects of atomic number (Z), absorption within the sample and the detector, (A) and X-ray induced fluorescence within the sample (F). They are abbreviated in the term ZAF corrections. The principles of these interactions are discussed in section 3.7.2. The quantitative calculations used to compensate for these other processes are termed ZAF corrections.

ZAF corrections are applied on the k-ratios. The k-ratio for any element is the ratio between the number of X-rays counted in the net peak and the number of X-rays counted in a sample of known concentration;

k-ratio = net peak counts / standard counts

The corrections are applied iteratively to produce values that reflect actual concentrations. Some constraints on the calculations are;

- sample must be microscopically smooth
- for validity of path length calculation
- sample must be microscopically homogenous (with respect to depth)
- absorption and fluorescence calculations assume material through which X-rays is pass the same as that at point of X-ray generation.

3.7.7.1 Standardless Analysis

It is possible to make certain reasonable assumptions that obviate the need for standards and empirical k-ratios. For pure element standards, the measured α emission intensities can be expressed as;

$$I \propto \epsilon f(\chi) R \omega \left(\frac{Q}{S}\right) \beta$$

Equation 3.7

where

ϵ = efficiency of detector

$f(\chi)$ = absorption correction

R = backscatter loss correction factor

ω = fluorescent yield

Q = ionisation cross-section

S = stopping power

β = fraction of total emitted radiation emitted as X-rays

All of these parameters except for epsilon are computed in the course of calculating normal ZAF corrections, without reference to standards data. In addition, detector efficiency can be theoretically computed on the basis of available detector parameters. Once I (std. counts) is

calculated, theoretical k-ratios can be produced. Normal iterative ZAF corrections can then proceed.

3.7.8 Experimental Details

A Link AN10000 EDX facility (linked to the SEM) with a ZAF analysis programme was used for semi-quantitative analysis of particles. The program takes into account the geometry of the specimen, the gun voltage and there are various options for calibration. The specimens examined were normal with respect to the beam, a gun voltage of 20keV was set, and an internal standard based on cobalt was used. The calibration element is used to establish spectrometer gain and effective beam current. Elements were entered into the program using the standardless analysis option. The analysis mode used assumes that intensities are available for the elements present. The totals are normalised to 100%. The normalisation is carried out by altering the effective value of the beam current internally so that the sum of apparent concentrations totals 100%.

3.7.9 IN738 Base Material

The majority of analyses were carried out on polished microsections. Some analysis was undertaken on a gold-coated slide that contained extracted carbide particles. Particles were selected for EDX analysis randomly. Particles containing elements with large atomic numbers (tantalum and niobium, for example) highlight in the backscattered imaging mode. In IN738LC these commonly correspond to the typical MC carbides found in the matrix and at grain boundaries. A selection of these were analysed (semi-quantitatively) to confirm the composition of the MC carbide. Carbides which precipitate preferentially at grain boundaries in this alloy (although they can also be found in the matrix), are usually chromium rich $M_{23}C_6$. Semi-quantitative analysis of these particles can be difficult because they are usually small but this was attempted where appropriate. Particular attention was paid to particles that have an atypical appearance. Note that, in the case of carbides, because of the absence of carbon in the analysis the concentrations will not give the full composition. However, the data can be used to calculate proportions of the elements analysed, pending re-normalisation due to overlapping phases, assuming an appropriate stoichiometry. This renormalisation technique can allow for compositions to be determined of particles smaller than the EDX spot, see section Appendix 3B.

The following elements were included in the analysis

Element	Ni	Cr	Co	Mo	W	Ti	Al	Ta	Nb	Zr
Line	K	K	K	L	L	K	K	L	L	L

3.7.10 MCrAlY Coatings

There are a number of different phases present in the coatings, some of these are visible primarily in the backscattered imaging mode, others in the secondary electron imaging mode. Hence both modes are used when viewing particles for EDX analysis. Most particles were larger than one micron. A few phases had sub-micron dimensions. For the coatings yttrium and rhenium were added to the elements listed above for quantitative analysis of IN738LC. When analysing individual particles an annotated photograph was taken to facilitate traceability of data. The re-normalisation technique applied to substrate carbides and described in Appendix 3B has not been applied to coating particles, as the compositions of these particles are not as well documented as those of IN738LC substrate particles.

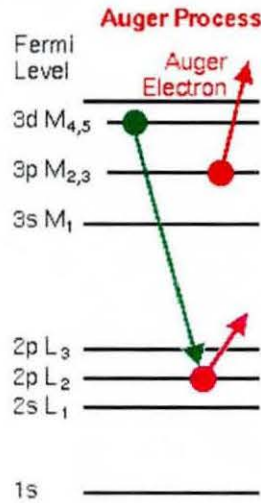
3.8 Auger Spectroscopy

Auger spectroscopy was developed to provide information on the chemical composition of a surface, just a few layers of atoms. The technique has a number of advantages over EDX analysis for certain applications, including;

- sensitive to surface
- better resolution for analysed spot
- sensitive to elements of low atomic number (including carbon)
- these latter two advantages are more relevant to this research.

3.8.1 Basic Theory

Auger electrons are produced by bombarding the specimen surface with low energy electrons (1 – 10 keV). Some of the atoms within the sample are ionised and Figure 3.12 shows an illustration of the electron rearrangement that can result.

Figure 3.12 Processes resulting in Auger electron emission

On ionisation of an inner energy level for example the L₂ shell, by a primary electron (purple), an electron from that shell is ejected. An electron (from the M₄ level in this example, green) may fill the vacant site releasing an amount of energy $E_{M_4} - E_{L_2}$. This energy may now be transferred to another electron (red) possibly in the M₃ level, which is then ejected from the solid. This latter electron is the Auger electron and its energy E is given by Equation 3.8

Equation 3.8 $E = E_{L_2} - E_{M_4} - E_{M_3}$

Since E_{L_2} , E_{M_4} and E_{M_3} are all characteristic of the particular element concerned it is possible by measuring the energies and number of Auger electrons to determine the chemical composition of the sample surface.

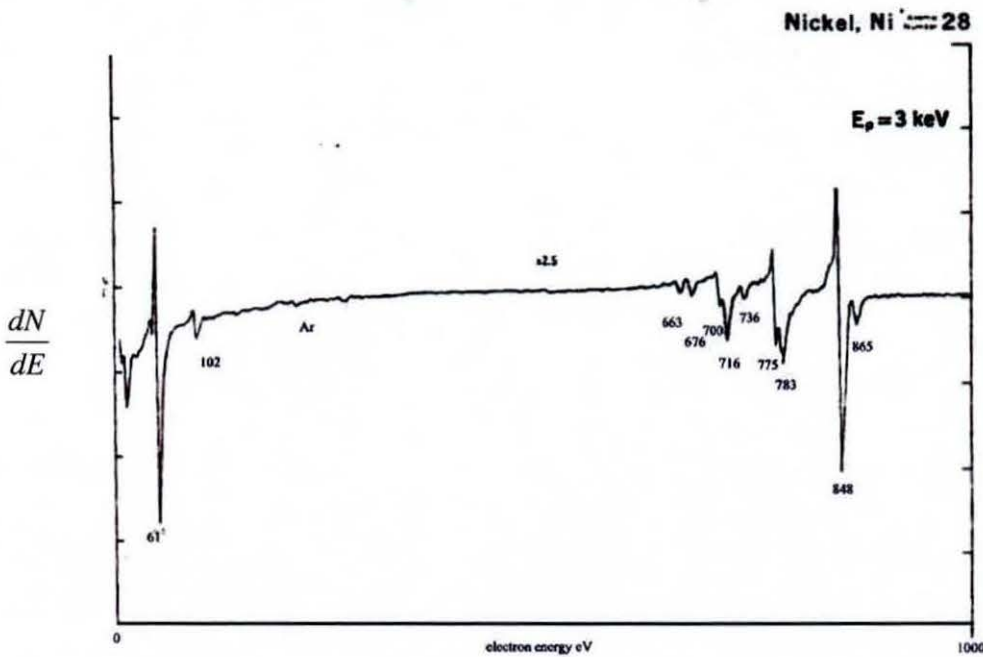
The energies of the Auger electrons are low, typically 20 to 1000 eV. Thus, even though they may be produced from as far within the solid as the beam penetrates, only those which are generated within the first two or three atomic layers below the surface can escape with their original energies intact. Those Auger electrons which originate further within the sample lose energy in extra inelastic collisions and may no longer be identified as such. This is what gives the technique its great surface sensitivity.

3.8.2 Auger Spectrum

Modern instruments allow secondary electron imaging of the sample surface. The same electron beam used to obtain the image is used for Auger analysis.

The raw spectrum plots the secondary electron distribution intensity against beam energy. The features of this energy distribution are relatively small in amplitude and occur on a large sloping background which makes their interpretation difficult. The spectra are therefore differentiated electronically so that dN/dE (E) versus E is displayed. This accentuates the background and accentuates the prominence of the Auger peaks. An example Auger spectrum for pure nickel is shown below;

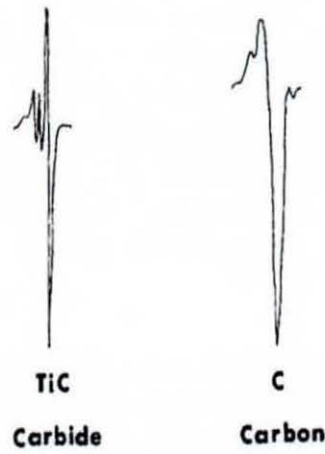
Figure 3.13 An Auger spectrum for pure nickel⁶⁵



By convention the energy of the Auger peak is taken to be the energy corresponding to the minimum of the negative part of the Auger transition, as this is usually the most sharp and prominent. For most elements, particularly those with atomic number greater than eleven, there are a number of Auger transitions. Peaks can be identified by comparison of the peak energy with charts, comparison with standard spectra. Peaks for different elements in the same materials may overlap, identification is then effected by consideration of subsidiary peaks. In the case where a single characteristic peak exists and superposition obscures it, its presence can normally be inferred from the precise shape of the composite peak.

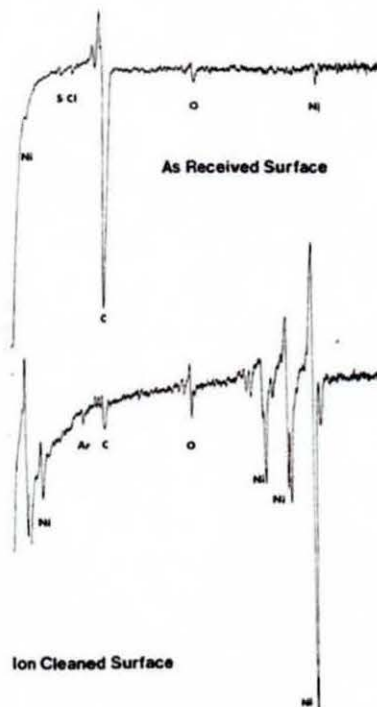
In a few cases the precise chemical configuration of the surface can cause distinct changes in peak shape which are easily recognised. For example the difference between free carbon and a carbide is detected in the shape of the carbon peak, as shown in Figure 3.14 below.

Figure 3.14 Peak shapes for carbon



3.8.3 Sample Cleaning

Most as-received samples carry a surface film of contamination deposited by the atmosphere, by handling, or other mechanisms. Carbon is the main contaminant, other species being O, Cl, S, Ca and N. This contamination can be removed by argon ion bombardment, see Figure 3.15

Figure 3.15 Comparison of as-received and cleaned samples of pure nickel⁶⁵

3.9 Thermodynamic Modelling

3.9.1 Introduction

For many years, phase diagrams have been used to represent the equilibrium structure of binary, ternary and occasionally higher order systems. More recently, techniques for the calculation of phase diagrams (CALPHAD) have been developed such that using suitable thermodynamic data, it is now relatively straightforward to predict the equilibrium concentration of phases present in a multicomponent alloy of specified composition as a function of temperature and pressure.

3.9.2 The Theory of Modelling Multicomponent Equilibria

The chemical equilibrium of any alloy system may be determined by minimising the total free energy of the system with respect to the amount and composition of the phases present, at fixed pressure in the case of Gibbs free energy or fixed volume in the case of Helmholtz free energy. Conventionally, Gibbs free energy is used in the CALPHAD approach. To carry out this minimisation, it is therefore necessary to express the Gibbs energies of all potential phases as a function of temperature and composition. The total Gibbs energy is then given by the weighted sum of the Gibbs energies of the individual phases. By minimising this total, the phases present at equilibrium can be identified.

3.9.2.1 Pure Elements

By convention the Gibbs energy of a pure element, i , in its standard state, ${}^0G_i^\phi(T)$, is referred to the enthalpy for its stable state ϕ at 298.15K, ${}^0H_i^\phi(298.15K)$; this is the standard element reference (SER). The Gibbs energy is thus denoted $G-H_{SER}$ where:

$$\text{Equation 3.9 } G - H_{SER} = {}^0G_i^\phi(T) - {}^0H_i^\phi(298.15K)$$

This can be described as a function of temperature, T , by an equation of the form:

$$\text{Equation 3.10 } G - H_{SER} = a + bT + cT \ln T + dT^2 + eT^3 + fT^{-1} + gT^7 + hT^{-9}$$

The coefficients a to h may be determined directly from measured values of heat capacity, entropy and enthalpy because the first and second differentials of $G - H_{SER}$ with respect to temperature are related to the absolute entropy and heat capacity of the element i at the same temperature. The same functional form may also be used to represent the same element in a solution in which it takes the structure ϕ which is different from that of the pure stable

element, since the expression ${}^0G_i^\phi(T) - {}^0H_i^\phi(298.15K)$ is equivalent to ${}^0G_i^\phi(T) - {}^0G_i^\phi(T) + G - H_{SER_i}$

For elements which display magnetic ordering, an additional term $G_{magnetic}$ must be added to the Gibbs energy equation. That is:

$$\text{Equation 3.11} \quad G_{magnetic} = RT \ln(1 + \beta) g(\tau)$$

where R is the universal gas constant, β is the average magnetic moment per atom of the alloy, expressed in Bohr magnetons and $\tau = T/T_c$, where T_c is the critical temperature for magnetic ordering.

3.9.2.2 Binary Compounds

The Gibbs energy of formation of a compound A_aB_b may be expressed as;

$$\text{Equation 3.12} \quad G_{A_aB_b} - a {}^0H_A^\phi(298.15K) - b {}^0H_B^\phi(298.15K) = f(T)$$

where a and b are constants, different from those in Equation 3.10, and the function $f(T)$ is identical to that given in Equation 3.10. Thus applying Equation 3.9 to each component of the compound in turn, Equation 3.12 becomes;

$$\text{Equation 3.13} \quad f(T) = G_{A_aB_b}^T - a {}^0G_A^{\phi,T} - b {}^0G_B^{\phi,T} + a(G - H_{SER_A}) + b(G - H_{SER_B})$$

$$\text{Equation 3.14} \quad f(T) = \Delta_f G_{A_aB_b}^T + a(G - H_{SER_A}) + b(G - H_{SER_B})$$

The term $\Delta_f G_{A_aB_b}^T$ is the Gibbs energy of formation of the compound at a given temperature, T , referred to the stable elements at the same temperature.

3.9.2.3 Solid and Liquid Solutions

In practice, almost all metallurgical systems contain components that exhibit solubility. Solution phases will be defined here as any phase in which there is solubility of more than one component. Thermodynamic modelling of solution phases lies at the core of the CALPHAD method.

The Gibbs energy of each solution phase is slightly complex than for a pure substance; it is made up of three distinct terms such that:

Equation 3.15 $G = G^{ref} + G^{id} + G^{ex}$

Here the first term, G^{ref} , is simply a weighted sum of the data for the pure elements, the second term, G^{id} , is the sum of the contributions from the configurational entropy to the Gibbs energy of mixing, and the third term, G^{ex} , represents the excess Gibbs energy of mixing.

The modelling of multicomponent systems is concerned mainly with deriving suitable expressions for the excess Gibbs energy. The model for this derivation is dependent on the nature of the solution phase.

There are nominally four types of solution phase;

- random substitutional
- sublattice
- ionic
- aqueous.

Random substitutional and sublattice are the most relevant to metallurgical systems and are considered in more detail.

3.9.2.3.1 Random substitutional

The random substitutional models are used for phases such as the gas phase or simple metallic liquid and solid solutions where components can mix on any spatial position which is available to the phase. This can be applied to dilute solutions, for which models exist, but have limited applicability.

Concentrated solution models are categorised under ideal and non-ideal solutions. An ideal substitutional solution is characterised by the random distribution of components on a lattice with an interchange energy equal to zero. Ideal solution models are often used for gases. The regular solution model is the simplest of the non-ideal models and basically considers that the magnitude and sign of interactions between the components in a phase are independent of composition. This has been developed for the sub-regular model where interaction energies are considered to change linearly with composition. The process has

been taken further, where a general formula in terms of a power series is used to account for most types of composition dependence. The most common method applies the Redlich-Kister equation.

The Redlich-Kister model is used for solutions where the interactions between components are fairly small, and takes the form of a polynomial in composition. For example, the binary interactions for an m component system, to s terms, takes the form:

Equation 3.16
$$\Delta G^{ex} = \sum_{i=1}^{m-1} \sum_{j=i+1}^m \sum_{r=0}^s A_{ij} x_i x_j (x_i - x_j)^r$$

where x_i and x_j are the mole fractions of components i and j respectively, and A_{ij} is a model parameter which can be temperature dependent. The ternary and higher order interactions may be added to this and take a similar form.

3.9.2.3.2 Sub-lattice Model

The sub-lattice model is generally used for solid solutions where the interactions between components are fairly large, or some ordering within the phases exists.

A sublattice phase can be envisaged as being composed of interlocking sublattices on which the various components can mix. The model does not define any crystal structure within its general mathematical formulation. Sublattice modelling is one of the predominant methods used to describe solution and compound phases. The model can account for different phase types including interstitial and intermetallic phases. A detailed treatment of the mathematics of the model is beyond the scope of this chapter, this can be found in Saunders⁶⁶. Some examples of its application are given below;

1. Line compounds

In these phases sublattice occupation is restricted by particular combinations of atomic size electronegativity etc, and there is a well defined stoichiometry of with respect to the components. Examples include transition metal borides, and silicides and some carbides.

2. Interstitial phases

These are predominant in steels and ferrous based alloys, where elements such as C and N occupy the interstitial sites of the ferrite and austenite lattices. In this case the

structure of the phase can be considered to consist of two sublattices, one occupied by the substitutional elements the other occupied by the interstitial elements.

3. Complex intermetallic compounds with significant variation in stoichiometry

Where there is significant solubility in binary systems there may be more than two crystallographic sub-lattices to consider. Examples include σ , μ , χ , and laves phases. In these case the sublattice model should, as closely as possible, follow the internal sublattice structure of the compound itself. Often, simplification is necessary.

4. Order disorder transformations

Some phases, which have preferential site occupation elements on different sublattices at low temperatures, can disorder at higher temperatures, with all elements mixing randomly on all sublattices.

3.9.2.4 Gaseous Species

Gaseous species^{67,68,68} may be represented by an expression identical to that given in Equation 3.12 with an additional term, $RT \ln P$, where P is the total pressure; the reference state is taken as the pure component at atmospheric pressure. The gas phase is assumed to form an ideal solution.

3.9.2.5 Prediction of Phase Equilibria

CALPHAD methods attempt to provide a true equilibrium calculation by considering the Gibbs energy of all phases and minimising the total the total Gibbs energy of the system. The calculation must be defined so that

- the number of degrees of freedom is reduced
- the Gibbs energy of the system can be calculated
- some iterative technique can be used to minimise the Gibbs energy.

It is then possible to predict equilibrium in two ways. In order to understand this, we recall that when the Gibbs energy of the system is at a minimum, the chemical potentials of the components are equalised throughout the system. Equilibrium can therefore be computed either by minimising the Gibbs energy of the system, or by equalisation of the chemical potentials.

In fact, due to an increasing interest in thermochemical modelling and in particular the calculation of phase diagrams, a number of commercial computer software packages have recently become available which carry out the Gibbs energy minimisation process. Of the

packages available, the two most often cited are *MTDATA*⁹ and *ThermoCalc*⁶⁹. Both of these packages provide facilities for the manipulation of thermodynamic data, allowing equilibrium in binary, ternary and higher order systems to be explored using the Gibbs energy models for phases previously discussed; the method by which the Gibbs energy minimisation is performed however differs between the two programs.

3.9.3 ThermoCalc Software and Ni-data Database

For modelling of nickel base superalloy systems a database is available that is compatible with ThermoCalc software. ThermoCalc is a software package that calculates equilibrium conditions for pure substances and solution phases⁶⁹. The software consists of a number of modules, including one for calculating equilibria, for selecting databases, listing data from databases and other functions. The module used in this research is POLY, which calculates phase equilibria. Each condition necessary for calculating an equilibrium is set separately, examples include;

- value of the temperature or the enthalpy (or entropy)
- value of the pressure or the volume
- activities or chemical potentials of components
- overall composition in total number of moles or mass or in mole or mass fractions.

According to the authors, the equilibrium calculation method used in the ThermoCalc POLY module is a minimisation of the integral Gibbs energy using a Lagrangian multiplier method for the constraints. In ThermoCalc, the algorithm has been implemented in more general way than for other, similar software packages, by using analytically calculated second derivatives which allows non-linear constraints. Apparently, this allows the user to set conditions in a more flexible way.

The calculation of thermodynamic equilibrium is an iterative process and it is necessary to provide some start values for the compositions of the phases in the system. ThermoCalc provides automatic start values generated from the databases that almost always work.

The user interface for ThermoCalc is a command line that allows for good flexibility but is not easily accessible for the occasional user. A windows interface has been developed for ThermoCalc, called Ettan. The Ettan interface uses windows, buttons and a mouse pointer to drive the ThermoCalc program. All graphical user interface commands are translated into text commands that then operate the normal ThermoCalc command line interface. Not all

commands available in the command line interface are included in Ettan, but those included enable calculation of composition and proportions of phases at thermodynamic equilibrium. The data generated via Ettan are stored in spreadsheet style text format.

In the Gibbs energy system (GES) module, the thermodynamic calculations needed for the calculations are stored. These are normally read in from an external database, although the user can interact with the data. A large number of models for the composition dependence have been implemented, including Redlich Kister and sublattice models (discussed in section 3.9.2.3). Each phase can be described by a different model. All parameters in the models can be temperature or pressure dependent.

A database for that has been developed for nickel base alloys is Ni-data⁷⁰. The Ni-data database, in conjunction with ThermoCalc software, allows prediction of multicomponent systems for nickel base alloys^{71,72}. The following elements are included;

Ni, Al, Co, Cr, Fe, Hf, Mo, Nb, Re, Ta, Ti, W, Zr, B, C, N

The phases included are;

Liquid, γ , γ' , NiAl, Ni₃Nb, γ' , η , Ni₄Mo, δ -NiMo, α (Cr,Mo,W), Laves_C14, Laves_C15, σ , μ , R, P, M(C,N), M₂₃(B,C)₆, M₆C, M₇(B,C)₃, M₂N, M₃B, M₂B_orth, M₂B_tetr, M₃B₂, Cr₅B₃, TiB₂.

The documentation for the database states that results from Ni-data have been extensively validated against experimental results reported for multi-component Ni-based alloys. The average difference between the calculations and experimental data for critical temperatures is close to 10°C.

Some nominal compositional limitations are given, shown in the table below. The documentation states that it may be possible to exceed some of the limits and still get reasonable results.

Table 3.5 Nominal composition limits for Ni-data, mass%

Element	Max./mass%
Co	25
Cr	30
Fe	50
Ta and W	15
Al and Ti	7.5% Al, 5% Ti
Hf	5
C	0.3
B, N, Zr	0.1

3.9.4 Experimental Details

The following software was used

1. ThermoCalc version M
2. Ettan version 1.00
3. Ni-data

The aim was to have a working system that would predict with reasonable accuracy equilibrium phases for IN738LC, SC2453 and RT122 compositions, and compositions in between those of the substrate and each coating.

The phases in the database, listed in the previous section, can be classified as present or absent by ThermoCalc. For a constant composition the combination of phases included was found to have an effect on the predicted equilibrium. For the IN738LC bar2 composition, if all phases were classified present, α phase was predicted over a wide temperature range, which was not considered accurate. Simple exclusion of α was not appropriate, as α was known to be present in SC2453 from experimental data. Thus a short programme of predictions was undertaken to determine which combination of phases in the Ni-data database produced the most reasonable equilibria for IN738LC, RT122 and SC2453, based on data from the literature and experimental work, available at that time. The following compositions in Table 3.6 were used for input.

Table 3.6 Composition data used for input into ThermoCalc / Ni-data system, mass%

Element	Deritend analysis	Subset of bulk chemical analysis	
		Bar 1	Coatings
		SC2453	RT122
Carbon	0.10		
Aluminium	3.47	10.4	6.96
Boron	0.01		
Cobalt	8.75	10.6	35.2
Chromium	16.04	21.5	18.6
Iron	0.09		
Molybdenum	1.76		
Nickel	Bal.	Bal.	Bal.
Niobium	0.79	0.02	0.04
Tantalum	1.72		
Titanium	3.33		
Tungsten	2.63		
Zirconium	0.05		
Al + Ti	6.8		
Rhenium		1.58	

These compositions are taken from the analysed compositions in Table 3.4. With respect to the coatings, the bulk chemical analysis was applied to small amounts of turnings, hence the confidence for trace element content being consistent is low. Only the major elements were therefore included in the predictions for the coatings.

These composition were entered into the ThermoCalc / Ni-data system, and the phases classified present were varied. The output was analysed with respect certain criteria;

1. α not to be significant in IN738LC
2. α to be present at 850° to 950°C in SC2453
3. β and γ to be significant phases at 850°C and 950°C in RT122

Whilst some basic system requirements are listed above, each predicted system was viewed with some care for absence of expected phases or prediction of anomalies. The following phase list gave a reasonable correlation for the systems listed in Table 3.6.

1. Liquid
2. Gamma
3. Gamma'
4. Eta
5. Beta
6. Gamma''
7. Sigma
8. R_phase
9. P_phase
10. Alpha
11. Re (hcp)
12. MC
13. $M_{23}C_6$
14. M_6C
15. M_7C_3
16. M_3B_2
17. MB_2

The phases classified absent are therefore, laves, mu and delta.

Note: for RT122, phase no. 11, Re is excluded.

The compositions in Table 3.6 and the phases above (with the exception of Re for RT122) were used for the basis of the thermodynamic equilibrium predictions.

Appendix 3A Analysis of EDX Data

Energy dispersive X-ray spectroscopy (EDX) on a scanning electron microscope (SEM) allows the determination of compositions of phases that are larger than the EDX spot. If the size of particles in the alloy under investigation is comparable with the area analysed by the EDX spot (1-2 μm), analysed compositions will contain contributions from the phase(s) surrounding the particle. To determine compositions of these small phases a method that takes account of this overlap has been developed by Starink, Omar and Thomson⁷³. Their method was applied to obtain compositions of lower carbides (M_{23}C_6 and M_6C) in a MarM002 alloy. The sizes of these lower carbides are generally smaller than 2 μm . This has been adapted for IN738. The general principles of the method follow.

For notation of compositions, vector notation will be used and the composition vector, \bar{x} , is defined as:

$$\text{Equation 3A.17} \quad \bar{x} = \begin{pmatrix} x_A \\ x_B \\ x_C \\ \dots \end{pmatrix}$$

where A, B, C .. etc. are the (major) metallic elements present in the alloy. Provided that the assessment of the phases present and their compositions is accurate every measured EDX composition, \bar{x}_{EDX} , should be a linear combination of the expected compositions, $\bar{x}_{P_i}^e$:

$$\text{Equation 3A.18} \quad \bar{x}_{EDX} = \sum_i f_{P_i} \bar{x}_{P_i}^e$$

where P_i are the phases present in the alloy and f_{P_i} are the fractions at which these respective phases contribute to the EDX signal. The optimal values of the fractions f can be determined by minimising the expression:

$$\text{Equation 3A.19} \quad \left| \bar{x}_{EDX} - \sum_i f_{P_i} \bar{x}_{P_i}^e \right| = \chi$$

The accuracy of the various assumptions and the expected compositions is reflected in the value of χ obtained - the smaller χ , the better the accuracy. For the method to be unambiguous in terms of identifying the phases which contribute to the compositions measured by EDX, it is necessary that one single clearly defined set of f_{P_i} values exists which

leads to a minimum value of χ . This situation arises if two conditions are met: i) the phases in the alloy must have quite distinct compositions, and ii) the number of phases present must be less than the number of different elements that can be accurately determined by EDX. These preconditions are thought to hold for Ni-base superalloys. The results of this minimisation can be applied to i) estimate the relative fractions of the phases present at a certain spot analysed ii) correct an analysed composition of a phase P_i for the contribution due to other nearby phases. To obtain such a corrected composition first χ in Equation 3A.19, should be minimised, and provided f_{P_j} is significantly larger than 0 the composition of phase P_j corrected for overlap is:

$$\text{Equation 3A.20} \quad \bar{x}_{P_j} = \frac{\bar{x}_{EDX} - \left(\sum_i^{i \neq j} f_{P_i} \bar{x}_{P_i}^e \right)}{\left\| \bar{x}_{EDX} - \left(\sum_i^{i \neq j} f_{P_i} \bar{x}_{P_i}^e \right) \right\|} \quad \text{with}$$

$$\|\bar{x}\| = x_A + x_B + x_C \dots \text{etc}$$

The method has been adapted for alloy IN738LC using compositions predicted for MTDATA thermodynamic modelling software and results of direct EDX analysis on extracted carbides. The following table shows the expected compositions used (excluding carbon, which cannot be detected by the EDX system used)

Table 3A.7 Compositions use for renormalisation

	Ni	Cr	Co	Mo	W	Ti	Al	Ta	Nb	Zr
γ	69.30	2.70	4.70	0.10	0.60	7.80	12.60	1.10	1.00	0.10
γ	52.32	29.54	12.30	1.52	1.06	0.42	2.57	0.06	0.04	0.01
$M_{23}C_6$	5.37	81.45	2.16	10.04	0.98	0	0	0	0	0
MC				0.0	3.2	58.0		17.0	18.7	3.2

The following points should be noted:

1. The compositions for γ and γ' and $M_{23}C_6$ are taken from ThermoCalc / Ni-data predictions at 850°C with IN738LC bar 1 composition (see Thermodynamic Modelling in Chapter 3, and Equilibrium Predictions in Chapter 4). The composition of $M_{23}C_6$ is renormalised with the carbon subtracted, as the EDX system used does not detect carbon. The composition from equilibrium predictions for MC carbide appeared to give a higher

Ti content than the EDX data. Hence for MC, data from extracted carbide are used, (these are considered to suffer from little interference of adjacent phases, see Experimental Data, XRD slides, Chapter 4). The extracted carbide composition is subjected to a 6 element renormalisation, see 3. below.

2. These compositions are considered to be valid for the temperatures used in the main testing programme (850°C - 950°C),
3. The final renormalisation step assumes certain elements not to be present and adjusts the proportions of the remaining elements to 100%. The following elements (without the carbon) are assumed present;

MC Mo, W, Ti, Ta, Nb, Zr

M₂₃C₆ Ni, Cr, Mo, Ti, Ta, Nb, Zr

Appendix 3B Extraction and XRD procedures

Preparing a sample.

Cut off a sample which can be dipped in acid whilst being gripped above the acid bath.

Grind away surface layers (coating, oxide) of the sample to expose the bare metal.

Preparing the acid solution.

Clean a ~2.5 litre bottle.

To prepare solution of 10% HCl and 1% tartaric acid in methanol, first weigh 20 g tartaric acid and put in 0.5 litre measuring glass. Add 0.5 litre alcohol. Pour into bottle.

Add additional 1 litre of alcohol to bottle.

Place 0.3 litre alcohol in measuring glass and add 0.2 litre HCl. Add to bottle.

Mark bottle clearly with solution and date of preparation.

Preparing the electrolytic cell

Prepare the set-up: solution (10% HCl and 1% tartaric acid in methanol, max. 4 months old) in beaker, and place stainless steel metal plate in beaker.

With power unit off: connect sample and steel plate to the power unit.

Slowly increase the output voltage of the power unit to the target voltage.

Pre-extraction to remove surface layers.

Preferably use an old acid solution from a previous experiment to limit HCl and alcohol consumption.

Set current density of 10 mA/m² (about 7-10 V).

Let dissolution process continue for a minimum of 30 min.

Dispose of the solution.

Clean beaker, sample and stainless steel plate.

Extracting a sample.

Rinse the sample with alcohol. Let dry. Weigh the sample.

Dangle area to be extracted in acid.

Set current density to 2 mA/m^2 (about 2-2.5V).

If bubbles appear at the sample surface the leads are the wrong way around. Liquid just below sample should start to get green.

Some alcohol may evaporate causing the current to decrease. Keep the current constant by adding some alcohol.

The solution will start to become light green.

If not using an ultrasonic bath, use alcohol to remove carbides from surface of sample every 15 min.

Extract for about 2-3 hours. The solution will be dark green. On the bottom of the beaker some very small dark particles (carbides) will have clustered together.

Take sample out of acid and rinse the part of the surface which was exposed to the acid with a little bit of alcohol. Collect alcohol in beaker with solution.

Weigh a glass microfibre filter.

Set up filtration equipment with glass microfibre filter.

Start filtering by adding the solution. Do not spill any of the solution.

To collect carbides that may be stuck to the steel plate, rinse the steel plate with pure alcohol, collecting the alcohol in the beaker. Remove the steel plate.

Keep refilling until all the green solution is filtered.

Use pure alcohol to get remainder of the carbides out of the beaker into the filtration unit.

Take out the filter paper and put it in a small sample box. Use a few drops of water to carefully rinse it; make sure that carbides remain on sample. Use some alcohol to rinse it. Let filter paper dry.

Rinse sample completely in alcohol and let dry.

Weigh the dried filter paper with carbides as well as the sample.

XRD sample preparation

Break glass slide to obtain correct length

Put a number of layers of sticky tape on one side so that sample is level with this sticky tape

Attach dried sample to a glass slide with double sided sticky tape.

XRD experiment

Sample in XRD machine (only for trained staff or technician)

Disk in computer, and start programme 'XRD' from drive A

Scan over 10 to 100° with angle interval 0.05° and time per angle as long as possible (use sample sequences t10017h or t10015h for 17h or 15h overnight experiments, respectively)

Data will be stored on disk.

Converting XRD files

Open program XRAYCONV.EXE

Enter input: <drive>:<directory>\<filename>.ASC output: <filename>.UDF

Edit <filename>.UDF by putting / at the end of file (use word, or notepad)

Put <filename>.UDF in directory C:\APD\DATA and open program Philips APD.EXE

Chose options: utilities, UDI/UDF file format , UDF->RD, this creates <filename>.RD

<filename>.RD can be analysed in PROFIT or in QUASAR

Analysis of XRD data

Once the data file from the XRD diffractometer has been converted it is loaded into the Philips ProFit V1.0 software package for analysis. The capabilities of this software include automatic setting of the background, fitting and deconvolution of peaks, and calculation of integrated intensities of peaks. ProFit produces quantitative data including the 2θ value and integrated intensity of each peak. These data are pasted into spreadsheet that calculates the interplanar spacings using the Bragg equation. The spreadsheet can also sum and divide selected peak integrated intensities in order to calculate volume fraction ratios of phases. The interplanar spacings can be used to identify the phases present by comparison with reference data from Powder Diffraction Files (PDF) cards⁶². G7/B09 was found to contain all examinable TiC and Cr₂₃C₆ peaks. To date significant quantities of phases other than M₂₃C₆ (based on Cr₂₃C₆ lattice) and MC (based on TiC lattice) have not been identified in the base alloy IN738.

Crystal structure information of a large number of compounds is stored in the powder diffraction file database. Each compound has a card which lists peak intensities and corresponding lattice spacings, in addition to other information such as lattice parameter and structure. For the first batch of samples all of the peaks were analysed using PDF cards. Since only the two aforementioned structures were found to be present, a procedure that avoided unnecessary repetition was developed for examining the traces and calculating the M₂₃C₆/MC ratio:

1. File G7/B09 will be placed into the background on examining any new file.
2. The foreground and background peaks will be compared manually to see if all peaks from the new file correspond to those of TiC and Cr₂₃C₆
3. If there are additional peaks these should be identified by using PDF files, the procedure may then have to be amended.
4. Carbide fractions will be calculated by using the following peaks

Table 3.7 Powder diffraction file data for calculation of $M_{23}C_6$ / MC ratio

Phase	PDF card no ⁶²	Lattice parameter /nm	Structure	d /Angstroms	Intensity *	hkl
TiC	32-1383	0.433	Cubic	2.1637	100	200
				2.499	78	111
$Cr_{23}C_6$	35-783	0.107	Cubic	2.0520	100	511
				2.383	23	420

* in %, relative to greatest peak

The integrated intensities of the above peaks will be summed for each phase and fractions calculated in a spreadsheet.

Appendix 3C Interplanar spacings of carbides, borides and intermetallics

The following table contains interplanar spacings (d-values) of carbides and intermetallic phases that may occur in nickel base superalloys. Relative intensities (in single phase powders) are taken from PDF files⁶²;

	h	k	l	d	2 x theta	I
M ₂₃ B ₆	2	0	0	5.35	16.6	5
Al ₄ C ₃	0	0	0	4.167	21.3	10
M ₆ C	2	2	0	3.907	22.7	7
M ₂₃ B ₆	2	2	0	3.783	23.5	60
M ₆ C	3	1	1	3.332	26.7	1
M ₂₃ C ₆	3	1	1	3.226	27.6	1
M ₂₃ B ₆	3	1	1	3.226	27.6	20
M ₆ C	2	2	2	3.19	27.9	0
HfO ₂ monoc	0	0	0	3.147	28.3	100
M ₂₃ C ₆	2	2	2	3.089	28.9	1
Cr ₇ C ₃	0	0	0	3.039	29.4	2
Al ₄ C ₃	0	0	0	2.872	31.1	54
WC	0	0	0	2.84	31.5	45
HfO ₂ monoc	0	0	0	2.823	31.7	78
ζ-TaC	0	0	0	2.82	31.7	20
Al ₄ C ₃	0	0	0	2.817	31.7	100
Al ₄ C ₃	0	0	0	2.775	32.2	13
M ₆ C	4	0	0	2.763	32.4	25
M ₂₃ C ₆	4	0	0	2.675	33.5	4
ζ-TaC	0	0	0	2.67	33.5	50
HfC	1	1	1	2.638	33.9	100
σ Cr-Co	2	2	1	2.62	34.2	5
M ₆ C	3	3	1	2.535	35.4	40
TaC	1	1	1	2.523	35.6	100
WC	0	0	0	2.518	35.6	100
Al ₄ C ₃	0	0	0	2.503	35.8	54
M ₂ C	1	0	0	2.501	35.9	25
ζ-TaC	0	0	0	2.48	36.2	100
M ₂₃ C ₆	3	3	1	2.455	36.6	1
(W,Ti)C	1	1	1	2.445	36.7	100
ζ-TaC	0	0	0	2.425	37	50
M ₂₃ C ₆	4	2	0	2.393	37.6	80
M ₂₃ B ₆	4	2	0	2.393	37.6	50
σ Cr-Co	3	1	1	2.36	38.1	20
ζ-TaC	0	0	0	2.3	39.1	70
Cr ₇ C ₃	0	0	0	2.296	39.2	33
M ₂ C	0	0	2	2.29	39.3	22
HfC	2	0	0	2.285	39.4	90
σ Cr-Co	0	0	2	2.26	39.9	20
M ₆ C	4	2	2	2.256	39.9	65
Al ₄ C ₃	0	0	0	2.248	40.1	83

σ Cr-Co	4	0	0	2.2	41	5
M ₂ C	1	0	1	2.195	41.1	100
TaC	2	0	0	2.185	41.3	70
M ₂₃ C ₆	4	2	2	2.184	41.3	60
M ₂₃ B ₆	4	2	2	2.184	41.3	90
σ Cr-Co	3	2	1	2.15	42	5
Cr ₇ C ₃	0	0	0	2.141	42.2	6
σ Cr-Co	1	1	2	2.128	42.4	100
M ₆ C	3	3	3	2.127	42.5	100
Cr ₇ C ₃	0	0	0	2.123	42.5	46
(W,Ti)C	2	0	0	2.118	42.7	100
Al ₄ C ₃	0	0	0	2.082	43.4	49
σ Cr-Co	3	3	0	2.066	43.8	50
M ₂₃ C ₆	5	1	1	2.059	43.9	100
M ₂₃ B ₆	5	1	1	2.059	43.9	100
Cr ₇ C ₃	0	0	0	2.048	44.2	100
Cr ₇ C ₃	0	0	0	2.025	44.7	13
σ Cr-Co	3	0	2	2.014	45	50
σ Cr-Co	2	1	2	1.962	46.2	50
ζ -TaC	0	0	0	1.96	46.3	10
M ₆ C	4	4	0	1.953	46.4	40
σ Cr-Co	4	1	1	1.926	47.1	100
Cr ₇ C ₃	0	0	0	1.902	47.8	5
M ₂₃ C ₆	4	4	0	1.892	48.1	80
M ₂₃ B ₆	4	4	0	1.892	48.1	70
Al ₄ C ₃	0	0	0	1.891	48.1	23
WC	0	0	0	1.884	48.3	100
σ Cr-Co	3	3	1	1.882	48.3	50
ζ -TaC	0	0	0	1.875	48.5	30
Cr ₇ C ₃	0	0	0	1.849	49.2	11
σ Cr-Co	2	2	2	1.831	49.8	20
Cr ₇ C ₃	0	0	0	1.816	50.2	24
M ₂₃ B ₆	5	3	1	1.809	50.4	40
M ₂₃ C ₆	5	3	1	1.809	50.4	22
M ₂₃ B ₆	6	0	0	1.783	51.2	10
M ₂₃ C ₆	6	0	0	1.783	51.2	20
σ Cr-Co	3	1	2	1.756	52	20
Cr ₇ C ₃	0	0	0	1.754	52.1	16
M ₂₃ B ₆	6	2	0	1.692	54.2	60
M ₂₃ C ₆	6	2	0	1.692	54.2	2
M ₂ C	1	0	2	1.689	54.3	17
Al ₄ C ₃	0	0	0	1.667	55	86
σ Cr-Co	0	0	0	1.658	55.4	5
σ Cr-Co	0	0	0	1.636	56.2	5
M ₂₃ C ₆	5	3	3	1.632	56.3	20
HfC	2	2	0	1.616	56.9	70
M ₂₃ C ₆	6	2	2	1.613	57	80
σ Cr-Co	0	0	0	1.61	57.2	20
z -TaC	0	0	0	1.555	59.4	70
M ₆ C	7	1	1	1.547	59.7	13
TaC	2	2	0	1.545	59.8	41
σ Cr-Co	0	0	0	1.532	60.4	20
M ₂₃ C ₆	5	5	0	1.513	61.2	20

(W,Ti)C	2	2	0	1.497	61.9	75
WC	0	0	0	1.454	64	20
M ₂ C	1	1	0	1.444	64.5	14
M ₆ C	7	3	1	1.439	64.7	12
WC	0	0	0	1.42	65.7	6
HfC	3	1	1	1.378	68	80
z-TaC	0	0	0	1.375	68.1	20
σ Cr-Co	0	0	0	1.356	69.2	20
M ₆ C	7	3	3	1.35	69.6	19
M ₂₃ C ₆	8	0	0	1.338	70.3	80
z-TaC	0	0	0	1.32	71.4	70
HfC	2	2	2	1.319	71.4	30
TaC	3	1	1	1.318	71.6	41
M ₂ C	1	0	3	1.303	72.5	14
M ₆ C	6	6	0	1.302	72.5	45
WC	0	0	0	1.294	73.1	25
(W,Ti)C	3	1	1	1.277	74.2	80
M ₆ C	5	5	5	1.276	74.3	11
TaC	2	2	2	1.262	75.3	14
WC	0	0	0	1.259	75.4	14
σ Cr-Co	0	0	0	1.257	75.6	50
WC	0	0	0	1.236	77.1	30
(W,Ti)C	2	2	2	1.223	78.1	25
s Cr-Co	0	0	0	1.222	78.2	50
M ₂ C	1	1	2	1.221	78.2	12
M ₆ C	7	5	3	1.213	78.9	4
σ Cr-Co	0	0	0	1.207	79.3	50
σ Cr-Co	0	0	0	1.199	79.9	50
Cr ₇ C ₃	0	0	0	1.188	80.8	16
σ Cr-Co	0	0	0	1.185	81.1	50
σ Cr-Co	0	0	0	1.175	81.9	50
σ Cr-Co	0	0	0	1.167	82.6	50
HfC	4	0	0	1.143	84.8	10
M ₆ C	7	5	5	1.111	87.8	13
TaC	4	0	0	1.093	89.7	6
(W,Ti)C	4	0	0	1.059	93.4	20
HfC	3	3	1	1.048	94.6	50
HfC	4	2	0	1.022	97.8	50

4 Characterisation of Alloy IN738LC

4.1 Introduction

The effect of thermal exposure on the microstructure of IN738LC can be characterised experimentally, and to an extent by thermodynamic predictions of equilibrium phases. The thermodynamic predictions can give an indication of how temperature and composition will affect stable phases in the alloy, but will not provide information on the kinetics of a phase transformation. The ultimate aim of the research is to produce a model that will act as a time - temperature recorder. Hence a feature that is affected by both exposure time and temperature must be identified experimentally. On identification of such a feature, the thermal exposure programme described in Test Programme (Chapter 3) would provide the data necessary to develop and use a time-temperature recorder model.

With the benefit of prior work on similar materials⁷⁴, interest has been focussed on a microstructural feature primarily affected by thermal exposure, carbide transformations. However, during the course of the general characterisation, the width of grain boundary γ was identified as a feature also worth investigating in more detail. The effect of very high temperature thermal exposure on carbides is also considered.

The characterisation on base material IN738LC is presented in two parts in this chapter;

1. Effect of thermal exposure on microstructure

To confirm the suitability of carbide evolution as a parameter that could be used for time/temperature correlation modelling. This section contains the bulk of the experimental work, including equilibrium predictions and microstructural analysis. A short quantitative study on measurement of grain boundary width is included.

2. Effect of very high temperature exposure on carbides

Limited information in the literature is available on the effect of very high temperatures on the carbides in IN738LC, hence this study. Such high temperatures might be experienced during unusual thermal cycles or blade reprocessing, particularly for replacement of coatings.

4.2 Effect of Thermal Exposure on Microstructure

Two data sets comprise this section;

- equilibrium predictions
- experimental characterisation.

Equilibrium predictions from the ThermoCalc/Ni database system described in Thermodynamic Modelling (Chapter 3) can give a good indication of the phases to be expected and the effect of temperature. Results from these predictions are therefore provided prior to the experimental data, and the presentation for both data sets is described in the following sections.

4.2.1 Format for Results and Data

4.2.1.1 Equilibrium Predictions

Fifteen elements were placed into the system, from the composition data given in Thermodynamic Modelling (Chapter 3). The phases in IN738LC in the temperature range 600-1300°C were predicted. The temperatures 850°C and 950°C were selected to show the proportions of the phases in more detail. In addition to this, with respect to IN738 and MCrAlY coating systems, the effects of chromium and aluminium diffusion were considered. In particular, the effect of;

- increasing chromium content
- increasing aluminium content
- reducing aluminium content.

To achieve this the calculations were carried with modified compositions, with step-wise changes being made to aluminium and chromium contents. The balancing element for modification was nickel in all cases.

4.2.1.2 Experimental Characterisation

The data are presented in a sequence of increasing thermal exposure, beginning with the virgin bar and ending with a sample that had experienced relatively long term thermal exposure. For this characterisation, certain samples were available. Some of the available material had been subjected to relatively short term creep and fatigue stress, however they were primarily analysed with a view to the thermal exposure they experienced. Creep stress,

fatigue and rejuvenation may also affect certain microstructural features and the effect of these may be considered in separate research programmes.

The samples used for characterisation of the effect of thermal exposure on IN738LC are listed below, and summarised in Table 4.1;

1. As cast bar, a sample of virgin, untreated material, G0
2. Plate sample that had experienced commercial heat treatment cycle only, G10
3. Two sets of samples which were available early in the test programme, for detailed characterisation of carbides;
 - a) test bars that had been fatigue tested at service temperatures, G1
 - b) test bars that had been creep tested at service temperatures, G2

The testing regime is given in Table 4.2. The G1 and G2 samples were used to carry out a detailed analysis of carbides

4. For analysis of longer term thermal exposure, samples from the IPTME thermal exposure programme were available. G12/5-X, which had been exposed at 950°C for 12000 hours, was selected
5. Carbides can be extracted from the superalloy matrix using established techniques⁶³. Extracted carbides from two samples suffering medium term thermal exposure, G7/A20 and G11/4-Z were examined by SEM/EDX.

As stated in the introduction to this chapter, interest in IN738LC in this research is focussed on carbides. Data are available in the literature on the effect of thermal exposure on γ/γ' morphology in nickel base superalloys, so the description of these phases here is limited. The carbides are discussed qualitatively with respect to morphology and distribution, and quantitatively with respect to composition and proportion.

For composition determination, EDX analysis was performed as detailed in Energy Dispersive X-ray (EDX) Analysis (Chapter 2). Carbon is not detected due to the detector window used and the elements included in the analysis are normalised to 100%. Further renormalisation for overlapping phases was applied (Appendix 3A), and these data are included.

X-ray diffraction on extracted particles was carried out as detailed in X-Ray Diffraction (Chapter 2) and Appendix 3B. The peaks obtained were compared against known carbide

peaks⁶² for identification. A table of deconvoluted peak data is supplied for each sample. An example trace for an IN738LC sample exposed at 915°C for 2448 hours is given in Figure 4.1, with labels for all detected MC and $M_{23}C_6$ peaks. The ratio of $M_{23}C_6$ to MC was calculated by the method described in Chapter 2, Appendix 3B.

To present the data for the above features, for each state described in section 4.2.1.2 (1 to 4), two pages of data are prepared for each sample. This first page contains;

- low and high magnification secondary and backscattered electron micrographs – carbide distribution
- high magnification secondary electron micrograph - γ morphology
- table of EDX data on carbide composition.

The etchant used was 1% citric acid, 1% ammonium sulphate in water, electrolytic, unless otherwise stated (see Optical Microscopy, Chapter 3, for etching details)

The data layout for this page is shown in

Figure 4.2.

The second page contains;

- table of XRD peak data for extracted carbides
- calculated ratio, $M_{23}C_6$: MC (details in Appendix 3B)

After the above data have been presented in sequence of increasing thermal exposure, for a more thorough examination of the carbides, the compositions of a number of carbides in all the samples were renormalised and averaged. The purpose was to find out whether the carbides exhibited a consistent stoichiometry. Additionally, a summary of the carbide ratios is given at the end.

Table 4.1 IN738LC sample history

	Exposure temp / °C	Exposure time / hours ¹	ID	Comments
1	None	None	G0	Virgin bar
2	845	24	G10	Commercial heat treatment (plate)
3 a	850	0	G1/1	Short term fatigue tests
	850	76	G1/0	
	850	82.00	G1/2	
	850	283.00	G1/3	
3 b	950	1065	G2/1	Rejuvenation and Creep tests (bar 1)
	950	1025	G2/2	
	950	1269	G2/3	
	950	1139	G2/4	
4	950	12000	G12/5-X	Thermal exposure (plate)
5 a	885	4833	G7/A20	Extracted carbides (creep test)
5 b	950	7200	G11/4-Z	Extracted carbides (plate)

¹ Does not include exposure prior to rejuvenation, where appropriate.

Table 4.2 Details of fatigue, creep and rejuvenation treatments for G1 and G2 groups

Lab ID	Test type	Pre rejuvenation					Rejuvenation treatment			Post-rejuvenation			
							HIP /°C	Solution °C / hrs	Age °C / hrs				
		Fatigue test data								Fatigue test data			
		Test temp / °C	Tension/Compression stress / MPa	Cycles	Life frac	Rupture				Test temp / °C	Tension/Compression stress / Mpa	Cycle	Rupture
G1/1	LCF	850	398/168	820	-	load fail	None	None	none	n/a	n/a	n/a	n/a
G1/0	LCF	850	316/181	410	0.5	not yet	None	1120/2	845/24	850	437/240	760	yes
G1/2	LCF	850	336/212	410	0.5	not yet	1180	1120/2	845/24	850	354/212	820	yes
G1/3	LCF	850	371/233	205	0.25	not yet	1200	1120/2	845/24	850	336/187	2830	yes
		Creep test data								Creep test data			
		Test temp / °C	Test stress / MPa	Life hours	Rupture					Test temp / °C	Test stress / MPa	Life hours	Rupture
G2/1	Creep	950	100	400	Not yet		None	None	None	950	100	1065.1	yes
G2/2	Creep	950	100	400	Not yet		None	1120/2	845/24	950	100	1025.1	yes
G2/3	Creep	950	100	400	Not yet		1180	1120/2	845/24	950	100	1269	yes
G2/4	Creep	950	100	400	Not yet		1200	1120/2	845/24	950	100	1139	yes

Figure 4.1 Example trace for X-ray diffraction of extracted carbides from IN738LC 915°C for 2448 hours

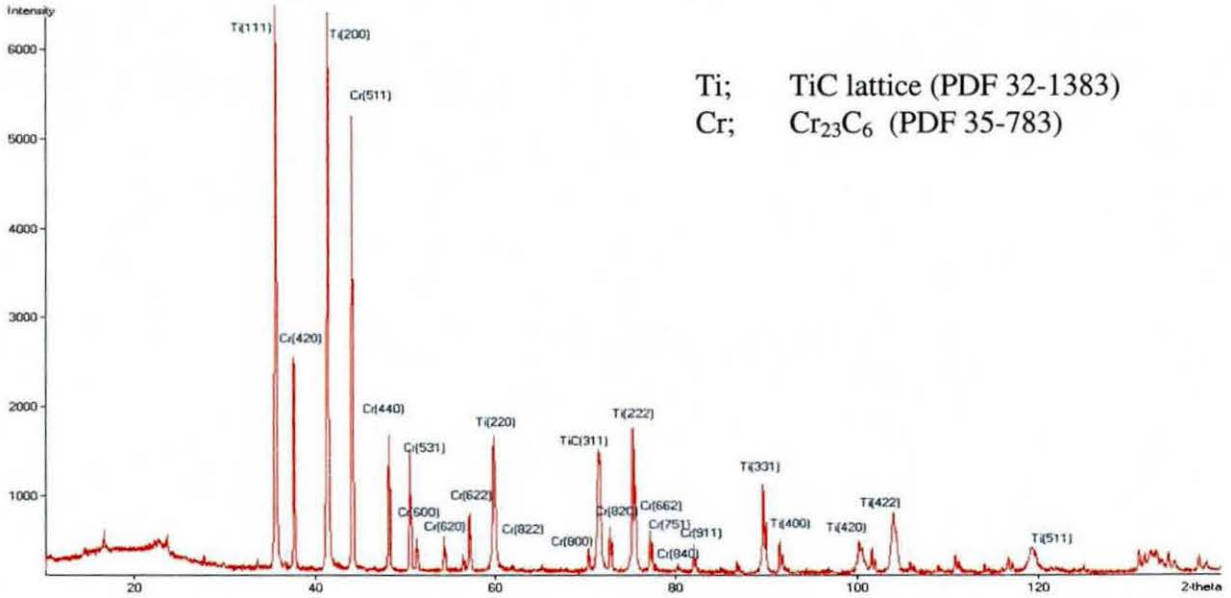


Figure 4.2 Layout for substrate data

IN738LC Characteristics

Low mag electron micrograph (carbides)	High mag Electron micrograph (carbides)	Higher mag electron micrograph (γ/γ')
Table, Example raw EDX data of carbides		
Raw		
Renormalised*		

* Renormalised EDX applies the correction for overlapping phases as detailed in Appendix 3A

4.2.2 Results - Equilibrium Predictions

The prediction for the bar 1 IN738LC composition shows that as temperature rises, the proportion of γ increases at the expense of γ' , Figure 4.3 a. The rate of this change increases sharply just above 1000°C. The predicted γ' solvus is in the region of 1150°C. Below about 1010°C, $M_{23}C_6$ is the stable carbide, above this temperature MC is the stable carbide. σ is predicted to exist at temperatures below 770°C (note that lower limit for these calculations is 600°C). In the temperature range 850°C to 950°C, the increase in proportion of γ with temperature is small, Figure 4.3 b.

Depleting aluminium at temperatures below about 1050°C, results in more γ at the expense of γ' , Figure 4.4 a-d. σ becomes less stable (probably an effect of chromium partitioning to the increasing amount of γ). An increase of Al from 3.47% to 5% has the opposite effect, with increased stability of σ being prominent. Whilst there is more γ at 950°C than at 850°C, Figure 4.4 e-f, show the effect of modifying aluminium content results in similar trends at these two temperatures.

An increase in the chromium content stabilises the σ phase, with the σ solvus increasing to 1080°C at 24 mass% Cr, Figure 4.5 a-d. The proportion of γ reduces, but its solvus was not affected. Hence above 1130°C the material is almost entirely γ . The direct effect of chromium depletion on γ' is minimal. The proportions of the phases at 850°C and 950°C are similar, Figure 4.5 e-f.

Figure 4.3 IN738LC Equilibrium bar 1 composition (G1)

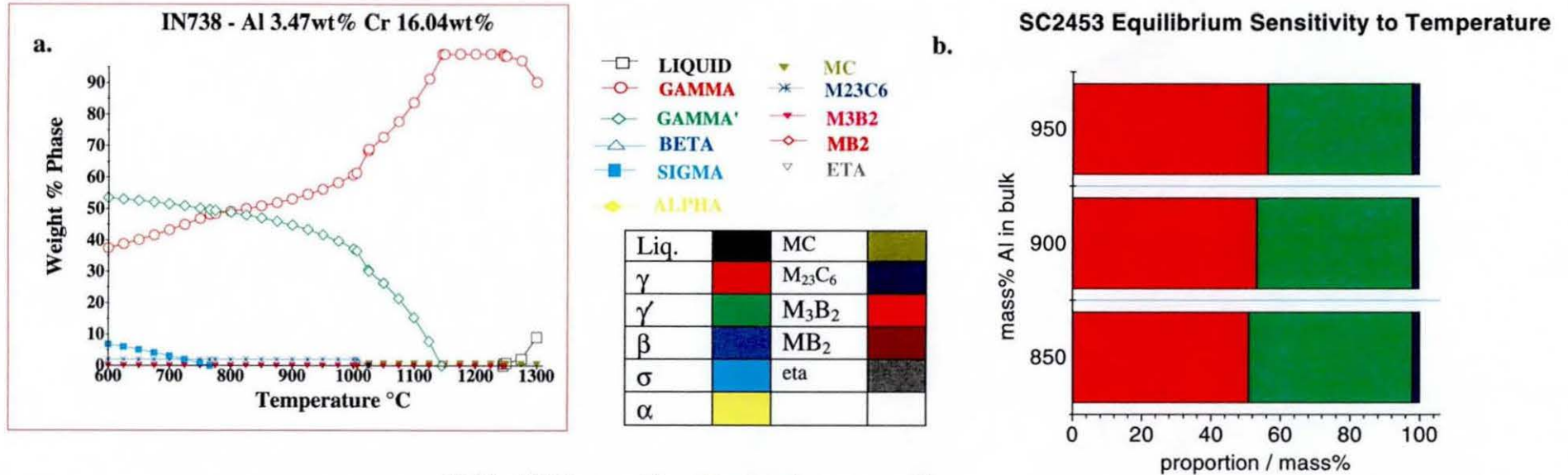
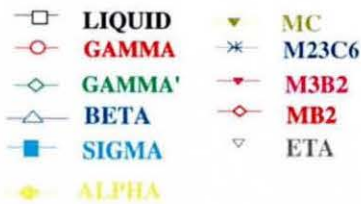
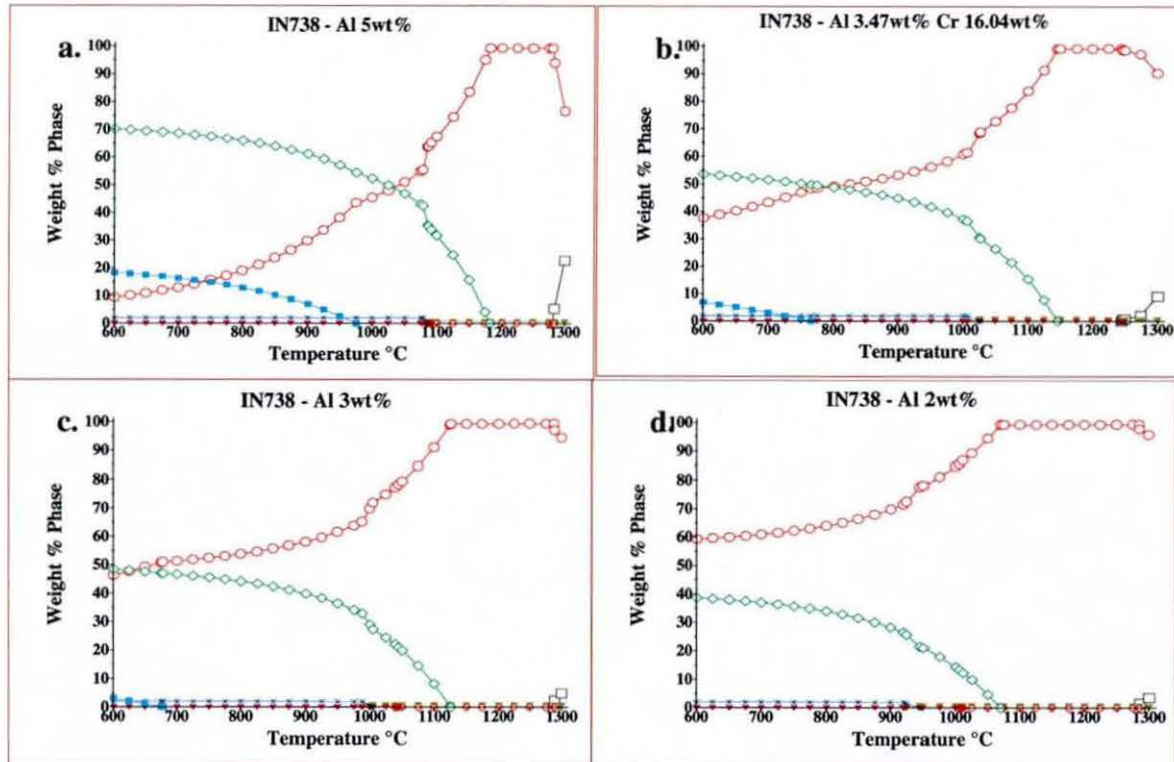


Table 4.3 Composition data for phases, atom%

phase	Temp/°C	Ni	Cr	Co	Mo	W	Ti	Al	Ta	Nb	Zr	C
Gamma	850	52.3	29.5	12.3	1.5	1.1	0.4	2.6	0.1	0	0	0
Gamma	900	53.3	28.3	11.8	1.5	1.1	0.7	3.1	0.1	0.1	0	0
Gamma	950	54.4	26.7	11.2	1.4	1.1	1.0	3.7	0.1	0.1	0	0
Gamma prime	850	69.3	2.7	4.7	0.1	0.6	7.8	12.6	1.1	1.0	0.1	0
Gamma prime	900	69.0	2.8	4.9	0.1	0.5	7.9	12.5	1.1	1.0	0.1	0
Gamma prime	950	68.7	3.0	5.1	0.1	0.5	8.0	12.4	1.1	1.0	0	0
M ₂₃ C ₆	850	4.3	64.6	1.7	8.0	0.8	0	0	0	0	0	20.7
M ₂₃ C ₆	900	4.8	64.1	1.9	7.6	0.9	0	0	0	0	0	20.7
M ₂₃ C ₆	950	5.4	63.7	2.0	7.1	1.1	0	0	0	0	0	20.6
MC	1050	0	0.5	0	0.2	1.0	32.2	0	8.6	7.7	1.5	48.3
Sigma	750	17.4	58.8	17.5	5.7	0.5	0	0	0	0	0	0

Figure 4.4 IN738LC – sensitivity of equilibrium to Al content (bar 1 composition)



Liq.	MC		
γ	$M_{23}C_6$		
γ'	M_3B_2		
β	MB_2		
σ	eta		
α			

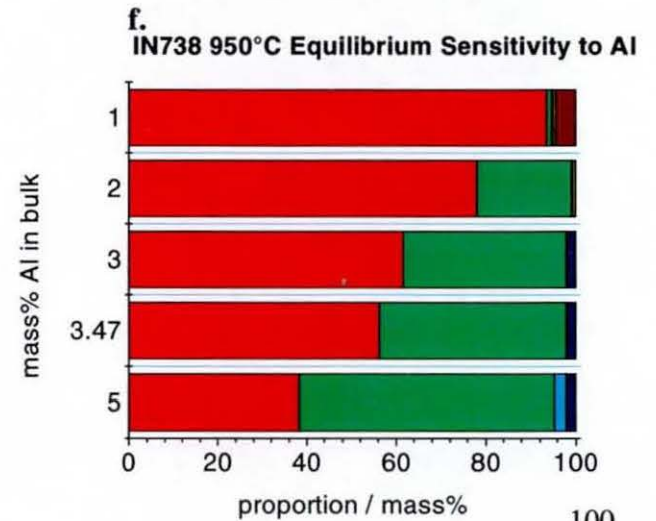
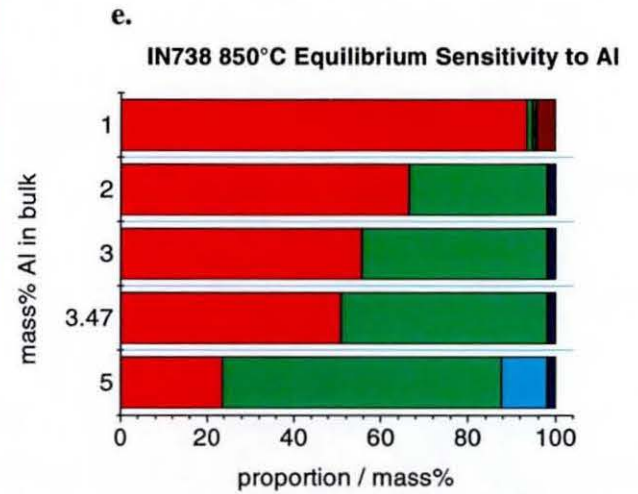
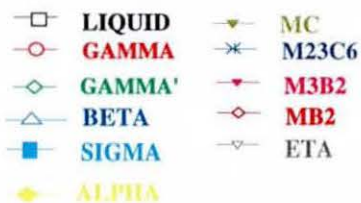
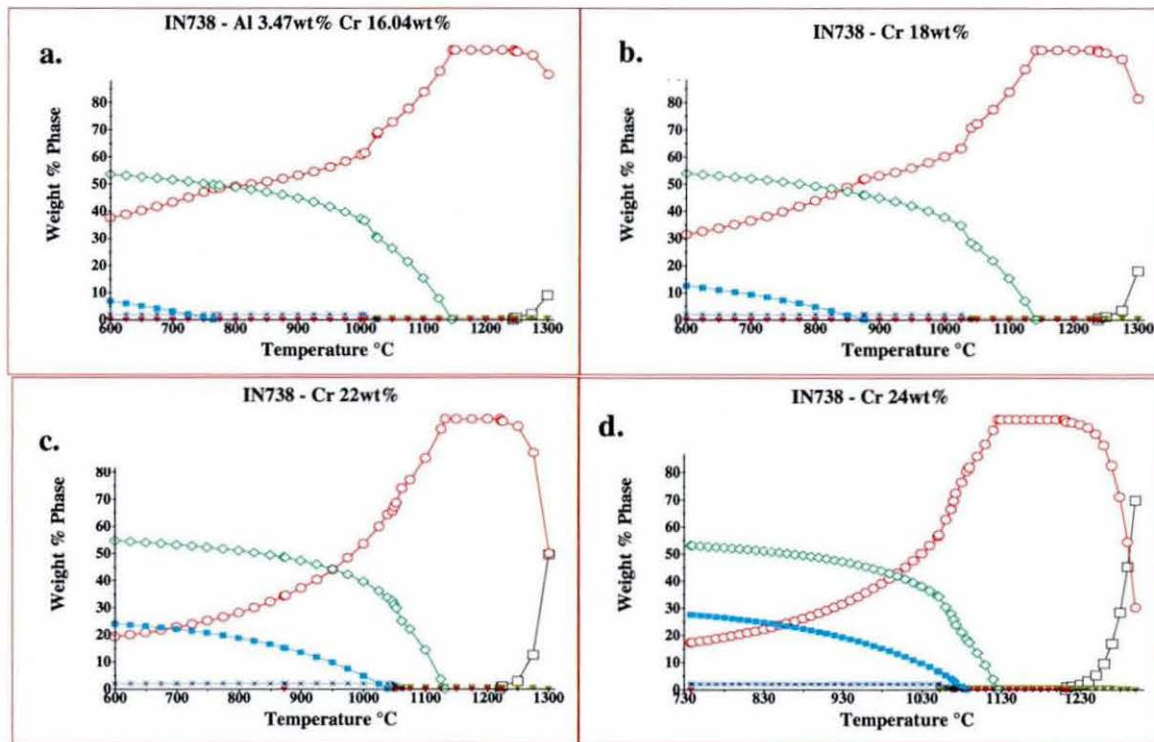
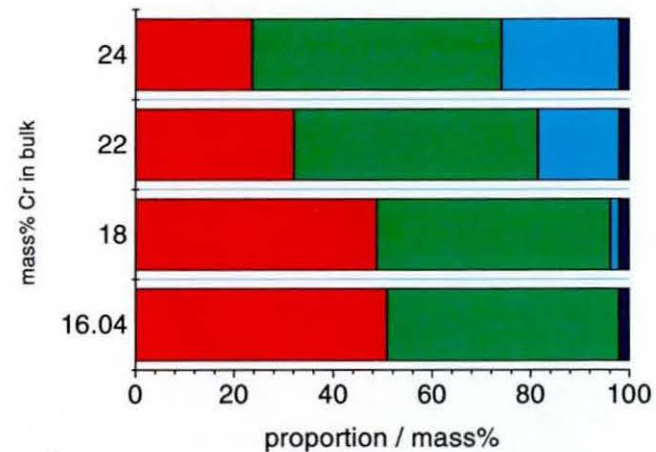


Figure 4.5 IN738LC – sensitivity of equilibrium to increasing Cr content (bar 1 composition)

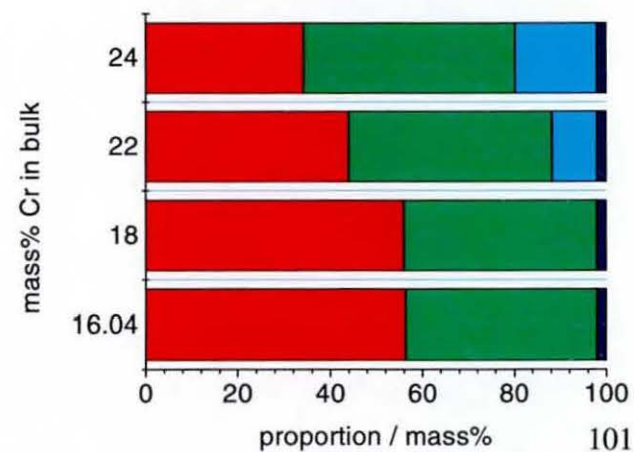


Liq.		MC	
γ		M ₂₃ C ₆	
γ'		M ₃ B ₂	
β		MB ₂	
σ		eta	
α			

e. IN738 850°C Equilibrium Sensitivity to Cr



f. IN738 950°C Equilibrium Sensitivity to Cr



4.2.3 Results - Experimental Data

4.2.3.1 Virgin bar (G0)

The virgin bar contains numerous MC carbides mainly at intergranular and intercellular positions, Figure 4.8 a,b. Most of these carbides are bright on backscattered electron imaging, indicating the presence of elements which have a high atomic mass. Energy dispersive X-ray (EDX) analysis showed that these carbides contain mainly titanium, tantalum and niobium, a typical composition being given in Table 4.5. Note that tantalum and niobium have high atomic mass. Some of the MC carbides were found to have darker centres in the backscattered imaging mode, Figure 4.8 b, indicating a variation of composition within the carbide. EDX analysis shows these carbides to be lean in tantalum and niobium, relative to the majority of MC carbides, Table 4.5. To differentiate between the two types of MC carbide they were given the sub-denominations Ti, Nb-rich MC carbide and Ti, Nb-lean MC carbide.

The γ particles appear to be present in two size groups, the particles in the larger group being around one micron in diameter, the smaller particles have a diameter that is sub-micron. The larger γ particles are blocky, Figure 4.8 c showing a triangular section. The shape of the cross section has some dependence on the orientation of the grain, the actual shape is probably cuboidal.

X-ray diffraction (XRD) data are shown in Table 4.6. Two types of lattice structure are evident, one corresponding to that of TiC and one corresponding to that of Cr_{23}C_6 . This confirms that both types of MC carbide, Nb-rich and Nb-lean, have the lattice structure of TiC. The particles with TiC and Cr_{23}C_6 structures shall henceforth be described by the more general terms MC and M_{23}C_6 , to reflect the compositions of the particles in IN738LC. No other carbides were identified. The data in Table 4.6 show that almost all of the carbide is MC, with trace amounts of M_{23}C_6 present. There are some peaks that have not been identified, but they are not considered to be due to typical phases that may occur in IN738LC.

4.2.3.2 Commercial Heat Treatment (G10)

The carbides in the commercially heat treated sample G10 are similar in appearance to those in G10. Ti, Nb-rich and Ti, Nb-lean carbides were both visible.

The XRD data in Table 4.8 show a predominance of MC carbide with trace amounts of $M_{23}C_6$. The carbide ratio $M_{23}C_6 : MC$ has increases slightly compared with the virgin bar material G0.

The γ is again blocky. Fine secondary γ spheroids are now also evident in the structure.

4.2.3.3 Short Term Thermally Exposed Samples (G1/3)

The two types of MC carbide are again evident in the G1 group Figure 4.10 a-c. Additionally, small amounts of precipitate at the grain boundary were observed, Figure 4.10 b being typical. EDX analysis shows high chromium content, Table 4.9. As the width of the carbide is sub-micron, the EDX data would have suffered from overlap of adjacent (nickel rich) phases. The grain boundary precipitate is considered to be $M_{23}C_6$ carbide. Both types of MC carbide are again evident.

The XRD data again indicate the presence of MC and $M_{23}C_6$ carbide. There is only a small amount of $M_{23}C_6$, not significantly more than in the commercially heat treated sample G10.

The primary γ is blocky in this sample, with fine spheroids of secondary γ evident.

4.2.3.4 Medium Term Thermally Exposed Sample (G2/2)

The microstructure exhibits less MC and more $M_{23}C_6$ than samples that experienced less severe thermal exposure, as indicated by Figure 4.11 a and b. The two types of MC carbide are still evident. The $M_{23}C_6$ forms a discontinuous grain boundary network, enveloped by γ , Figure 4.11 b. Typical compositions of the phases are given in Table 4.11.

XRD data, Table 4.12 reveal evidence of two carbides, MC and $M_{23}C_6$. $M_{23}C_6$ now has a more significant presence than previous samples (less thermal exposure), with more of the minor peaks evident. The $M_{23}C_6 / MC$ ratio is an order of magnitude greater than the sample exposed at 850°C for a shorter period, G1/3.

The primary γ morphology is spheroidal Figure 4.11 c. Very few fine spheroids are apparent. The sample pictured, G2/2, had experienced some rejuvenation treatment, which may have affected the γ morphology, however γ are generally seen to become more rounded with increasing thermal exposure.

4.2.3.5 Long Term Thermally Exposed Sample (G12/5-X)

Sample G12/5-X, an example of long term thermal exposure (12000 hours at 950°C), exhibits a relatively small amount of MC carbide. $M_{23}C_6$ was predominant, Figure 4.12 a-c. This was

confirmed by the XRD technique. A thick grain boundary network of γ was evident, enveloping $M_{23}C_6$ carbide where present. The thickness of the γ envelope was greater than that of the sample G2/2 (which experience less thermal exposure).

The primary γ is now spheroidal, as discussed above. There is a chromium rich phase present, the identity of which is not certain.

4.2.3.6 Examination of Extracted Carbide Particles

Carbide particles extracted for the purpose of X-ray diffraction, by the method detailed in Appendix 3A, were prepared for scanning electron microscopy by sputter coating with gold. The particles are expected to consist of carbides, the γ/γ matrix being dissolved by the extraction technique.

On examination of extracted particles exposed at 885°C and 950°C for 4833 and 7200 hours respectively, three types of carbide were found, Figure 4.13 a-c. One contained a significant amount of niobium on EDX analysis. The niobium containing particle also exhibited significant amounts of chromium and zirconium, the exact identity of this phase was not determined. This particle could be a form of carbide, but this was not confirmed. The XRD data did not identify it any further

MC (Ti) and $M_{23}C_6$ carbides were also evident. The two variants Ti, Nb-rich MC carbide and Ti, Nb-lean, could not be distinguished on this examination, as the difference in composition appears only to be at the core. The core is visible when the carbides are cross-sectioned as they would be in a metallographically prepared microsection, but not on extracting whole carbides.

The composition of the MC carbide is similar to that found for Ti, Nb-rich MC found in the microsections of the investigated samples (sections 4.2.3.1 to 4.2.3.5), with the niobium content being slightly higher. Note that the EDX data may still suffer slightly from interference of adjacent phases, but this effect is considered to be less severe than in a metallographic microsection.

The vast majority of carbide was either MC or $M_{23}C_6$, with the niobium containing particles being very few in number. The MC carbides are in general tetrahedral at one end, with bone like appendages Figure 4.13 a and b. $M_{23}C_6$ particles are cubic. The $M_{23}C_6$ carbide appears to nucleate on and grow from MC carbide particles. The $M_{23}C_6$ at the grain boundaries interconnect, and was found to result in a mesh like structure.

4.2.4 Short Quantitative Study on Measurement of Width of Grain Boundary Zone

4.2.4.1 Introduction

The grain boundary effect measured consists of $M_{23}C_6$ carbide with an envelope of γ . Whilst the γ envelope appears (on simple visual examination) to increase in width with time and temperature, temperatures approaching and beyond the solidus of $M_{23}C_6$ will affect this feature due to dissolution of $M_{23}C_6$. A small number of samples were selected for measurement of width of grain boundary zone. A single temperature was chosen, 950°C, with four different exposure times, 1296, 2400, 4800, 7200 hours.

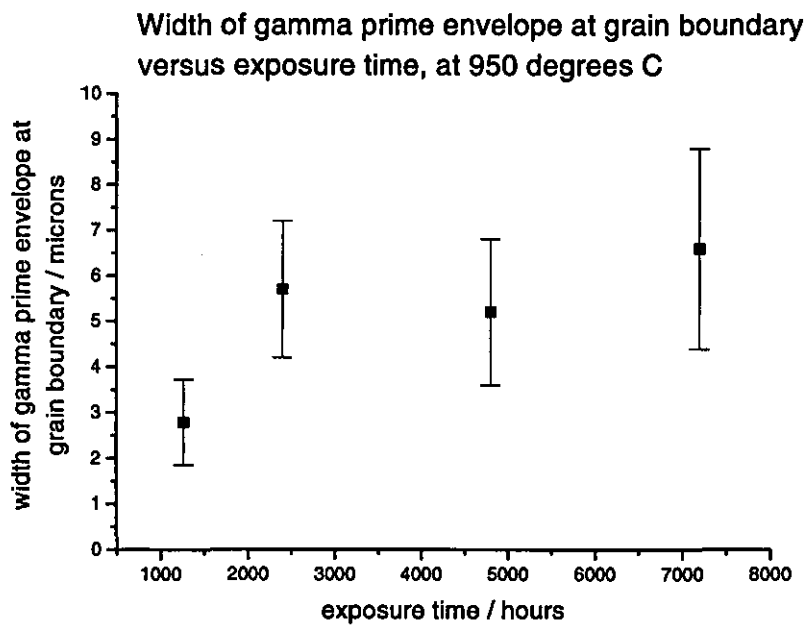
Measurements were carried out in the following manner;

The microsections were prepared and etched in 1% ammonium sulphate/citric acid solution in water (electrolytic). Approximately 10 digital images were taken from each sample, to include grain boundary regions, at a magnification of x1000 or x1250 (G13/4-Y). An image of a graticule was also taken, to enable measurement. An image analysis package was used to measure the width of the grain boundary envelope. Approximately 20 measurements per picture were taken. A mean and standard deviation were calculated.

The results are as shown in Table 4.4 and Figure 4.6.

Table 4.4 Width of grain boundary zone in selected samples exposed at 950°C

Lab ID	Temp /°C	Exposure time/ hours	Width /microns	Stdev
G2/3	950	1269	2.79	0.94
G13/4-X	950	2400	5.7	1.5
G13/4-Y	950	4800	5.2	1.6
G13/4-Z	950	7200	6.6	2.2

Figure 4.6 Effect of thermal exposure on width of grain boundary zone at 950°C

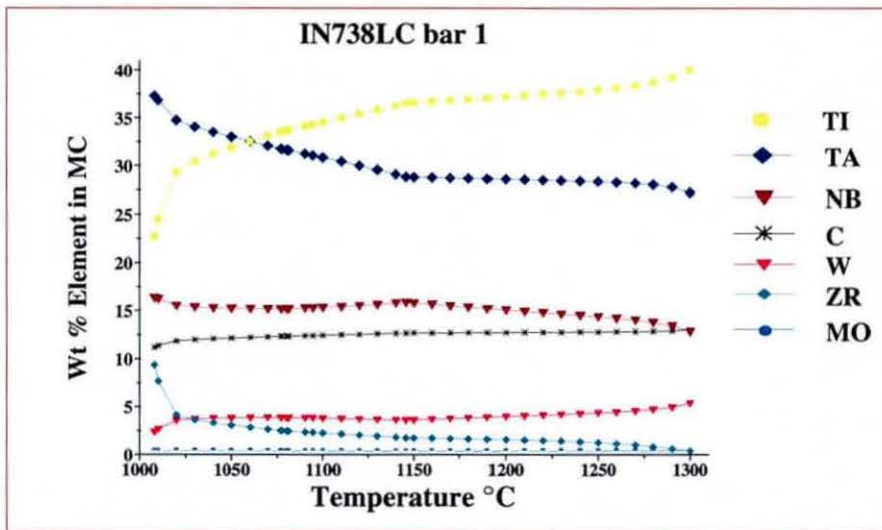
4.2.5 Discussion

4.2.5.1 Carbides

The carbide types observed were;

- MC carbide, Ti, Nb rich
- MC carbide, Ti, Nb lean
- $M_{23}C_6$.

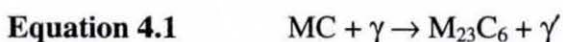
It has been shown that after casting and commercial heat treatment the majority of carbides are MC carbides. Almost all of the MC carbides are close to the TiC lattice structure. There are two types of MC carbide with the TiC lattice structure, the majority Ti, Nb-rich, with a few Ti, Nb-lean. The Ti, Nb-lean carbides appear to be lean in elements of high atomic number only at the core (from backscattered electron imaging). The averaged and renormalised compositions of these two carbide types are shown in Figure 4.14 a and b for the Ti, Nb-rich and Ti, Nb-lean respectively. Whilst there is some variation, no trend with respect to thermal exposure is apparent. The composition of the Ti, Nb-rich carbide is considered relatively consistent. The Ti, Nb-lean carbide also shows consistency after renormalisation is applied, but it should be noted that this variant exhibits a composition profile through its cross section. The presence of Ti, Nb-lean MC carbide is probably due to the solidification sequence. ThermoCalc/Ni-data predictions in Figure 4.7 below show that at higher temperatures, a higher proportion of titanium and a lower proportion of niobium is a more stable composition for MC carbide. Thus, it is likely that the Ti, Nb-lean MC carbide particles are amongst the first to solidify, the majority of carbide particles (Ti, Nb-rich) form later in the solidification sequence and are richer in niobium and tantalum.

Figure 4.7 Equilibrium prediction of effect of temperature on weight% of elements in MC

For the purposes of further discussion, the term MC carbide will be used to refer to Ti carbide, both Nb rich and Nb lean variants. The positioning of MC carbides at grain boundary and intercellular positions is consistent with these carbides being amongst the first solid particles to nucleate. Solidification of the melt would have segregated the carbides to the aforementioned positions. XRD results show only trace amounts of $M_{23}C_6$ in the virgin bar and commercially heat treated samples. No other carbides were found by SEM/EDX or XRD.

More evidence of $M_{23}C_6$ is apparent on the samples that experienced thermal exposure. In sample G1/3, which had been exposed at 850°C for 283 hours fine grain boundary precipitates of $M_{23}C_6$ were found. More severe thermal exposure (950°C for 1025 hours) resulted in a significantly higher volume fraction of $M_{23}C_6$, which formed a grain boundary network. The two most severely thermally exposed samples exhibited a grain boundary network of $M_{23}C_6$ surrounded by a γ' envelope. The $M_{23}C_6$: MC ratio was found to increase with thermal exposure.

The basic reaction for transformation of MC to $M_{23}C_6$ is



The occurrence of this reaction in nickel base superalloys is reported in Sims *et al*³. The current work, particularly the examination of extracted carbides, gives a further insight into

the morphologies involved and the nature of the reaction. The MC carbides have a tetrahedral type morphology whereas the $M_{23}C_6$ is cuboidal. The quantity of $M_{23}C_6$ increased with extent of thermal exposure, accompanied by a decrease in the quantity and size of MC carbide, as evidenced by the $M_{23}C_6$: MC ratios in Table 4.16 and Figure 4.15. This ties in with ThermoCalc calculations, which predict that all carbon is in $M_{23}C_6$ at equilibrium, in the temperature range of the samples investigated, Figure 4.3 a. The increase in the $M_{23}C_6$: MC ratio with respect to thermal exposure appears to be relatively systematic. In Figure 4.15 which plots $M_{23}C_6$: MC versus time for a number of temperatures, the rate of increase of the ratio is generally greater with increasing temperature. Exposure time at each temperature also results in the $M_{23}C_6$: MC ratio increasing. Thus, the $M_{23}C_6$: MC ratio shows good potential for use in a time-temperature recorder model that could be applied to IN738LC.

Examination of extracted carbides clarifies some of the mechanisms of the reaction in Equation 4.1. The $M_{23}C_6$ appears to nucleate on the MC carbide and grow with thermal exposure. At grain boundary positions, the $M_{23}C_6$ cuboids interconnect, forming a mesh like structure. A γ' envelope also appears around the $M_{23}C_6$, corroborating the occurrence of the reaction in Equation 4.1. Thus, it can be said that chromium from the γ in the matrix diffuses to MC carbides and reacts with the carbon to form $M_{23}C_6$ cuboids. The depletion of chromium from the matrix adjacent to grain boundary regions will result in γ' being more stable than γ (γ has a much higher solubility for chromium) in these regions, hence the grain boundary envelope of γ' . The most significant diffusion process will be that of chromium from the matrix to the transforming carbide, and the maximum distance diffused is likely to be related to the thickness of the γ' grain boundary envelope.

4.2.5.2 Matrix Phases and γ' Grain Boundary Envelope

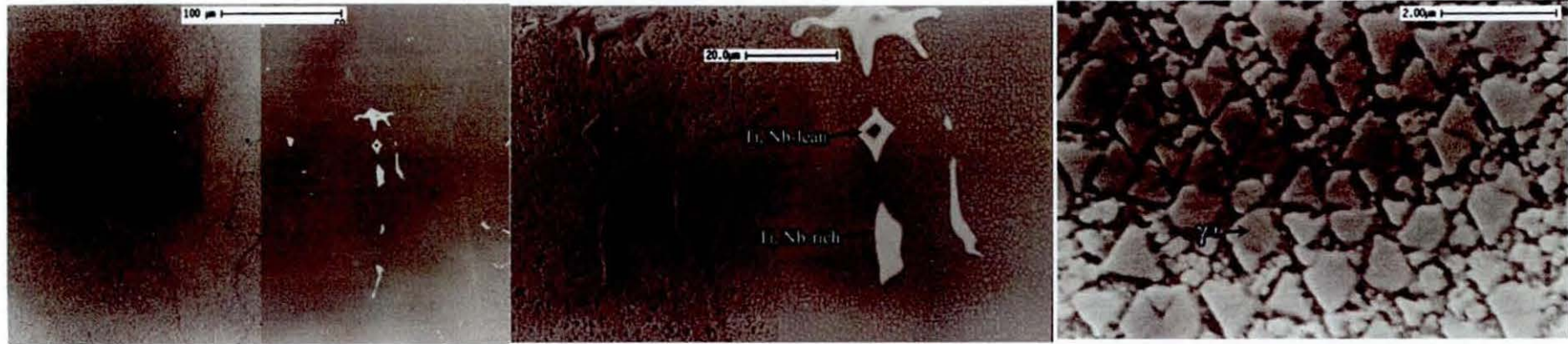
A feature related to the carbide transformation that is affected by thermal exposure is the width of the γ' grain boundary envelope that surrounds $M_{23}C_6$. The results do show an overall increase in grain boundary width with exposure time, but the percentage error in the data is large. The rate of increase of the γ' envelope with thermal exposure requires further investigation, to determine whether statistically sound data can be obtained that will define a relationship with temperature and time.

The primary γ is seen to become more spheroidal on thermal exposure, a well documented feature in nickel base superalloys. Whilst the $\gamma' : \gamma$ volume fraction ratio has not been measured in this research, equilibrium predictions (Figure 4.3 a) and the literature (e.g.

Durand-Charre¹ chapter 6) suggest that it decreases with temperature. The corresponding increase in γ size is discussed by Durand-Charre¹ in chapter 7 and Sims *et al*³ in chapter 9. The increase in γ size with thermal exposure has been used to create time-temperature recorder models for nickel base superalloys, for example Srinivasan's model for U520⁴⁰. However there are difficulties in quantitative measurement of γ size, extensive image analysis being required. Such a model could be attempted for IN738LC, but interest for this alloy is focussed on carbide transformations, where quantitative measurements can be carried out by less laborious methods.

4.2.6 Experimental Data

Figure 4.8 G0 Virgin Bar –microscopy data



a. Scanning electron micrograph, backscattered electron image

b. Scanning electron micrograph, backscattered electron image

c. Scanning electron micrograph, secondary electron image

Table 4.5 Typical EDX data for carbide composition, atom%,

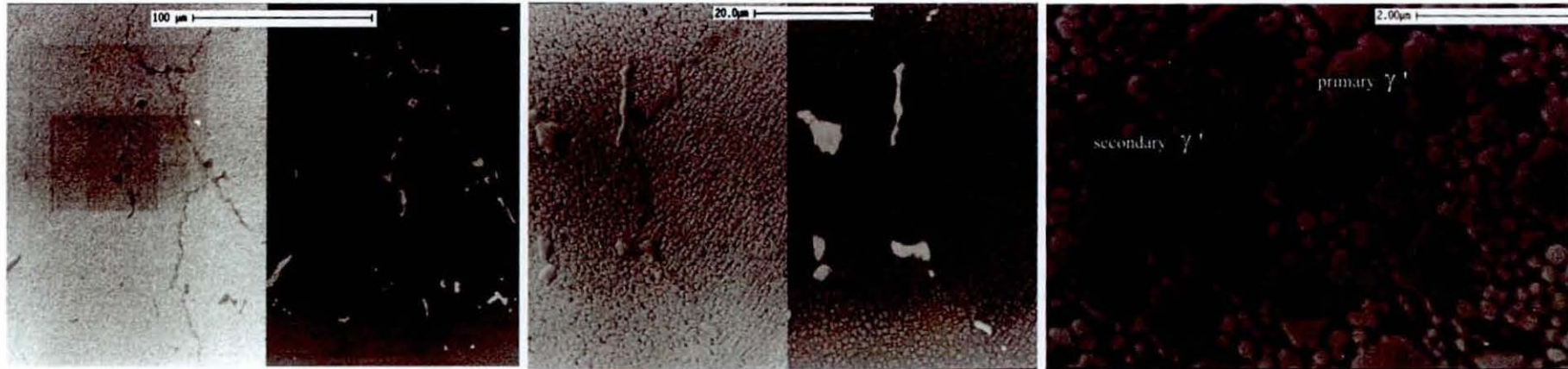
	Data type	Ni K	Cr K	Co K	Mo L	W L	Ti L	Al K	Ta L	Nb L	Zr L
Ti, Nb-rich MC	Raw	4.6	1.9	0.3	4.0	3.5	50.2	0	23.4	11.8	0
	Renorm				4.2	3.7	54.1		25.3	12.8	0
Ti, Nb-lean MC	Raw	2.1	1.0	0.6	0.1	0.8	85.4	4.2	4.1	1.5	0
	Renorm				0.1	0.9	92.9		4.5	1.6	0

Table 4.6 G0 Virgin bar XRD data

2θ	absolute intensity / counts	d spacing / Angstroms	integrated intensity / counts ²	peak identity	h	k	l	lattice parameter / Angstroms
25.886	912	3.4419	25062.2	filter				
31.6	2130	2.8313	7603.1					
35.69	3986	2.5157	21517.7	TiC	1	1	1	4.357
37.883	94	2.3750	389.6	Cr23C6	4	2	0	10.621
41.437	3729	2.1791	19951.7	TiC	2	0	0	4.358
44.238	212	2.0474	944.2	Cr23C6	5	1	1	10.639
59.928	1414	1.5435	7162.5	TiC	2	2	0	4.366
66.105	345	1.4135	1932.2					
71.562	639	1.3185	5498.7	TiC	3	1	1	4.373
75.357	244	1.2613	3703.4	TiC	2	2	2	4.369
89.596	71	1.0941	843.2	TiC	4	0	0	4.376
100.261	313	1.0044	3151.4	TiC	3	3	1	4.378
103.934	343	0.9788	5436.5	TiC	4	2	0	4.377
119.267	87	0.8935	1673.4	TiC	4	2	2	4.377
122.687	23	0.8785	5795					
132.221	194	0.8432	6830.7	TiC	5	1	1	4.381

$M_{23}C_6 / MC = 0.032$

Figure 4.9 G10 Commercial heat treatment 1120°C for 2 hours, 845°C for 24 hours – microscopy data



a. Scanning electron micrograph, secondary (left) and backscattered (right) electron images

b. Scanning electron micrograph, secondary (left) and backscattered (right) electron images

c. Scanning electron micrograph, secondary electron image

Table 4.7 Typical EDX data for carbide composition, atom%,

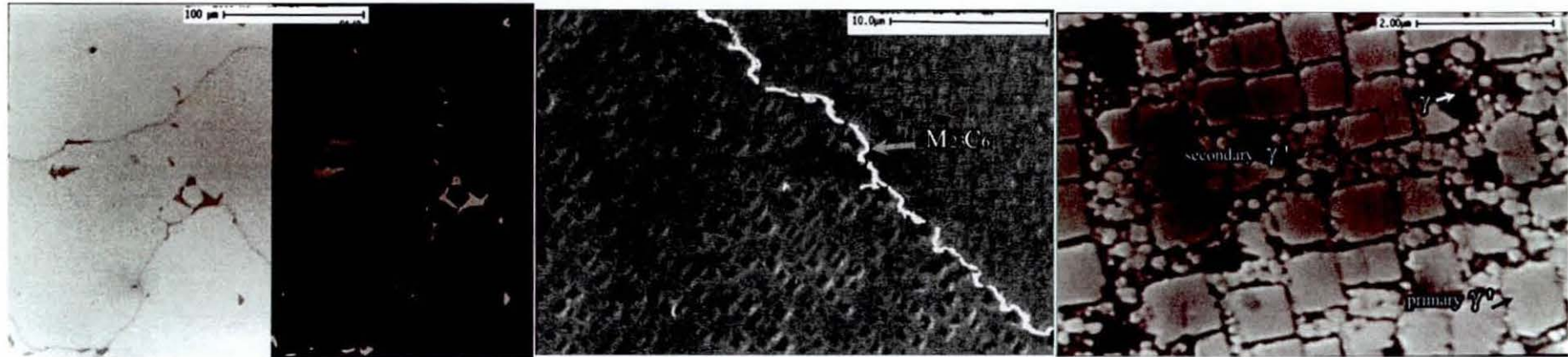
	Data type	Ni K	Cr K	Co K	Mo L	W L	Ti L	Al K	Ta L	Nb L	Zr L
Ti, Nb-rich MC	Raw	3.9	1.5	0.6	3.9	3.2	48.0	0	17.6	19.6	1.5
	Renorm				4.0	3.4	51.2		18.8	20.9	1.6
Ti, Nb-lean MC	Raw	3.3	1.5	0.4	1.2	2.3	74.5	0	11.5	4.9	0
	renorm				0.7	2.3	84.2		8.9	3.9	0

Table 4.8 G10 Commercial heat treatment 1120°C for 2 hours, 845°C for 24 hours – microscopy data

2θ	absolute intensity / counts	d spacing / Angstroms	integrated intensity / counts ²	peak identity	h	k	l	lattice parameter / Angstroms
22.897	44	3.8840	969.7	n/a				
25.804	444	3.4526	9946.4	filter				
27.662	26	3.2248	189.4	n/a				
31.483	826	2.8416	2829	??				
35.754	6749	2.5113	39243.6	TiC	1	1	1	4.350
37.871	290	2.3757	1657.2	Cr ₂₃ C ₆	4	2	0	10.624
41.495	5585	2.1762	32981.2	TiC	2	0	0	4.352
44.219	449	2.0483	2600.2	Cr ₂₃ C ₆	5	1	1	10.643
45.756	122	1.9830	1083.2	??				000
48.559	82	1.8749	4548.4	Cr ₂₃ C ₆	4	4	0	10.606
50.686	96	1.8011	505.9	Cr ₂₃ C ₆	5	3	1	10.655
59.96	2316	1.5428	19182.3	TiC	2	2	0	4.364
66.028	224	1.4149	571.6	??				
71.621	1461	1.3176	14064.8	TiC	3	1	1	4.370
75.355	495	1.2613	4971.3	TiC	2	2	2	4.369
89.724	208	1.0929	2606.6	TiC	4	0	0	4.372
100.343	359	1.0038	5578.3	TiC	3	3	1	4.376
104.034	501	0.9781	8340	TiC	4	2	0	4.374
119.247	283	0.8936	8764.3	TiC	4	2	2	4.378
132.368	284	0.8427	8654.8	TiC	5	1	1	4.379

M₂₃C₆ / MC = 0.045

Figure 4.10 G1/3 exposed at 850°C for 283 hours (fatigue test) – microscopy data



a. Scanning electron micrograph, secondary (left) and backscattered (right) electron images

b. Scanning electron micrograph, secondary electron image
Etchant : Kalling's reagent

c. Scanning electron micrograph, secondary electron image

Table 4.9 Typical EDX data for carbide composition, atom%

		Ni K	Cr K	Co K	Mo L	W L	Ti L	Al K	Ta L	Nb L	Zr L
Ti, Nb-rich	Raw	2.9	1.5	0.6	3.8	3.9	49.6	0	21.4	15.2	0.8
	Renorm				3.9	4.1	52.5		22.6	16.1	0.8
Ti, Nb-lean	Raw	2.4	1.0	0.5	0.8	1.6	82.4	0	8.2	3.2	0
	Renorm				0.9	1.6	85.7		8.5	3.3	0
M ₂₃ C ₆	Raw	47.0	32.1	8.4	2.2	0	3.1	5.7	0.4	1.0	0
	Renorm	5.8	72.9		8.3		11.5		0.3	2.3	0

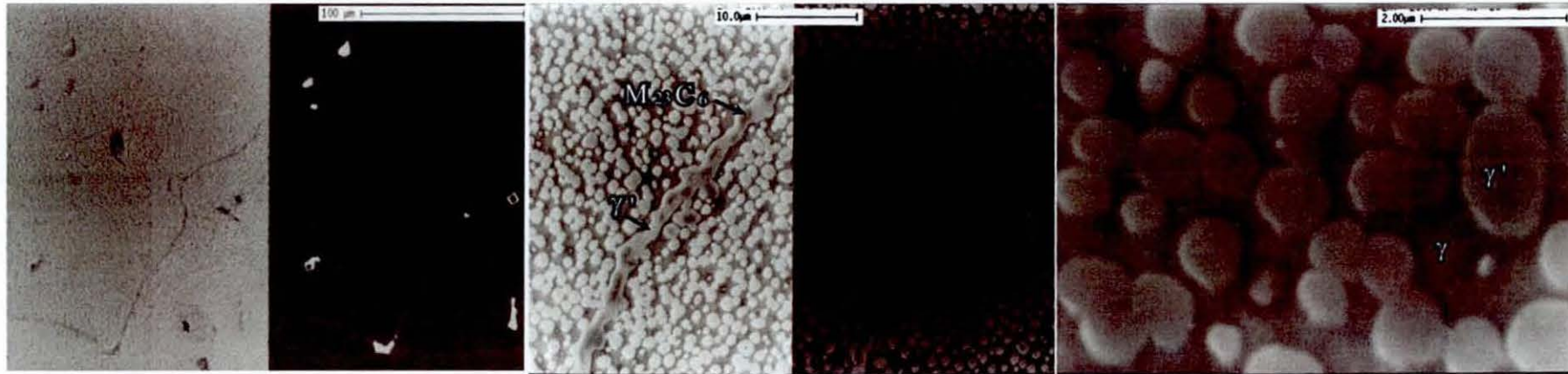
Table 4.10 G1/3 exposed at 850°C for 283 hours (fatigue test) – XRD data

2θ	absolute intensity	d spacing / Angstroms	integrated intensity / counts ²	peak identity	h	k	l	lattice parameter / Angstroms
25.867	889	3.4444	24606.5					
28.4	108	3.1427	107.8					
29.149	58	3.0636	57.6					
31.564	1294	2.8345	4822.1	??				
35.568	5400	2.5240	24364.3	TiC	1	1	1	4.372
37.75	227	2.3830	915.3	Cr ₂₃ C ₆	4	2	0	10.657
41.304	7291	2.1858	38244.7	TiC	2	0	0	4.372
44.1	346	2.0535	1994.5	Cr ₂₃ C ₆	5	1	1	10.670
44.612	160	2.0311	643.8					
45.589	131	1.9898	898.5					
59.845	629	1.5455	5281.2	TiC	2	2	0	4.371
66.107	164	1.4134	953.1	??				
71.458	989	1.3202	8789.1	TiC	3	1	1	4.379
75.251	393	1.2628	3302.5	TiC	2	2	2	4.374
89.576	165	1.0943	2083.5	TiC	4	0	0	4.377

M₂₃C₆ / MC = 0.046

Note: scan up to 90° (2θ) in this sample

Figure 4.11 G2/2 sample exposed at 950°C for 1025 hours



a. Scanning electron micrograph, secondary (left) and backscattered (right) electron images

b. Scanning electron micrograph, secondary (left) and backscattered (right) electron images

c. Scanning electron micrograph, secondary electron image

Table 4.11 Typical EDX data for carbide composition, atom%

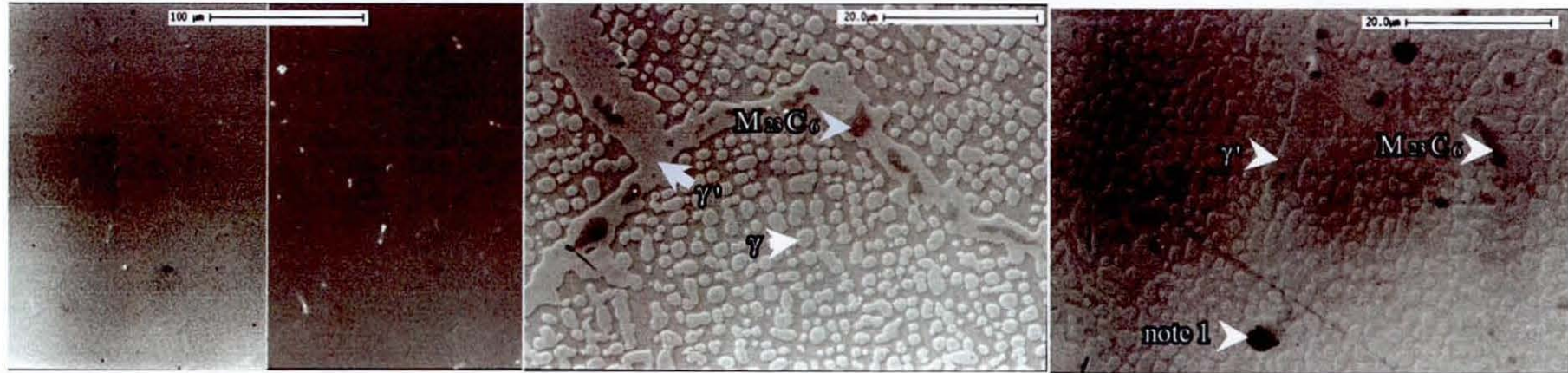
	Data type	Ni K	Cr K	Co K	Mo L	W L	Ti L	Al K	Ta L	Nb L	Zr L
Ti, Nb-rich MC	Raw	3.3	1.5	0.4	3.5	3.7	49.6	0	22.5	15.1	0.2
	Renorm				3.3	3.9	52.7		23.8	16.0	0.2
Ti, Nb-lean MC	Raw	2.3	1.0	0.4	0.3	0.8	81.2	4.8	6.5	2.7	0
	Renorm				0.4	0.8	88.7		7.1	2.9	0
M ₂₃ C ₆	Raw	21.0	60.8	3.6	4.8	1.6	2.3	2.1	1.4	1.7	0.8
	Renorm	5.7	79.6	0	6.7	0	2.9	0	1.9	2.2	1.1

Table 4.12 G2/2 sample exposed at 950°C for 1025 hours n- XRD data

2θ	absolute intensity	d spacing / Angstroms	integrated intensity / counts ²	peak identity	h	k	l	lattice parameter / Angstroms
27.719	63	3.2183	242					
35.582	5652	2.5231	27269.4	TiC	1	1	1	4.370
37.651	1681	2.3891	6445.9	Cr ₂₃ C ₆	4	2	0	10.684
41.315	5863	2.1853	33137.1	TiC	2	0	0	4.371
44.005	3339	2.0577	14477.2	Cr ₂₃ C ₆	5	1	1	10.692
48.119	956	1.8910	4143.2	Cr ₂₃ C ₆	4	4	0	10.697
50.468	751	1.8083	3531.1	Cr ₂₃ C ₆	5	3	1	10.698
51.242	238	1.7828	1078.7	Cr ₂₃ C ₆	6	0	0	10.697
54.212	190	1.6920	906.4	Cr ₂₃ C ₆	6	2	0	10.701
57.081	360	1.6135	1818.1	Cr ₂₃ C ₆	6	2	2	10.703
59.763	2127	1.5474	14819.7	TiC	2	2	0	4.377
70.43	116	1.3369	1079.8	Cr ₂₃ C ₆	8	0	0	10.695
71.478	1109	1.3199	10345.7	TiC	3	1	1	4.377
72.815	372	1.2989	2142	Cr ₂₃ C ₆	8	2	0	10.711
75.262	995	1.2626	10226.3	TiC	2	2	2	4.374
77.093	262	1.2371	1994.8	Cr ₂₃ C ₆	6	6	2	10.785
81.907	116	1.1762	842.7	Cr ₂₃ C ₆	9	1	1	10.715
86.726	69	1.1228	220.1					
89.669	409	1.0934	4651.4	TiC	3	3	1	4.766
91.392	131	1.0772	1534.7	Cr ₂₃ C ₆	7	7	1	10.718
100.144	257	1.0053	3357.2	TiC	4	0	0	4.021
101.572	107	0.9950	1137.3					
103.945	521	0.9787	7865.6	TiC	4	2	0	4.377
105.928	64	0.9658	713					
110.88	110	0.9361	962.2					
116.755	24	0.9053	451.4					
119.075	359	0.8944	7022.6	TiC	4	2	2	4.382
119.407	13	0.8929	401.2					
130.913	94	0.8475	515.7					
132.379	245	0.8426	5307.9	TiC	5	1	1	4.378

$$M_{23}C_6 / MC = 0.35$$

Figure 4.12 G12/5-X exposed at 950°C for 12000 hours



a. Scanning electron micrograph, secondary (left) and backscattered (right) electron images

b. Scanning electron micrograph, secondary electron image

c. Scanning electron micrograph, secondary electron image

Table 4.13 Typical EDX data for particle composition, atom%

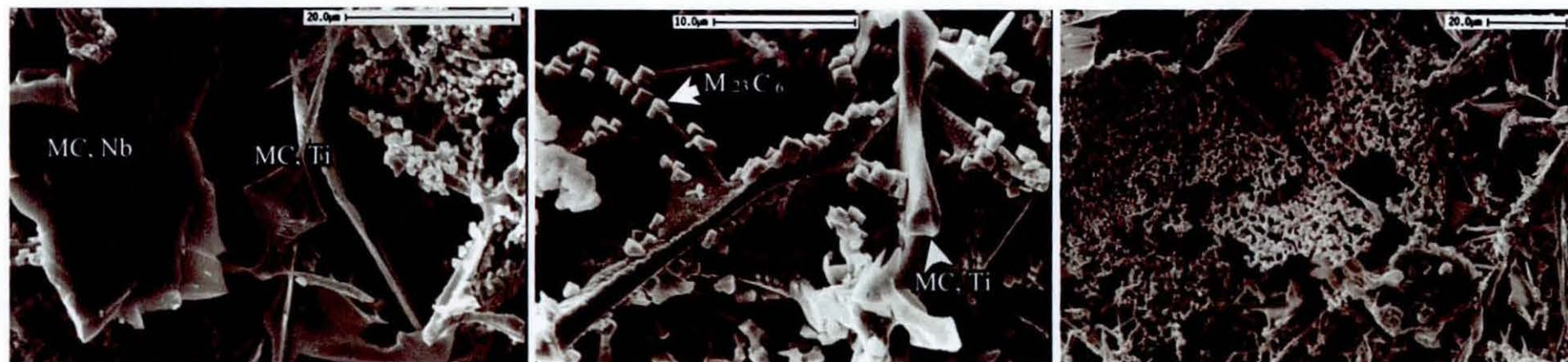
		Ni K	Cr K	Co K	Mo L	W L	Ti L	Al K	Ta L	Nb L	Zr L
Ti, Nb-rich MC	Raw	6.4	2.3	1.7	4.8	3.0	47.8	0	20.6	13.3	0
	Renorm				5.2	3.3	53.5		23.1	14.9	0
Ti, Nb-lean MC	Raw	6.2	83.5	1.8	4.3	2.8	0.7	0.2	0.4	0	0
	renorm	5.8	88.5		4.5		0.7		0.5	0	0
M ₂₃ C ₆	Raw	6.2	83.5	1.8	4.3	2.8	0.7	0.2	0.4	0	0
	renorm	5.8	88.5		4.5		0.7		0.5	0	
Note 1	raw	61.6	16.9	8.5	0.6	1.3	4.1	5.7	0.4	0	0

Table 4.14 G12/5-X exposed at 950°C for 12000 hours

2θ	absolute intensity	d spacing / Angstroms	integrated intensity / counts ²	peak identity	h	k	l	lattice parameter / Angstroms
33.558	319	2.6705	1059					
35.634	1862	2.5195	10146	TiC	1	1	1	4.364
37.633	8765	2.3902	31586	Cr ₂₃ C ₆	4	2	0	10.689
41.356	12348	2.1832	52807	TiC	2	0	0	4.366
43.912	2567	2.0619	9513					
43.984	22537	2.0587	81487	Cr ₂₃ C ₆	5	1	1	10.697
48.109	6733	1.8913	27734	Cr ₂₃ C ₆	4	4	0	10.699
50.46	7206	1.8086	25160	Cr ₂₃ C ₆	5	3	1	10.700
51.21	2387	1.7839	6856	Cr ₂₃ C ₆	6	0	0	10.703
54.208	2050	1.6921	7931	Cr ₂₃ C ₆	6	2	0	10.702
56.366	995	1.6323	3606	Cr ₂₃ C ₆	5	3	3	10.704
57.095	3429	1.6132	15514	Cr ₂₃ C ₆	6	2	2	10.701
59.842	890	1.5455	6675	TiC	2	2	0	4.371
65.213	299	1.4306	1240					
70.335	1298	1.3385	5901	Cr ₂₃ C ₆	8	0	0	10.708
71.598	607	1.3179	6374	TiC	3	1	1	4.371
72.844	2906	1.2984	15397	Cr ₂₃ C ₆	8	2	0	10.707
75.321	6336	1.2618	15873	TiC	2	2	2	4.371
75.535	2969	1.2587	8336	Cr ₂₃ C ₆	8	2	2	10.681
77.149	2329	1.2364	5842	Cr ₂₃ C ₆	6	6	2	10.778
77.376	1209	1.2333	3436	Cr ₂₃ C ₆	7	5	1	10.681
77.73	239	1.2286	792					
80.15	374	1.1975	2057	Cr ₂₃ C ₆	8	4	0	10.710
81.969	1392	1.1754	3742	Cr ₂₃ C ₆	9	1	1	10.709
82.213	681	1.1726	2077	Cr ₂₃ C ₆	9	3	1	11.186
84.9 ₂₃	374	1.1419	1250	TiC	3	3	1	4.978
86.716	495	1.1229	1589	TiC	4	0	0	4.492
89.692	3918	1.0932	12741	Cr ₂₃ C ₆	7	7	1	10.877
89.98	1806	1.0904	5409					

$$M_{23}C_6 / MC = 1.8$$

Figure 4.13 XRD slides G7/A20 and G11/4-Z



a. Scanning electron micrograph, secondary electron image

b. Scanning electron micrograph, secondary electron image

c. Scanning electron micrograph, secondary electron image

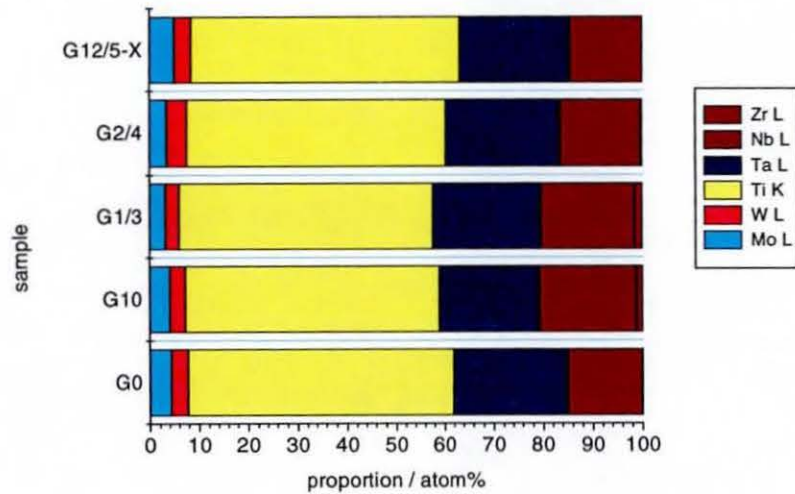
Table 4.15 Typical EDX data for particle composition, atom%

	Ni K	Cr K	Co K	Mo L	W L	Ti K	Al K	Ta L	Nb L	Zr L
MC, Ti	0.5	5.9	0.2	0	4.2	46.4	0	20.2	21.3	1.4
MC, Nb	2	39.4	1.9	0	3.1	11	0	5.3	27.4	9.8
M ₂₃ C ₆ spot	3.6	82.5	1.3	1.9	2	2.6	0	0.9	4.5	0.7

Figure 4.14 Summary of EDX data for MC carbides

a.

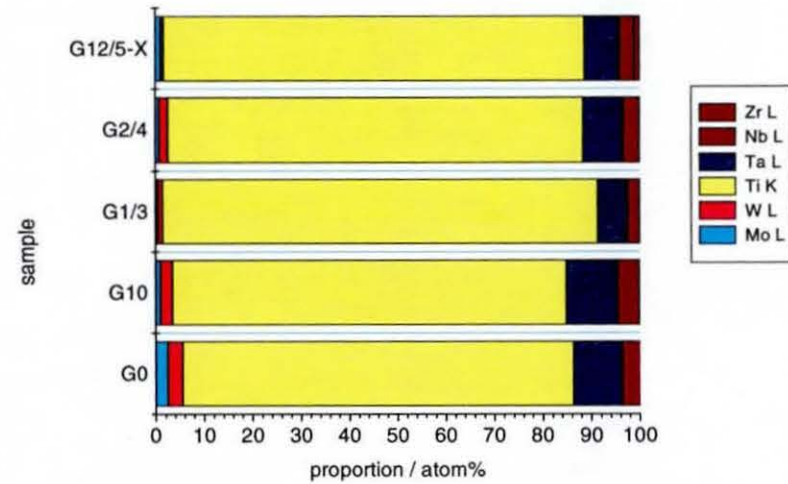
Averaged and re-normalised compositions of
Ti, Nb-rich MC Carbides for thermally exposed samples



Renormalisation as in Appendix 3A

b.

Averaged and re-normalised compositions of
Ti, Nb-lean MC Carbides for thermally exposed samples

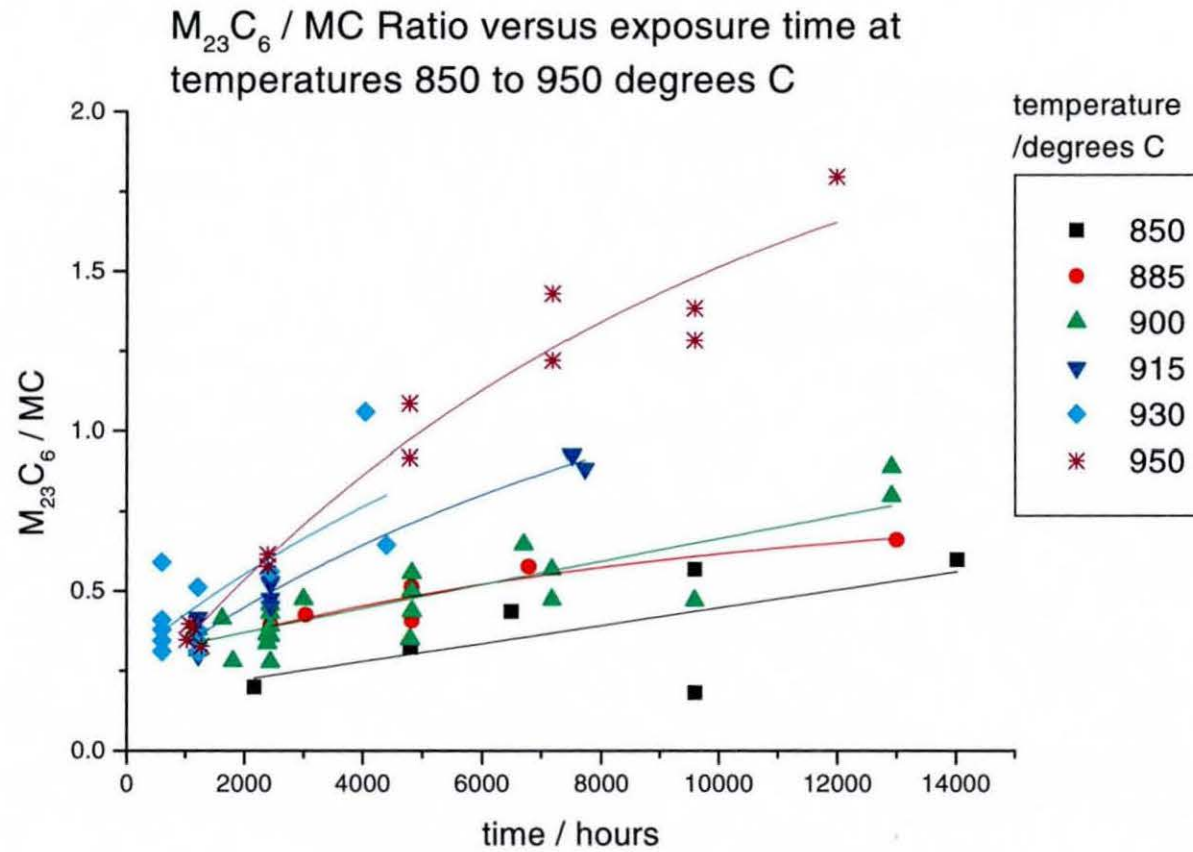


Simple 6 element renormalisation

Table 4.16 Full list of experimentally determined $M_{23}C_6$ / MC ratios

Lab ID	test temp/°C	time / hours	$M_{23}C_6$ / MC
G0			0.032
G10			0.059
G10			0.039
G10			0.045
G8			0.000
G9			0.005
G7/A01			0.017
G7/D01			0.013
G7/C01			00
G1/1	850		000
G1/0	850	76	057
G1/2	850	82	0.101
G1/3	850	283	046
G14/203	850	21700	0.200
G11/8-W	850	48000	0.323
G14/201	850	65000	0.436
G12/2-X	850	96000	0.568
G13/2-X	850	96000	0.182
G14/839	850	14025	0.599
G7/A20	885	4833	0.407
G7/A20	885	4833	0.514
G7/A10	885	6802	0.577
G7/A09	885	130100	0.661
G7/A19	885	144008	0.394
G7/A11	885	144009	0.425
G7/C10	900	1224	0.379
G7/D10	900	1224	0.379
G7/B10	900	1224	0.350
G7/B04	900	1816	0.280
G11/2-Z	900	24000	0.336
G12/2-Z	900	24000	0.363
G7/B11	900	2448	0.457
G7/D11	900	2448	0.358
G7/C11	900	2448	0.430
G7/C11	900	2448	0.391
G12/7-W	900	48000	0.349
G7/C12	900	4833	0.501
G7/B12	900	4833	0.436
G7/D12	900	4833	0.555
G12/7-X	900	72000	0.473
G12/3-X	900	72000	0.568
G13/3-Y	900	96000	0.470
G7/A16	900	144001	0.313
G7/A08	900	144002	0.413
G7/A07	900	144003	0.474
G7/A17	900	144004	0.277
G7/A06	900	144005	0.645
G7/A18	900	144006	0.499
G7/A04	900	144007	0.889
G7/A04	900	144007	0.798
G7/C08	915	1224	0.366
G7/D08	915	1224	0.416
G7/A14	915	1224	0.298
G7/B09	915	2448	0.451
G7/D09	915	2448	0.528
G7/A15	915	2448	0.475
G7/C09	915	2448	0.523
G7/B03	915	7743	0.883
G7/A03	915	1440000	0.926
G7/B06	930	612	0.310
G7/C06	930	612	0.410
G7/A12	930	612	0.590
G7/D06	930	612	0.379
G7/D06	930	612	0.344
G7/C07	930	1224	0.309
G7/B07	930	1224	0.512
G7/D07	930	1224	0.376
G7/A13	930	1224	0.342
G7/D02	930	2448	0.560
G7/B02	930	4056	1.059
G7/A02	930	4408	0.644
G2/2	950	1025.10	0.346
G2/1	950	1065.10	0.397
G2/4	950	1139	0.385
G2/3	950	1269	0.327
G12/8-X	950	24000	0.615
G13/4-X	950	24000	0.577
G11/4-Y	950	48000	0.917
G12/4-Y	950	48000	1.085
G11/4-Z	950	72000	1.220
G13/4-Z	950	72000	1.429
G12/5-W	950	96000	1.383
G13/5-W	950	96000	1.284
G12/5-X	950	120000	1.796
G11/5-Z	1000	24000	0.722
G12/5-Z	1000	24000	0.771
G12/6-W	1000	48000	0.779
G12/6-X	1000	96000	0.345
G13/6-X	1000	96000	0.722

Figure 4.15 Graph of experimentally determined $M_{23}C_6$: MC ratios, with simple trendlines (exponential first order fit)



4.3 Effect of Very High Temperature Exposure on Carbides

4.3.1 Introduction

The specific objective of this section is to analyse how the carbides respond to short term, very high temperature exposure, such as that during the initial solution treatment and/or any rejuvenation treatments and for example when a blade is recoated. To this effect, emphasis was placed on XRD results, to characterise which carbides were present, and EDX analysis, to give an indication of their composition. The plate sample of IN738LC with composition described in Materials (Chapter 3) was used.

The plate was given a typical commercial treatment. This consisted of solutioning at 1120°C for two hours followed by ageing at 845°C for 24 hours, cooling in air after both treatments. This condition will henceforth be referred to as the 'unexposed' condition. Thermal exposure was carried out on separate samples from the plate at 1120, 1150, 1190°C for four hours and twenty hours and at 1235°C for four hours, respectively. The test programme is summarised below.

Table 4.17 Very high temperature thermal exposure treatments

Sample ID	Exposure temp. / °C	Exposure time / hours
G10	None	None
G10/1	1120	4
G10/2	1120	20
G10/3	1150	4
G10/4	1150	20
G10/5	1190	4
G10/6	1190	20
G10/7	1235	4

4.3.2 Results

The microstructure of the unexposed sample included blocky carbides throughout the matrix and at grain boundaries. The microstructures of all of the exposed samples again contained large amounts of Ti, Nb-rich carbides but did not show evidence of $M_{23}C_6$ carbides. Dendritic contrast was evident in samples exposed at up to 1150°C. XRD traces indicated that the unexposed sample contained MC (TiC lattice) carbide with small amounts of $M_{23}C_6$ carbide ($Cr_{23}C_6$ lattice). Note that very small amounts of $M_{23}C_6$ may not be easily visible on

optical microscopy. The XRD traces for the exposed samples again indicated the presence MC type carbides but not $M_{23}C_6$. The data are summarised in Table 4.19.

Scanning electron microscopy and EDX analysis revealed that the MC carbides in both the unexposed and exposed samples were mainly Ti, Nb-rich with small amounts Ti, Nb-lean.

EDX analysis of the Ti, Nb-rich carbide particles indicates that these carbides contained titanium, tantalum, tungsten and niobium. Little variance was found between the compositions of the unexposed sample and the sample exposed at 1190°C for 20 hours. The data are shown in Table 4.20. Averaging the results, a suggested composition of Ti, Nb-rich carbide is $(Ti_{0.48}Nb_{0.23}Ta_{0.19}Mo_{06}W_{04})C$.

4.3.3 Discussion

Data on the lattice parameters of $(Ti,Hf)C$ and $(Hf,W)C$ (with $x_{Hf} < x_W$) shows that in these ternary carbides the influence of the metallic elements on the lattice parameter of the FCC MC carbide phase is in good approximation linear and additive⁷. If it is assumed to also hold for $(Ta,Ti,Hf,W,Zr)C$ and $(Ti,Ta,Nb,Zr)C$, the lattice parameter, a , of the Ti, Nb-rich carbide in IN738LC is given by:

$$\text{Equation 4.2} \quad a_{MC} = x_{Ti} a_{TiC} + x_{Ta} a_{TaC} + x_{Mo} a_{MoC} + x_W a_{WC} + x_{Zr} a_{ZrC} + x_{Nb} a_{NbC}$$

Values of the lattice parameters of binary MC carbides are given in Table 4.18

Table 4.18 Lattice parameters of some carbides

Carbide	Lattice parameter/ Angstroms	Source
TiC	4.3274	PDF 32-1382
TaC	4.4547	PDF 35-801
MoC	2.898	Pearson ⁷⁵
WC	2.9004	Pearson
NbC	4.4702	PDF 10-181

According to the above equation the lattice parameter of the $(Ti_{0.48}Nb_{0.23}Ta_{0.19}Mo_{06}W_{04})C$ carbides in IN738LC should equal 0.424nm. This compares reasonably well with the measured lattice parameter of 0.436nm. Starink⁷ suggests that this difference in measured and calculated lattice parameter could be due to off-stoichiometry (in this instance a depletion) of the C-content. This would result in a composition of $(Ti_{0.48}Nb_{0.23}Ta_{0.19}Mo_{06}W_{04})C_{(1-x)}$ where $x > 0$.

In conclusion, it can be said that short term exposure at high temperatures in IN738LC causes dissolution of $M_{23}C_6$. It should be noted that the initial amount of $M_{23}C_6$ in this instance was relatively small. No further carbide reactions were evident. The composition of the Ti, Nb-rich type carbide was found to be unaffected by exposure under test conditions. There is, therefore an indication that transformations involving MC and $M_{23}C_6$ carbides in IN738LC are reversible.

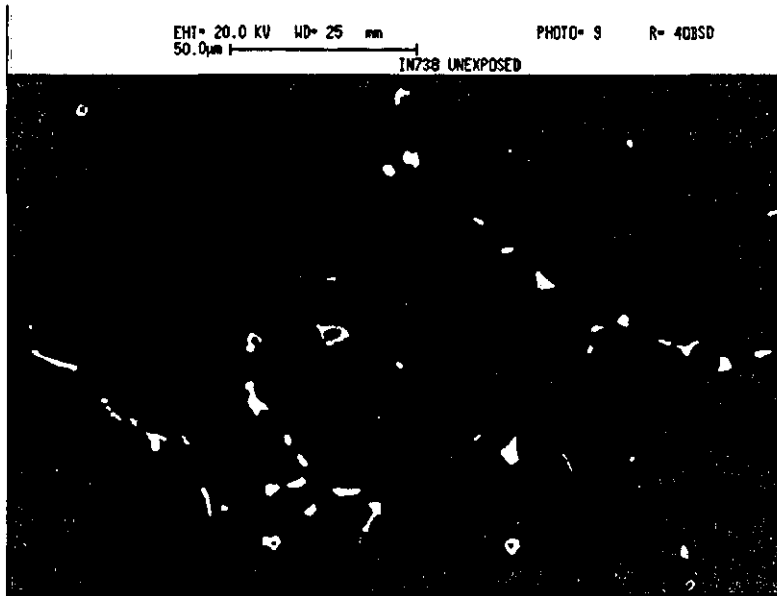


Figure 4.16 Unexposed sample

scanning electron micrograph in backscattered imaging mode
etchant: Kalling's Reagent



Figure 4.17 Exposed at 1190°C for 20 hours

scanning electron micrograph in backscattered imaging mode
etchant: Kalling's Reagent

Table 4.19 Results of XRD analysis

Sample ID	Vol. Fraction ratio $M_{23}C_6/MC$
G10	0.061
G10/1	0
G10/2	0
G10/3	0
G10/4	0
G10/5	0
G10/6	0
G10/7	0

Table 4.20 Re-normalised² and averaged compositions of Ti, Nb-rich carbide

Element	G10 Unexposed Ti, Nb-rich	G10/6 1190 C 20 hours Ti, Nb-rich
	atom %	atom %
Mo L	6.1	6.3
W L	4.1	4.1
Ti K	48.9	47.8
Ta L	18.9	18.9
Nb L	21.9	22.9

² This was a simple renormalisation process, weighting the selected elements to 100%. The raw EDX data for this batch of samples were considered to give an abnormally high zirconium signature, hence the renormalisation did not include zirconium

5 Characterisation of Coatings

5.1 Introduction

The aim of this research is to enable development of a model that will act as a time temperature recorder for an IN738LC substrate / coating system. Innogy are evaluating four MCrAlY coatings (see Chapter 2). From these, two were selected by Innogy for detailed analyses. These two coatings are SC2453 (coating A) and RT122 (coating D); the major elements from the bulk chemical analysis presented in Chapter 2 are given in Table 5.1 below. Coating RT122 has more than three times (by mass) cobalt than SC2453. SC2453 contains additions of rhenium.

Table 5.1 Coating compositions, mass%

Element	Bulk chemical analysis	
	RT122	SC2453
Aluminium	6.96	10.4
Cobalt	35.2	10.6
Chromium	18.6	21.5
Nickel	Bal.	Bal.
Rhenium	<0.01	1.58
Yttrium	0.33	0.64

Heat treatment of the IN738LC substrate / coating systems has been carried out at IPTME at temperatures ranging from 850°C to 1000°C and times up to 14400 hours, see Chapter 2. For detailed examination two temperatures for both coatings were initially selected, to take into account thermal as well as kinetic effects on microstructural evolution. On the basis of early samples and equilibrium predictions, the selected temperatures were 850°C and 950°C.

Amongst the features to be investigated are;

- prediction of equilibrium phases
- composition profile of major elements
- phases present in coatings
- phases present in interdiffusion layer
- effect of temperature and time on the microstructure of both the coating and interdiffusion zone.

5.2 Format for Data and Results

Four data sets are provided for each coating;

1. Equilibrium predictions
2. Experimental data for the as-coated sample
3. Experimental data for each thermally exposed sample
4. Selected experimental data for coating and interdiffusion layer in time and temperature sequence (effectively summarises experimental findings).

For the experimental data there are some conventions used in the thesis relating to the presentation of charts and micrographs. The format of the composition profile is described in schematic form in Figure 5.3.1a and the general convention for micrographs is shown in Figure 5.3.1b. The EDX data given with the photographs are generally for individual, representative particles, for which phase overlap is at a minimum. Full EDX data are given in Appendices 5A and 5B.

The presentation of data for each data set above is described in more detail in the following sections.

5.2.1 Thermodynamic Predictions for Coating

ThermoCalc software together with the Ni database was used to obtain predictions for equilibrium conditions for both coatings, with parameters set out in Thermodynamic Modelling-Chapter 3. This provides a data set of phase proportions and compositions for comparison with experimental data. Investigating the effect of depleting the bulk composition in aluminium and chromium can give an indication of the effect of diffusion of these elements on the phases present. The data are concisely described in the results section for each coating and also used for subsequent discussion.

To facilitate analysis of the effect of a change in composition on the phases in the coating, selected compositions were modified for input. The data presented are as follows;

- as-coated composition
- composition modified – Al depletion
- composition modified – Cr depletion.

The analysed composition of coatings given in Table 5.1 was used to calculate the equilibrium phases present over the temperature range 600°C to 1300°C. The proportions of

phases in mass% were plotted against temperature in a line graph. The data for the two temperatures 850°C and 950°C are presented in more detail using stacked bar charts.

The adjustments to composition were carried out separately. The mass proportion of the aluminium or chromium was lowered in steps individually, the balance being made up by nickel. The phases in the temperature range 600°C to 1300°C were predicted. In some instances the software / database system imposes limitations on compositions and temperature ranges, the exact cause not being clear. The line and stacked bar chart formats used to present original compositions were repeated for these adjusted compositions.

5.2.2 As-Coated Sample

The particles in the as-coated sample are fine and not easily identifiable by SEM/EDX analysis, hence micrographs and raw EDX data are provided for information. The following data are provided;

- composition profile
- coating EDX data
- interdiffusion zone EDX data.

5.2.3 850°C and 950°C Exposure, 4800 hours to 12000 hours, Sample Sequence

The experimental investigations generated a large amount of data. Each thermally exposed sample is given a three-page layout shown in Figure 5.3.2. A structured format for the description of data is implemented for the results sections. The thermally exposed samples are considered in sequence, beginning at the lower temperature, 850°C and minimum exposure time of 4800 hours and rising to 950°C and extended exposure time of 12000 hours. The features of each are described in the following sequence;

- a) composition profile
- b) coating phases
- c) interdiffusion phases.

For coating D (RT122) backscattered electron imaging did not provide additional information, due to similarity in atomic number contrast, and was therefore not included.

5.2.4 850°C and 950°C Exposure, 4800 hours to 12000 hours, Temperature and Time Sequence

Selected micrographs and composition have been taken from the data in section 5.2.3 and reproduced in temperature and time sequence. This is to facilitate analysis of the effect of thermal exposure on microstructure and phase composition. The following is a summary of the data presented;

- low magnification optical micrographs and some backscattered electron micrographs of the complete coating
- high magnification backscattered electron micrographs of phases in coating
- phase map for coating
- EDX data for phases in coating
- high magnification backscattered electron micrographs of phases in interdiffusion layer
- phase map for interdiffusion layer
- EDX data for phases in interdiffusion layer.

5.3 Appearance and Composition of Phases

To facilitate examination of the data, a summary of the appearance of the phases, as found in this research, has been prepared and is presented in Table 5.2. It should be noted that for these observations the sample was etched in an electrolytic cell. The solution comprised 1% ammonium sulphate, 1% citric acid in water. A potential difference of 5V was applied for 4 seconds, with the sample as the anode and stainless steel cathode. It should be noted that these shades are relative and somewhat subjective; the actual shades may vary depending on microscope settings (particularly optical), but are able to act as a guide to phase identification.

Table 5.2 Features of phases

	Beta β	Gamma γ	Sigma σ	Alpha α	Gamma prime γ'
Description	NiAl	Ni	Cr rich TCP	Cr	Ni ₃ (Al,Ti)
Optical	Mid-grey	Dark grey	Light	Light	Light grey
Secondary electron	Light	Dark	Bright on beta, dark on gamma prime	Dark	Light grey
Backscattered electron	Dark	Dark ?	Bright or mid-grey *	Bright or mid-grey *	
Condition	Not etched	Etched	Etched	Not etched	Not etched

* dependent on rhenium content.

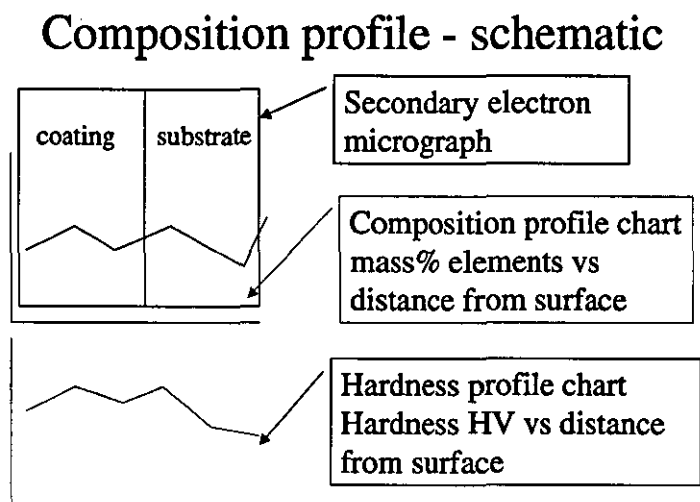
Furthermore, it is worthwhile presenting some typical composition data for these phases to enable comparison with EDX data. ThermoCalc software was used to predict compositions of phases for RT122 and SC2543 as stated in section 5.2.1. For information purposes, a selection of composition data is presented in Table 5.3. These data are taken from predictions of SC2453 coating composition, simply because at one temperature or another, all the phases predicted for IN738LC, RT122, and SC2453 are predicted using the SC2453 composition. Specific data for each system are given in the appropriate results section.

Table 5.3 Example composition data (thermodynamic predictions) for phases in SC2453, atom%

phase	Temp/°C	Ni	Cr	Co	Al	Re
Alpha	850	1.2	88.9	5.0	0.1	4.8
Beta	850	52.8	8.50	7.70	31.0	0
Gamma	900	48.0	28.2	14.5	9.1	0.1
Gamma prime	850	62.2	9.7	7.9	20.1	0
Sigma	850	11.4	65.8	21.0	0	1.7

Figure 5.3.1 Data layout for composition profile and general micrographs

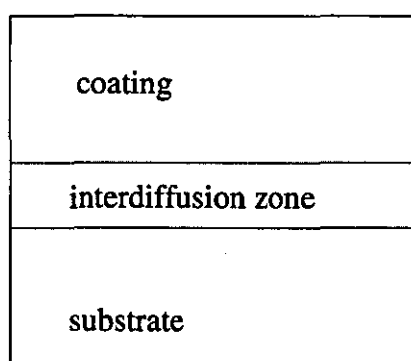
a.



Note : distance from surface on charts corresponds with that on micrograph

b.

Micrographs - schematic



All micrographs presented in this orientation (except composition profile)

Figure 5.3.2 Data layout for thermally exposed samples**a. Coating-interdiffusion-substrate**

Coating / substrate electron micrograph	Coating / substrate optical photograph
EDX composition Profile	
Microhardness Profile	

b. Coating characteristics

Coating phases	Coating phases	Coating phases
Optical micrograph	Secondary electron micrograph	Backscattered electron micrograph
Table- Example raw EDX data of phases		

c. Interdiffusion characteristics

Interdiffusion phases	Interdiffusion phases	Interdiffusion phases
Optical micrograph	Secondary electron micrograph	Backscattered electron micrograph
Table- Example raw EDX data of phases		

For coating D, RT122, backscattered electron imaging did not provide additional information and was therefore not included.

5.4 Coating RT122

5.4.1 Results - Equilibrium Predictions

1. The predictions calculate a simple two phase system for RT122 over the temperature range 700°C to 1300°C. Over this temperature range, γ increases at the expense of β , Figure 5.4.1. The proportions of the two phases at 850°C, 900°C and 950°C are similar, with only a slight decrease in β on increasing temperature, Figure 5.4.1 b.
2. Depleting the aluminium content quickly results in deficiency of β , with no β present at 3.5 mass%, Figure 5.4.2. At 850°C and 950°C, the quantity of β rapidly depletes with decreasing aluminium content, less than 10% volume fraction β with 5% mass aluminium at both temperatures, Figure 5.4.2 e,f.
3. Reduction in chromium content results in depletion of γ , with γ' increasing. This is to be expected as chromium is more soluble in γ than γ' . β also depletes, leaving a mixture of γ/γ' at low temperatures and just γ above 1000°C. This is shown in Figure 5.4.3. At 850°C the β depletes with decreasing chromium content, at the lower contents giving rise to significant amounts of γ' . The same depletion is observed at 950°C, although with less γ' than at 850°C, Figure 5.4.3 f,g.

Figure 5.4.1 As-coated composition

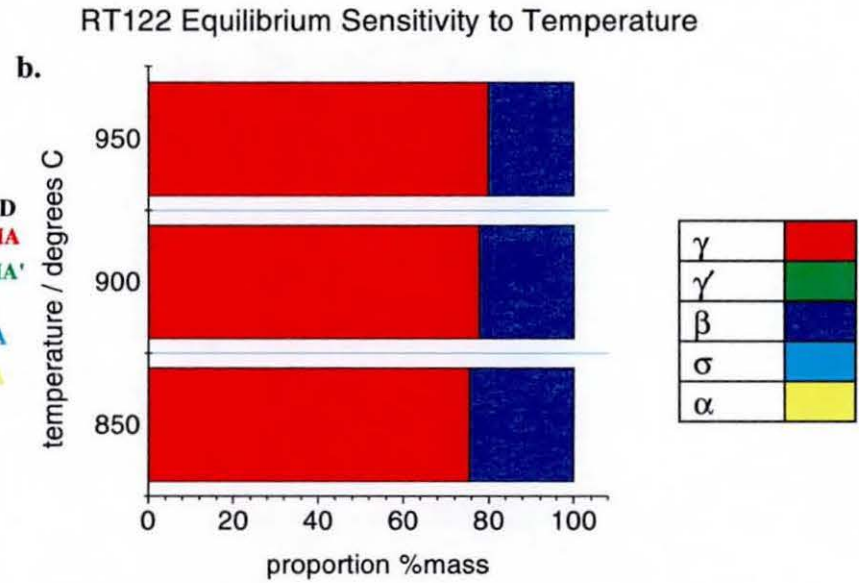
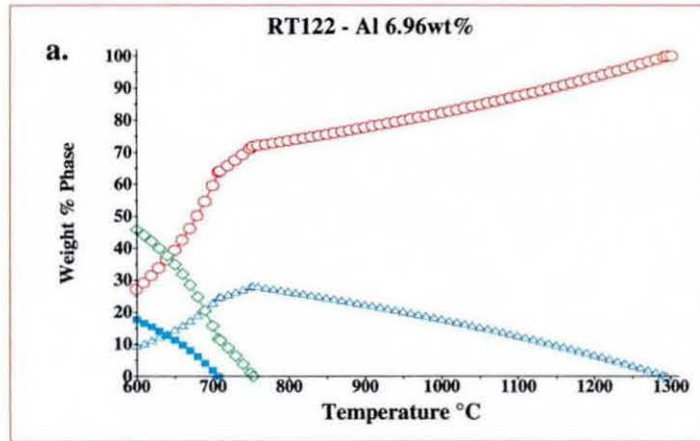
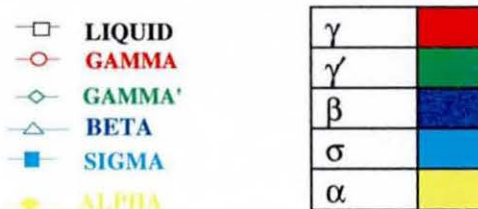
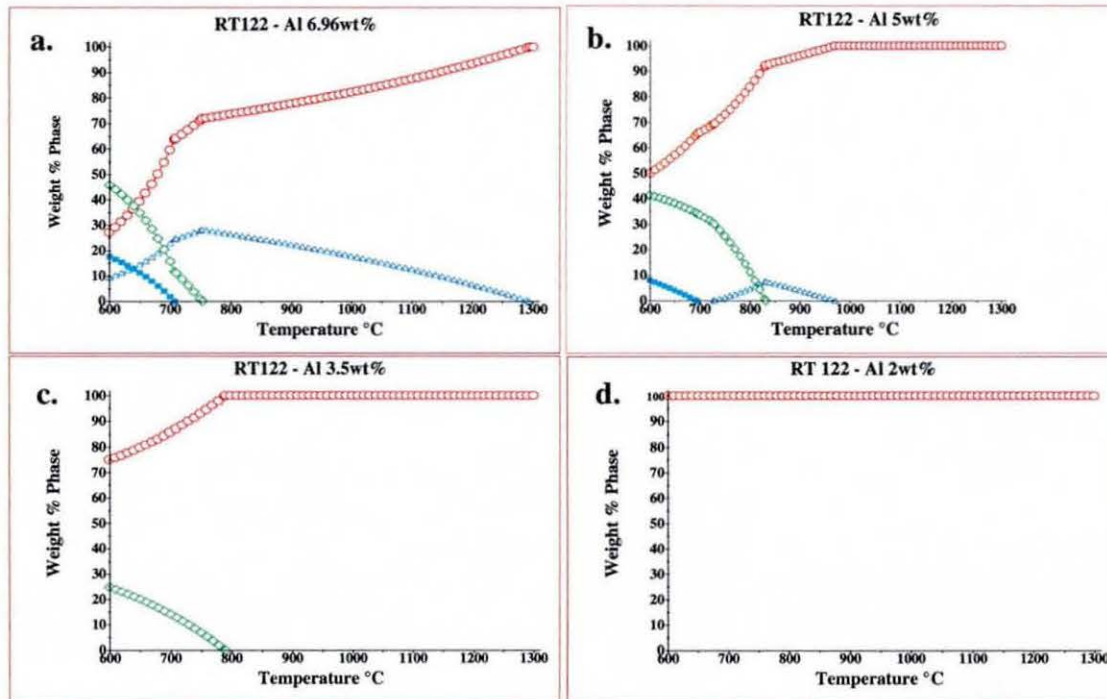


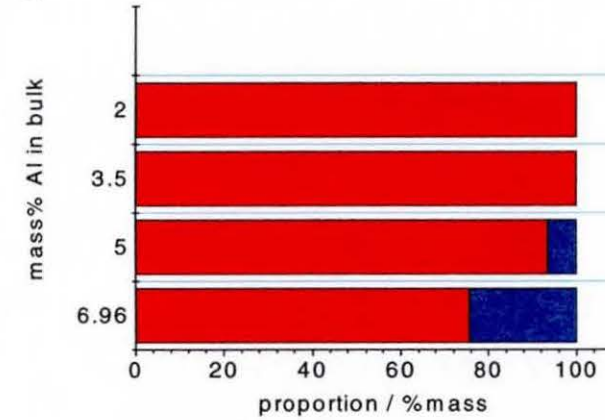
Table 5.4 Composition of phases, atom%

Phase	Temp/ °C	Ni	Cr	Co	Mo	W	Ti	Al	Ta	Nb	Zr
Beta	850	43.1	7.0	18.7				31.2			
Gamma	850	32.8	23.4	36.5				7.3			
Beta	900	42.8	7.1	19.0				31.1			
Gamma	900	33.1	22.9	35.9				8.0			
Beta	950	42.8	7.1	19.0				31.1			
Gamma	950	33.4	22.4	35.4				8.8			

Figure 5.4.2 Composition modified – Al depletion



e. RT122 850°C Equilibrium Sensitivity to Al



f. RT122 950°C Equilibrium Sensitivity to Al

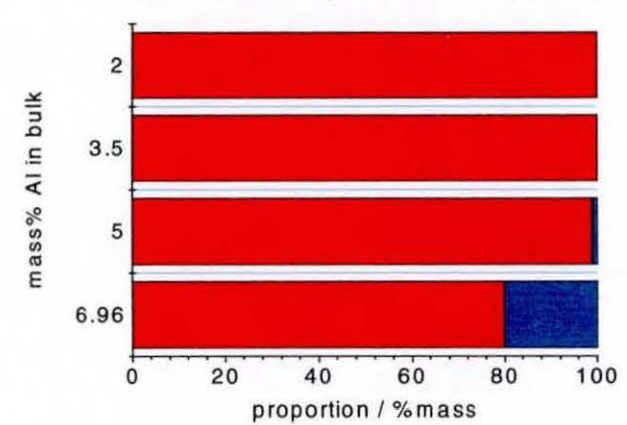
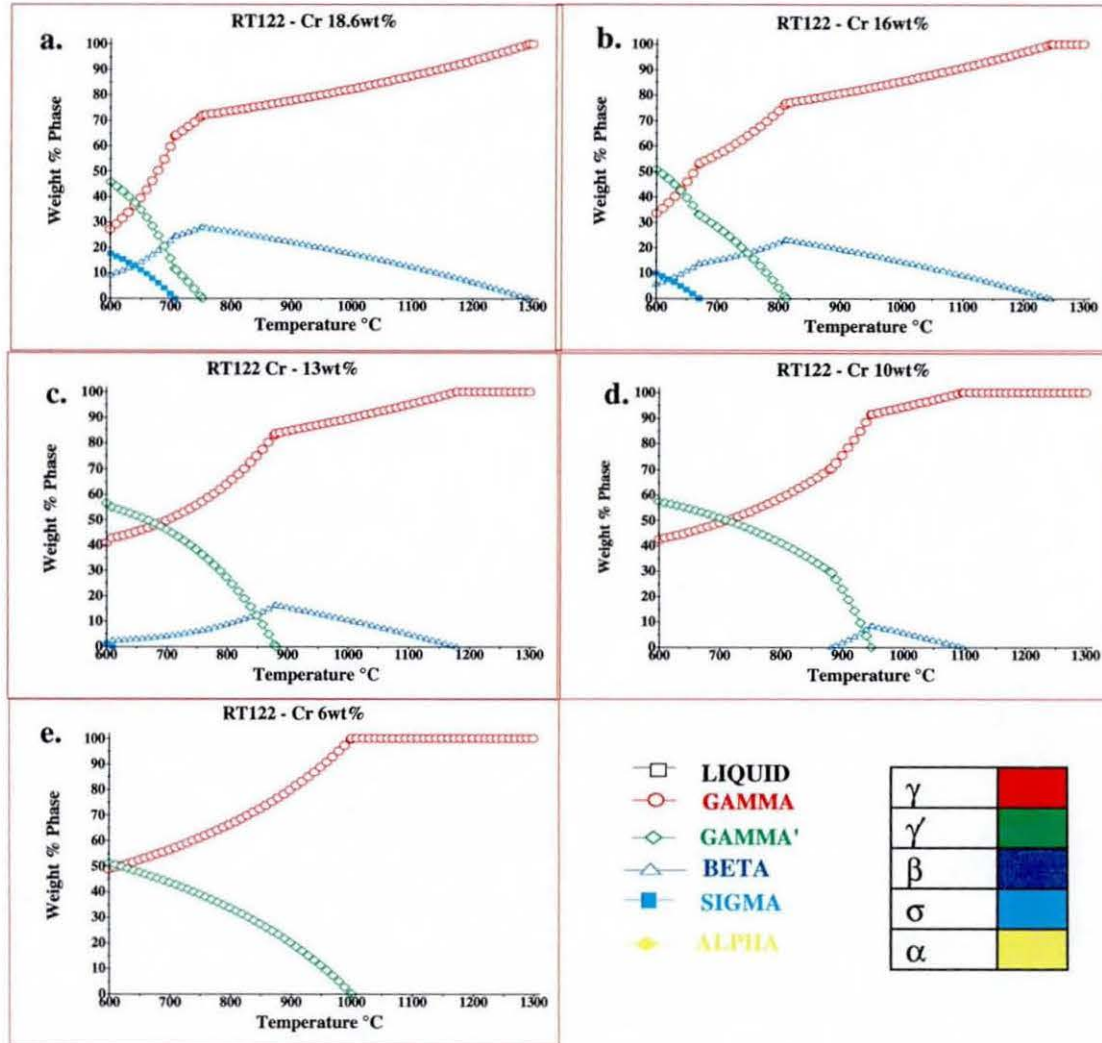
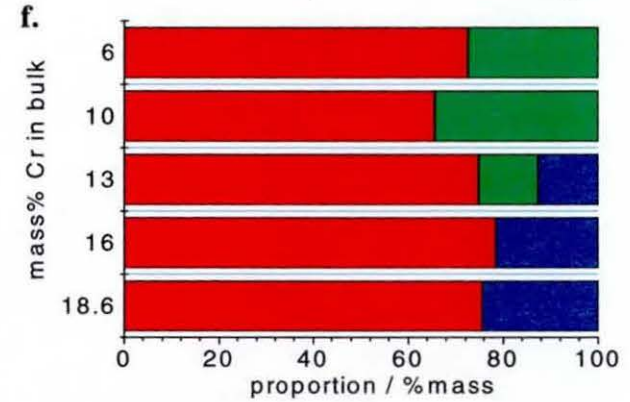


Figure 5.4.3 Composition modified – Cr depletion

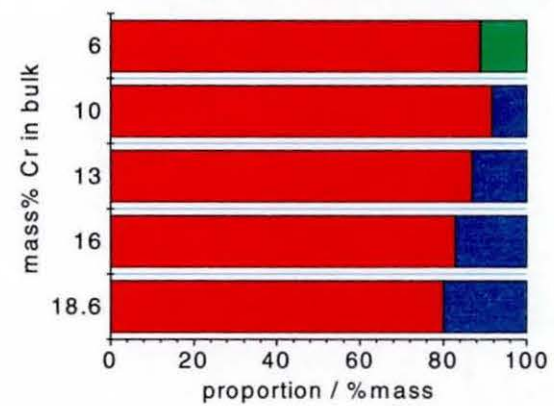


f. RT122 850°C Equilibrium Sensitivity to Cr



g.

RT122 950°C Equilibrium Sensitivity to Cr

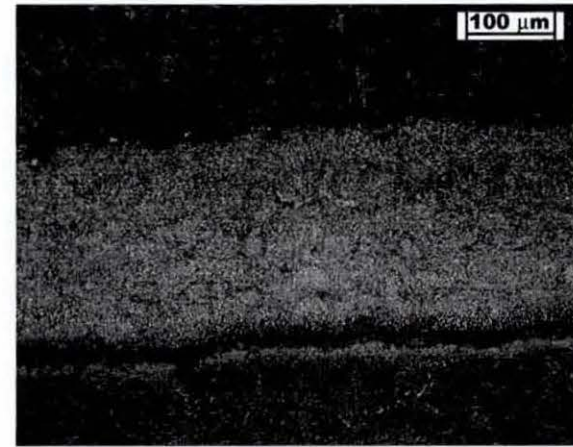
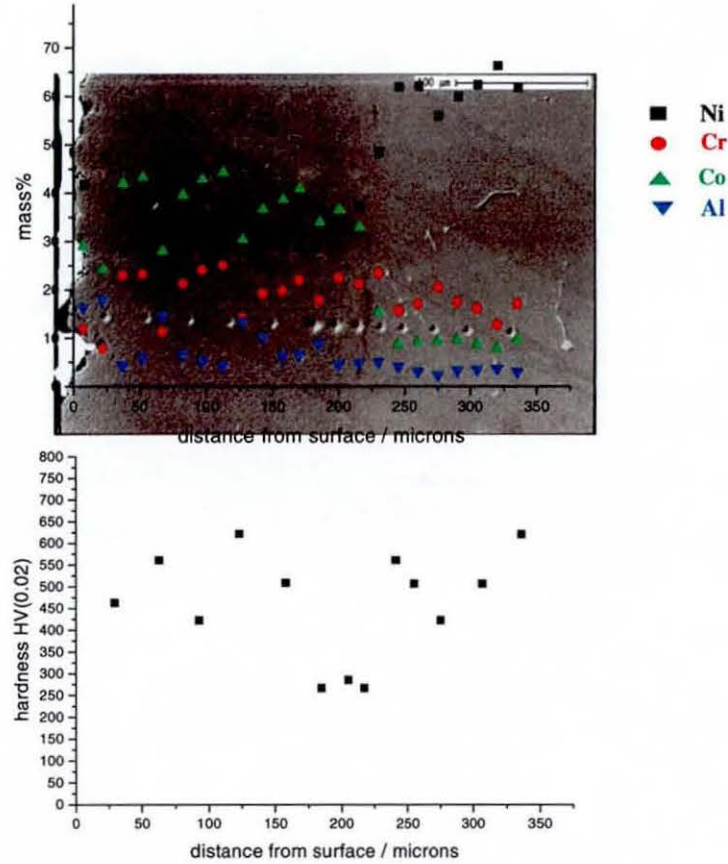


5.4.2 Results -As-coated

1. The composition profile, Figure 5.4.4 a, shows that the cobalt decreases from approximately 35 mass% in the coating to its substrate level of approximately 10 mass%, where it is found to exhibit less scatter. In the coating there are some low points for cobalt content, which then gradually increases. This is the converse of the aluminium content in the same regions. The chromium is also more uniform in the substrate than in the coating. The hardness exhibits noticeable scatter, but shows that the coating is of a similar hardness to the base material. The coating near the substrate is lower in hardness than the other regions, with a possible decrease in the vicinity of the interdiffusion zone.
2. The phases in the coating are β and γ as shown in Figure 5.4.5 a,b. The particle sizes are quite small, in the order of a few microns, but large enough to obtain satisfactory EDX data for composition of phases, given in Table 5.6.
3. The purpose of the interdiffusion zone is simply to act as a bonding layer to mechanically join the coating to the substrate. In the post-coated state it is a thin layer, the phases not easily identifiable, Figure 5.4.6 a. The particles are indistinct and the width of some is small, hence EDX data are considered to suffer from overlap with adjacent phases and should be treated with caution. The EDX data for particles at the interdiffusion zone are given in Table 5.6.

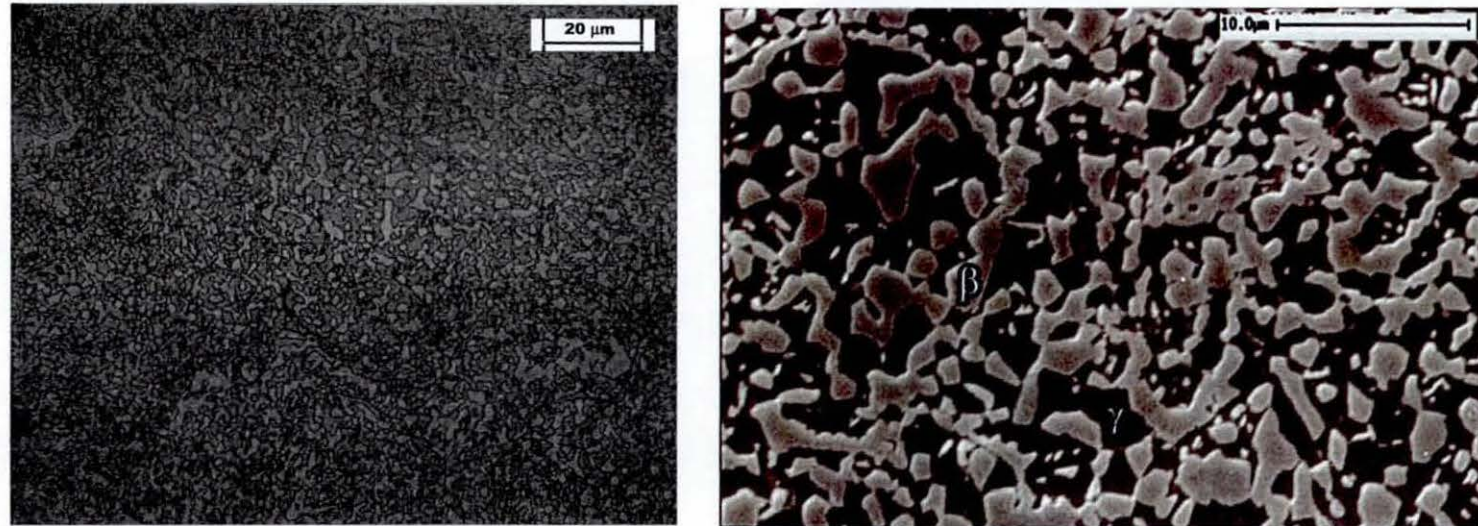
Figure 5.4.4 G12/6-Z unexposed, coating – interdiffusion – substrate profile

a. Scanning electron micrograph, secondary image with composition profile and microhardness traverse



b. Optical bright field

Figure 5.4.5 G12/6-Z unexposed –coating characteristics



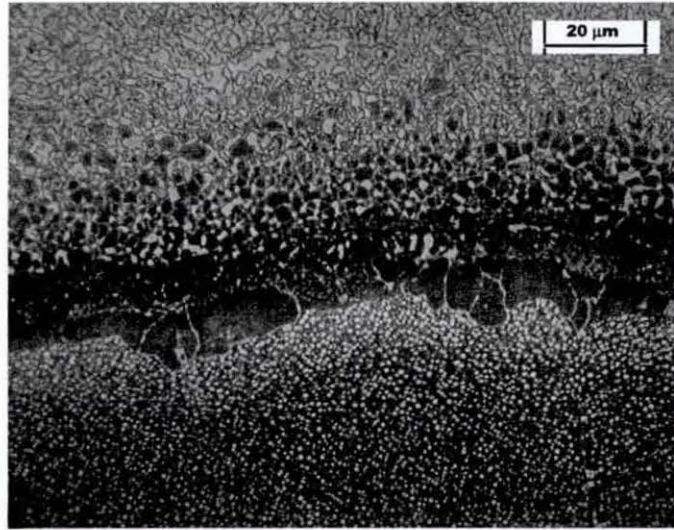
a. Optical bright field

b. Scanning electron micrograph,
secondary mage

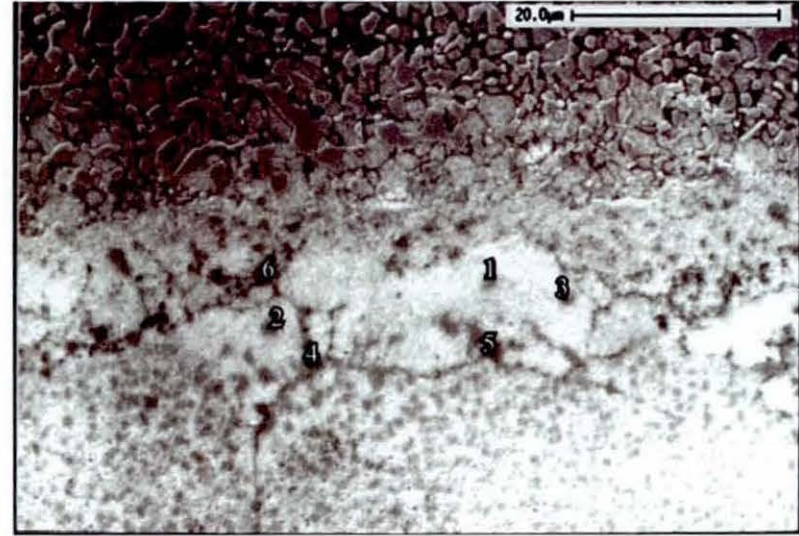
Table 5.5 Typical EDX data compositions of phases, atom%

	Ni K	Cr K	Co K	Mo L	W L	Ti K	Al K	Ta L	Nb L	Zr L	Re L	Y L
β	39.3	6.1	18.5	0.0	0.4	0.1	35.5	0.0	0.0	0.0	0.1	0.0
γ	27.2	23.2	37.2	0.1	0.3	0.0	11.3	0.0	0.0	0.1	0.3	0.2

Figure 5.4.6 G12/6-Z interdiffusion zone characteristics



a. Optical bright field



b. Scanning electron micrograph, secondary image annotated

Table 5.6 Full EDX data for as coated interdiffusion zone

Lab ID	particle ID	type	Ni K	Cr K	Co K	Mo L	W L	Ti K	Al K	Ta L	Nb L	Zr L	Re L	Y L
G12/6-Z	spot 1		43.5	19.4	22.5	0.4	1.2	1.6	11.1	0.0	0.0	0.0	0.4	0.0
G12/6-Z	spot 2		47.4	18.2	19.1	0.7	0.8	1.6	12.1	0.0	0.0	0.0	0.1	0.0
G12/6-Z	spot 3		44.6	19.2	22.5	0.5	0.8	1.4	10.9	0.1	0.0	0.0	0.0	0.0
G12/6-Z	spot 4		50.2	17.3	16.7	0.7	1.3	2.3	11.3	0.0	0.0	0.0	0.2	0.0
G12/6-Z	spot 5		43.7	13.3	13.3	0.9	1.2	13.4	5.2	5.6	3.2	0.0	0.2	0.0
G12/6-Z	spot 6		39.8	18.7	24.3	0.3	0.6	5.0	10.4	0.7	0.3	0.0	0.0	0.0

5.4.3 Results – Thermal Exposure – Sample Sequence

5.4.3.1 Thermal Exposure at 850°C for 4800 Hours

1. There is much more scatter in this composition profile Figure 5.4.7 a, than in the as-coated sample. There does appear to be a band near the outer surface where the cobalt is low, aluminium is high and chromium low. The chromium is low at the interdiffusion zone. The hardness in the coating is slightly lower than in the as-coated sample. The hardness of the coating and substrate are relatively similar.
2. The phases are again β and γ , Figure 5.4.8 a,b and Table 5.8. Some depletion of the β phase is beginning to occur at the outer surface, Figure 5.4.7 b. There are fine bands in the coating, Figure 5.4.7 b and Figure 5.4.8 a. The content of these bands is not obvious. They appear to consist of very small particles interspersed with larger particles.
3. The precise definition of what comprises the interdiffusion zone is not clear, Figure 5.4.9. However, in the substrate layer just below the coating, the γ/γ' morphology is different to that of the bulk substrate. γ of coating composition penetrates into the substrate at grain boundaries in the aforementioned region. This region has an appearance suggesting recrystallisation has occurred and for the purposes of describing the results is termed the recrystallised region. Note that whilst there is γ penetrating into the grain boundaries of the recrystallised region, the majority of the grain boundary phase is γ' . Figure 5.4.9 a, shows both phases, the γ being darker than the γ' . There are particles at the original interface. Whilst there are not easily definable phases comprising the interdiffusion zone, some EDX data of the region are given in Table 5.9.

5.4.3.2 Thermal Exposure at 850°C for 9600 Hours

1. There is less scatter in the composition profile than the previous exposure, Figure 5.4.10 a. The band mentioned at 4800 hours exposure is again evident and chromium is slightly low at the interdiffusion zone. The hardness profile exhibits a peak at the centre of the coating and a trough at the interdiffusion zone.
2. The phases in the coating are again β and γ , Figure 5.4.11 and Table 5.10. There is evidence of a β depleted layer at the outer surface, Figure 5.4.10b. The fine bands are again evident, in Figure 5.4.7 b and Figure 5.4.8 a.
3. The interdiffusion zone is again associated with recrystallised γ/γ' , with the γ' coalescing, Figure 5.4.12. EDX data are shown in Table 5.11. The analysis of the original interface (O.I.) particle will suffer from overlap of adjacent phases, but does indicate significant

titanium and cobalt content. There is possibly the beginnings of a β depleted zone on the coating side, Figure 5.4.10 b and Figure 5.4.12 a,b.

5.4.3.3 Thermal Exposure at 950°C for 4800 Hours

1. The high aluminium signature at the outer surface, Figure 5.4.13 a, is probably due to the external Al_2O_3 layer. The concentration of the elements appear to uniformly rise gradually and drop sharply in layers through the coating, with the exception of aluminium content which is converse to that of cobalt. The aluminium content also shows a slight increase at the interdiffusion zone, where chromium exhibits a trough. The layers indicated by the composition profiles are mirrored in the hardness profile, with a low hardness being recorded at the interdiffusion zone.
2. The phases are γ and β as before, however it is becoming apparent that there is less β and more γ , Figure 5.4.14. The compositions are given in Table 5.12. There is a distinct β depletion zone at the outer surface, Figure 5.4.13 b. Whilst there are groups of small particles, the fine banding found at 850°C is less apparent.
3. The interdiffusion zone exhibits a widening layer of γ on the substrate side, with occasional precipitates of β , Figure 5.4.15, and Table 5.13. The recrystallised γ/γ' and grain boundary γ' are evident, as with the previous exposure. The penetration of grain boundary γ' is more extensive, Figure 5.4.13 b. On the coating side, a β depletion layer, consisting of γ , is becoming evident.

5.4.3.4 Thermal Exposure at 950°C for 9600 Hours

1. There are single and two phase zones within the coating, Figure 5.4.16 a. The composition profile is fairly uniform in the single phase zones. The aluminium is higher in the two phase zone. Through the recrystallised region of the substrate, the composition profile gradually reaches base-material levels, except at one point that has the appearance of a single-phase zone. The hardness of the outer section of the coating is similar to that of the substrate, the inner zone of the coating rises in hardness going towards the substrate.
2. The coating exhibits distinct β depletion zones at the outer surface and adjacent to the interdiffusion zone, Figure 5.4.16 b. The core of the coating is still a mixture of β and γ , but the proportion of β is further reduced, Figure 5.4.17 and Table 5.14.

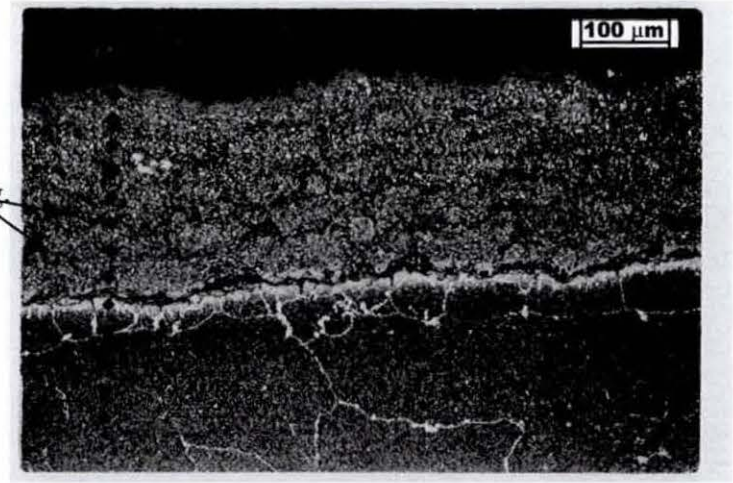
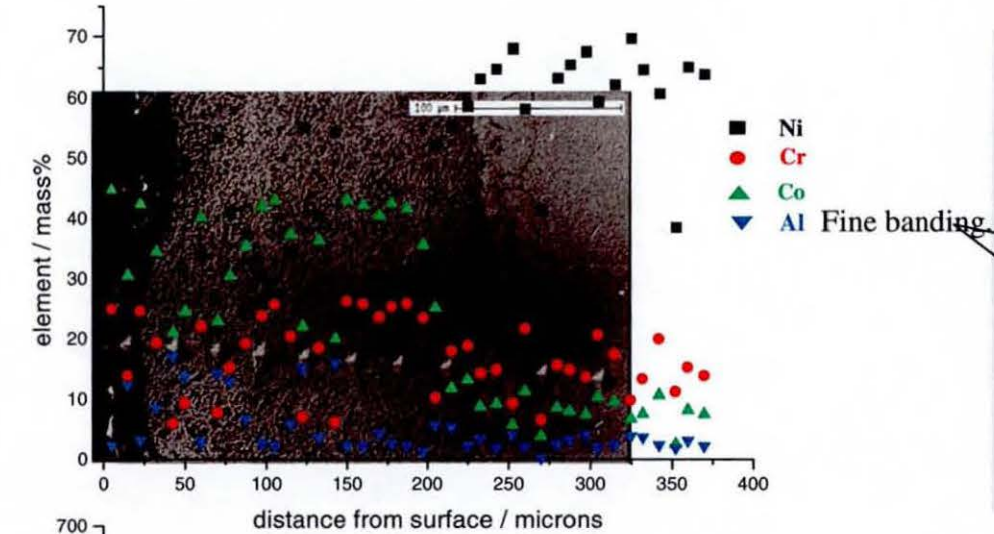
3. The interdiffusion zone exhibits a single phase γ zone on the substrate side of the OI as well as the coating side, Figure 5.4.17 and Table 5.15. Below the γ zone, the recrystallised γ/γ' and grain boundary γ' are again evident. The grain boundary γ' is more extensive than in the previous exposure time. γ phase appears to additionally envelop the γ' , the γ forming an intergranular network.

5.4.3.5 Thermal Exposure at 950°C for 12000 Hours

1. The composition profile, Figure 5.4.19 a, is similar to that at 950°C 9600 hours, with the two phase zone being thinner. This two phase zone has higher aluminium content. The chromium on the substrate side exhibits some noticeable high points. There is scatter in the hardness data, but a low point could be observed at the interdiffusion zone. Two high points in hardness are evident in the coating, this could be a result of hardness indents locating on a phase that has relatively high hardness. The hardness of each phase has not been specifically determined in this research, hence the relative hardness of the phases is not known.
2. The coating consists mainly of γ , with some β at the core, Figure 5.4.19 b and Figure 5.4.20 a,b. The compositions of the core phases are given in Table 5.16.
3. The interdiffusion layer is similar to that described for 950°C 9600 hours, with larger γ zones and more extensive γ' penetration into the substrate, Figure 5.4.19 b and Figure 5.4.21 a,b, compositions in Table 5.17.

Figure 5.4.7 G12/2-W exposed at 850°C for 4800 hours, coating – interdiffusion – substrate profile

a. Scanning electron micrograph, secondary image with composition profile and microhardness traverse



b. Optical bright field

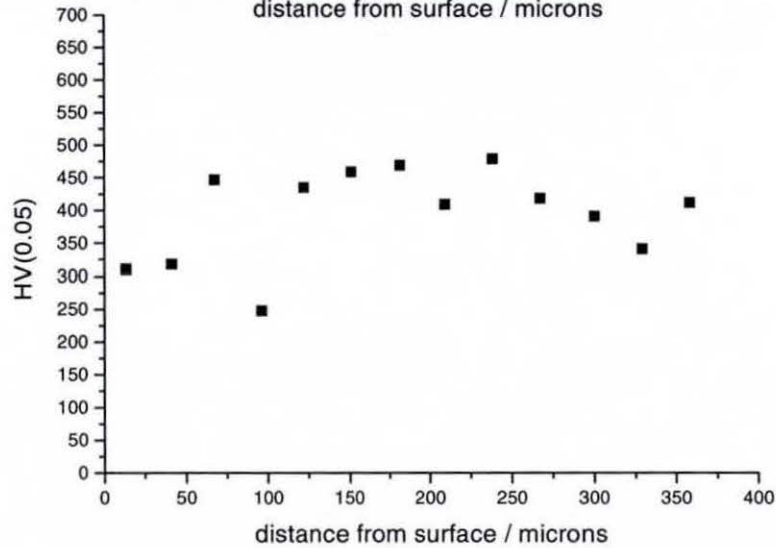
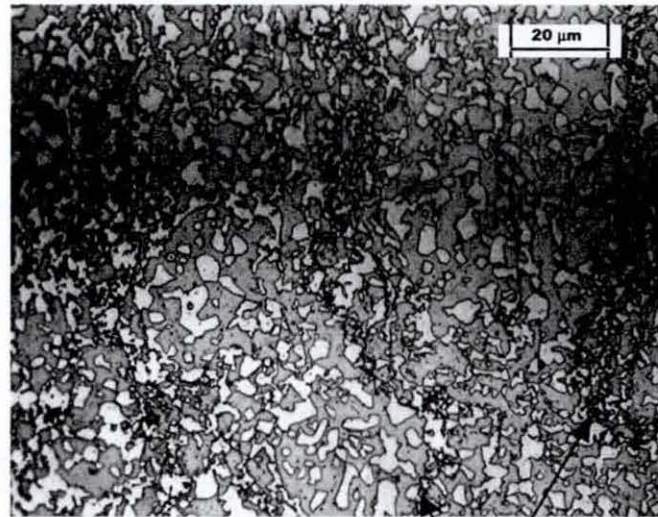
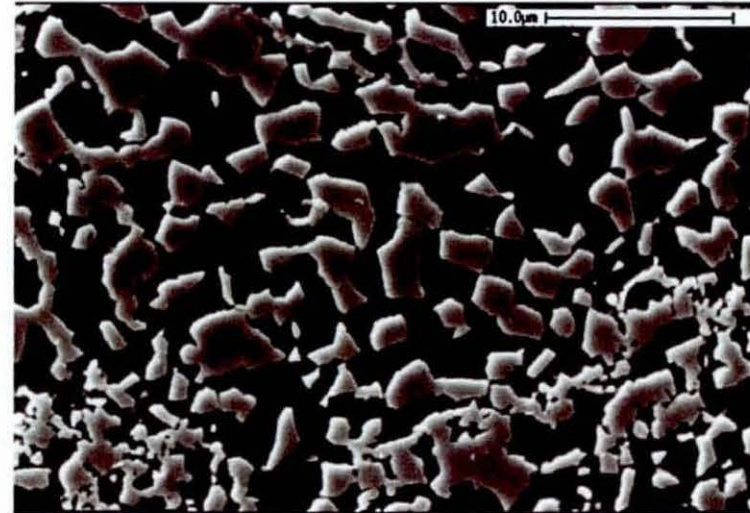


Figure 5.4.8 G12/2-W exposed at 850°C for 4800 hours – coating characteristics



a. Optical bright field



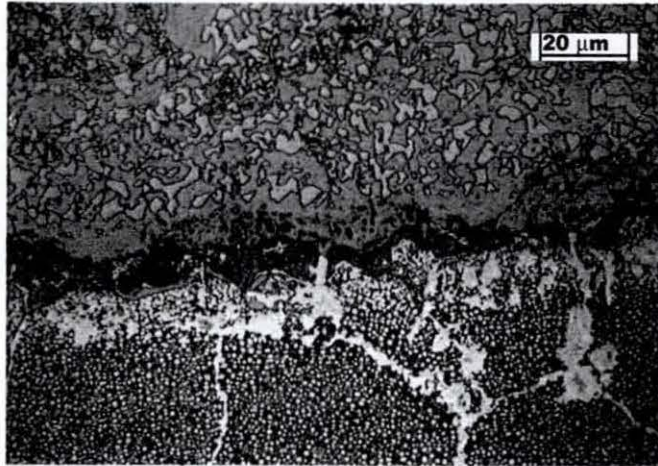
b. Scanning electron micrograph, secondary image

Fine banding

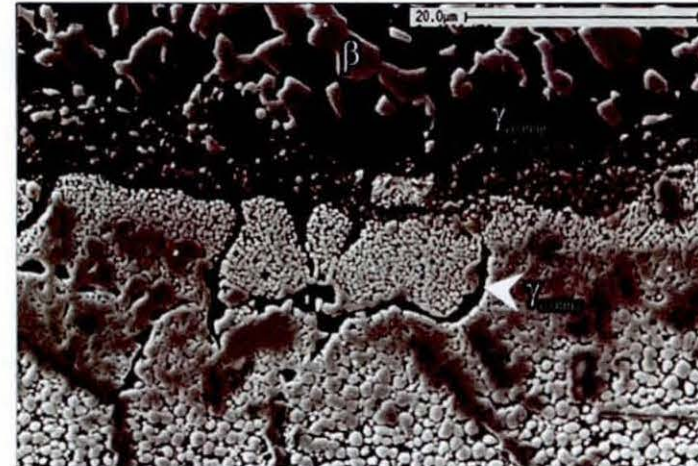
Table 5.8 Typical EDX data for compositions of phases, atom%

	Ni K	Cr K	Co K	Mo L	W L	Ti K	Al K	Ta L	Nb L	Zr L	Re L	Y L
β	38.6	5.5	15.4	0	2.6	0.3	37.6	0	0.1	0	0	0
γ	23	30.1	39.2	0	1.8	0	5.9	0	0	0	0	0

Figure 5.4.9 G12/2-W exposed at 850°C for 4800 hours – interdiffusion characteristics



a. Optical bright field



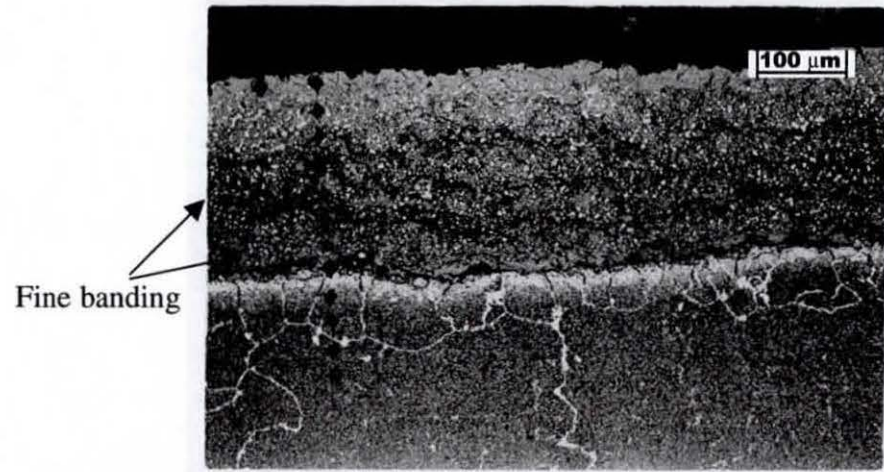
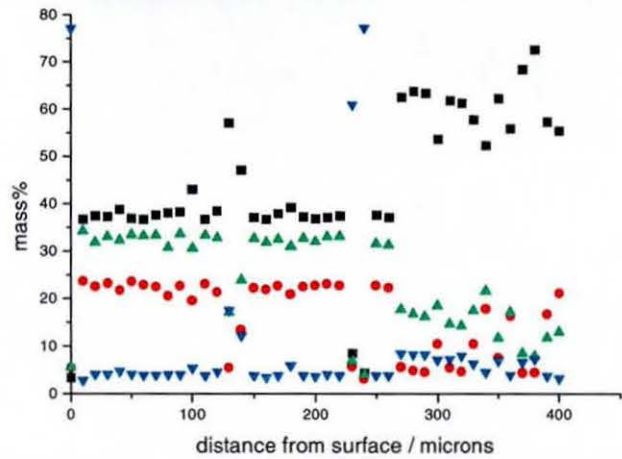
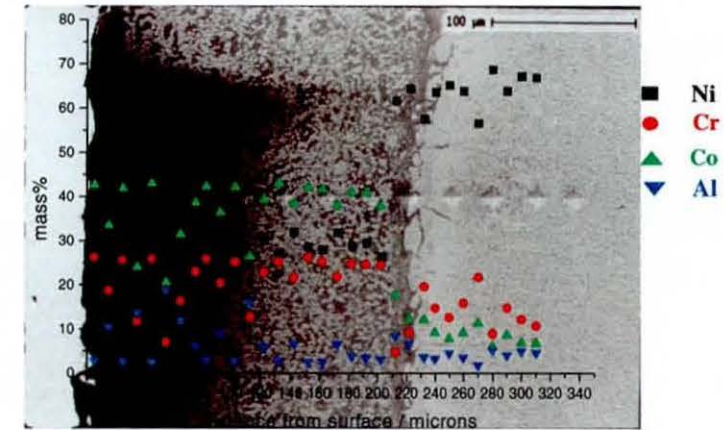
b. Scanning electronmicrograph, secondary image

Table 5.9 Typical EDX data for compositions of phases, atom%

	Ni K	Cr K	Co K	Mo L	W L	Ti K	Al K	Ta L	Nb L	Zr L	Re L	Y L
β	39.2	5.8	14.7	0	2.6	0.5	37.3	0	0	0	0	0
γ substr.	49.8	7.4	17.1	0	3.7	3.2	18.8	0	0	0	0	0
γ coat	24	30.1	37.8	0.2	1.6	0.2	6.1	0	0	0	0	0

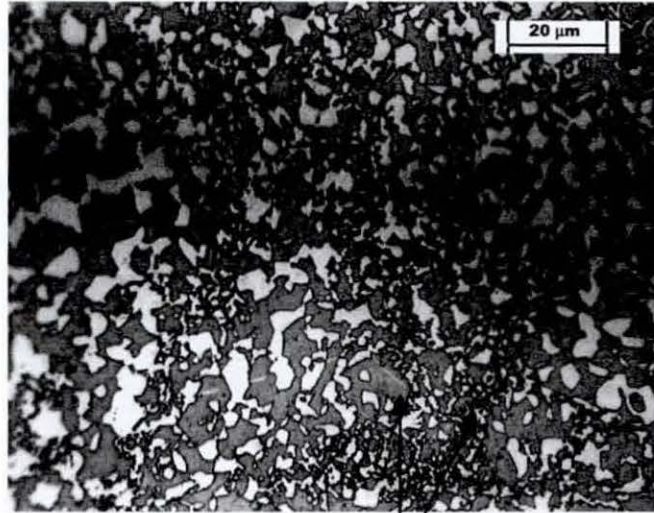
Figure 5.4.10 G12/2-X exposed at 850°C for 9600 hours, coating – interdiffusion – substrate profile

a. Scanning electron micrograph, secondary image with composition profile and microhardness traverse



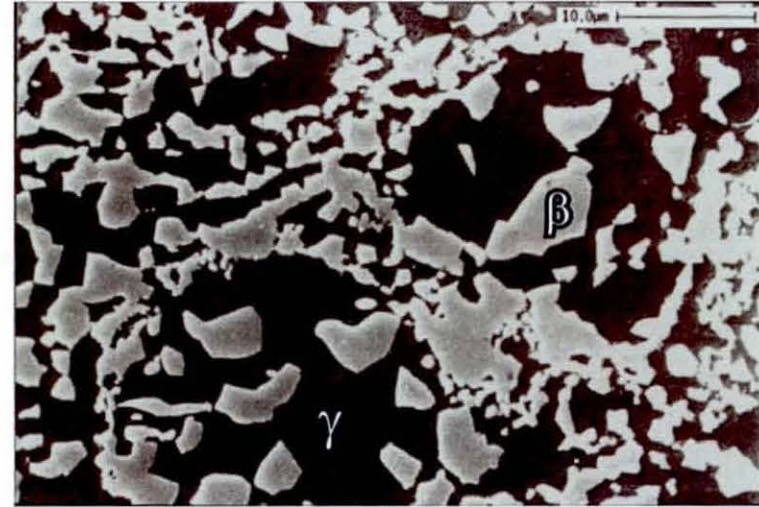
b. Optical bright field

Figure 5.4.11 G12/2-X exposed at 850°C for 9600 hours – coating characteristics



a. Optical bright field

Fine banding

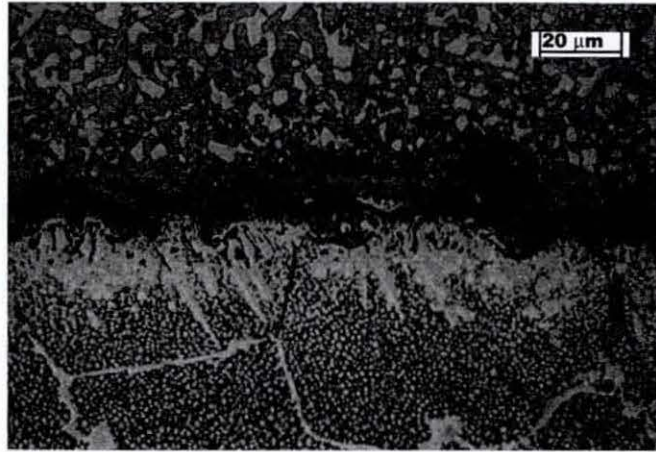


b. Scanning electron micrograph, secondary image

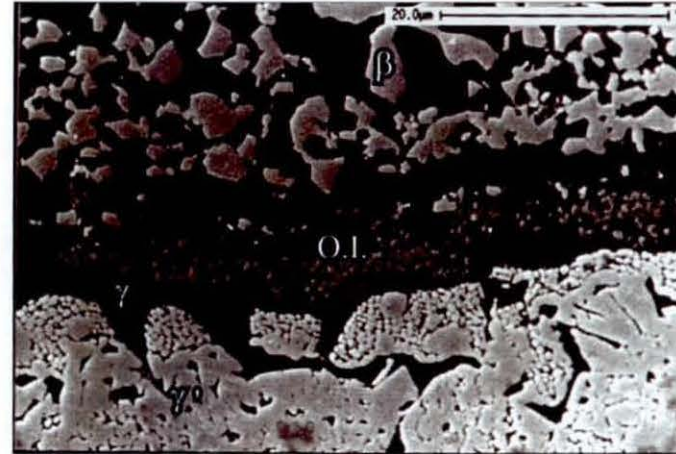
Table 5.10 Typical EDX data for compositions of phases, atom%

	Ni K	Cr K	Co K	Mo L	W L	Ti K	Al K	Ta L	Nb L	Zr L	Re L	Y L
β	47.4	5.2	15.5	0.2	0.1	0.4	31.1	0	0	0	0	0
γ	25.5	28.3	41	0	0.1	0.2	4.7	0.1	0	0	0	0

Figure 5.4.12 G12/2-X exposed at 850°C for 9600 hours – interdiffusion characteristics



a. Optical bright field



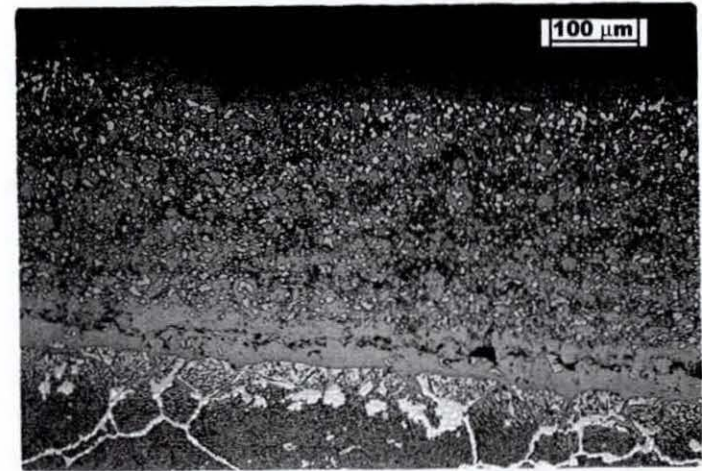
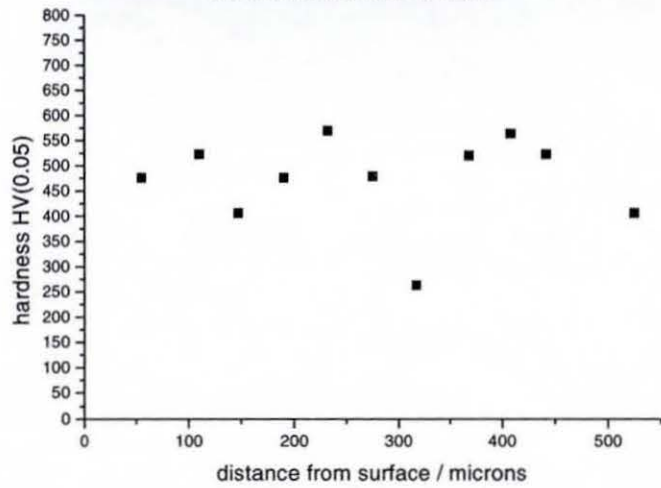
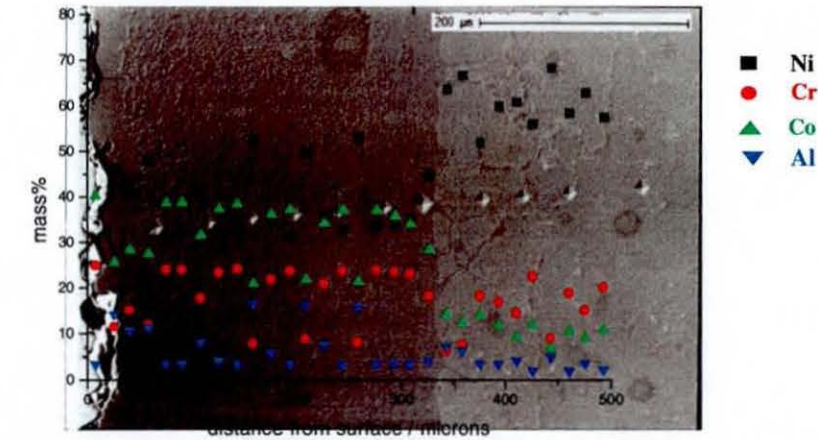
b. Scanning electron micrograph, secondary image

Table 5.11 Typical EDX data for compositions of phases, atom%

	Ni K	Cr K	Co K	Mo L	W L	Ti K	Al K	Ta L	Nb L	Zr L	Re L	Y L
γ	26.1	28.5	39.1	0.4	0.8	0.3	4.5	0.2	0	0	0	0
OI Particle	23.2	25.2	32.7	0	0.5	13.2	4.3	0.6	0.1	0	0	0
β	46.0	5.8	16.7	0	0.6	0.4	30.2	0	0	0	0	0
γ substr.	49.6	11.6	23	0.2	0.9	1.9	12.2	0.3	0	0	0	0

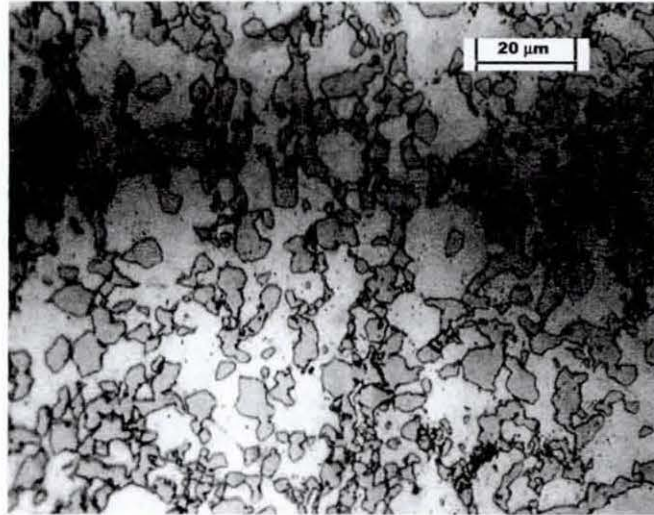
Figure 5.4.13 G12/4-Y exposed at 950°C for 4800 hours – coating – interdiffusion – substrate profile

a. Scanning electron micrograph, secondary image with composition profile and microhardness traverse

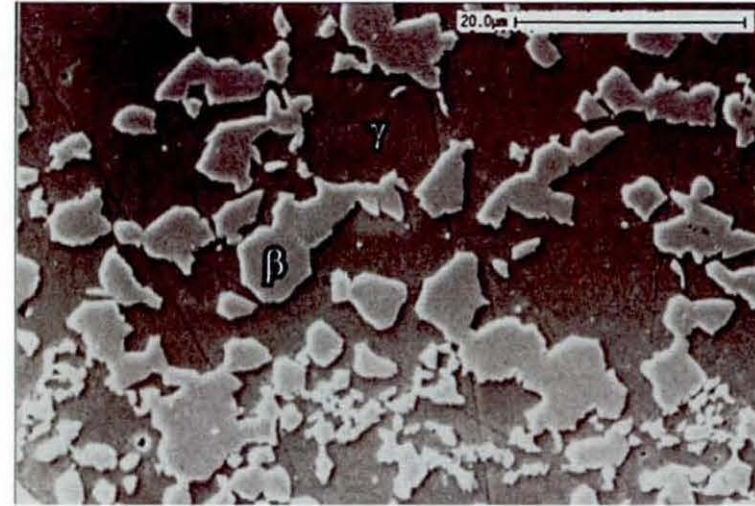


b. Optical bright field

Figure 5.4.14 G12/4-Y exposed at 950°C for 4800 hours – coating characteristics



a. Optical bright field

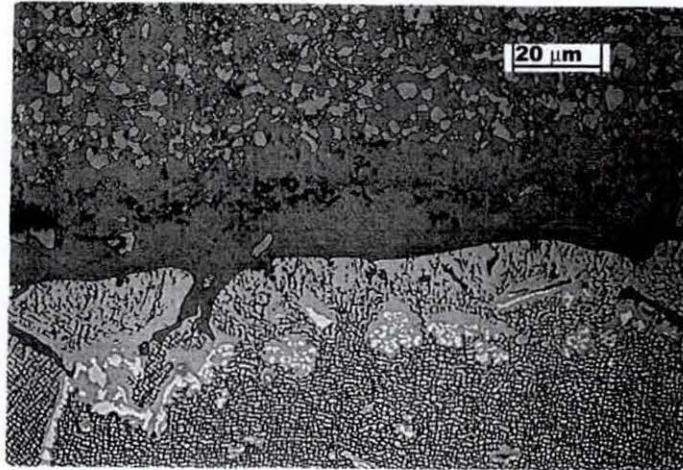


b. Scanning electron micrograph, secondary image

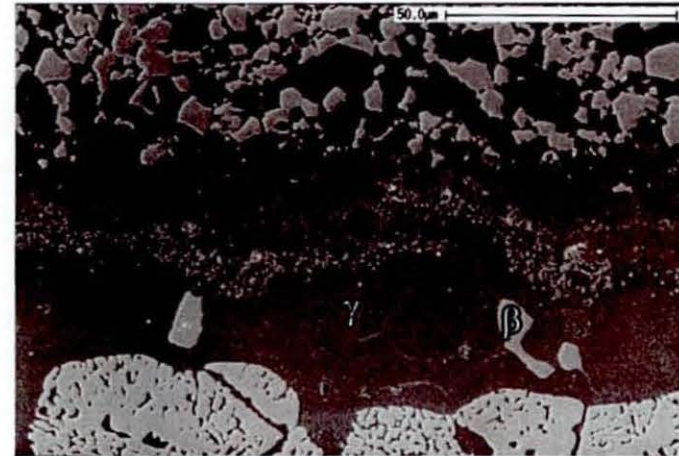
Table 5.12 Typical EDX data for compositions of phases, atom%

	Ni K	Cr K	Co K	Mo L	W L	Ti K	Al K	Ta L	Nb L	Zr L	Re L	Y L
β	39.2	5.8	14.7	0	2.6	0.5	37.3	0	0	0	0	0
γ	27.3	28.1	35.6	0.2	2.2	0.5	6.0	0	0	0	0	0

Figure 5.4.15 G12/4-Y exposed at 950°C for 4800 hours – interdiffusion characteristics



a. Optical bright field

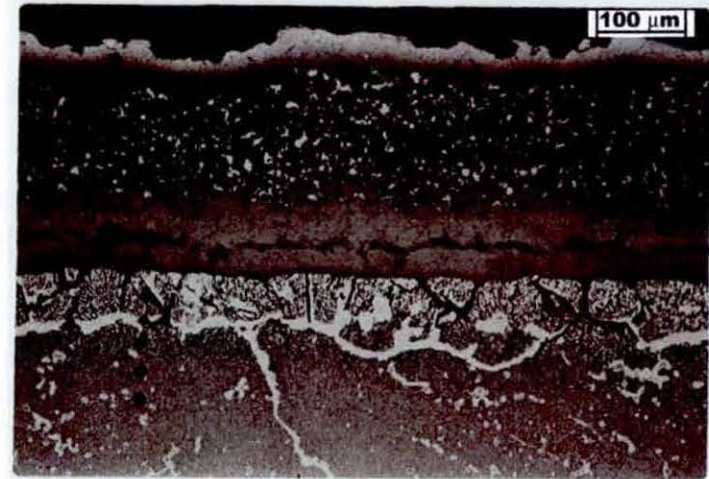
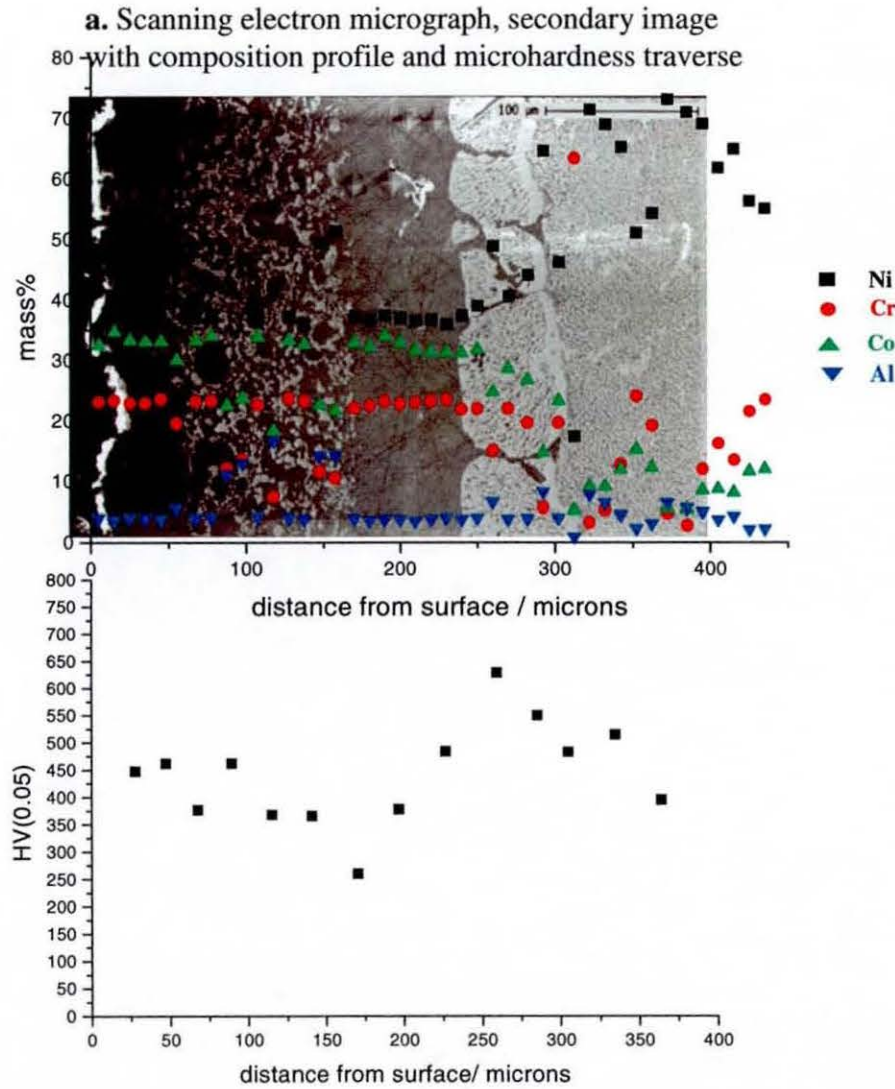


b. Scanning electron micrograph, secondary image

Table 5.13 Typical EDX data for compositions of phases, atom%

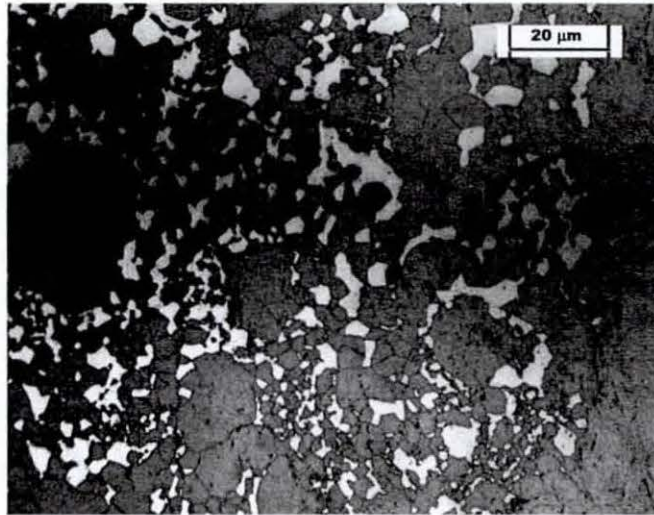
	Ni K	Cr K	Co K	Mo L	W L	Ti K	Al K	Ta L	Nb L	Zr L	Re L	Y L
β	39.2	5.8	14.7	0	2.6	0.5	37.3	0	0	0	0	0
γ	27.3	28.1	35.6	0.2	2.2	0.5	6	0	0	0	0	0

Figure 5.4.16 G12/5-W exposed at 950°C for 9600 hours – coating – interdiffusion – substrate profile

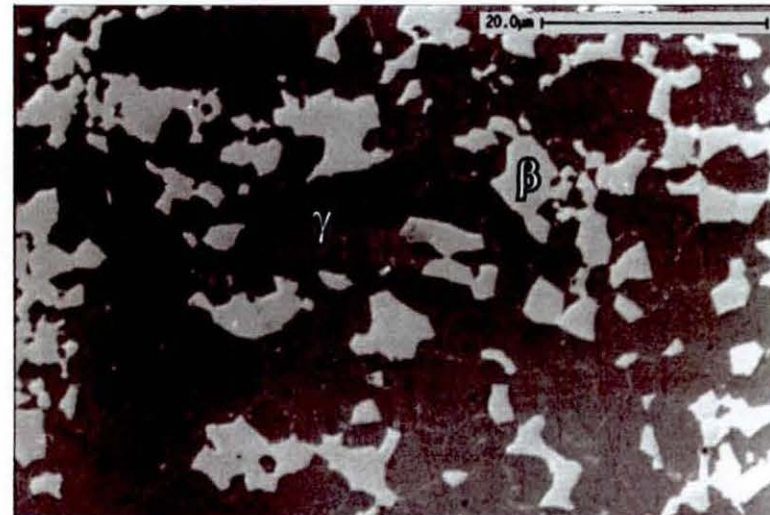


b. Optical bright field

Figure 5.4.17 G12/5W exposed at 950°C for 9600 hours – coating characteristics



a. Optical bright field

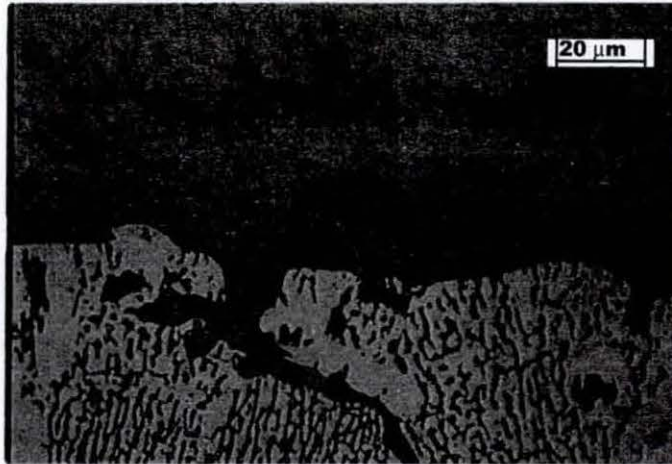


b. Scanning electron micrograph, secondary image

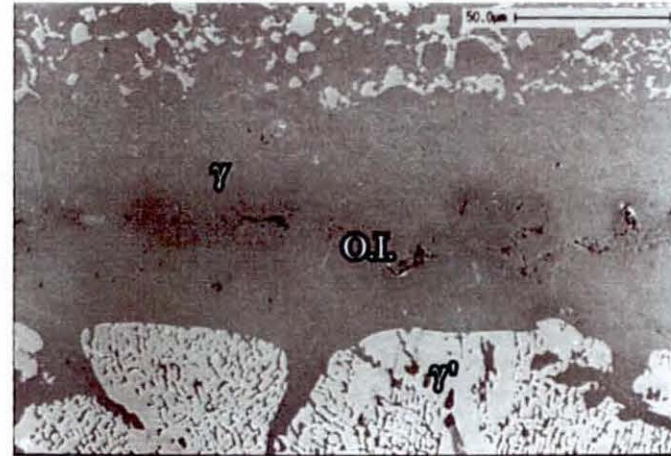
Table 5.14 Typical EDX data for compositions of phases, atom%

	Ni K	Cr K	Co K	Mo L	W L	Ti K	Al K	Ta L	Nb L	Zr L	Re L	Y L
β	49	6.3	14.8	0	0.3	1.1	28.4	0	0	0	0	0
γ	35.1	25.1	31.3	0.4	0.2	0.5	6.8	0	0	0	0	0

Figure 5.4.18 G12/5W exposed at 950°C for 9600 hours – interdiffusion characteristics



a. Optical bright field



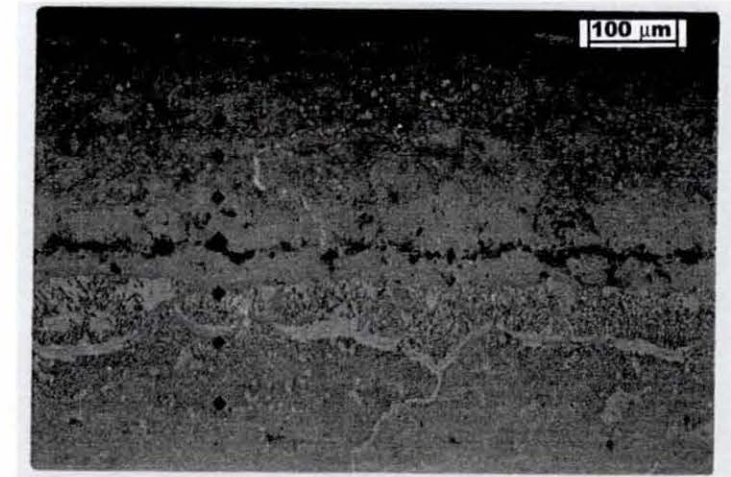
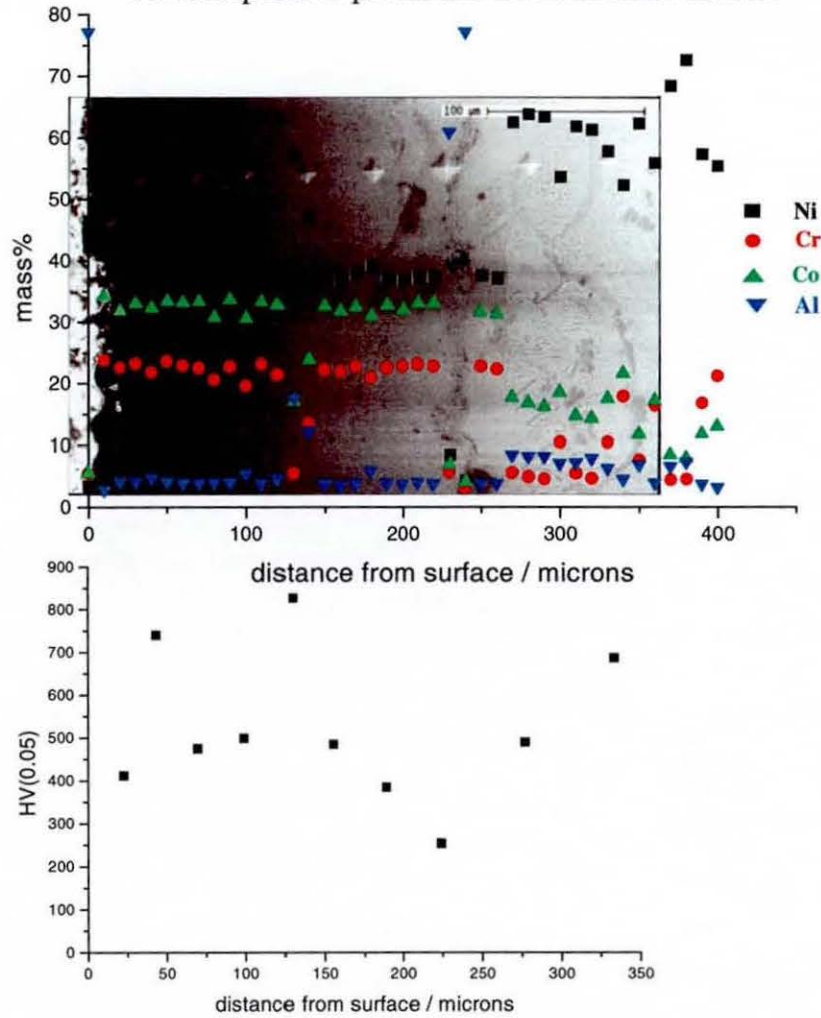
b. Scanning electron micrograph, secondary image

Table 5.15 Typical EDX data for compositions of phases, atom%

	Ni K	Cr K	Co K	Mo L	W L	Ti K	Al K	Ta L	Nb L	Zr L	Re L	Y L
γ	34.9	24.8	31.8	0.4	0.5	0.6	6.8	0.1	0	0	0	0
OI Particle	31.6	22.3	24.7	1.6	0.5	13.3	5.6	0.2	0.2	0	0	0
γ substr.	58.2	5.6	16.3	0.2	0.7	3.4	14.3	1	0.1	0	0	0

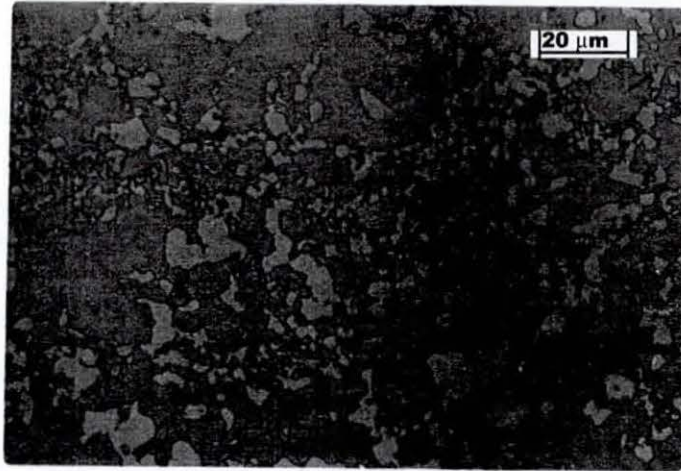
Figure 5.4.19 G12/5-X exposed at 950°C 12000 –coating – interdiffusion – substrate profile

a. Scanning electron micrograph, secondary image with composition profile and microhardness traverse

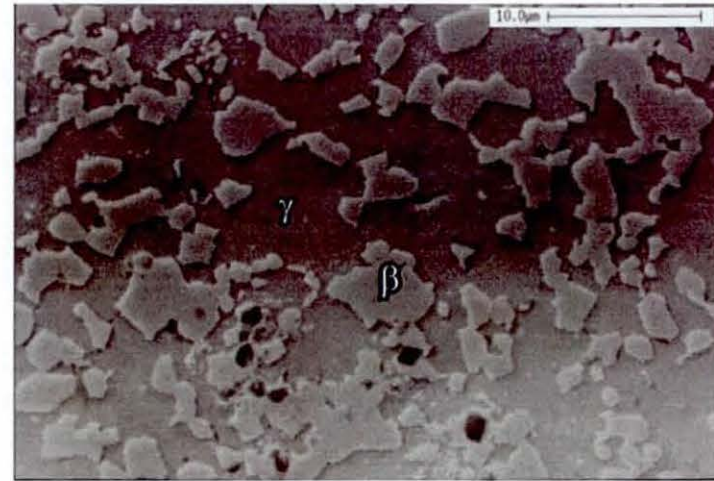


b. Optical bright field

Figure 5.4.20 G12/5-X exposed at 950°C for 12000 hours – coating characteristics



a. Optical bright field

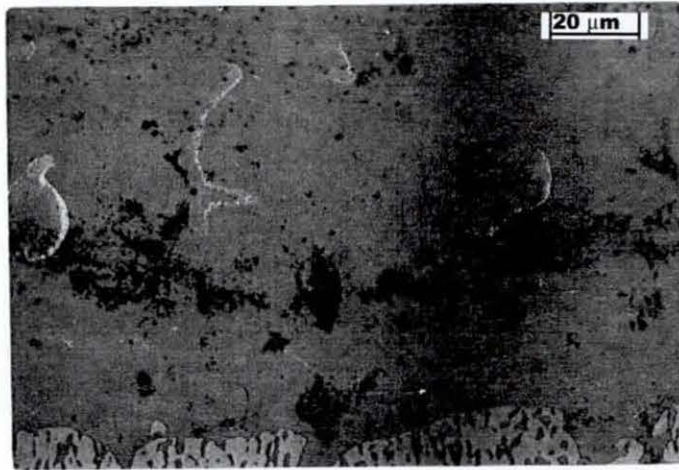


b. Scanning electron micrograph, secondary image

Table 5.16 Typical EDX data for compositions of phases, atom%

	Ni K	Cr K	Co K	Mo L	W L	Ti K	Al K	Ta L	Nb L	Zr L	Re L	Y L
β	43.7	7.9	15.6	0	0.3	1	31.5	0	0	0	0	0
γ	34.9	24.1	30.5	0.3	0.6	0.6	8.9	0.1	0	0	0	0

Figure 5.4.21 G12/5-X exposed at 950°C for 12000 hours – interdiffusion layer characteristics



a. Optical bright field



b. Scanning electron micrograph, secondary image

Table 5.17 Typical EDX data for compositions of phases, atom%

	Ni K	Cr K	Co K	Mo L	W L	Ti K	Al K	Ta L	Nb L	Zr L	Re L	Y L
γ	34.3	24.1	31.2	0.5	0.4	0.7	8	0.1	0	0	0	0
O.I.	19.6	13.9	17	0.4	0.4	3.2	45.5	0	0	0	0	0

5.4.4 Results – Thermal Exposure - Temperature and Time Sequence

Selected micrographs and composition data have been taken from the data in section 5.4.4 and have been reproduced in temperature and time sequence. This is to facilitate the analysis of the effect of thermal exposure on microstructure and phase composition. The following is a summary of the data presented.

Figure 5.4.22 Low magnification optical micrographs of the complete coating

- β depletion zone at outer surface
- β depletion zone at inner surface
- interdiffusion zone consisting of mainly γ
- extent of interdiffusion zone increases with thermal exposure
- recrystallised region substrate below interdiffusion zone featuring;
 - 1) smaller grain size than bulk substrate
 - 2) change in morphology of γ/γ'
- penetration of coating γ into recrystallised grain boundaries at the higher temperature

Figure 5.4.23 High magnification optical micrographs of phases in coating

- core coating consists of γ and β
- proportion of γ increases with thermal exposure as that of β decreases

Figure 5.4.24 Phase map for coating

- bulk coating consistently contains γ and β
- equilibrium prediction for coating phases is γ and β

Table 5.18 EDX data for phases in coating

- measured compositions of γ and β phases consistent

Figure 5.4.25 High magnification secondary electron micrographs of phases in interdiffusion layer

- layer of small particles represent O.I.
- mainly γ at interdiffusion zone

- morphology of γ/γ' in recrystallised region below interdiffusion zone different to that of bulk substrate
- proportion of γ' in recrystallised region increases on thermal exposure

Figure 5.4.26 Phase map for interdiffusion layer

- γ and β exist at interdiffusion the most thermal exposure resulting in just γ

Table 5.19 EDX data for phases in interdiffusion layer.

- compositions of phases relatively consistent.

Figure 5.4.22 Effect of thermal exposure on coating, optical micrographs

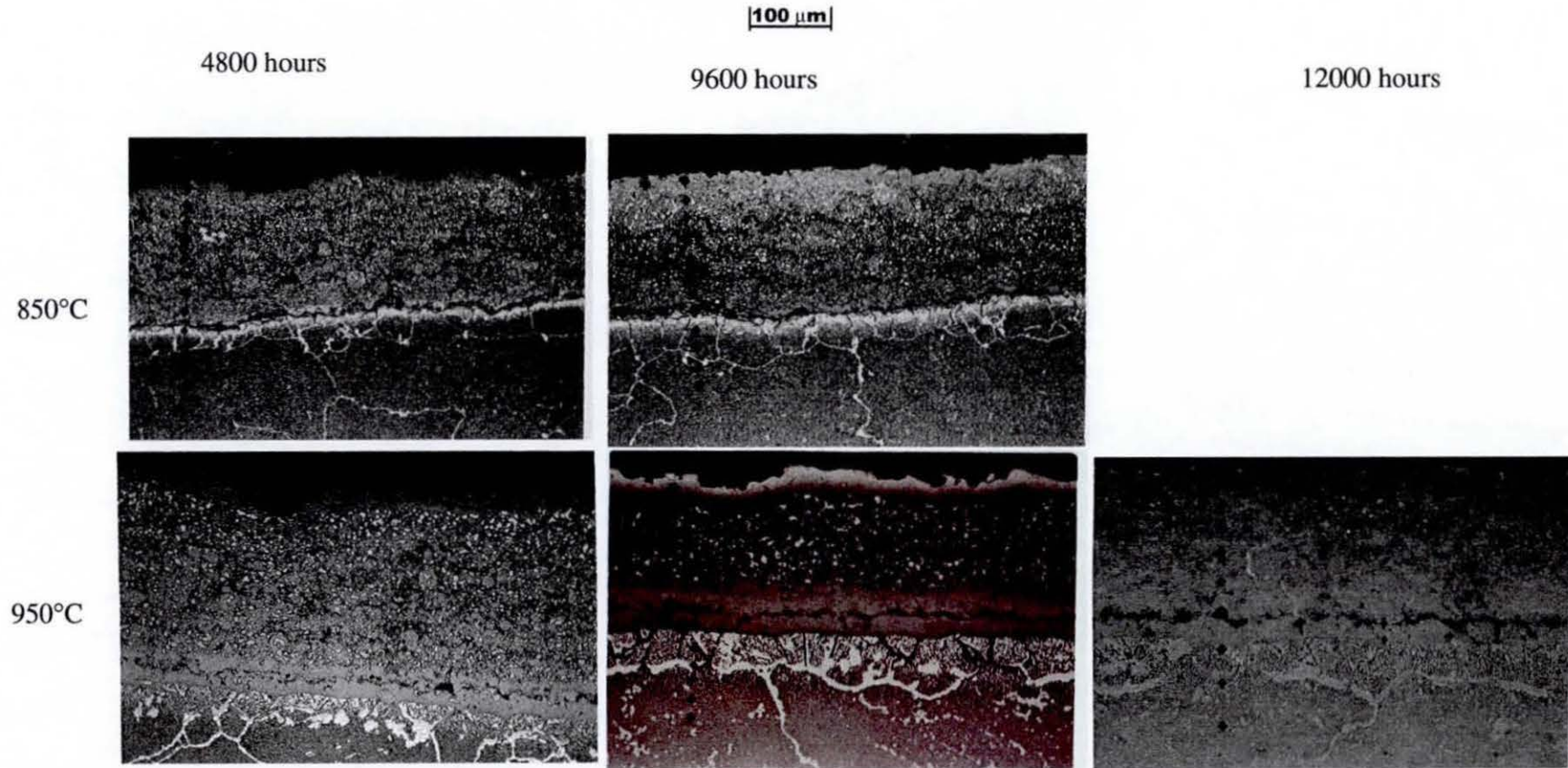


Figure 5.4.23 Effect of thermal exposure on core coating, optical micrographs (β -bright, γ -dark)

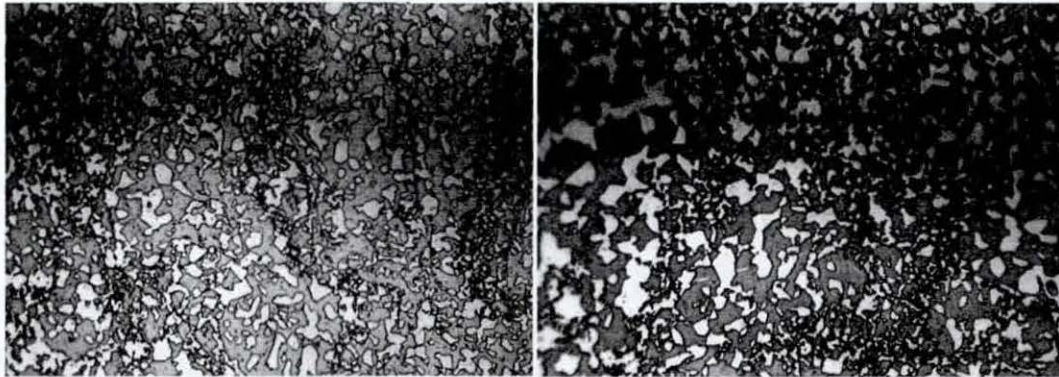
20 μm

4800 hours

9600 hours

12000 hours

850°C



950°C

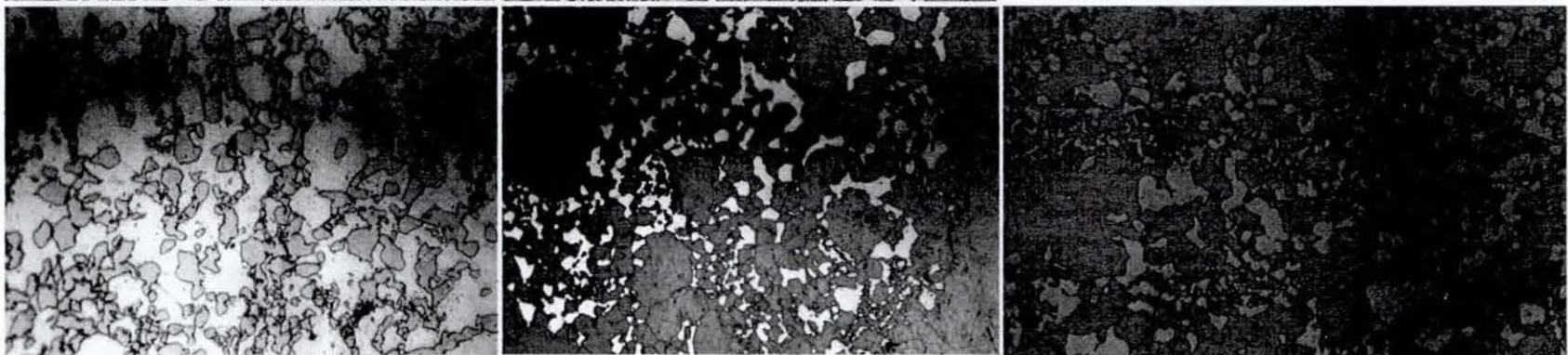
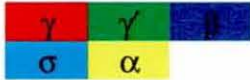
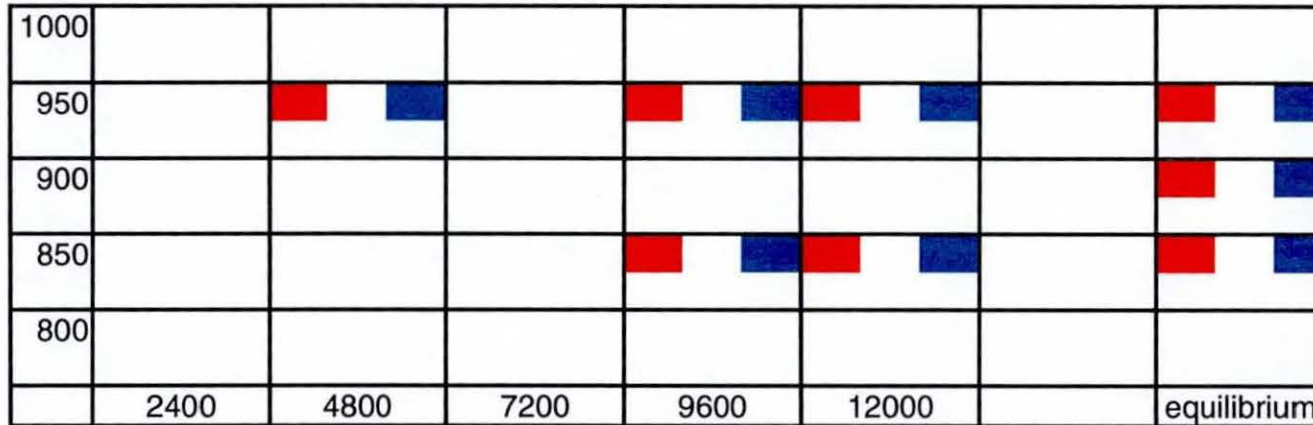


Figure 5.4.24 Phase map for coating experimentally determined at 850°C and 950°C, 4800 to 1200 hours, with equilibrium calculations at 850°C, 900°C and 950°C

key



temp / °C



time / hours

Table 5.18 Effect of thermal exposure on composition of coating phases, EDX data, atom%

Phase	Temp/°C	Time/hrs	Ni K	Cr K	Co K	Mo L	W L	Ti K	Al K	Ta L	Nb L	Zr L	Re L	Y L
Beta	850	4800	38.6	5.46	15.38	0	2.58	0.25	37.6	0	0.1	0.042	0	0
Beta	850	9600	47.4	5.2	15.5	0.2	0.1	0.4	31.1	0	0	0	0	0
Beta	950	4800	47.4	5.2	15.5	0.2	0.1	0.4	31.1	0	0	0	0	0
Beta	950	9600	49	6.3	14.8	0	0.3	1.1	28.4	0	0	0	0	0
Beta	950	12000	43.7	7.9	15.6	0	0.3	1	31.5	0	0	0	0	0
Gamma	850	4800	23	30.1	39.2	0	1.8	0	5.9	0	0	0	0	0
Gamma	850	9600	25.5	28.3	41	0	0.1	0.2	4.7	0.1	0	0	0.1	0
Gamma	950	4800	27.3	28.1	35.6	0.2	2.2	0.5	6	0	0	0	0	0
Gamma	950	9600	35.1	25.1	31.3	0.4	0.2	0.5	6.8	0	0	0	0	0
Gamma	950	12000	34.9	24.1	30.5	0.3	0.6	0.6	8.9	0.1	0	0	0	0

Figure 5.4.25 Effect of thermal exposure on interdiffusion zone, secondary electron micrographs (magnification varies)

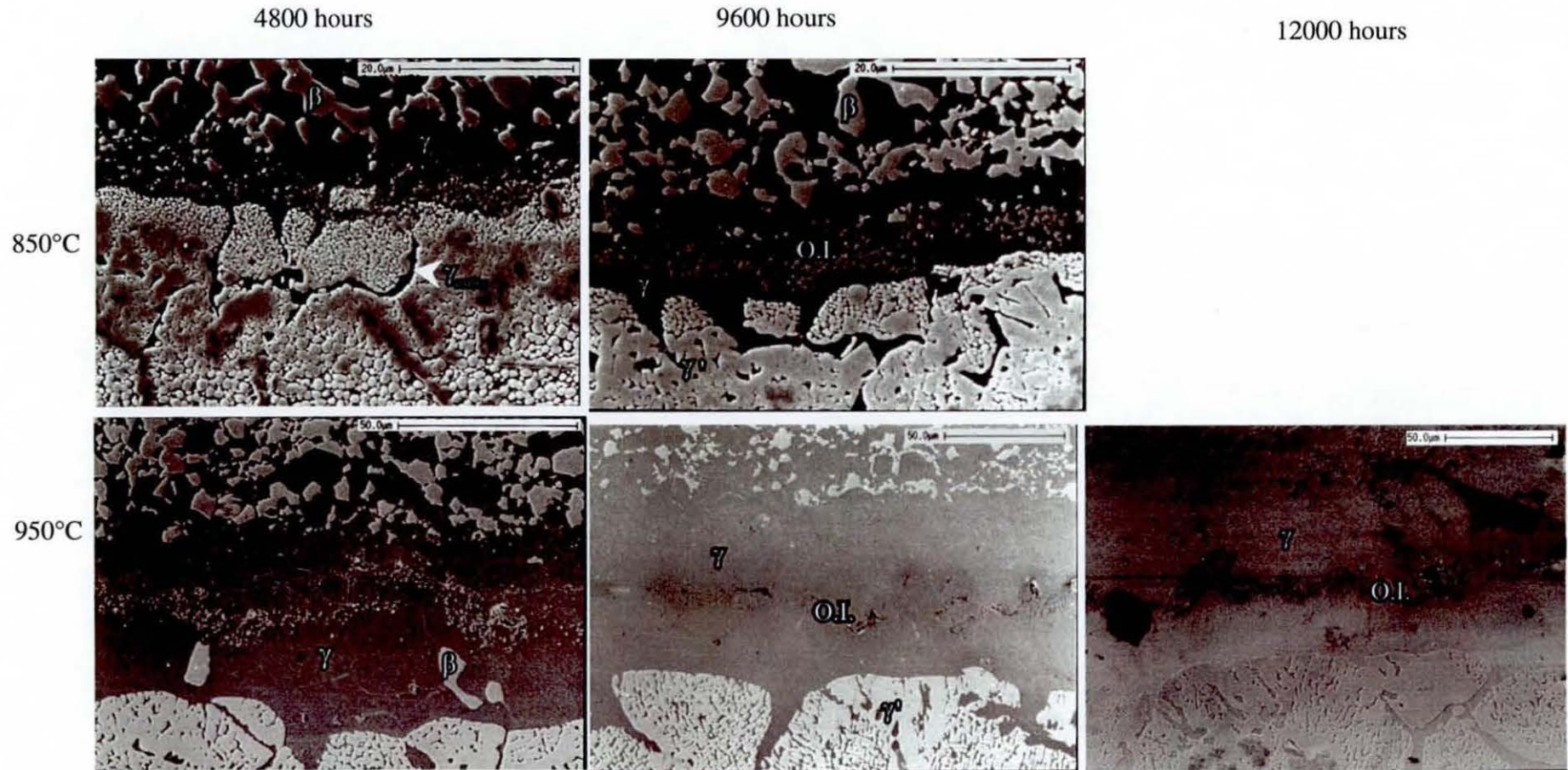
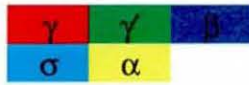
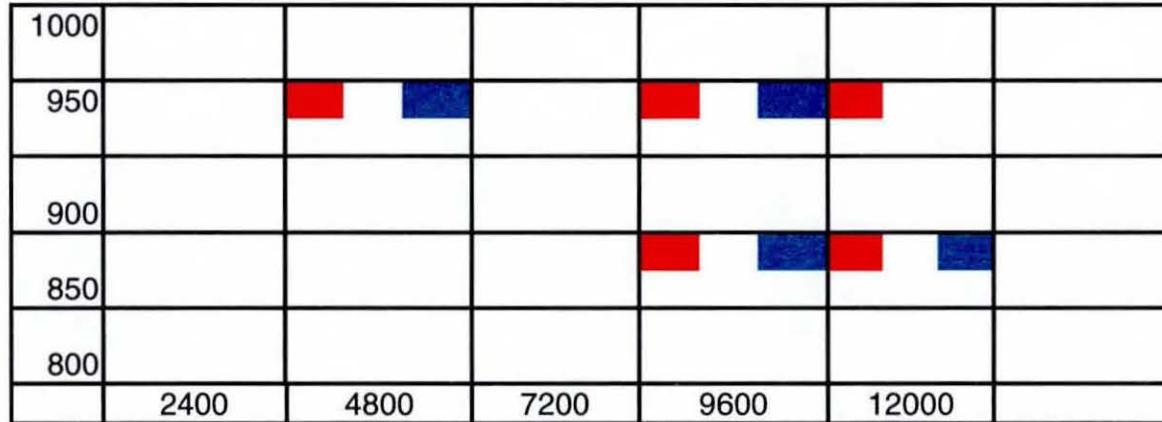


Figure 5.4.26 Phase map for interdiffusion phases, experimentally determined

key



temp/ °C



time / hours

Table 5.19 Effect of thermal exposure on composition of interdiffusion zone phases, EDX data, atom%

Phase	Temp/°C	Time/hrs	Ni K	Cr K	Co K	Mo L	W L	Ti K	Al K	Ta L	Nb L	Zr L	Re L	Y L
Beta	850	4800	39.2	5.8	14.7	0	2.6	0.5	37.3	0	0	0	0	0
Beta	850	9600	46.0	5.8	16.7	0	0.6	0.4	30.2	0	0	0	0	0.0
Beta	950	4800	39.2	5.8	14.7	0	2.6	0.5	37.3	0	0	0	0	0
Beta	950	9600	Not present											
Beta	950	12000	Not present											
Gamma	850	4800	24	30.1	37.8	0.2	1.6	0.2	6.1	0	0	0	0	0
Gamma	850	9600	26.1	28.5	39.1	0.4	0.8	0.3	4.5	0.2	0	0	0	0
Gamma	950	4800	27.3	28.1	35.6	0.2	2.2	0.5	6	0	0	0	0	0
Gamma	950	9600	34.9	24.8	31.8	0.4	0.5	0.6	6.8	0.1	0	0	0	0
Gamma	950	12000	34.3	24.1	31.2	0.5	0.4	0.7	8	0.1	0	0	0	0

5.4.5 Discussion

The γ and β phase microstructure of the coating is a typical composition for MCrAlY coatings with a significant cobalt content. Many features evident on thermal exposure of this coating have been investigated by other authors (although not in a systematic time and temperature sequence), these include;

- β depletion at the outer surface
- β depletion zone in the coating above the O.I. (original interface)
- γ zone below the O.I.

One feature has not been found in the literature;

- the recrystallised layer below the interdiffusion zone.

These features are considered in more detail in the following sections.

5.4.5.1 β Depletion at Outer Surface

The outer layer β depletion zone develops over time and temperature. The feature has not been quantitatively defined in this research, but is seen to increase in temperature and time. This feature has been observed in thermally exposed MCrAlY / superalloy systems by a number of authors including Srinivasan and Cheuvu^{40,41,49}. It is generally accepted that the cause of the depletion is due to diffusion of aluminium to the outer surface to form the protective oxide Al_2O_3 . The extent of this β depletion layer increased with temperature and time as seen in Figure 5.4.22. Srinivasan⁴⁰ investigated this feature with a view to using it in a model for time/temperature correlation. In a Co 32% Ni21% Cr9% Al (by mass) MCrAlY coating on a U520 substrate the β depletion layer width was measured as a function of time and temperature. The relationship between the width and time for various temperatures was found to be parabolic;

$$\text{Equation 5.4.1} \quad w_o = kt^{1/2}$$

where

w_o is the width of the outer depletion zone

k is the parabolic rate constant

t is exposure time.

Cheruvu states that steady state external scale formation is predominantly a parabolic rate process. However, it should be noted that the external surface of in-service blades, as distinct from laboratory heat treated samples, suffers from temperature variability. This temperature variability is an extra factor that would have to be taken into account if the outer β depletion layer were to be used to model time/temperature correlation.

5.4.5.2 β Depletion Layer at Inner Surface

A β depletion zone at the inner layer of the coating is also evident. This layer again varies with time and temperature. Investigators that have found this effect include Srinivasan and others^{40,76,41;43}. This inner depletion zone is said to be due to diffusion of aluminium towards the substrate, this being the result of the aluminium concentration profile, which has a higher content in the coating than in the substrate. Again, the extent of this inner depletion layer is time and temperature dependent, Figure 5.4.22, and a relationship between the width of the inner β depleted layer and time, was found by Srinivasan⁴⁰, i.e.

Equation 5.4.2 $w_i = kt^{1/2}$

where

w_i is the width of the inner depletion zone

k is the parabolic rate constant

t is time

This feature could potentially be used for simple time-temperature predictions. This is a more suitable feature with respect to this research, as it would not suffer from the temperature variability that affects the outer surface of a turbine blade.

5.4.5.3 Interdiffusion Zone

The definition of exactly what region comprises the interdiffusion zone requires some consideration. The position of the original interface (O.I.) is indicated by non-metallic particles, Figure 5.4.25. In cases where interdiffusion results in a distinct microstructure, definition may be simple. A microstructure for the interdiffusion zone should be distinguishable from the coating. Layers either side of the interdiffusion zone could be termed 'diffusion affected' zones, as their microstructures would be affected by inward and outward diffusion of elements on thermal exposure.

For $\gamma+\beta$ coating systems, an interdiffusion zone consisting of a $\gamma+\beta$ growth zone is often described^{43,49,47}. The β precipitates in the γ being the result of aluminium diffusion from the coating as described above. In the RT122/IN738LC system, the interdiffusion zone appears to be mainly γ , with a few β precipitates, Figure 5.4.22 and Figure 5.4.25.

An equilibrium prediction for IN738 increasing Al to 5 mass%, Figure 5.4.2, did not predict precipitation of β . However, 5 mass% Al was the limit that could be calculated by the ThermoCalc software and Ni-database under the conditions applied. Assuming the interdiffusion zone to consist of the γ layer below the O.I., the width of the zone does increase with time and temperature.

The region in the substrate where there is a change in morphology of γ/γ' and grain boundary penetration of coating phases is of note. The grain size indicated by the grain boundaries are not typical for IN738, being much smaller than would be expected for the bulk substrate. It was reported that the surface of the substrate might have been shot-peened prior to coating application. This would have induced residual stress into the surface. Subsequent thermal exposure could result in recrystallisation, resulting in the relatively small grains. Inward and outward diffusion of elements with respect to the coating would also have an effect. The combination of these effects could be the cause of the unusual γ/γ' morphology.

The presence of this recrystallised region could account for the lack of β in the interdiffusion zone, as reported by other authors. The grain boundaries create fast paths for diffusion of aluminium into the substrate, giving rise to substantial precipitation of γ' , following the boundaries away from the interface into the substrate. This will undoubtedly affect the growth rate of the interdiffusion zone, and may well be the cause for the absence of β phase in this region, as compared with other studies of similar systems.

Ellison⁴⁷ developed a model for time/temperature correlation based on interdiffusion zone thickness. The coating was GT-29 (CoCrAlY) and the substrate DS GTD-111. A parabolic relationship between interdiffusion zone thickness and exposure time was found;

Equation 5.4.3 $\xi^2 = k_p t$

ξ is growth of interdiffusion zone

k_p is parabolic rate constant

t is exposure time

Ellison attempts to provide a physical basis for his model by expressing the rate constant in terms of interdiffusion coefficients and activation energies.

However for the RT122/IN738LC system studied in this research, the effects of the recrystallised region have implications for the using a method based on interdiffusion zone thickness to model time/temperature correlation. Ellison⁴⁷ did not report such effects in his system and therefore his model may not be directly applicable to this research.

5.5 Coating SC2453

5.5.1 Results - Equilibrium Predictions

1. Thermodynamic equilibrium predictions provide a good introduction to the phases likely to be present in the coating. Calculation details have been presented Chapters 3 and 5.1. The phases β , γ , α , γ' , and σ are predicted at various temperature ranges within the 600°C to 1300°C calculation limits, Figure 5.5.1 a. β was the only phase predicted to be present over the whole of the above temperature range. A temperature around 900°C is particularly important, this being the point of a number transitions. Below 900°C (from 600°C) the proportions of β and σ increase at the expense of γ' and α . At around 900°C γ' and σ dissolve and γ precipitates. The proportions of β and α both exhibit a sharp rise at the same temperature. In the temperature range 900°C to 1300°C, the proportion of γ rises, with β and α both decreasing. Figure 5.5.1 b clearly shows the depletion of γ' and σ , with the precipitation of γ , at 850°C, 900°C and 950°C.
2. The compositions of the phases at these temperatures are given in Table 5.20. The notable change in composition, with an increase in temperature from 850°C to 950°C, is the rhenium content of α , increasing from 4.8 atom% to 9.4 atom%,
3. In addition to equilibrium predictions for the bulk alloy composition, predictions were made for modified compositions depleting the aluminium content and the chromium content.
4. The modified coating composition depleting the aluminium content shows that initially γ and γ' become more stable over a wide temperature range with β reducing in stability, Figure 5.5.2 a-c. As the aluminium reaches a low content where β is no longer present at equilibrium, further Al depletion results in γ increasing in volume fraction at the expense of γ' , Figure 5.5.2 d, e. The aluminium rich phases deplete more quickly with aluminium content at 950°C than at 850°C, where there is a more gradual transition for β and γ' to γ then to γ , Figure 5.5.2 f, g. Note that with the original bar composition γ' is not present at 950°C, but depletion of aluminium can result in γ' at this temperature.
5. Depletion of chromium content has also been investigated. Over the chromium content range 21.5 to 12 mass%, γ and γ' become more stable, and as expected the Cr-rich phases σ and α less stable, Figure 5.5.3 a-d. The proportion of β decreases more at lower

temperatures than at higher temperatures, Figure 5.5.3 e,f. The change is not as significant as that generated by aluminium depletion. 900°C is still a transitional temperature; the temperature range over which transitions occur broadens with depletion of chromium. There is a marked difference in the phases present at 850°C and 950°C, Figure 5.5.3 e, f. γ is only present at the higher of these temperatures. β reduces in stability with depleting aluminium at both temperatures.

Figure 5.5.1 As-coated composition

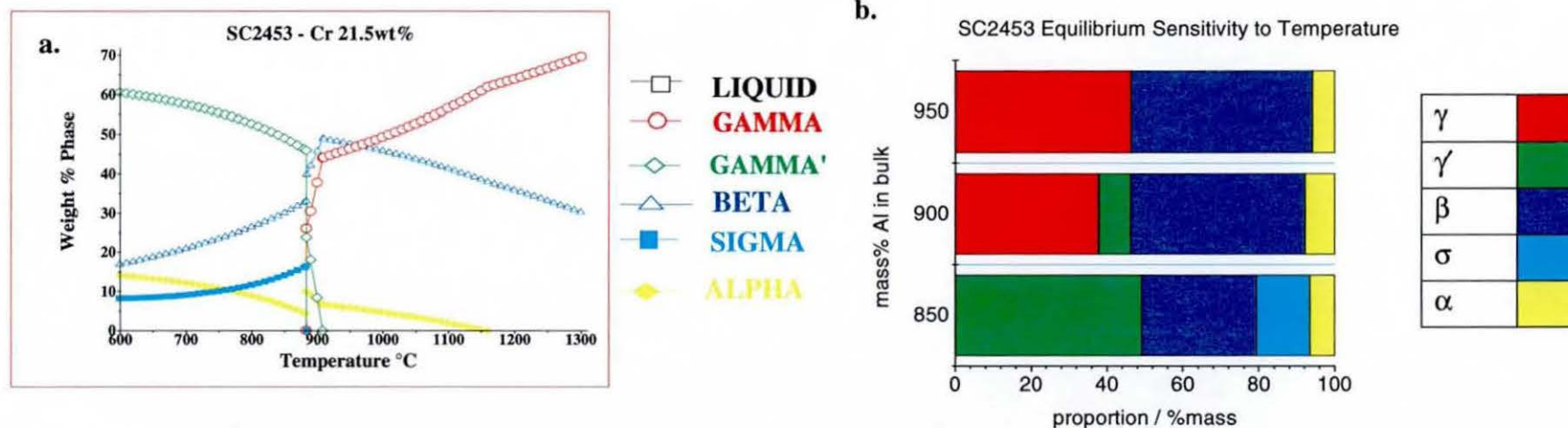


Table 5.20 Compositions of phases, atom%

Phase	Temp/°C	Ni	Cr	Co	Mo	W	Ti	Al	Ta	Nb	Zr	Re	Y
Alpha	850.00	1.2	88.9	5.0				0.1				4.8	
Alpha	900.00	1.7	87.0	4.6				0.1				6.7	
Alpha	950.00	2.0	84.4	4.0				0.1				9.4	
Beta	850.00	52.8	8.5	7.7				31.0				0	
Beta	900.00	53.9	8.7	6.9				30.5				0	
Beta	950.00	54.6	8.7	6.3				30.4				0	
Gamma	850.00	Not present											
Gamma	900.00	48.0	28.2	14.5				9.1				0.1	
Gamma	950.00	49.6	27.2	12.9				10.1				0.3	
Gamma prime	850.00	62.2	9.7	7.9				20.1				0	
Gamma prime	900.00	62.2	10.4	7.4				20.0				0	
Gamma prime	950.00	Not present											
Sigma	850.00	11.4	65.8	21.0				0				1.7	
Sigma	900.00	Not present											
Sigma	950.00	Not present											

Figure 5.5.2 Composition modified – Al depletion

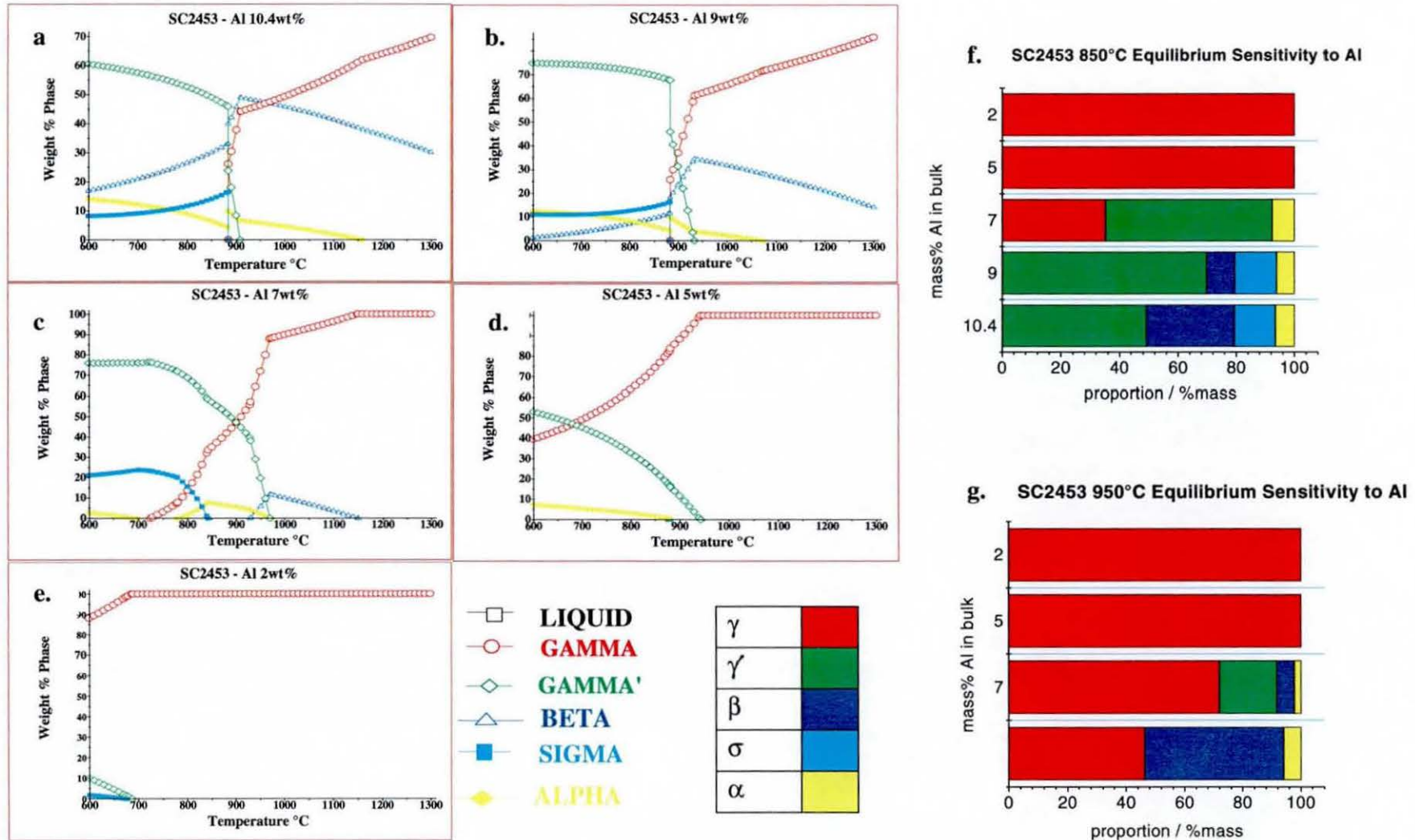
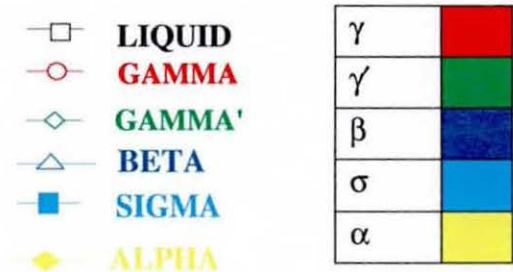
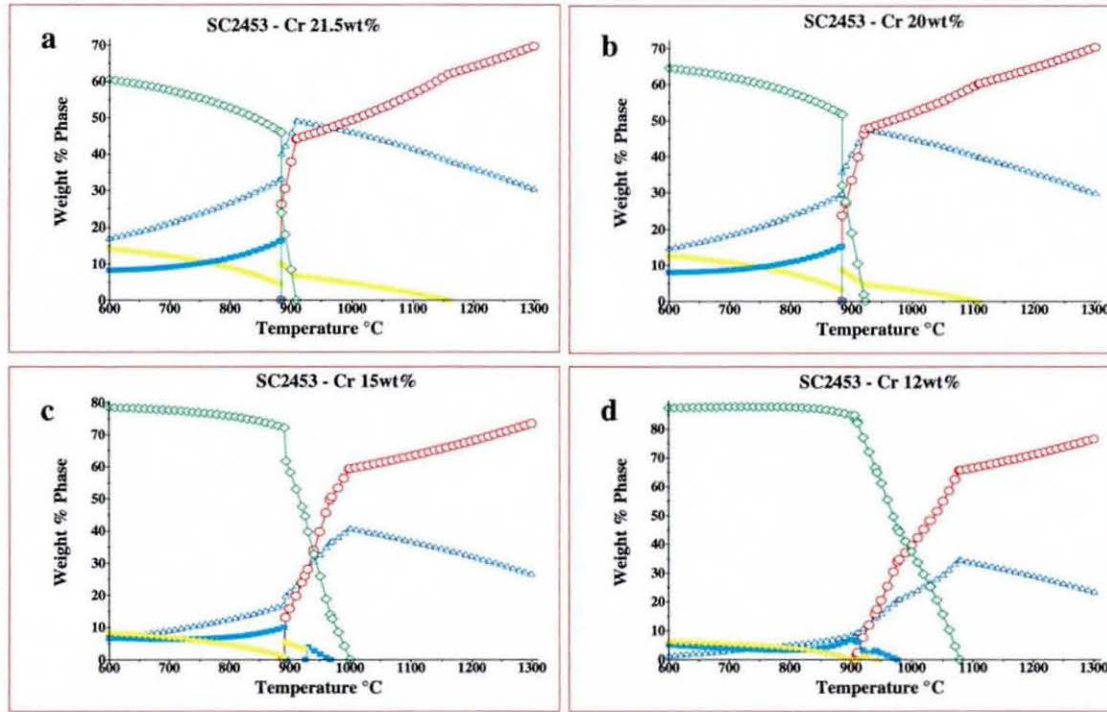
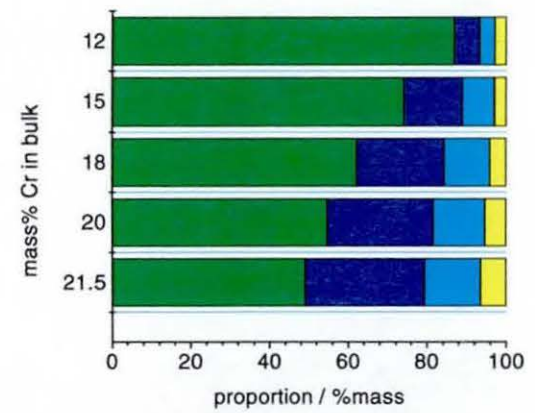


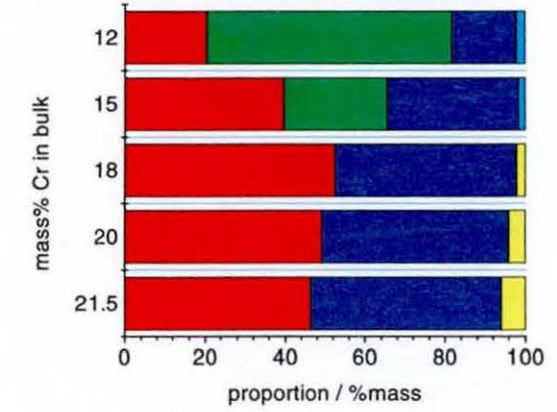
Figure 5.5.3 Composition modified – Cr depletion



e. SC2453 850°C Equilibrium Sensitivity to Cr



f. SC2453 950°C Equilibrium Sensitivity to Cr

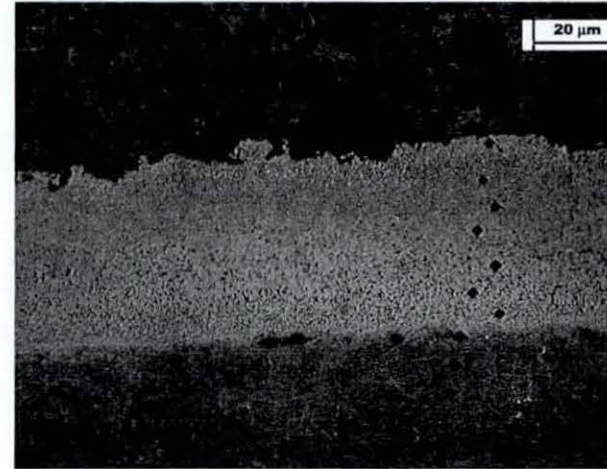
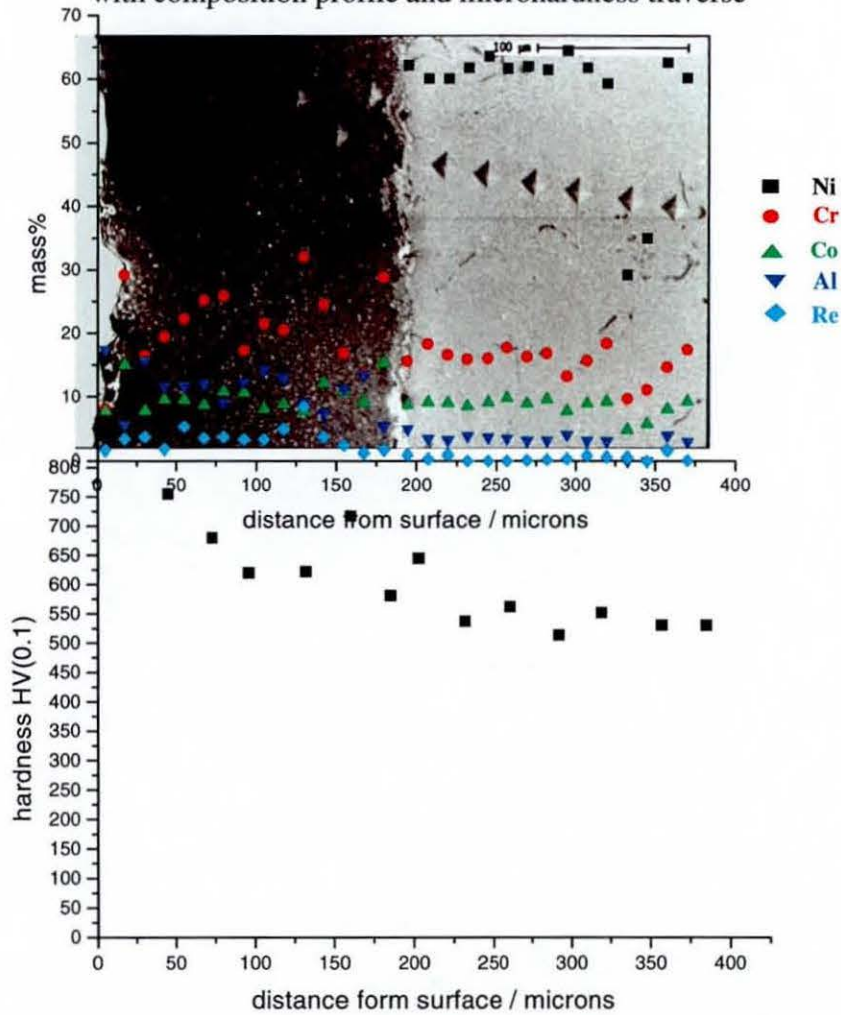


5.5.2 Results – As-Coated

1. This sample has experienced the post-coating heat treatment and no further thermal exposure. The details supplied state that there was a solution treatment at 1120°C and ageing at 845°C. Typical times for these processes are 2 hours and 24 hours respectively.
2. The composition profile within the coating showed one or two bands that had low cobalt and chromium contents, with higher aluminium contents, Figure 5.5.4 a. The hardness profile indicates that the coating is harder than the substrate and there is a variation in hardness within the coating, possibly corresponding with cobalt content, Figure 5.5.4 a.
3. The particle sizes were quite small, Figure 5.5.4 b indicating a range from <1µm to 3µm. The EDX data must therefore be treated with some caution due to overlap of the electron beam with different phases. Examples of particle composition data are however given in Table 5.21. Some identification of phases was possible despite the aforementioned difficulty. The phases present in the 'as-coated' state are mainly β , γ , σ and γ , Figure 5.5.5, with α evident in small amounts near the interdiffusion zone and also near the outer surface. The α contains rhenium, Table 5.22, and is indicated by the brighter particle bands in Figure 5.5.4c. For reference the complete EDX analysis data and scanning electron micrograph annotated with spot positions are given in Table 5.22 and Figure 5.5.6 respectively.
4. The interdiffusion layer after the coating process is a bonding layer, the phases not being clearly defined, Figure 5.5.7 a-c. Raw EDX data did not conclusively define the phases present. However, there was no needle-like phase. The EDX data and scanning electron micrograph annotating spot positions are given in Table 5.23, and Figure 5.5.8 respectively.

Figure 5.5.4 G13/6-Z unexposed coating – interdiffusion – substrate profile

a. Scanning electron micrograph, secondary image with composition profile and microhardness traverse



b. Optical bright field



c. Scanning electron micrograph, backscattered image

Figure 5.5.5 G13/6-Z as-coated coating characteristics

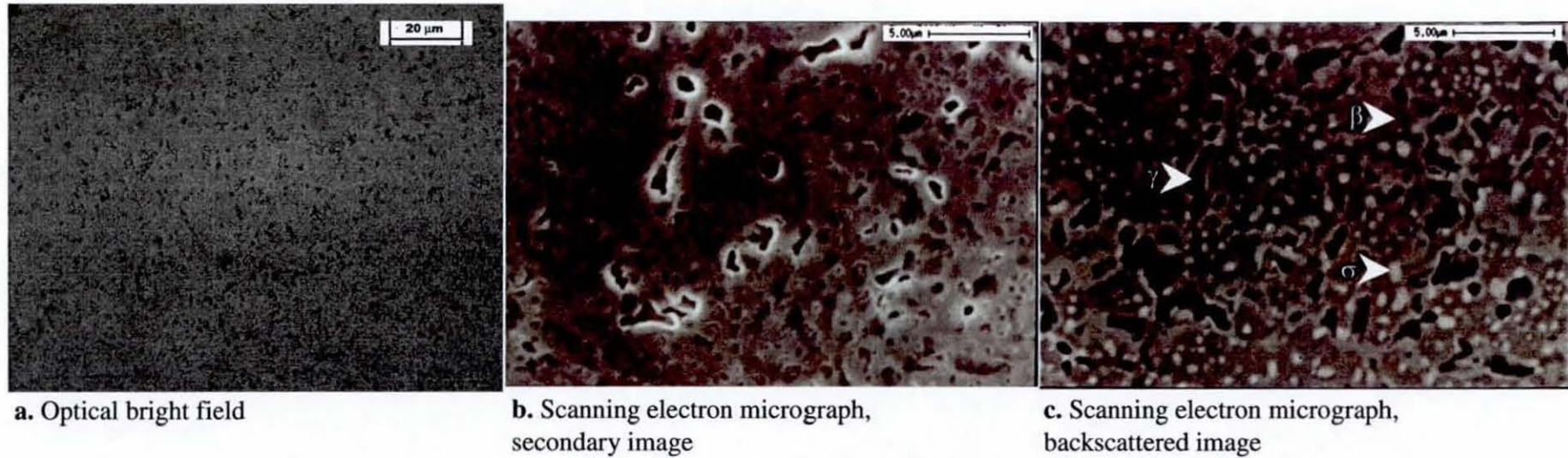


Table 5.21 Typical EDX composition data, atom%

	Ni K	Cr K	Co K	Mo L	W L	Ti K	Al K	Ta L	Nb L	Zr L	Re L	Y L
β	49.4	11.5	6.4	0	0	0.2	31.9	0	0	0	0.6	0
γ	49.0	22.2	15.4	0	0.1	0	12.6	0	0	0	0.8	0
σ	29.1	47.1	5.7	0	0.3	0	14	0	0	0	3.9	0

Note: this data suffers from interference of adjacent phases and is provided for information, and absolute values should be treated with caution

Figure 5.5.6 G13/6-Z unexposed, backscattered electron micrograph, annotated for EDX points on coating



Scanning electron micrograph, backscattered image

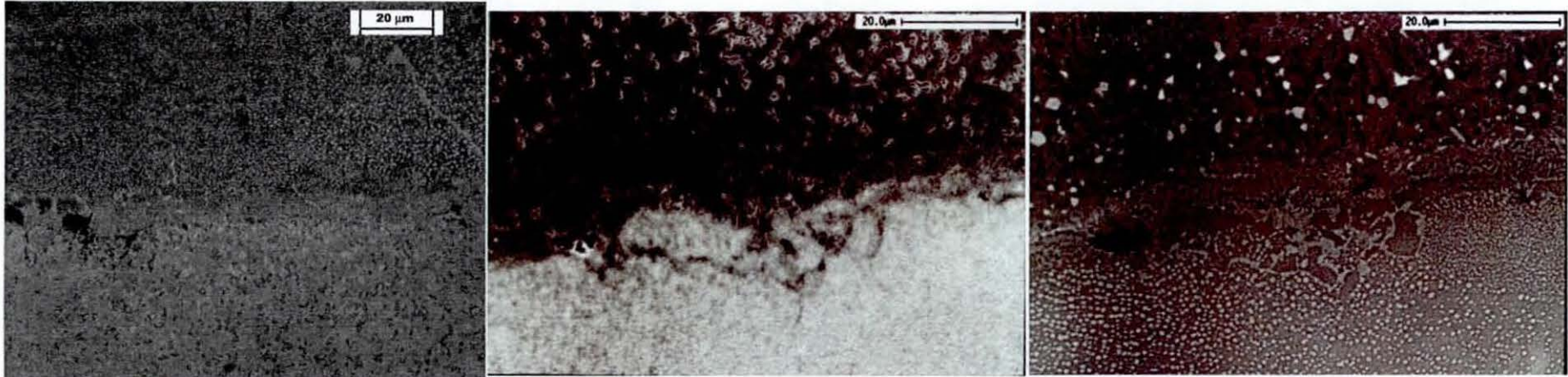
Table 5.22 Full EDX data for G13/6-Z as coated coating

Lab ID	particle ID	type	Ni K	Cr K	Co K	Mo L	W L	Ti K	Al K	Ta L	Nb L	Zr L	Re L	Y L
G13/6-Z	spot 1	γ	49.3	24.3	17.1	0.0	0.1	0.2	8.0	0.0	0.0	0.0	1.1	0.0
G13/6-Z	spot 2	γ	49.0	22.2	15.4	0.0	0.1	0.0	12.6	0.0	0.0	0.0	0.8	0.0
G13/6-Z	spot 3	γ	50.6	30.6	7.7	0.1	0.3	0.1	6.8	0.0	0.0	0.0	1.4	2.3
G13/6-Z	spot 4		53.0	18.1	9.7	0.0	0.5	0.3	18.0	0.0	0.0	0.0	0.4	0.0
G13/6-Z	spot 5		43.8	18.9	6.1	0.0	0.3	0.0	29.8	0.0	0.0	0.0	1.1	0.0
G13/6-Z	spot 6		52.4	18.7	8.2	0.0	0.2	0.1	19.9	0.0	0.0	0.0	0.5	0.0
G13/6-Z	spot 7		49.4	11.5	6.4	0.0	0.0	0.2	31.9	0.0	0.0	0.0	0.6	0.0
G13/6-Z	spot 8		47.0	15.4	6.7	0.0	0.7	0.1	29.4	0.0	0.0	0.0	0.7	0.0
G13/6-Z	spot 9		51.6	18.8	7.8	0.0	0.4	0.1	20.9	0.0	0.0	0.0	0.5	0.0
G13/6-Z	spot 10		49.8	19.4	12.4	0.0	0.6	0.2	16.8	0.0	0.0	0.0	0.9	0.0
G13/6-Z	spot 11	σ	30.5	42.1	5.9	0.0	0.3	0.1	17.7	0.0	0.0	0.0	3.4	0.0
G13/6-Z	spot 12	σ	29.1	47.1	5.7	0.0	0.3	0.0	14.0	0.0	0.0	0.0	3.9	0.0
G13/6-Z	spot 13	σ	41.9	30.3	8.0	0.0	0.7	0.0	17.3	0.0	0.0	0.0	1.8	0.0
G13/6-Z	*	α	10.3	76.5	3.1	0.0	0.1	0.2	4.4	0.1	0.0	0.0	5.4	0.0
G13/6-Z	*	α	7.0	80.6	2.8	0.0	0.5	0.0	2.7	0.0	0.0	0.0	6.5	0.0
G13/6-Z	*	α	41.3	24.8	7.3	0.0	0.4	0.0	24.8	0.0	0.0	0.0	1.4	0.0

* Bright particles near outer surface of coating

Note: this data suffers from interference of adjacent phases and is provided for information, and absolute values should be treated with caution. Some attempt has been made at phase identity. Spots 4 to 6 and 7 to 9 are probably β and γ respectively.

Figure 5.5.7 G13/6-Z as-coated interdiffusion zone characteristics



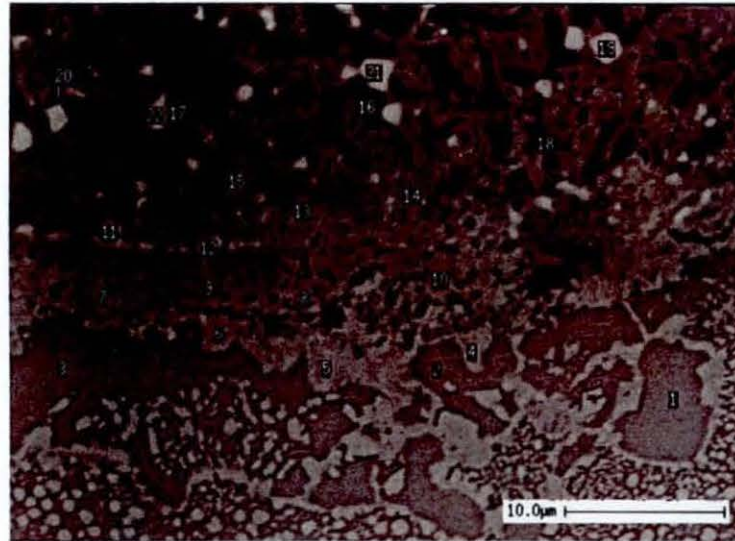
a. Optical bright field

b. Scanning electron micrograph,
secondary image

c. Scanning electron micrograph,
backscattered image

Figure 5.5.8 G13/6-Z unexposed, backscattered electron micrograph, annotated for EDX points on interdiffusion zone

Table 5.23 Full EDX data for G13/6-Z as-coated interdiffusion



Scanning electron micrograph, backscattered image

Note: the data suffer from interference of adjacent phases and is provided for information, and absolute values should be treated with caution. Some attempt has been made at phase identity.

Lab ID	particle ID	Type	Ni K	Cr K	Co K	Mo L	W L	Ti K	Al K	Ta L	Nb L	Zr L	Re L	Y L
G13/6-Z	spot 1	γ	56.1	20.2	9.3	0.2	1.3	1.9	10.9	0.1	0.0	0.0	0.0	0.0
G13/6-Z	spot 2	γ	54.6	20.1	10.7	0.4	1.2	1.7	11.2	0.0	0.0	0.0	0.1	0.0
G13/6-Z	spot 3	γ	51.9	22.1	10.1	0.4	0.9	1.4	12.8	0.2	0.0	0.0	0.2	0.0
G13/6-Z	spot 4	γ	39.1	34.7	13.6	1.2	1.0	1.4	8.3	0.4	0.0	0.0	0.3	0.0
G13/6-Z	spot 5	γ	42.0	31.2	12.3	0.8	0.8	1.4	11.2	0.0	0.0	0.0	0.3	0.0
G13/6-Z	spot 6	γ	54.3	17.6	9.2	0.6	0.9	1.6	15.5	0.2	0.0	0.0	0.1	0.0
G13/6-Z	spot 7	O.I.	44.8	27.3	13.2	0.1	0.8	0.9	12.3	0.0	0.0	0.0	0.7	0.0
G13/6-Z	spot 8	O.I.	51.8	22.2	12.1	0.2	1.3	1.1	10.5	0.0	0.0	0.0	0.8	0.0
G13/6-Z	spot 9	O.I.	46.9	29.0	10.5	0.1	0.8	1.1	10.8	0.0	0.0	0.0	0.7	0.0
G13/6-Z	spot 10	O.I.	48.5	24.3	11.7	0.1	1.4	1.0	12.1	0.3	0.0	0.0	0.6	0.0
G13/6-Z	spot 11	α	31.3	47.7	5.2	0.0	0.4	0.5	12.1	0.0	0.0	0.0	2.7	0.0
G13/6-Z	spot 12	α	24.3	58.9	4.5	0.0	1.3	0.7	6.4	0.0	0.0	0.0	3.9	0.0
G13/6-Z	spot 13	α	41.8	31.5	13.5	0.4	0.3	0.7	11.2	0.0	0.0	0.0	0.6	0.0
G13/6-Z	spot 14		62.3	7.6	7.5	0.0	0.6	1.1	20.1	0.0	0.0	0.0	0.3	0.5
G13/6-Z	spot 15		41.1	34.6	6.6	0.0	0.7	0.9	15.4	0.0	0.0	0.0	0.8	0.0
G13/6-Z	spot 16	β	53.3	6.2	6.6	0.1	0.5	0.3	32.8	0.0	0.0	0.0	0.2	0.0
G13/6-Z	spot 17	β	52.1	9.0	6.2	0.1	0.8	0.4	31.3	0.0	0.0	0.0	0.1	0.0
G13/6-Z	spot 18		52.1	11.9	7.0	0.0	0.2	0.5	27.9	0.0	0.0	0.0	0.4	0.0
G13/6-Z	spot 19	α	21.1	58.3	4.1	0.0	0.4	0.2	11.1	0.0	0.0	0.0	4.7	0.0
G13/6-Z	spot 20		8.0	79.8	2.8	0.0	0.1	0.2	2.8	0.0	0.0	0.0	6.3	0.0
G13/6-Z	spot 21	α	24.3	55.7	4.3	0.0	0.9	0.2	10.3	0.0	0.0	0.0	4.2	0.0
G13/6-Z	spot 22		15.0	68.2	3.4	0.0	1.4	0.2	5.4	0.0	0.0	0.0	6.4	0.0

5.5.3 Results – Thermal Exposure – Sample Sequence

5.5.3.1 Thermal Exposure at 850°C 4800 hours

1. The composition profile in Figure 5.5.9 a, shows a high concentration of cobalt at the interdiffusion zone. The aluminium in the coating is slightly lower than average at the outer and inner layers. The chromium profile in the coating suffers from scatter, but does appear to be high at the interdiffusion layer, gradually reducing towards the substrate level. The rhenium content in the coating is higher than average at a number of points through the section. The hardness profile shows that the coating hardness reaches a peak approximately at the centre of its cross-section. The hardness of the substrate is generally lower than that of the coating and is uniform.
2. The phases in the coating are β , γ , σ and γ , Figure 5.5.10 a-c, compositions given in Table 5.24. There is a relatively small amount of γ phase, (Figure 5.5.10 b). The γ appeared to contain a high proportion of yttrium, according to EDX data. The σ phase seems to be present in two different size groups (Figure 5.5.10 c). EDX data for the smaller size group (note 1 Table 5.24) suffer from some interference of overlapping phases, hence these data do not conclusively identify the phase as σ . However, the phase has the optical and etching characteristics of σ . The compositions of the phases are reasonably close to the predicted equilibrium compositions in Table 5.20. There is a band at the inner layer of the coating that appears to be depleted in the darkest phase (on backscattered electron imaging, Figure 5.5.9 c). This suggests depletion of the β phase is beginning to occur.
3. Auger analysis was carried out on some particles considered to be σ and some of these smaller particles. A simple quantitative analysis of relative amounts of nickel, chromium and cobalt was attempted to see if the proportions of each of these compared to EDX results for σ . Ni, Co and Cr are the major elements in σ phase. The peak heights on the Auger spectra for these three elements were measured, and a simple normalisation (to 100%) carried out. Two small particles were analysed, Figure 5.5.11 a, b and one particle of σ phase, Figure 5.5.11 c. Normalisation was also performed on sample EDX data for the same elements in σ , to enable comparison. The data are shown in Table 5.25. The results are not conclusive, but do show that chromium is the major element, without reaching the very high level that would suggest α phase. For very small particles, sample

drift or the analysis spot not being entirely in one phase may affect the data. The data in Table 5.25, along with the etching characteristics do suggest that these small particles are σ phase.

4. The interdiffusion zone consists of σ phase in a γ matrix, Figure 5.5.12 a-c. The σ is present in two morphologies, predominantly a needle like form but also the more equiaxed, globular form seen in the bulk coating. The needles tend to appear towards the substrate side of the interdiffusion zone, with some needles extending beyond into γ/γ substrate regions, Figure 5.5.12 a. At the interface with the coating there is a layer of σ particles, with some additional small particles bright on electron backscattered imaging. These latter particles were too small for EDX analysis in the system used, but the etching and imaging characteristics suggest rhenium containing α . There is an additional chromium rich phase (note 2), dark on secondary and very dark on backscattered electron imaging. The identity of this phase has not been determined, it may be a carbide or a form of α . An additional script like phase, note 3, was dark on secondary but mid grey on backscattered electron imaging. This latter phase is not therefore considered to be the same as note 2. Identification of the phase note 3 is more difficult as the particle size is too small for quantitative EDX analysis. These phases have not been analysed in detail in this research as they are present in small volume fraction, but could be the subject of further work. In the substrate below the interdiffusion zone, the γ phase from the coating begins to penetrate the substrate in a 'finger-like' form, Figure 5.5.9 b.

5.5.3.2 Thermal Exposure at 850°C 9600 hours

1. The composition profile (Figure 5.5.13) for chromium shows a more definable trend, being generally more high in the centre of the coating and depleted at the outer and inner layers before rising through the interdiffusion zone to the substrate level. The aluminium appears to have high and low bands in the coating that are converse to cobalt content. The rhenium content in the coating exhibits a broad peak with a maximum towards the centre of the section, a small peak is also evident on the coating side of the interdiffusion zone. The hardness profile within the coating shows a gradual increase from the mid-section toward the substrate reaching a peak on the coating side of the O.I. The substrate is softer than the coating. The interdiffusion zone has an intermediate hardness with respect to the coating and substrate.

2. Some banding in the coating, Figure 5.5.13 b, is beginning to occur. The β , γ , σ and γ phases persist, Figure 5.5.14 a-c. The compositions, Table 5.27, were similar to those at the previous exposure time. The depletion of the dark phase (considered to be β) at the inner layer is again evident, Figure 5.5.13 c.
3. In the interdiffusion zone, the σ (both forms) and γ are again present but the dark phase is not, Figure 5.5.15 a-c and Table 5.28. The compositions of the phases are given in Table 5.28. There is again a layer of σ particles at the interface with the interdiffusion zone, these particles being slightly higher in rhenium than the σ towards the substrate side. The penetration of γ phase from interdiffusion zone into the substrate is slightly more evident; these fingers now connect, Figure 5.5.13 b.

5.5.3.3 Thermal Exposure at 950°C 4800 hours

1. The composition profile after 4800 hours, Figure 5.5.16, shows aluminium depletion at outer and inner layers of the coating. The chromium profile again exhibits scatter in the coating, but was seen to be low on the substrate side of the interdiffusion zone. Cobalt content is converse to aluminium content. The rhenium appears to be slightly higher at the outer surface and at the interdiffusion layer. The hardness of the coating is reduced compared to that of the samples exposed at 850°C. The coating appears to have higher hardness toward the mid-section. There is now some variation in hardness on the substrate side of the interdiffusion zone. Figure 5.5.17 shows that the particles in the coating are much coarser at this temperature than at 850°C
2. The coating consists of four phases. β , σ and γ are present as at 850°C but γ is not evident, instead α is present as a major constituent rather than in the small amounts detected at 850°C. Both the α and σ contain rhenium, Table 5.29. Note that rhenium has a high atomic number and α and σ do not contain other heavy elements. Electron backscattered imaging of rhenium containing α and σ will therefore result in bright imaging of these particles, whereas α and σ that are deficient in rhenium will be relatively dark. Backscattered imaging, Figure 5.5.17, suggests the rhenium content of these two phases is consistent in the bulk coating.
3. The interdiffusion zone consists of γ and α , with a layer of rhenium containing α at the interface with the coating, Figure 5.5.18 a-c. EDX data, Table 5.30, and backscattered electron imaging, Figure 5.5.18 c, show that the α particles in the bulk of the zone have

varying rhenium content. The thin layer of α particles at the interface with the coating is again evident. This layer has a rhenium content in the region of 4 atom%. The penetration of phases into the substrate is again evident. This feature is more pronounced at 950°C than at 850°C, now having the appearance of an intergranular network below the interdiffusion zone, Figure 5.5.16 b. Backscattered electron imaging suggests that the α that is penetrating into the substrate (along with γ'), contains less rhenium than α that is closer to the coating.

4. Carbon analysis, Figure 5.5.19. As EDX data do not give information on carbon content, other microanalysis techniques were applied to selected particles that may have contained carbon. In particular, those particles containing elements known to combine with carbon, such as chromium were analysed. The particles described as α were subjected to wavelength dispersive analysis (WDS). Some WDS data (under the same conditions) for the substrate are provided for comparison in Table 5.31. WDS indicates that α particles at the interdiffusion layer and the coating, Figure 5.5.19 a,b contained noteworthy amounts of carbon relative to other phases. This was investigated further by Auger analysis.
5. Initial Auger analysis, Figure 5.5.20 was carried out on α particles, a γ' point and on $M_{23}C_6$ particles in the substrate. The carbon peaks for the $M_{23}C_6$ particles are typical for a carbide. The α particle also exhibits a carbon peak. However, the shape of this peak suggests that the particle is not a carbide, implying that the carbon is in solid solution. The γ' particle (which is adjacent to the measured α particle) exhibits minimal carbon, showing that the carbon peak for the α is not due to a surface film or preparation artefact. Further Auger analysis, Figure 5.5.21 did not conclusively confirm the previous results. These data indicate a carbon peak on the substrate side of the interdiffusion zone α that is more similar in appearance to that of $M_{23}C_6$, compare b and c to a, Figure 5.5.21. α in the coating does however exhibit a non-carbide type carbon peak, Figure 5.5.21 d.
6. The nature of the effect of carbon on coating and interdiffusion zone particles is considered to be as follows;
 - α in the coating contains carbon in solid solution
 - equiaxed Cr rich particles at interdiffusion zone are α particles, containing carbon in solid solution

- grain boundary Cr rich particles on substrate side of interdiffusion zone may be $M_{23}C_6$ carbides.

5.5.3.4 Thermal Exposure at 950°C 9600 hours

1. The pattern for the elements, Figure 5.5.22 a, is similar to that at 950°C 4800 hours. The composition profile in the coating again exhibits scatter. There is however, a discernible trend in the interdiffusion zone, which is higher in aluminium and lower in chromium than the substrate. The rhenium profile exhibits a number of high points in the coating. The magnitude of these high points reduces towards the interdiffusion layer. The hardness in the coating is now similar to that previously seen for the substrate. The hardness at the interdiffusion zone is noteworthy, the level being higher than either the coating or the substrate, tending to the substrate level going into the bulk of the material.
2. Banding through the section of the coating is evident, Figure 5.5.22 b, c. Overall, the phases β , σ , α and γ remain, Figure 5.5.23 a-c and Table 5.32. The banding appears to arise from two effects;
 - σ is present only in a band at the outer surface
 - α is deficient at the outer surface.
3. The proportion of β is low at the inner zone of the coating, moderate at the core, and beginning to deplete at the outer surface, Figure 5.5.22 c. This latter depletion is more apparent using optical microscopy which reveals a high proportion of the (optically) dark α phase, Figure 5.5.22 b.
4. The phases in the interdiffusion zone are again α and γ' , Figure 5.5.24 a-c and Table 5.33. The α particles closer to the coating appear to be higher in rhenium than those closer to the substrate, Figure 5.5.24 c. The intergranular penetration of the interdiffusion phases into the substrate is extensive, Figure 5.5.22 b.

5.5.3.5 Thermal Exposure at 950°C 12000 hours

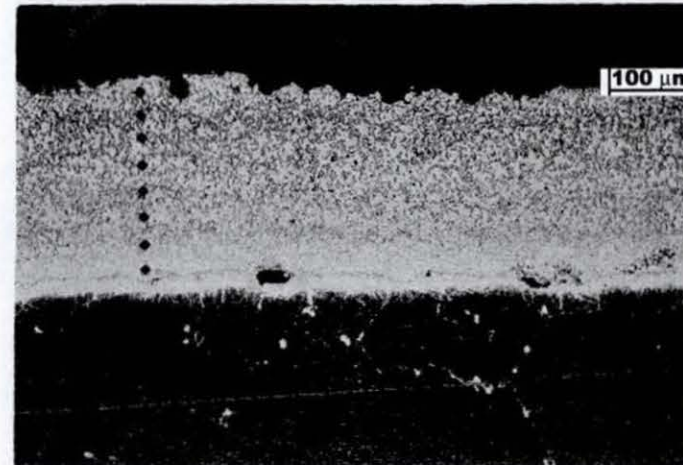
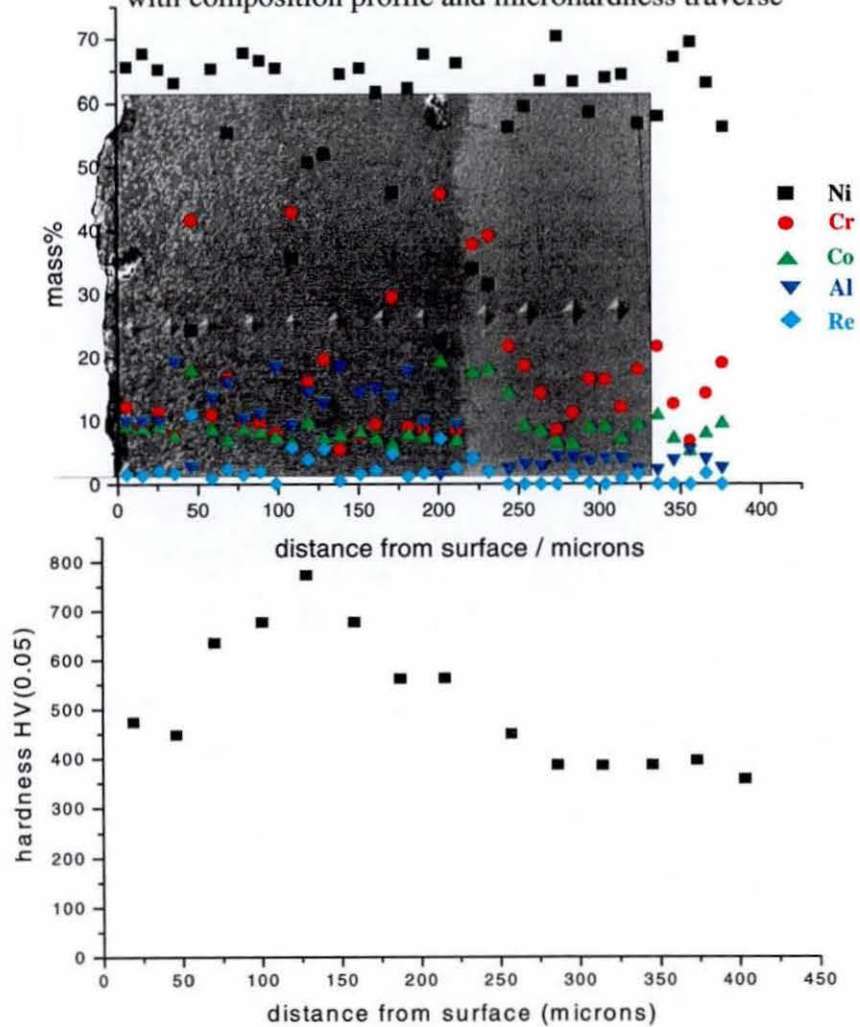
1. The composition profile for the elements, Figure 5.5.25 a, shows some discernible characteristics. The aluminium is depleted at the outer and inner zones of the coating, and is higher in the interdiffusion zone than in the base material. The chromium is depleted at the core of the coating and on the substrate side of the interdiffusion zone. The average rhenium content near the outer surface is slightly higher than at the core.

There are some high points in rhenium content through the coating, and a small peak on the substrate side of the interdiffusion zone. The hardness at the interdiffusion zone is significantly less than either the coating or the substrate.

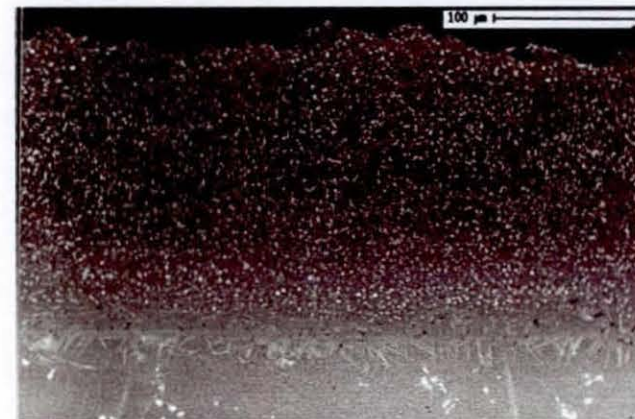
2. The phases in Figure 5.5.26 a-c (with Table 5.34) again show banding in the coating, Figure 5.5.25 c. The layers are similar to those at 950°C 9600 hours, but with greater depletion of β phase;
 - σ is present only in a band at the outer surface
 - α is deficient at the outer surface.
3. The proportion of β is low at the inner zone of the coating, moderate at the core, and beginning to deplete at the outer surface.
4. The interdiffusion zone again contains α and γ , Figure 5.5.27 a-c and Table 5.35. The α phase in the interdiffusion zone forms a more uniform layer than previous exposure times at this temperature and is rhenium containing. The α penetrating into the substrate remains rhenium deficient, Figure 5.5.27 c.

Figure 5.5.9 G13/2-W exposed at 850°C for 4800 hours – coating - interdiffusion - substrate

a. Scanning electron micrograph, secondary image with composition profile and microhardness traverse

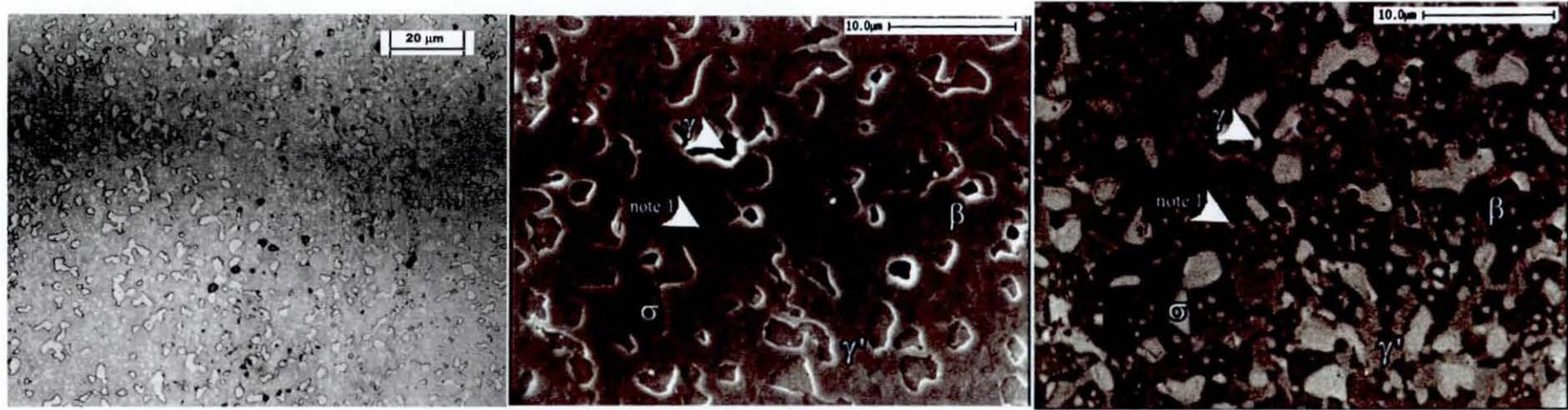


b. Optical bright field



c. Scanning electron micrograph, backscattered image

Figure 5.5.10 G13/2-W exposed at 850°C for 4800 hours – coating characteristics



a. Optical bright field

b. Scanning electron micrograph,
secondary image

c. Scanning electron micrograph,
backscattered image

Table 5.24 Typical EDX composition data, atom%

	Ni K	Cr K	Co K	Mo L	W L	Ti K	Al K	Ta L	Nb L	Zr L	Re L	Y L
β	51.1	6.2	6.1	0	1.3	0	35	0	0	0	0.3	0
γ	57	11.7	7.5	0	1.5	0.1	21.8	0	0	0	0.4	0
γ	58.0	13.7	6.3	0	0.9	0.2	8.6	0	0	0	0.6	11.7
σ	13.1	61.8	19.9	0	0.9	0	1.3	0	0	0	3	0
Note 1	17	65.7	4.4	0	0	0	9.7	0.1	0	0	2.9	0

Figure 5.5.11 Auger spectroscopy on G13/2-W coating particles ‘note 1’

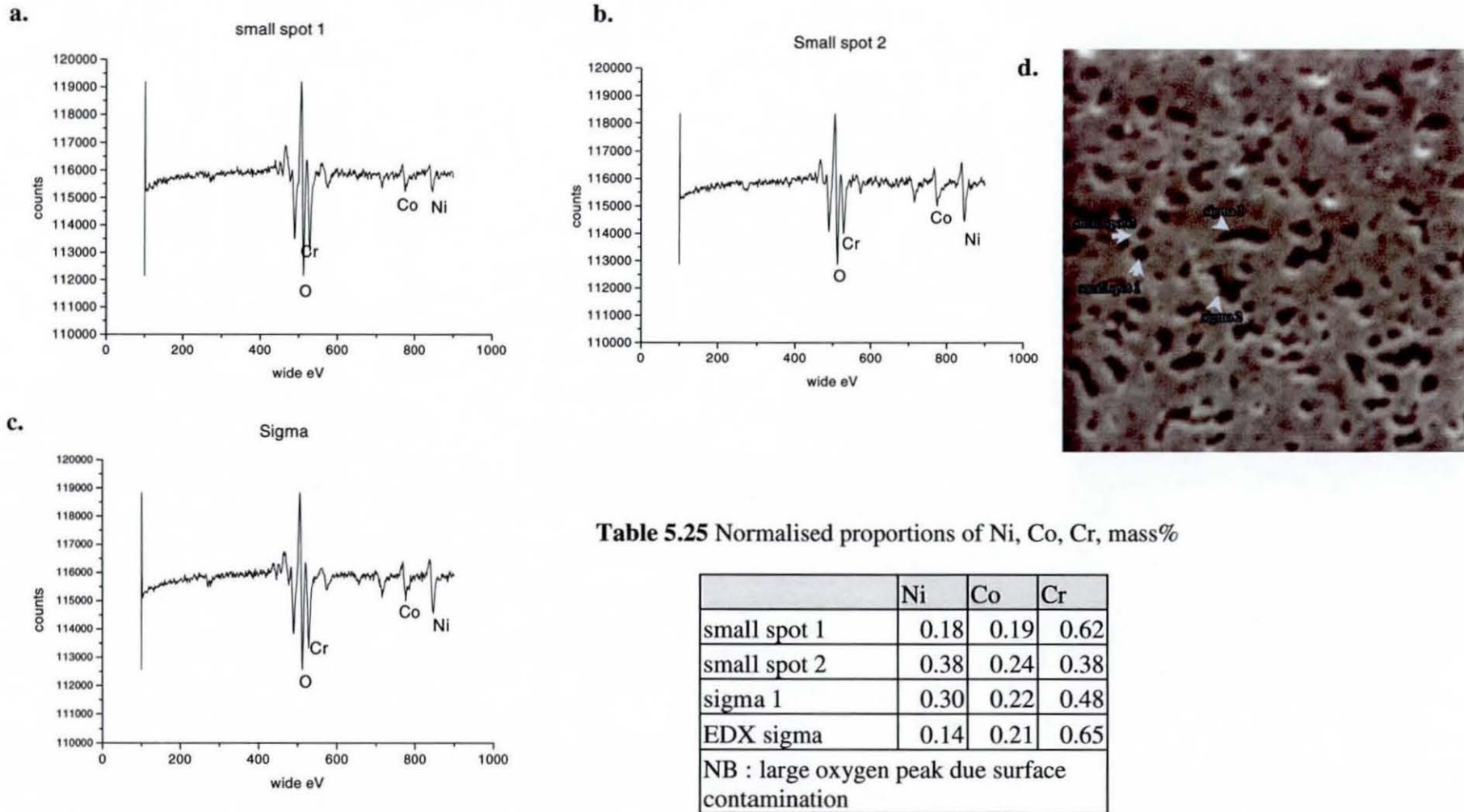
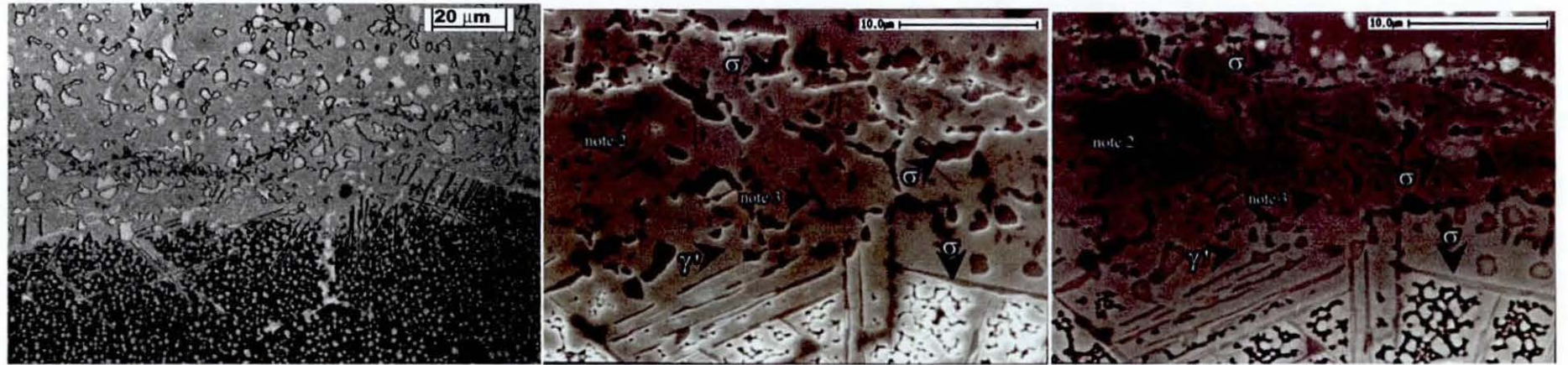


Figure 5.5.12 G13/2-W exposed at 850°C for 4800 hours – interdiffusion characteristics



a. Optical bright field

b. Scanning electron micrograph, secondary image

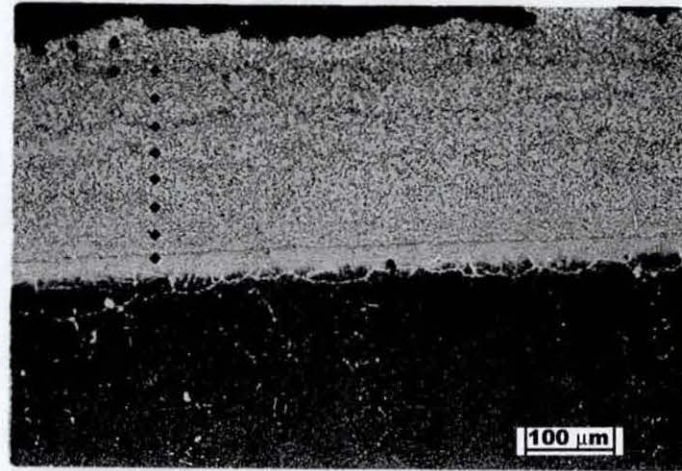
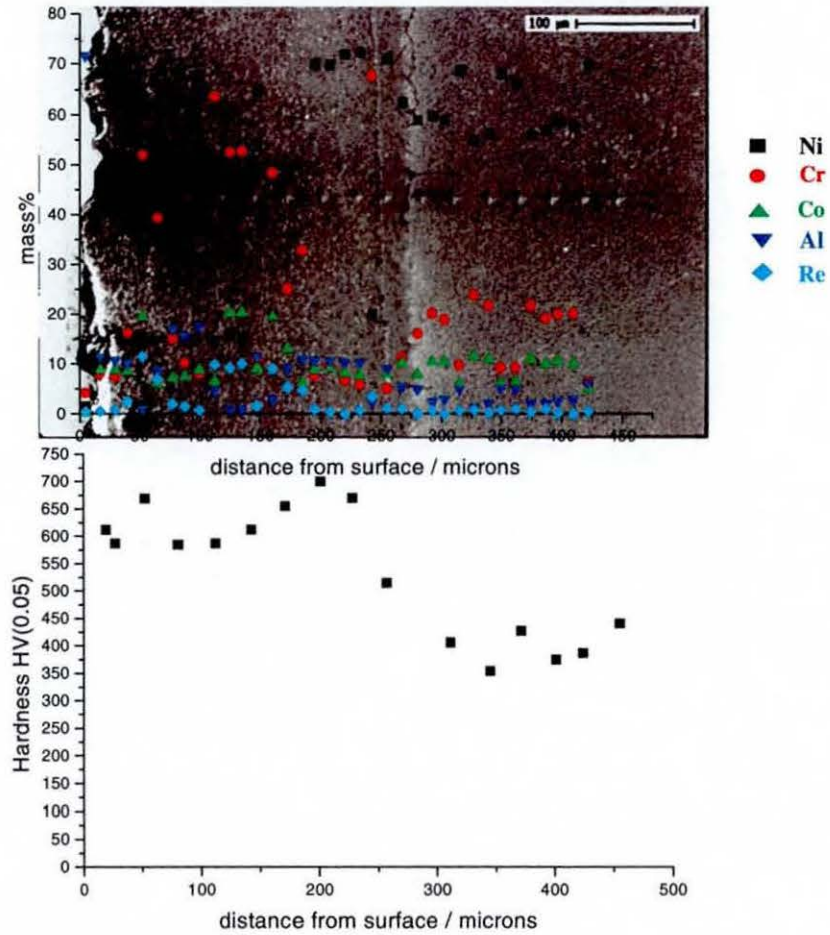
c. Scanning electron micrograph, backscattered

Table 5.26 Typical EDX composition data, atom%

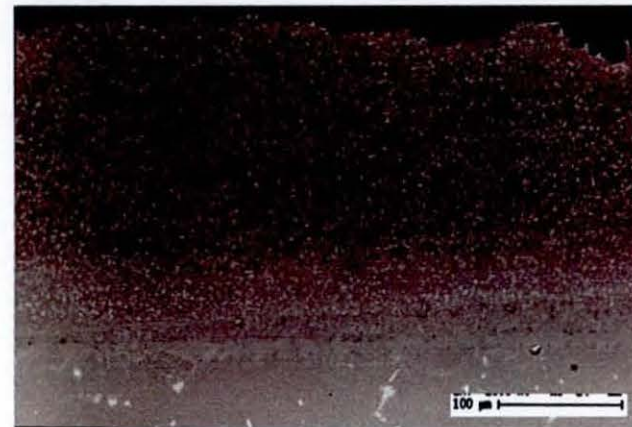
	Ni K	Cr K	Co K	Mo L	W L	Ti K	Al K	Ta L	Nb L	Zr L	Re L	Y L
γ	58.5	10.6	8.1	0.1	1.7	1.8	18.7	0	0	0	0.3	0
σ equiaxed	15.7	59.2	20.4	0.7	1.4	0.3	1.7	0	0	0	0.6	0
σ needle	16.1	57.4	20.8	2.2	1.5	0.5	1.1	0	0.3	0	0.2	0
Note 2 (dark phase)	20.0	69.9	3.1	0	0.9	0.6	5.1	0	0	0	0.4	0
σ layer	26.0	49.8	19.0	0.7	0.6	0.7	1.5	0.1	0	0	1.5	0

Figure 5.5.13 G13/2-X exposed at 850°C for 9600 hours – coating - interdiffusion - substrate

a. Scanning electron micrograph, secondary image with composition profile and microhardness traverse

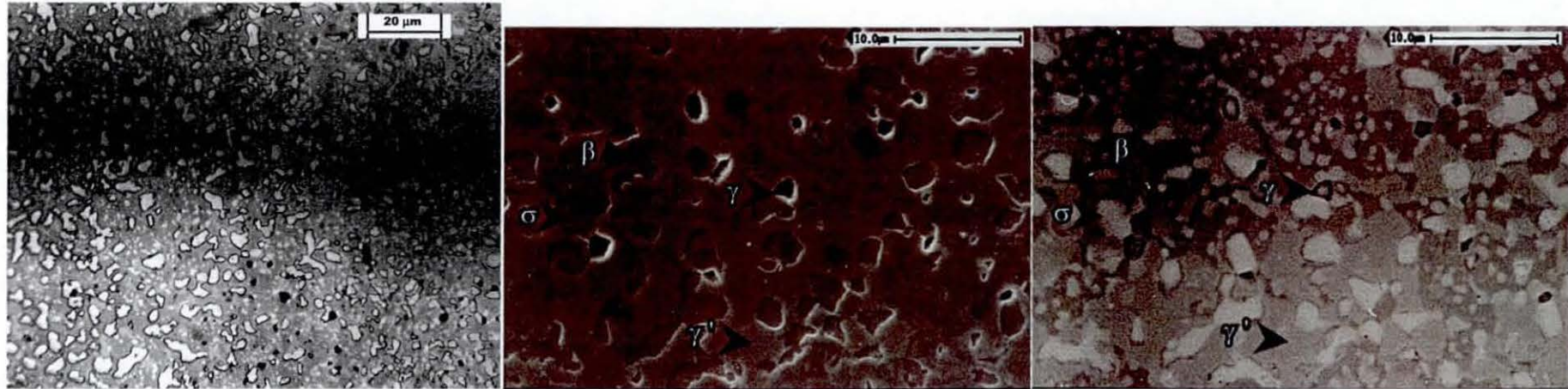


b. Optical bright field



c. Scanning electron micrograph, backscattered

Figure 5.5.14 G13/2-X exposed at 850°C for 9600 hours – coating characteristics



a. Optical bright field

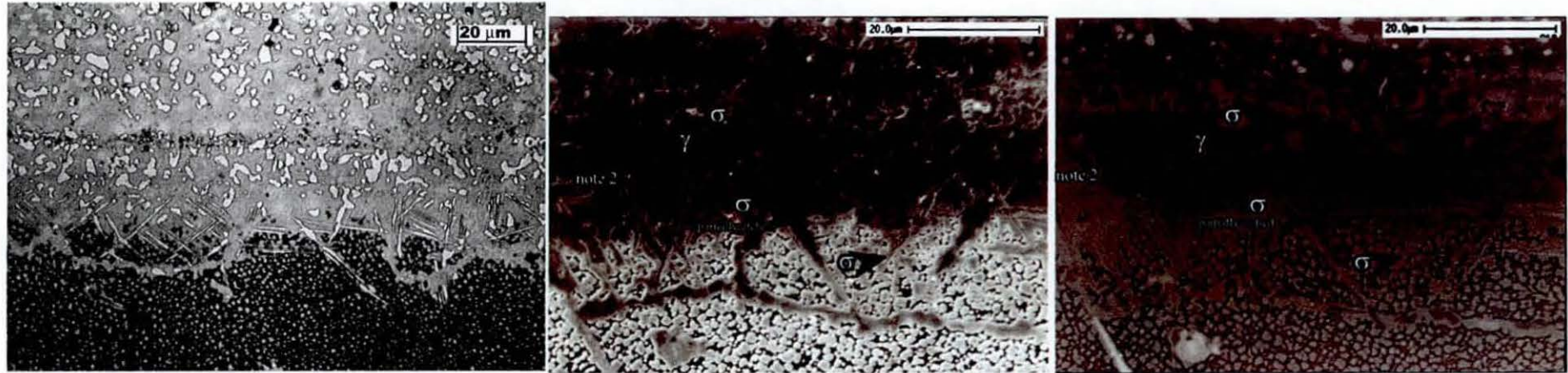
b. Scanning electron micrograph,
secondary image

c. Scanning electron micrograph,
backscattered image

Table 5.27 Typical EDX composition data, atom%

	Ni K	Cr K	Co K	Mo L	W L	Ti K	Al K	Ta L	Nb L	Zr L	Re L	Y L
β	55.6	6.4	6.4	0.1	0.6	0.2	30.2	0.2	0	0	0.3	0.1
γ	58.9	13.8	5.7	0.2	0.2	0.2	10.1	0	0	0	0.4	10.5
γ'	64.7	8.0	7.7	0	0.2	0.3	18.8	0	0	0	0.3	0
σ	14.1	61.0	20	0	0	0	1.6	0	0	0	3.3	0

Figure 5.5.15 G13/2-X exposed at 850°C for 9600 hours – interdiffusion characteristics



a. Optical bright field

b. Scanning electron micrograph,
secondary image

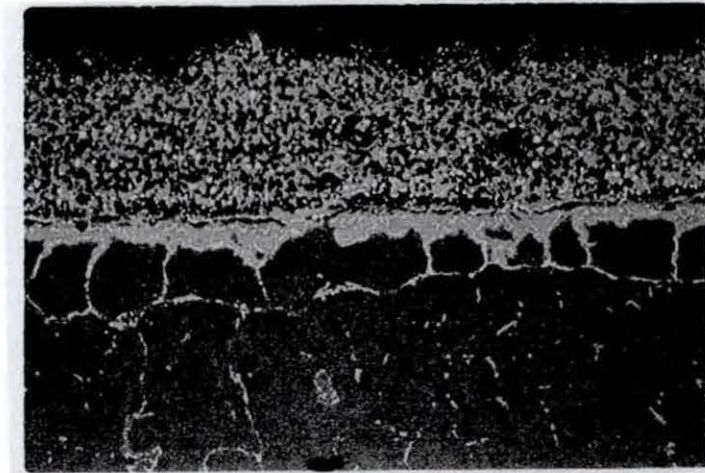
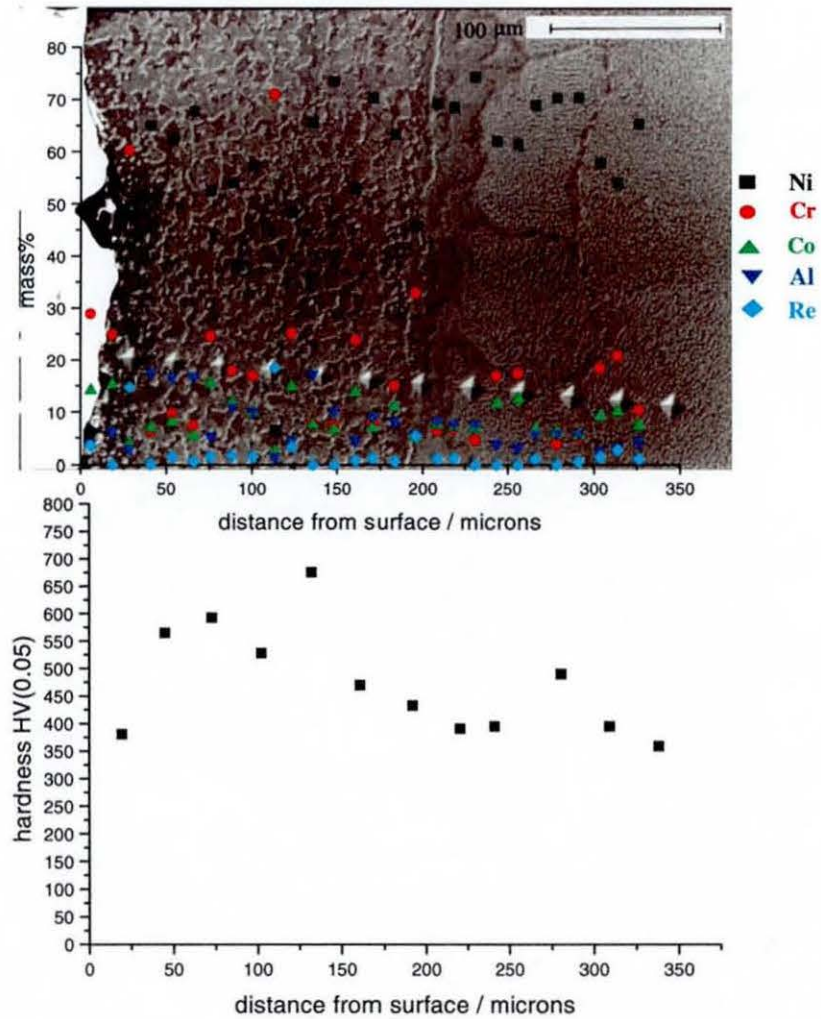
c. Scanning electron micrograph,
backscattered image

Table 5.28 Typical EDX composition data, atom%

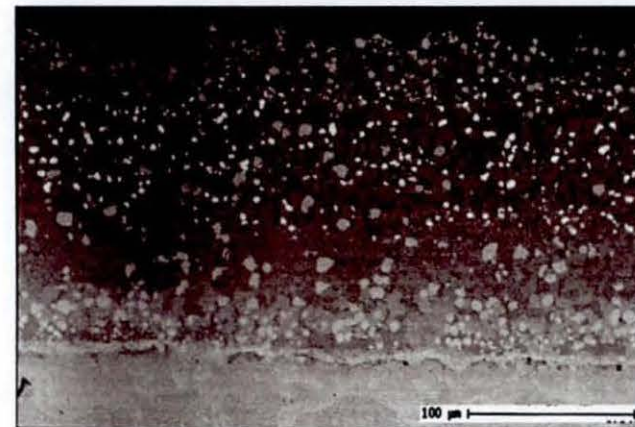
	Ni K	Cr K	Co K	Mo L	W L	Ti K	Al K	Ta L	Nb L	Zr L	Re L	Y L
γ	63.1	4	6.6	0	1.1	4.6	15	0.3	0	0	0.3	0
σ	27.5	47.6	17.7	2.5	1.6	1.3	1.2	0.2	0	0	0.2	0
σ layer	14.6	60.3	20.9	0.6	0.6	0.2	1.5	0	0	0	1.3	0

Figure 5.5.16 G13/4-Y exposed at 950°C for 4800 hours – coating - interdiffusion - substrate

a. Scanning electron micrograph, secondary image with composition profile and microhardness traverse

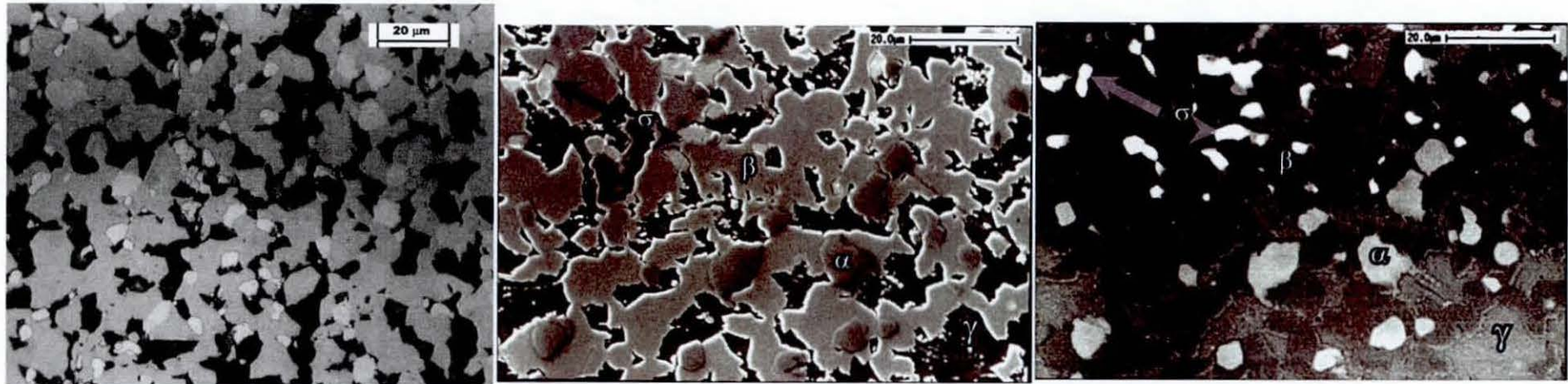


b. Optical bright field



c. Scanning electron micrograph, backscattered

Figure 5.5.17 G13/4-Y exposed at 950°C for 4800 hours – coating characteristics



a. Optical bright field

b. Scanning electron micrograph, secondary image

c. Scanning electron micrograph, backscattered image

Table 5.29 Typical EDX composition data, atom%

	Ni K	Cr K	Co K	Mo L	W L	Ti K	Al K	Ta L	Nb L	Zr L	Re L	Y L
β	51.6	8.2	5.8	0.1	1.4	0.2	32.4	0	0	0	0.3	0
γ	45.4	28.7	13.7	0.2	1.6	0.3	9.3	0	0	0	0.8	0
α	4.6	85.5	2.2	0	0.8	0	1.4	0.3	0	0	5.2	0
σ	15.6	57.9	14.1	0	1.4	0	2.4	0	0	0	8.7	0

Figure 5.5.18 G13/4-Y exposed at 950°C for 4800 hours – interdiffusion characteristics

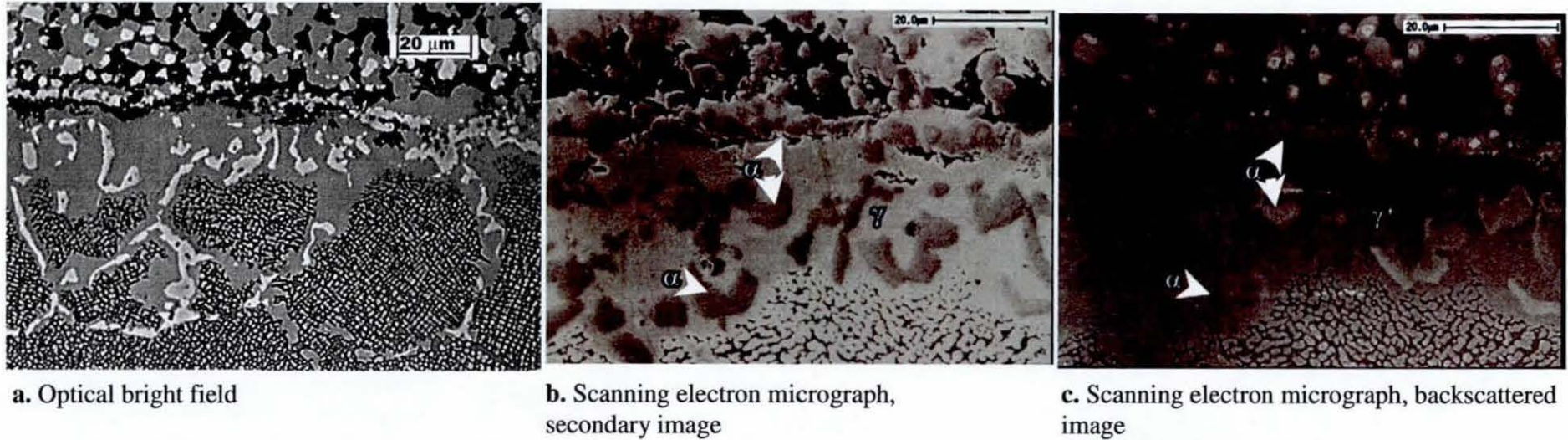
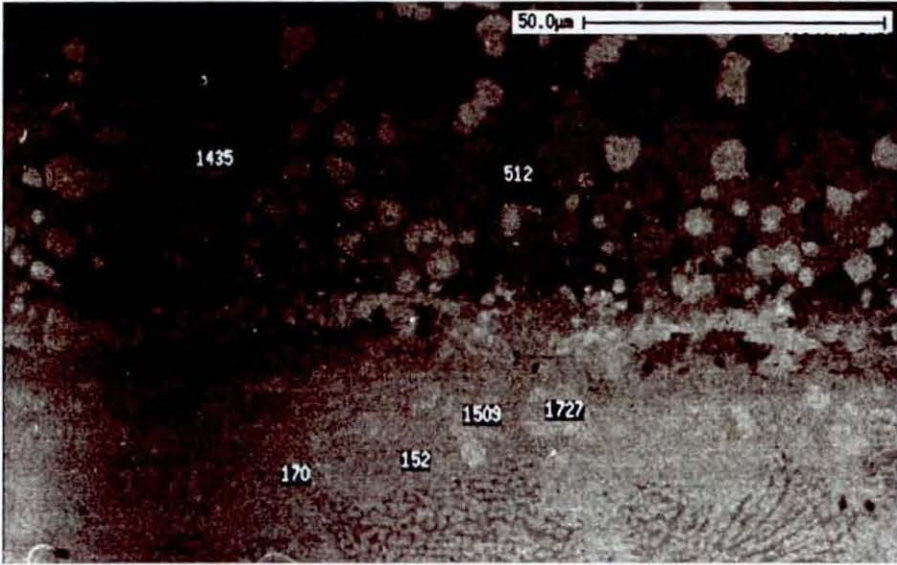


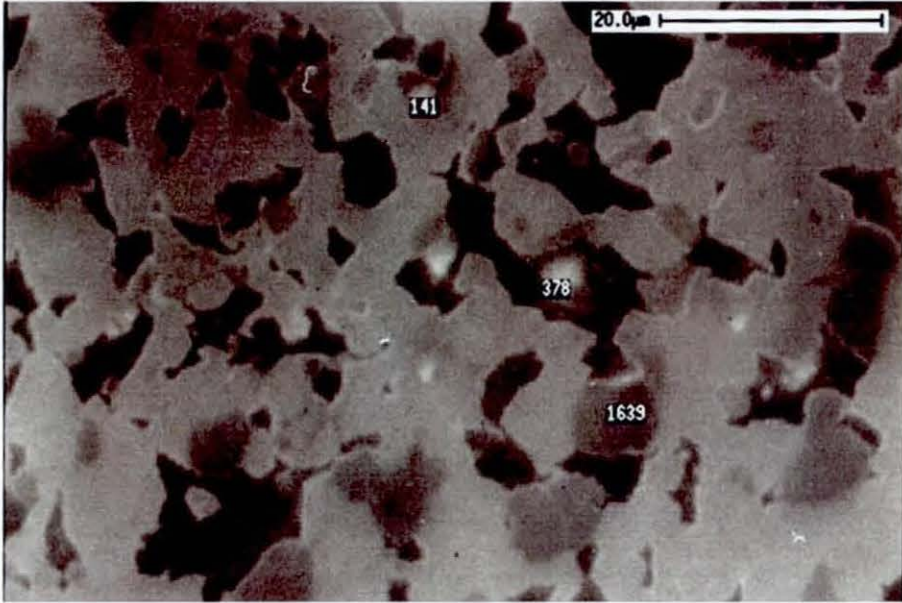
Table 5.30 Typical EDX composition data, atom%

	Ni K	Cr K	Co K	Mo L	W L	Ti K	Al K	Ta L	Nb L	Zr L	Re L	Y L
γ	64.1	5.9	6.2	0	2	2.7	18.7	0	0	0	0.3	0
α	5.3	87.7	2	0.3	1.5	0.1	1	0	0	0	2.1	0
α layer	4.8	86.2	2.3	0	1.2	0.1	1.1	0.2	0	0	4.1	0

Figure 5.5.19 G13/4-Y wavelength dispersive analysis for carbon



a. scanning electron micrograph, backscattered imaging data – wavelength dispersive energy counts / 10 sec for carbon



b. scanning electron micrograph, secondary imaging data – wavelength dispersive energy counts / 10 sec for carbon

Table 5.31 Typical WDS data for carbon in IN738LC substrate (counts / 10 sec)

$M_{23}C_6$	1888
γ/γ' matrix	260-339

Figure 5.5.20 G13/4-Y exposed at 950°C for 4800 hours – Auger analysis for carbon

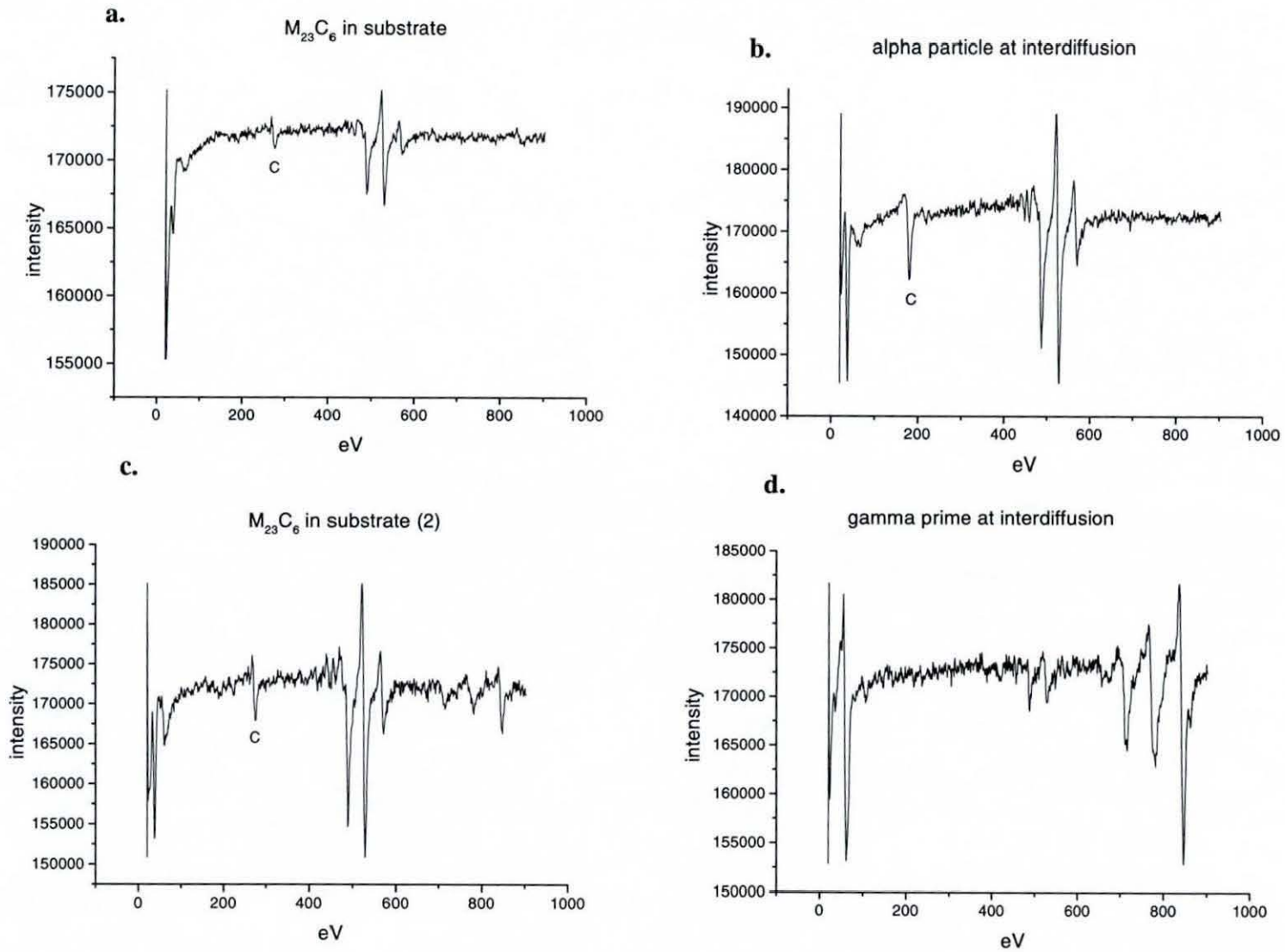


Figure 5.5.21 G13/4-Y exposed at 950°C for 4800 hours – Auger analysis for carbon

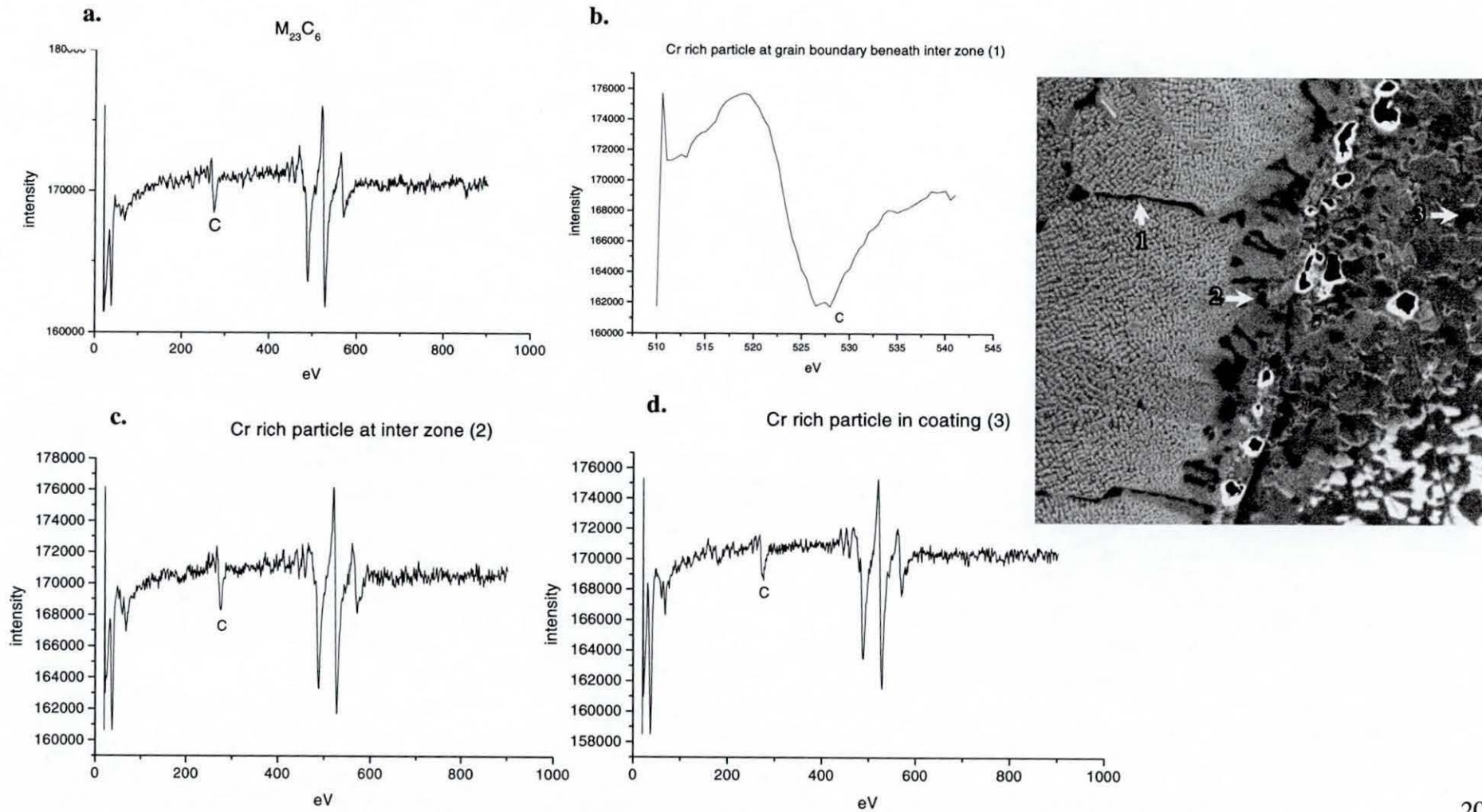
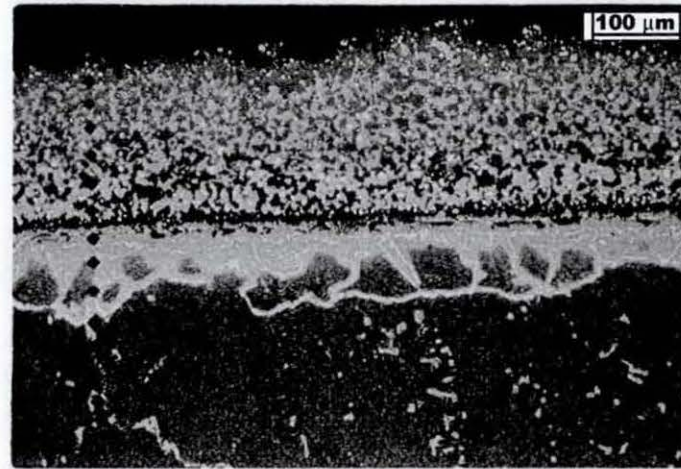
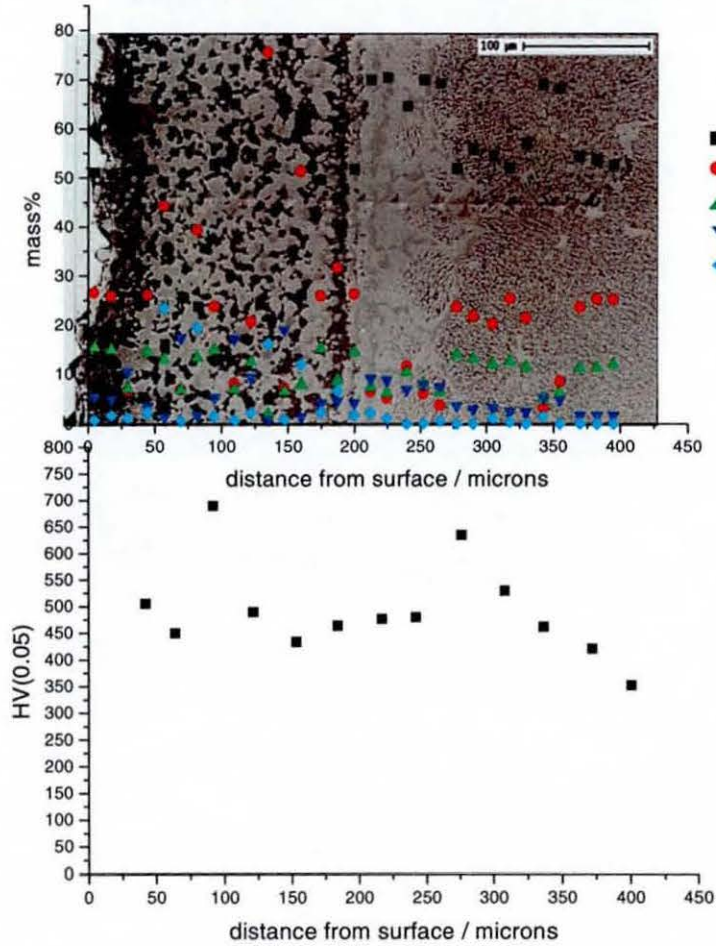
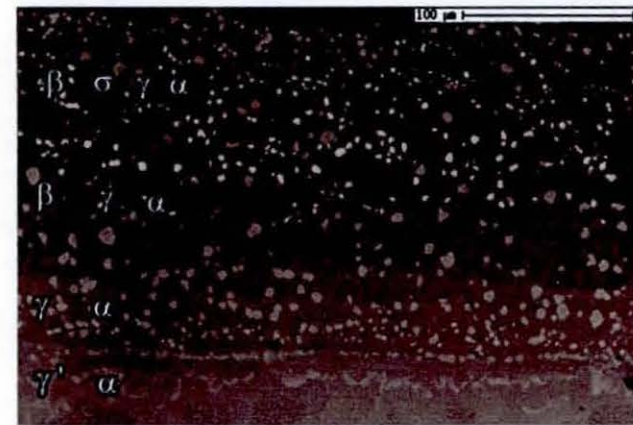


Figure 5.5.22 G13/5-W exposed at 950°C for 9600 hours – coating - interdiffusion - substrate

a. Scanning electron micrograph, secondary image with composition profile and microhardness traverse

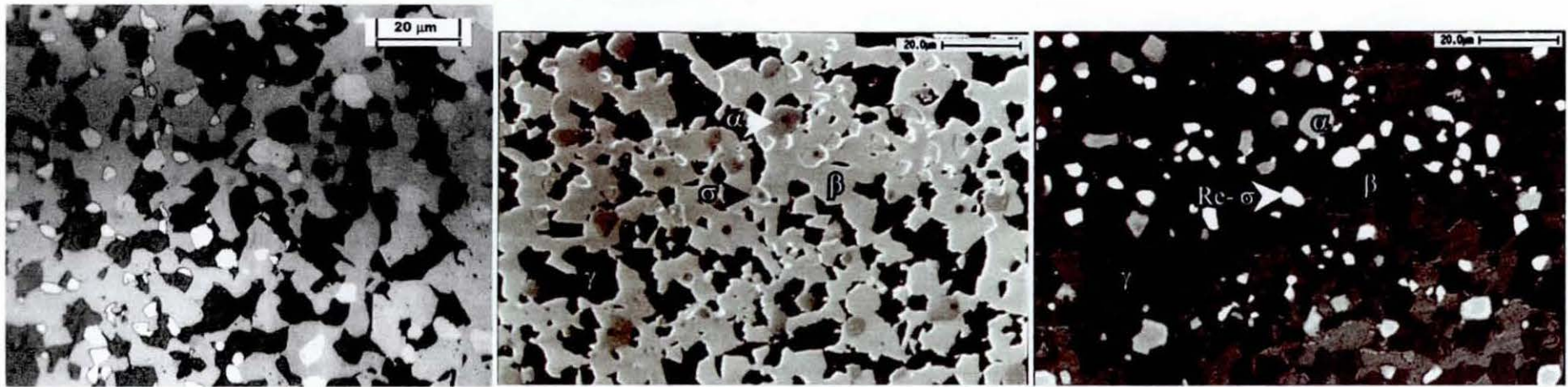


b. Optical bright field



c. Scanning electron micrograph, backscattered

Figure 5.5.23 G13/5-W exposed at 950°C for 9600 hours – coating characteristics



a. Optical bright field

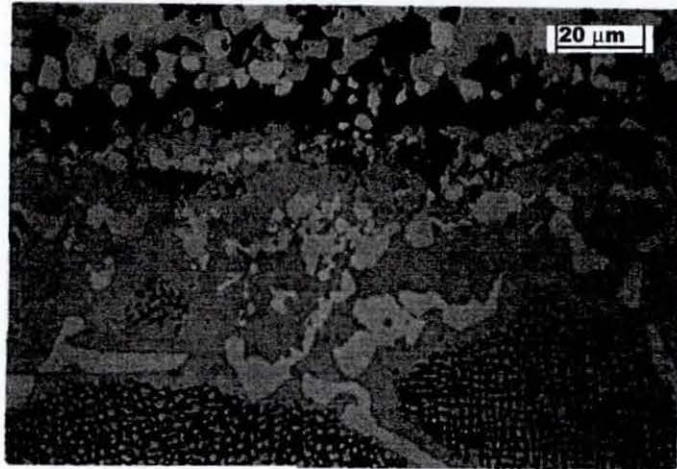
b. Scanning electron micrograph,
secondary image

c. Scanning electron micrograph,
backscattered image

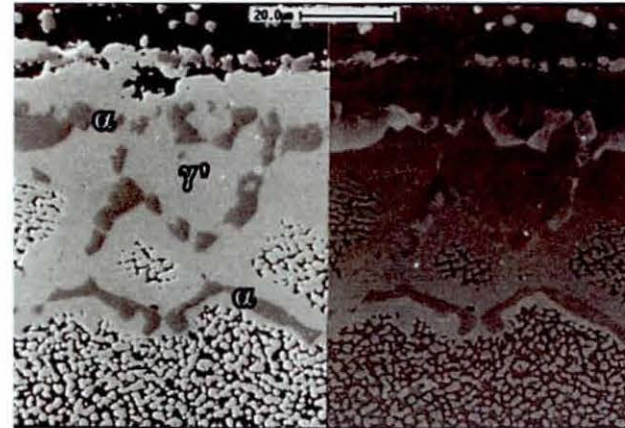
Table 5.32 Typical EDX composition data, atom%

	Ni K	Cr K	Co K	Mo L	W L	Ti K	Al K	Ta L	Nb L	Zr L	Re L	Y L
β	58.2	6.5	5.9	0	0.36	0.3	28.6	0	0	0	0.14	0
γ	47.5	27.9	14.1	0.22	0.8	0.22	8.2	0	0	0	0.92	0
α	5	85.5	2.4	0	0.43	0.04	0.9	0.16	0	0	5.6	0
σ	15.8	57.9	14.4	0	0.86	0	2.15	0.03	0	0	8.8	0

Figure 5.5.24 G13/5-W exposed at 950°C for 9600 hours – interdiffusion characteristics



a. Optical bright field



b. Scanning electron micrograph, secondary and backscattered images

Table 5.33 Typical EDX composition data, atom%

	Ni K	Cr K	Co K	Mo L	W L	Ti K	Al K	Ta L	Nb L	Zr L	Re L	Y L
γ	68.4	5.2	6.6	0	1.1	3.0	15.4	0.1	0.1	0	0.2	0
α	5.6	86.4	2.2	2.5	2.0	0.3	0.47	0	0	0	0.3	0
α (Re)	4.9	88.1	2.2	0.2	1.2	0.2	0.6	0	0	0	2.7	0

Figure 5.5.25 G13/5-X exposed at 950°C for 12000 hours – coating - interdiffusion - substrate

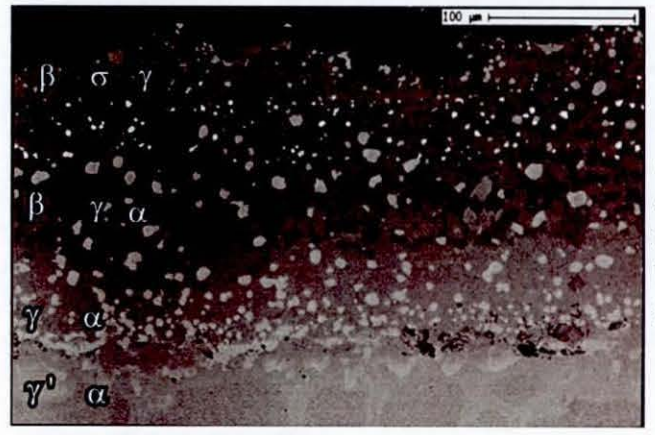
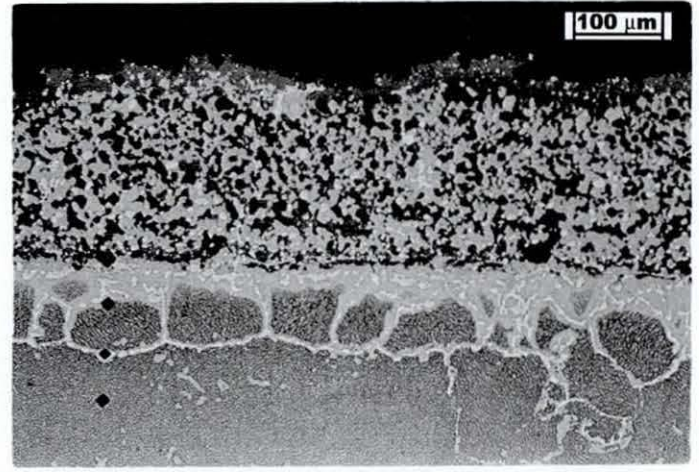
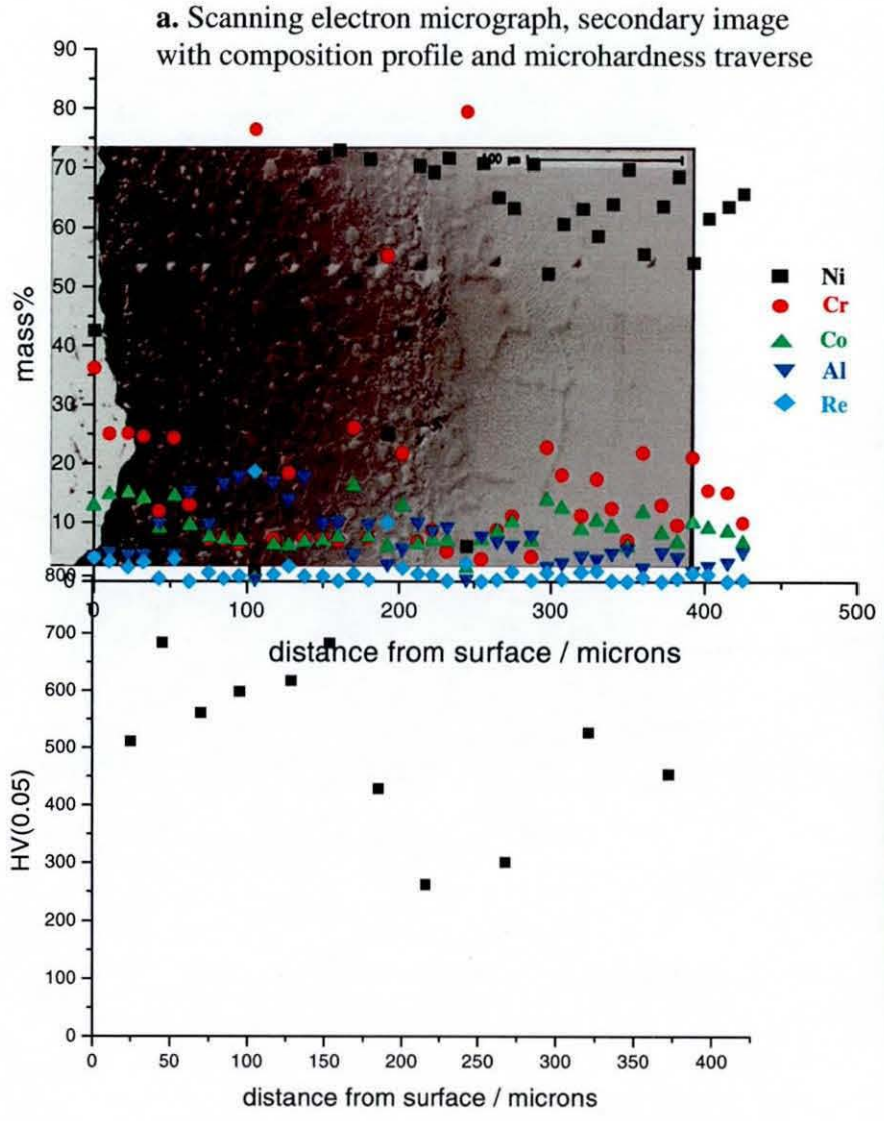
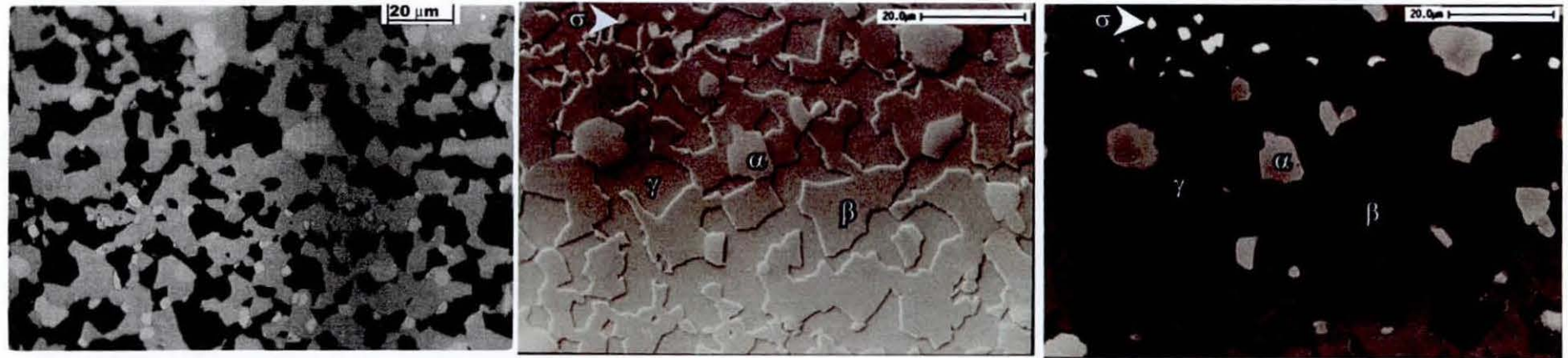


Figure 5.5.26 G13/5-X exposed at 950°C for 12000 hours – coating characteristics



a. Optical bright field

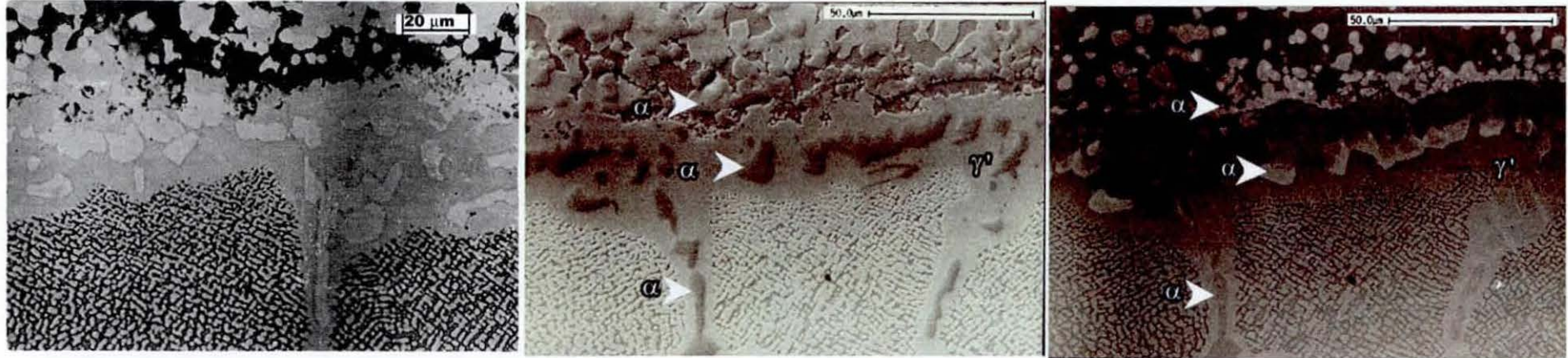
b. Scanning electron micrograph, secondary image

c. Scanning electron micrograph, backscattered image

Table 5.34 Typical EDX composition data, atom%

	Ni K	Cr K	Co K	Mo L	W L	Ti K	Al K	Ta L	Nb L	Zr L	Re L	Y L
α	4.7	85.3	2.4	0	0.4	0	1.5	0.1	0	0	5.6	0
γ	47.9	27.2	13.9	0.2	0.6	0.2	9.3	0.1	0	0	0.8	0
β	55.1	6.3	6.1	0	0.5	0.4	31.6	0	0	0	0	0
σ	17.3	54.7	14.5	0	1.2	0	2.3	0	0	0	10	0

Figure 5.5.27 G13/5-X exposed at 950°C for 12000 hours –interdiffusion characteristics



a. Optical bright field

b. Scanning electron micrograph, secondary image

c. Scanning electron micrograph, backscattered image

Table 5.35 Typical EDX composition data, atom%

	Ni K	Cr K	Co K	Mo L	W L	Ti K	Al K	Ta L	Nb L	Zr L	Re L	Y L
α	5.5	86.4	1.5	3.1	2.5	0.2	0.7	0	0	0	0	0
α layer	5.1	87.9	1.9	0	1	0	0.4	0.4	0	0	3.4	0
γ	63.4	8	6.1	0.2	0.3	2.7	19	0	0	0	0	0.3

5.5.4 Results – Thermal Exposure - Temperature and Time Sequence

Selected micrographs and composition have been taken from the data in section 5.5.3 and have been reproduced in temperature and time sequence. This is to facilitate the analysis of the effect of thermal exposure on microstructure and phase composition. The following is a summary of the data presented

Figure 5.5.28 Low magnification optical micrographs of the complete coating

- higher temperature results in much larger particle size
- extent of interdiffusion zone increases with thermal exposure
- penetration of interdiffusion phases in substrate

Figure 5.5.29 Low magnification backscattered electron micrographs of the complete coating

- α exists in bands at outer and inner layers of coating
- banding in the coatings, more evident at 950°C
- β depletion at outer and inner layer of thermal exposure, at both temperatures
- β depletion at inner layer more severe than at outer layer, both temperatures
- at 950°C, depletion of σ at core and inner layer of coating

Figure 5.5.30 High magnification backscattered electron micrographs of phases in coating

- at 850°C bulk coating phases are γ , β , σ (equiaxed) and small amount of γ
- at 950°C bulk coating phases are γ , β , σ (equiaxed) and α .

Figure 5.5.31 Phase map for coating

- at 850°C experimentally find γ , β , σ (and some γ), equilibrium prediction is γ , β , σ , α
- at 950°C experimentally find γ , β , σ and α , equilibrium prediction is γ , β , α

Table 5.36 EDX data for phases in coating

- rhenium content of σ appears to increase at higher exposure temperature
- γ contains high significant amount of yttrium

Figure 5.5.32 High magnification backscattered electron micrographs of phases in interdiffusion layer

At 850°C

- interdiffusion zone consists of γ and σ
- most σ is TCP needle form, some is equiaxed
- rhenium content of TCP form is lower than equiaxed form
- thin layer of small, equiaxed rhenium containing σ particles at interface between coating and interdiffusion layer

At 950°C

- interdiffusion zone consists of γ and α
- thin layer of small, equiaxed rhenium containing α particles at interface between coating and interdiffusion layer
- rhenium content of α in bulk interdiffusion zone varies
- interdiffusion phases penetrate into substrate

Figure 5.5.33 Phase map for interdiffusion layer

- at 850°C experimentally find γ and σ phases
- at 950°C experimentally find γ and α phases

Table 5.37 EDX data for phases in interdiffusion layer

- rhenium content of α does vary

Figure 5.5.28 Effect of thermal exposure on coating microstructure – optical micrographs

100 μm

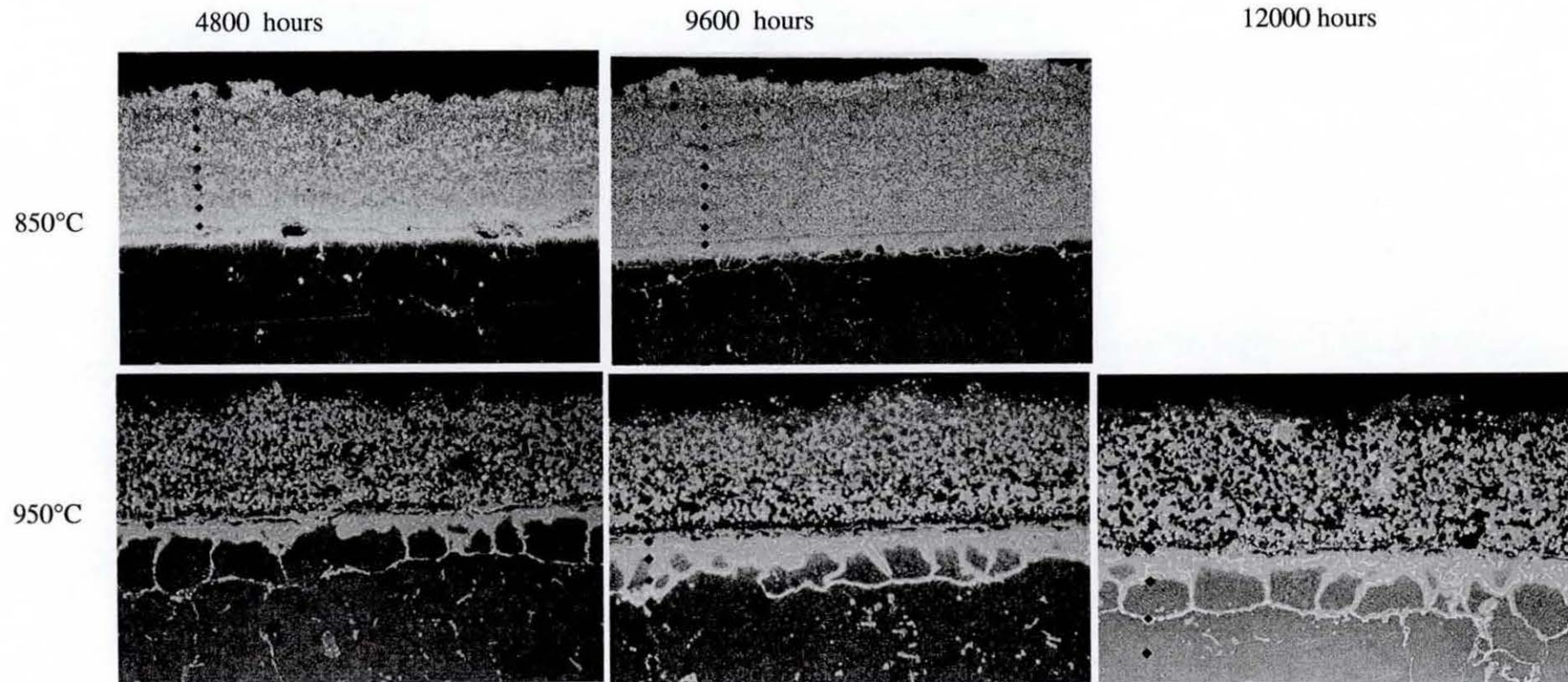


Figure 5.5.29 Effect of thermal exposure on coating microstructure – backscattered electron micrographs (magnification varies)

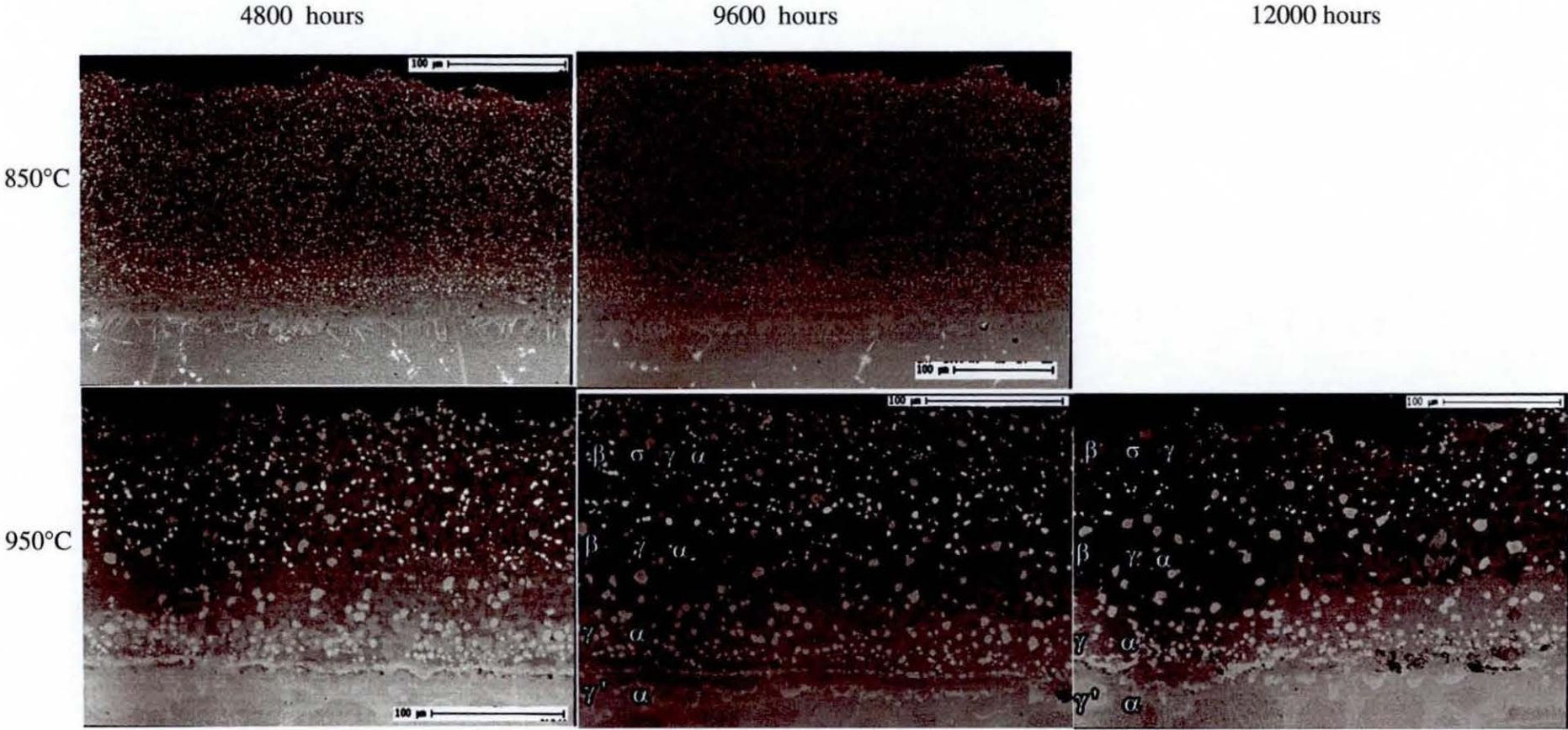


Figure 5.5.30 Effect of thermal exposure on core coating microstructure – backscattered electron micrographs (magnification varies)

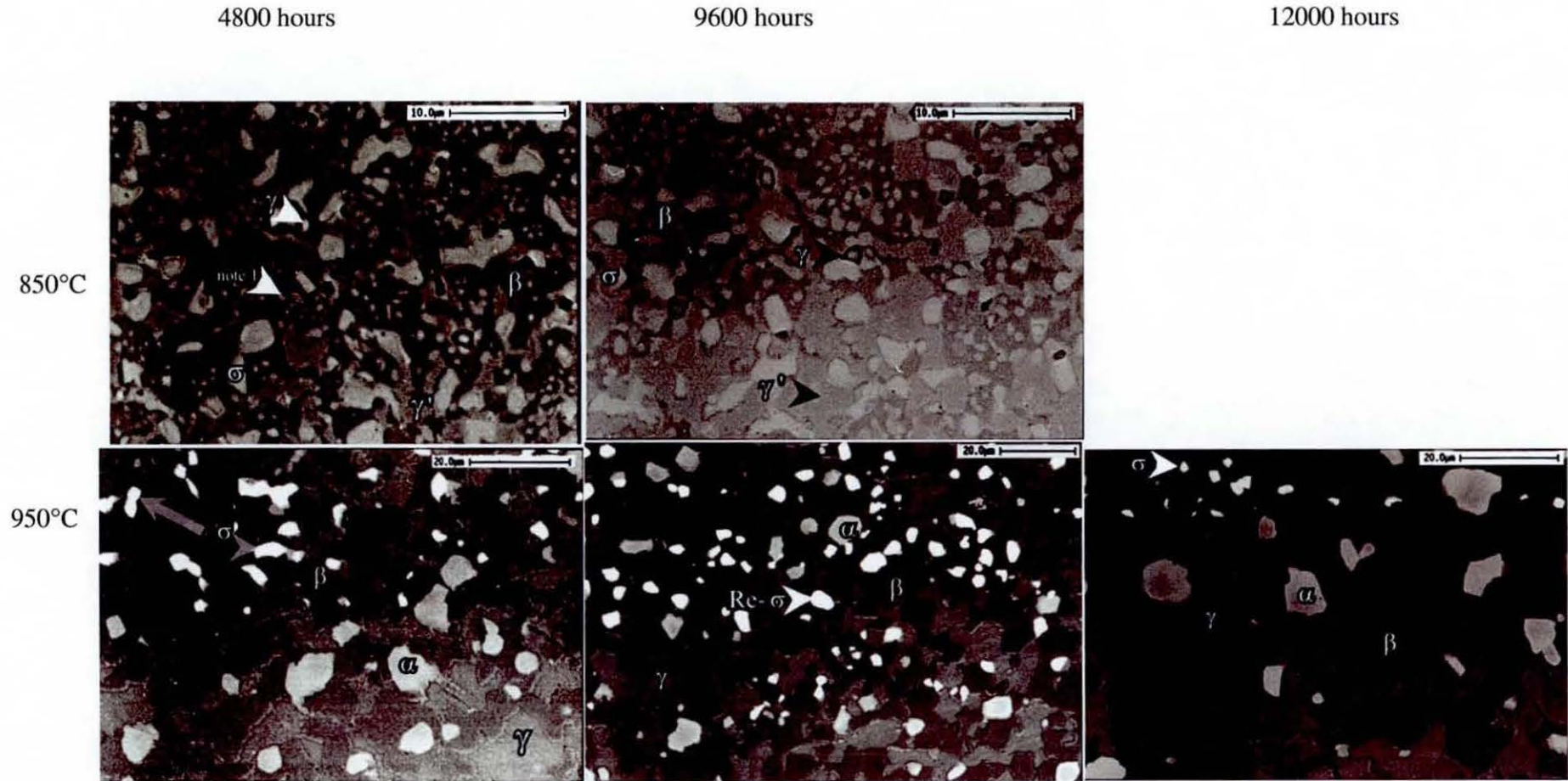
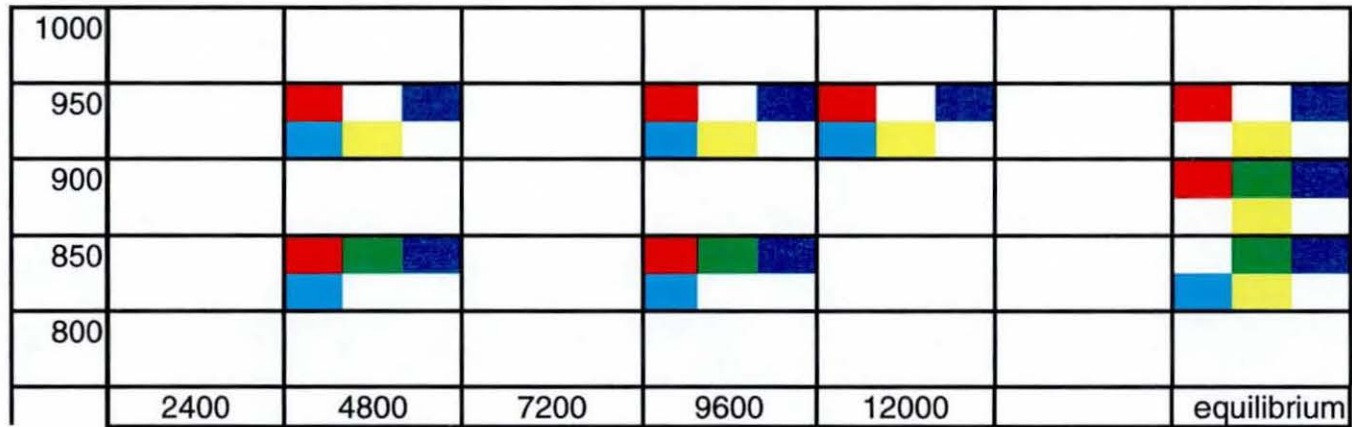


Figure 5.5.31 Phase map for SC2453 coating, experimentally determined at 850°C and 950°C, 4800 to 1200 hours, with equilibrium calculations at 850°C, 900°C and 950°C

key



temp / °C



time / hours

Table 5.36 Effect of thermal exposure on composition of bulk coating phases, EDX data, atom%

Phase	Temp/°C	Time/hrs	Ni K	Cr K	Co K	Mo L	W L	Ti K	Al K	Ta L	Nb L	Zr L	Re L	Y L
Alpha	850	4800	Not present											
Alpha	850	9600	Not present											
Alpha	950	4800	4.6	85.5	2.2	0.0	0.8	0.0	1.4	0.3	0.0	0.0	5.2	0.0
Alpha	950	9600	5.0	85.5	2.4	0.0	0.4	0.0	0.9	0.2	0.0	0.0	5.6	0.0
Alpha	950	12000	4.7	85.3	2.4	0.0	0.4	0.0	1.5	0.1	0.0	0.0	5.6	0.0
Beta	850	4800	51.1	6.2	6.1	0.0	1.3	0.0	35.0	0.0	0.0	0.0	0.3	0.0
Beta	850	9600	55.6	6.4	6.4	0.1	0.6	0.2	30.2	0.2	0.0	0.0	0.3	0.1
Beta	950	4800	51.6	8.2	5.8	0.1	1.4	0.2	32.4	0.0	0.0	0.0	0.3	0.0
Beta	950	9600	58.2	6.5	5.9	0.0	0.4	0.3	28.6	0.0	0.0	0.0	0.1	0.0
Beta	950	12000	55.1	6.3	6.1	0.0	0.5	0.4	31.6	0.0	0.0	0.0	0.0	0.0
Gamma	850	4800	58.0	13.7	6.3	0	0.9	0.2	8.6	0	0	0	0.6	11.7
Gamma	850	9600	58.9	13.8	5.7	0.2	0.2	0.2	10.1	0.0	0.0	0.0	0.4	10.5
Gamma	950	4800	45.4	28.7	13.7	0.2	1.6	0.3	9.3	0.0	0.0	0.0	0.8	0.0
Gamma	950	9600	47.5	27.9	14.1	0.2	0.8	0.2	8.2	0.0	0.0	0.0	0.9	0.0
Gamma	950	12000	47.9	27.2	13.9	0.2	0.6	0.2	9.3	0.1	0.0	0.0	0.8	0.0
Gamma prime	850	4800	57.0	11.7	7.5	0.0	1.5	0.1	21.8	0.0	0.0	0.0	0.4	0.0
Gamma prime	850	9600	64.7	8.0	7.7	0.0	0.2	0.3	18.8	0.0	0.0	0.0	0.30	0.0
Gamma prime	950	4800	Not present											
Gamma prime	950	9600	Not present											
Gamma prime	950	12000	Not present											
Sigma	850	4800	13.1	61.8	19.9	0.0	0.9	0.0	1.3	0.0	0.0	0.0	3.0	0.0
Sigma	850	9600	14.1	61.0	20.0	0.0	0.0	0.0	1.6	0.0	0.0	0.0	3.3	0.0
Sigma	950	4800	15.6	57.9	14.1	0.0	1.4	0.0	2.4	0.0	0.0	0.0	8.7	0.0
Sigma	950	9600	15.8	57.9	14.4	0.0	0.9	0.0	2.2	0.0	0.0	0.0	8.8	0.0
Sigma	950	12000	17.3	54.7	14.5	0.0	1.2	0.0	2.3	0.0	0.0	0.0	10.0	0.0

Figure 5.5.32 Effect of thermal exposure on interdiffusion layer- backscattered electron micrographs (magnification varies)

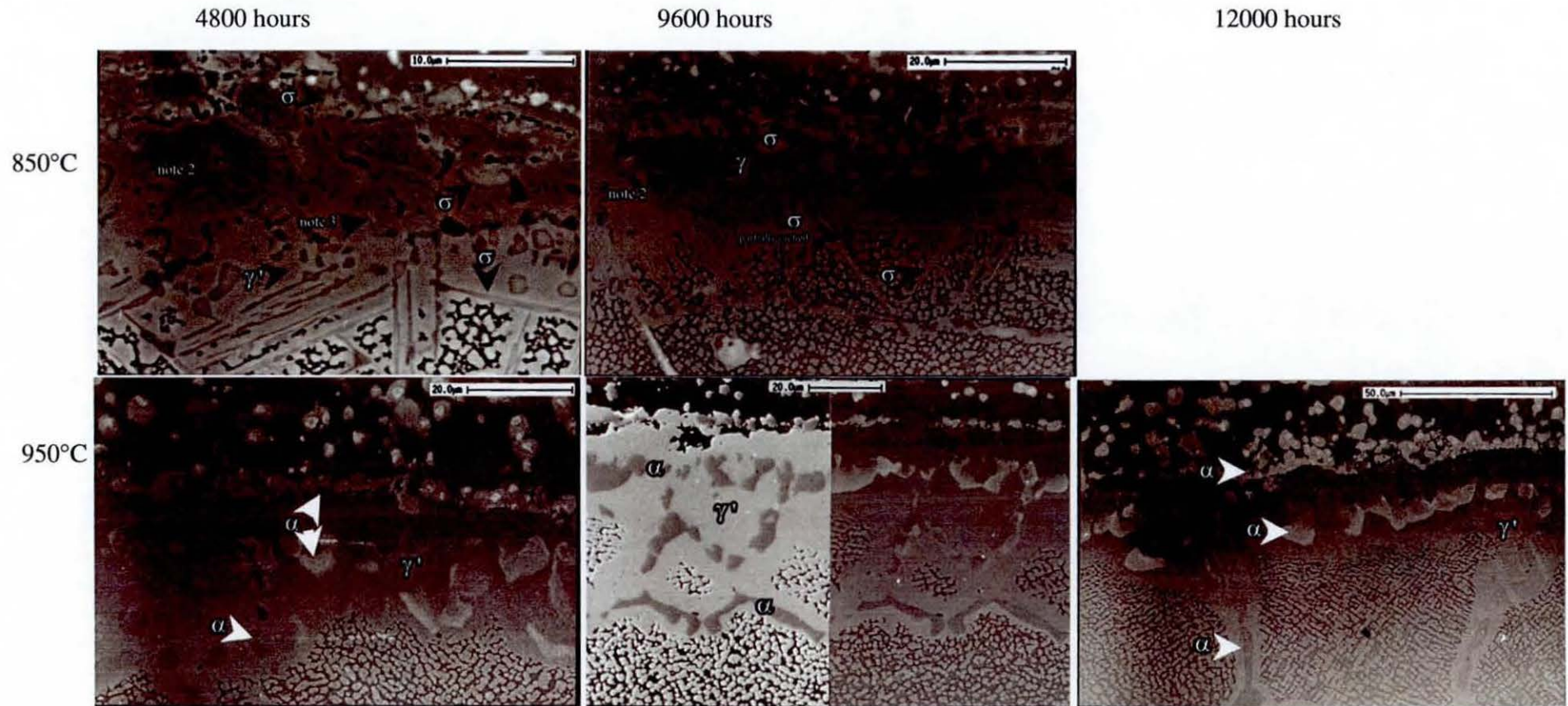
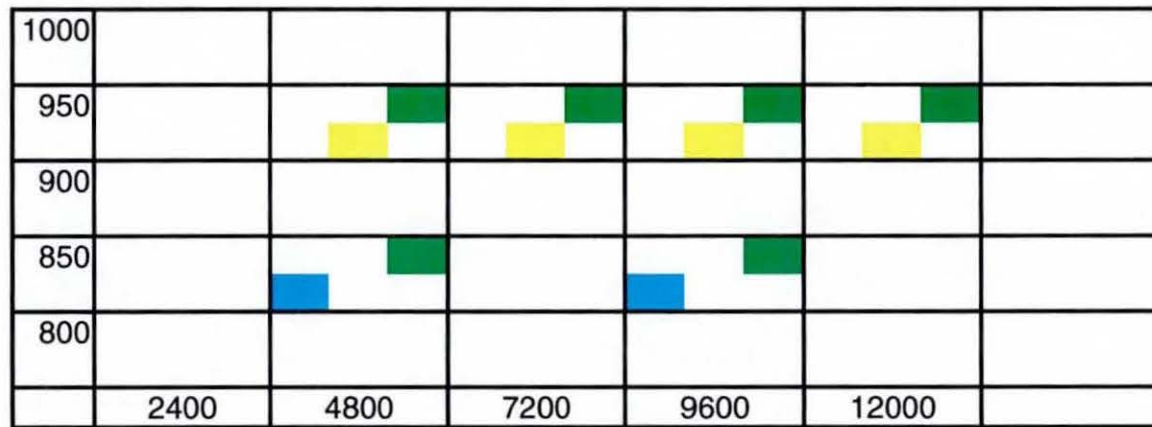


Figure 5.5.33 Phase map SC2453 interdiffusion layer, experimentally determined

key



temp / °C



time / hours

Table 5.37 Effect of thermal exposure on composition of bulk interdiffusion zone phases, EDX data, atom%

Phase	Temp°C	Time/hrs	Ni K	Cr K	Co K	Mo L	W L	Ti K	Al K	Ta L	Nb L	Zr L	Re L	Y L
Alpha	850	4800	Not present											
Alpha	850	9600	Not present											
Alpha	950	4800	5.3	87.7	2.0	0.3	1.5	0.1	1.0	0.0	0.0	0.0	2.1	0.0
Alpha	950	9600	5.6	86.3	2.2	2.5	2.0	0.4	0.5	0.0	0.0	0.0	0.3	0.0
Alpha	950	12000	5.5	86.4	1.5	3.1	2.5	0.2	0.7	0.0	0.0	0.0	0.0	0.0
Beta	850	4800	Not present											
Beta	850	9600	Not present											
Beta	950	4800	Not present											
Beta	950	9600	Not present											
Beta	950	12000	Not present											
Gamma	850	4800	Not present											
Gamma	850	9600	Not present											
Gamma	950	4800	Not present											
Gamma	950	9600	Not present											
Gamma	950	12000	Not present											
Gamma prime	850	4800	58.5	10.6	8.1	0.1	1.7	1.8	18.7	0.0	0.0	0.0	0.3	0.0
Gamma prime	850	9600	63.1	4.0	6.6	0.0	1.1	4.6	15.0	0.3	0.0	0.0	0.3	0.0
Gamma prime	950	4800	64.1	5.9	6.2	0.0	2.0	2.7	18.7	0.0	0.0	0.0	0.3	0.0
Gamma prime	950	9600	68.4	5.2	6.6	0.0	1.1	3.0	15.4	0.1	0.05	0.0	0.2	0.0
Gamma prime	950	12000	63.4	8.0	6.1	0.2	0.3	2.7	19.0	0.0	0.0	0.0	0.0	0.30
Sigma	850	4800	15.7	59.2	20.4	0.7	1.4	0.3	1.7	0.0	0.0	0.0	0.6	0.0
Sigma	850	9600	27.5	47.6	17.7	2.5	1.6	1.3	1.2	0.2	0.0	0.0	0.2	0.0
Sigma	950	4800	Not present											
Sigma	950	9600	Not present											
Sigma	950	12000	Not present											

5.5.5 Discussion

5.5.5.1 Coating

Compared with literature available on NiCoCrAlY coatings (such as RT122), there is much less on MCrAlY coatings that contain additions of rhenium. Czech *et al*^{38;44,44}, have carried out some investigations concentrating on mechanical properties with limited data being given on phases in the coating. Ellison⁷⁶ has carried out a relatively detailed study of a Sicoat 2453 / IN738 system. The data of these authors are useful for comparison.

The two temperatures 850°C and 950°C exhibit different characteristics with respect to particle size, phases present and banding. The coarsening of the particles at the higher temperature is expected, as higher input of energy results in larger particles growing at the expense of smaller ones. Some of the phase changes are governed by a tendency towards equilibrium, others are governed by changes in composition over time (due to inward and outward diffusion of elements). The coating is initially relatively homogenous with respect to phase distribution, with some α phase at the inner and outer layers. Thermal exposure has a number of effects on the coating, including;

- increasing particle size
- outer β depletion
- inner β depletion
- σ depletion at core and inner layers.

5.5.5.1.1 Outer β Depletion Layer

The depletion of β at the outer surface at 950°C will be due to loss of Al to the oxide layer. This can be illustrated by the equilibrium predictions that calculate depletion of β on reducing aluminium content, Figure 5.5.2. Czech³⁸ reports the presence of a rhenium containing α layer below the Al_2O_3 oxide, in a NiCoCrAlYRe coating (Al 16 and 24 atom%, Re 3atom%), on IN738LC, exposed at 1000°C for 3000 hours. Czech described less β depletion than for comparable samples without Re. No such layer was apparent at the outer surface in samples examined during the course of this research. Ellison⁷⁶ in his Sicoat 2453/ IN738 system does not report the presence a layer of rhenium rich particles at the outer surface (at 1000°C 9110 hours exposure) but does have an outer β depleted zone.

Despite the lack of such a layer at the outer surface in IPTME samples, the extent of β depletion in that region, whilst still evident, was less than in RT122. The general presence of rhenium containing particles may have contributed, particularly if the mechanism is an indirect one affecting the activities of Cr and Al as suggested by Czech³⁸.

5.5.5.1.2 Inner β Depleted Layer

There is also a β depleted layer at the inner surface, at 950°C and probably at 850°C. At the higher of the two temperatures, there appears to be more β depletion at the inner layer of the coating than the outer layer. The low aluminium in some of the composition profiles e.g. Figure 5.5.22 and Figure 5.5.25 corroborates this. There is a layer of rhenium containing particles (σ at 850°C and α at 950°C) at the interdiffusion zone. These layers were not found to be continuous and contained rhenium to about 4 mass%. Whether these layers inhibit the diffusion of aluminium is not certain. A direct comparison of extent of β phase depletion with coating RT122 may prove useful in determining this.

Czech³⁸, in the system discussed in the previous section, found an inner β depletion zone in the coating that contained 16 atom% Al but not in that containing 24 atom% Al.

The most likely driving force for the diffusion of aluminium from the coating towards the substrate is the concentration profile of aluminium through the coating and substrate. The aluminium content of the coating is approximately 10 mass%, that of the substrate is approximately 3.5 mass%. Note that this difference in aluminium content between coating and substrate is greater than that for RT122 (Al 6.9 mass%). Aluminium thus diffuses towards the substrate, the likely result being the formation of a high proportion of γ at the interdiffusion zone. Whereas in RT122 the aluminium is considered to have taken fast grain boundary diffusion paths into the recrystallised region of the substrate, the presence of rhenium containing particles at the interdiffusion zone in SC2453 may have inhibited this. The formation of large amounts of γ in the recrystallised region is not evident in SC2453, as in RT122, corroborating the above hypothesis.

5.5.5.1.3 σ Depletion at Core and Inner Layers

σ is apparent in the coating at 950°C as well as 850°C. The equilibrium predictions suggest that the solvus of σ is around 900°C. σ may therefore be a metastable phase at 950°C, or the actual solvus could be slightly higher than the predicted one.

Note Figure 5.5.29 - 950°C, where σ appears to be depleting over time particularly in the inner and middle bands, but still remaining in the outer band. This implies a transformation (over this exposure time) governed by diffusion. The decomposition of σ could be due to diffusion of Cr from the coating towards the substrate. Alternatively, a phase transformation could be taking place, noting that σ is not predicted to be a stable phase at this temperature, with chromium partitioning to other phases within the coating.

The other chromium rich phase, α , is expected at equilibrium but occurs only in small amounts in the as-coated state and after thermal exposure at 850°C up to 9600 hours, mainly segregated towards the inner and outer zones of the coating. It is possible that more significant amounts of α will precipitate on further exposure at this temperature; this is dependent on the kinetics of the reaction. The presence of significant amounts of α at the higher temperature can be expected, as α and not σ is the significant Cr-rich phase predicted at equilibrium for this temperature, Figure 5.5.1a and b.

5.5.5.2 Interdiffusion Zone

There is a clear difference in the microstructure of the interdiffusion zone at 850°C and at 950°C, hence these temperatures are considered separately. As there is an increasing amount of discussion in the literature concerning measurement of interdiffusion zone width, a section describing such measurement for the SC2453/IN738LC system studied in this research is included.

5.5.5.2.1 Measurement of Interdiffusion Zone

Many investigators report the width of the interdiffusion zone. In the case of the SC2453/IN738LC system, the nature of the interdiffusion zone, particularly the finger like penetration of phases into the substrate make quantification of the increase in the size of the zone difficult. Hence, extent of the interdiffusion zone is considered. It can be said that the microstructures exhibit a greater quantity of co-diffused material at 950°C than at 850°C for the same exposure time. There does appear to be a tendency for an increase in the extent of the interdiffusion zone with exposure time, and further work using image analysis techniques could quantify this.

5.5.5.2.2 Thermal Exposure at 850°C

The σ phase was not present in the unexposed sample, being found on thermal exposure only at the lower of the two temperatures, 850°C. Further, the morphology of the majority of σ at the interdiffusion zone was needle like, rather than the equiaxed form found in the bulk coating. The σ at the interdiffusion zone therefore precipitates as a TCP phase on thermal exposure at 850°C. The existence of layers of TCP σ under coatings has been reported in Sims *et al*³ Chapter 8, where he also states that the TCP platelet form of σ is composed of close packed layers of atoms forming in nets aligned with the octahedral planes in the FCC matrix (γ). It appears that the platelet form can also form in γ' , the other main phase in the interdiffusion zone, but not in the coating structure, where the other predominant phase is β .

The presence of the σ phase at 950°C but not 850°C will be due to relative thermodynamic stability at the composition of the interdiffusion layer. The cause of the variation of the rhenium content of the α is not known.

The γ phase can be said to form the matrix of the interdiffusion zone at both temperatures, and persists with thermal exposure.

5.5.5.2.3 Thermal Exposure at 950°C

At the interface between the coating and the interdiffusion layer, thin layers of rhenium-containing α particles appear to be present.

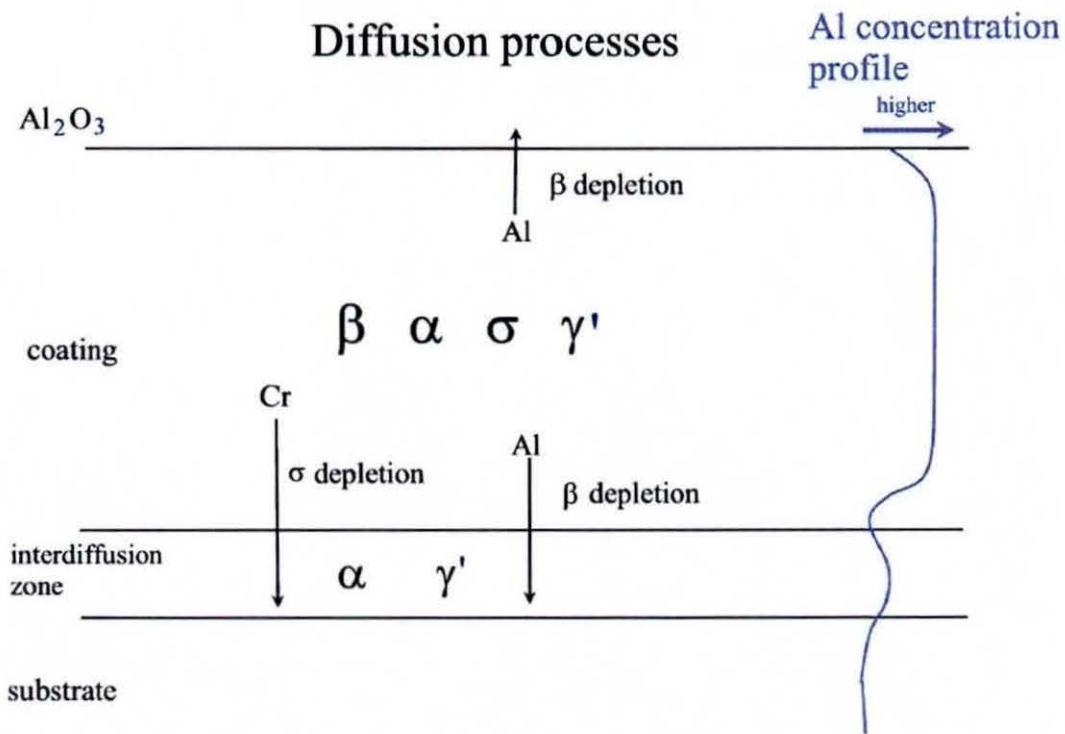
The interdiffusion zone consisted of γ and α ; no σ was evident in the interdiffusion zone at this temperature. Thermodynamic calculations for IN738LC, SC2543 and modified compositions thereof, show that the solution temperature of σ does vary with composition. At the composition of the interdiffusion layer, the solution temperature of σ can be said to be below 950°C. Ellison⁷⁶ reports an interdiffusion zone at 1000°C consisting of γ and α rather than γ and α . The α phase also contains variable amounts of rhenium.

Wavelength dispersive analysis and Auger analysis showed that the α particles at the interdiffusion layer contained carbon. As stated section 5.5.3.3 the carbon is considered to be in solid solution in α at the interdiffusion zone, particle 2 in Figure 5.5.21. Further into the substrate, the chromium diffusing from the substrate may result in $M_{23}C_6$ carbides, Figure 5.5.21. There are not sufficient data within this research to confirm this and further crystallographic techniques such as transmission electron microscopy may be necessary for

phase determination of carbon containing particles. Additionally the carbon analysis that has been carried out was qualitative rather than quantitative, hence the amount of carbon in the particles has not been determined. The identification of the chromium rich phase at the interdiffusion zone as α is still however, considered most likely on the basis of the evidence available.

A summary of the proposed diffusion processes and related phase changes at 950°C is given in Figure 5.5.34 below.

Figure 5.5.34 Schematic of diffusion processes at 950°C



Appendix 5A Comprehensive EDX Data for RT122 (atom%)

Lab ID	Spot ID	phase	Ni K	Cr K	Co K	Mo L	W L	Ti K	Al K	Ta L	Nb L	Zr L	Re L	Y L	region
G12/4-Y	1		30.5	26.6	30.6	0.3	2.5	0.6	9.0	0.0	0.0	0.0	0.0	0.0	inter
G12/4-Y	2		30.6	26.5	30.8	0.4	2.5	0.4	8.7	0.0	0.0	0.0	0.0	0.0	inter
G12/4-Y	3		28.7	27.1	32.6	0.1	2.2	0.5	8.8	0.0	0.0	0.0	0.0	0.0	inter
G12/4-Y	4		28.6	27.4	32.6	0.2	2.3	0.4	8.5	0.0	0.0	0.0	0.0	0.0	inter
G12/4-Y	5		19.6	18.9	21.7	0.7	1.5	5.8	16.0	0.0	0.0	0.7	0.0	15.2	inter
G12/4-Y	6		21.6	20.7	24.1	0.4	1.7	0.2	19.6	0.0	0.0	0.8	0.0	10.9	inter
G12/4-Y	7		12.4	13.0	12.9	0.5	0.0	52.7	6.2	1.6	0.7	0.0	0.0	0.0	inter
G12/4-Y	8		27.5	25.3	29.9	0.4	2.3	3.2	11.5	0.0	0.0	0.0	0.0	0.0	inter
G12/4-Y	9		40.5	6.1	13.9	0.0	2.7	1.1	35.7	0.0	0.0	0.0	0.0	0.0	inter
G12/4-Y	10		40.6	6.3	13.8	0.0	2.7	1.0	35.6	0.0	0.0	0.0	0.0	0.0	inter
G12/4-Y	1	Gamma	27.7	27.3	33.7	0.2	2.2	0.3	8.7	0.0	0.0	0.0	0.0	0.0	coat
G12/4-Y	2	Gamma	27.8	27.2	34.2	0.1	2.1	0.3	8.3	0.0	0.0	0.0	0.0	0.0	coat
G12/4-Y	3	Gamma	27.5	27.5	34.3	0.0	2.0	0.2	8.4	0.0	0.0	0.0	0.0	0.0	coat
G12/4-Y	4	beta	38.7	6.7	15.4	0.0	2.5	0.7	36.0	0.0	0.0	0.0	0.0	0.0	coat
G12/4-Y	5	beta	38.9	6.4	15.4	0.1	2.2	0.7	36.3	0.0	0.0	0.0	0.0	0.0	coat
G12/4-Y	6	beta	38.5	6.1	14.9	0.1	2.7	0.8	35.6	0.0	0.0	0.0	0.0	1.3	coat
G12/2-W	1	Gamma	27.3	28.1	35.6	0.2	2.2	0.5	6.0	0.0	0.0	0.0	0.0	0.0	inter
G12/2-W	2	Gamma	39.6	19.1	27.2	0.2	2.9	2.3	8.6	0.0	0.0	0.0	0.0	0.0	inter
G12/2-W	3	Gamma	29.7	26.3	33.1	0.3	2.5	0.8	7.2	0.0	0.0	0.0	0.0	0.0	inter
G12/2-W	4	Gamma	24.0	30.1	37.8	0.2	1.6	0.2	6.1	0.0	0.0	0.0	0.0	0.0	inter
G12/2-W	5	Gamma	24.2	30.0	37.6	0.2	1.9	0.3	5.9	0.0	0.0	0.0	0.0	0.0	inter
G12/2-W	6	G. prime	53.5	4.6	15.9	0.1	3.3	4.5	18.1	0.0	0.0	0.0	0.0	0.0	inter
G12/2-W	7	G. prime	49.8	7.4	17.1	0.0	3.7	3.2	18.8	0.0	0.0	0.0	0.0	0.0	inter
G12/2-W	8	beta	39.2	5.8	14.7	0.0	2.6	0.5	37.3	0.0	0.0	0.0	0.0	0.0	inter
G12/2-W	9	beta	39.8	5.4	14.6	0.0	2.5	0.5	37.2	0.0	0.0	0.0	0.0	0.0	inter
G12/2-W	10		33.3	44.0	5.4	2.0	3.2	3.8	8.2	0.0	0.0	0.0	0.0	0.0	inter
G12/2-W	11		51.8	14.1	9.3	0.8	4.0	4.6	15.4	0.0	0.0	0.0	0.0	0.0	inter
G12/2-W	12		37.1	3.8	12.2	1.2	0.4	25.6	6.7	6.6	6.5	0.0	0.0	0.0	inter
G12/2-W	1	Gamma	23.0	30.1	39.3	0.0	1.8	0.0	5.9	0.0	0.0	0.0	0.0	0.0	coat
G12/2-W	2	Gamma	22.5	30.0	40.1	0.1	1.6	0.1	5.6	0.0	0.0	0.0	0.0	0.0	coat
G12/2-W	3	Gamma	22.8	29.8	39.6	0.0	1.7	0.1	6.1	0.0	0.0	0.0	0.0	0.0	coat
G12/2-W	4	Beta	38.6	5.5	15.4	0.0	2.6	0.2	37.6	0.0	0.1	0.0	0.0	0.0	coat
G12/2-W	5	Beta	36.1	8.0	17.2	0.0	2.2	0.2	36.3	0.0	0.0	0.0	0.0	0.0	coat
G12/2-W	6	Beta	36.2	8.0	17.2	0.0	2.5	0.2	35.9	0.0	0.0	0.0	0.0	0.0	coat
G12/2-X	1	Gamma	27.5	28.4	39.2	0.3	0.3	0.4	4.0	0.0	0.0	0.0	0.1	0.0	inter
G12/2-X	2	Gamma	26.7	28.4	39.4	0.3	0.7	0.2	4.2	0.0	0.0	0.0	0.2	0.0	inter
G12/2-X	3	Gamma	26.1	28.5	39.1	0.4	0.8	0.3	4.5	0.2	0.0	0.0	0.2	0.0	inter
G12/2-X	4	OI	23.2	25.2	32.7	0.0	0.5	13.2	4.3	0.6	0.1	0.0	0.3	0.0	inter
G12/2-X	5	OI	24.7	26.8	36.2	0.4	1.0	5.8	4.6	0.4	0.0	0.0	0.1	0.0	inter
G12/2-X	6	OI	23.2	23.9	33.4	0.0	0.4	14.1	4.5	0.2	0.0	0.0	0.2	0.0	inter
G12/2-X	7	G. prime	49.6	11.6	23.0	0.2	0.9	1.9	12.2	0.3	0.0	0.0	0.2	0.0	inter
G12/2-X	8	G. prime	56.8	6.3	18.8	0.3	0.9	3.1	13.5	0.0	0.0	0.0	0.2	0.0	inter
G12/2-X	9	G. prime	56.1	6.5	18.6	0.3	0.8	3.0	13.8	0.6	0.0	0.0	0.3	0.0	inter
G12/2-X	1	Gamma	26.1	27.9	40.4	0.1	0.3	0.1	5.0	0.0	0.0	0.0	0.1	0.0	coat
G12/2-X	2	Gamma	25.5	28.3	41.0	0.0	0.1	0.2	4.7	0.1	0.0	0.0	0.1	0.0	coat
G12/2-X	3	Gamma	25.9	28.1	40.9	0.3	0.0	0.1	4.7	0.0	0.0	0.0	0.1	0.0	coat

Appendix 5A

Lab ID	Spot ID	phase	Ni K	Cr K	Co K	Mo L	W L	Ti K	Al K	Ta L	Nb L	Zr L	Re L	Y L	region
G12/2-X	4	Beta	46.0	5.8	16.7	0.0	0.6	0.4	30.2	0.0	0.0	0.0	0.3	0.0	coat
G12/2-X	5	beta	46.3	5.6	16.2	0.2	0.3	0.3	30.8	0.0	0.0	0.0	0.2	0.0	coat
G12/2-X	6	beta	47.4	5.2	15.5	0.2	0.1	0.4	31.1	0.0	0.0	0.0	0.0	0.0	coat
G12/5-W	1	beta	49.0	6.3	14.8	0.0	0.3	1.1	28.4	0.0	0.0	0.0	0.0	0.0	coat
G12/5-W	2	beta	49.7	6.2	14.2	0.1	0.5	0.9	27.8	0.0	0.0	0.0	0.5	0.0	coat
G12/5-W	3	beta	48.9	6.6	15.8	0.0	0.1	0.8	27.6	0.0	0.0	0.0	0.2	0.0	coat
G12/5-W	4	gamma	35.1	25.1	31.3	0.4	0.2	0.5	6.8	0.0	0.0	0.0	0.0	0.0	coat
G12/5-W	5	gamma	35.3	24.5	31.9	0.4	0.3	0.7	6.9	0.0	0.0	0.0	0.0	0.0	coat
G12/5-W	6	gamma	34.9	25.0	31.6	0.2	0.8	0.5	6.5	0.2	0.0	0.0	0.4	0.0	coat
G12/5-W	1	gamma	35.4	25.0	30.8	0.5	0.8	0.5	6.7	0.0	0.0	0.0	0.2	0.0	inter
G12/5-W	2	gamma	34.9	24.8	31.8	0.4	0.5	0.6	6.8	0.1	0.0	0.0	0.0	0.0	inter
G12/5-W	3	gamma	35.8	24.8	31.3	0.2	0.6	0.5	6.8	0.0	0.0	0.0	0.1	0.0	inter
G12/5-W	4	OI	34.2	24.9	30.3	0.6	0.2	2.3	7.4	0.0	0.0	0.0	0.0	0.0	inter
G12/5-W	5	OI	31.6	22.3	24.7	1.6	0.5	13.3	5.6	0.2	0.2	0.0	0.0	0.0	inter
G12/5-W	6	g. prime	58.2	5.6	16.3	0.2	0.7	3.4	14.3	1.0	0.1	0.0	0.2	0.0	inter
G12/5-W	7	g. prime	58.6	5.9	16.3	0.3	0.5	3.5	14.3	0.2	0.2	0.0	0.2	0.0	inter
G12/5-X	1	Gamma	34.9	24.1	30.5	0.3	0.6	0.6	8.9	0.1	0.0	0.0	0.0	0.0	coat
G12/5-X	2	Gamma	35.5	24.2	31.0	0.4	0.2	0.7	7.9	0.2	0.0	0.0	0.0	0.0	coat
G12/5-X	3	Gamma	35.2	24.3	30.7	0.3	0.6	0.8	8.0	0.0	0.0	0.0	0.3	0.0	coat
G12/5-X	4	Beta	43.7	7.9	15.6	0.0	0.3	1.0	31.5	0.0	0.0	0.0	0.0	0.0	coat
G12/5-X	5	Beta	45.8	6.0	14.2	0.0	0.2	0.9	33.0	0.0	0.0	0.0	0.0	0.0	coat
G12/5-X	6	Beta	46.0	6.4	14.1	0.2	0.4	0.8	32.1	0.0	0.0	0.1	0.1	0.0	coat
G12/5-X	7	dark spot	12.1	4.9	5.7	0.0	0.0	67.0	6.9	0.1	0.1	1.4	0.0	1.6	coat
G12/5-X	8	dark spot	22.4	7.6	10.5	0.2	0.5	47.5	8.2	0.0	0.0	1.8	0.1	1.2	coat
G12/5-X	1	Gamma	34.5	24.6	30.6	0.2	0.8	0.4	8.2	0.4	0.0	0.0	0.4	0.0	inter
G12/5-X	2	Gamma	34.3	24.1	31.2	0.5	0.4	0.7	8.4	0.1	0.0	0.0	0.3	0.0	inter
G12/5-X	3	OI	19.6	13.9	17.0	0.4	0.4	3.2	45.5	0.0	0.0	0.0	0.0	0.0	inter
G12/5-X	4	Gamma	35.5	25.1	30.2	0.3	0.4	0.5	7.8	0.0	0.0	0.0	0.3	0.0	inter
G12/5-X	5	gamma	31.4	22.4	26.1	0.6	0.3	12.3	6.0	0.6	0.4	0.0	0.0	0.0	inter

Appendix 5B Comprehensive EDX data for SC2453 (atom%)

Lab ID	Spot ID	phase	Ni K	Cr K	Co K	Mo L	W L	Ti K	Al K	Ta L	Nb L	Zr L	Re L	Y L	region
G13/4-Y	1	beta	51.6	8.2	5.8	0.1	1.4	0.2	32.4	0.0	0.0	0.0	0.3	0.0	mid coat
G13/4-Y	2	beta	53.1	6.5	5.2	0.0	1.5	0.4	32.8	0.0	0.0	0.0	0.5	0.0	mid coat
G13/4-Y	3	beta	51.6	8.2	5.8	0.1	1.4	0.2	32.4	0.0	0.0	0.0	0.3	0.0	mid coat
G13/4-Y	4	gamma	45.4	28.7	13.7	0.2	1.6	0.3	9.3	0.0	0.0	0.0	0.8	0.0	mid coat
G13/4-Y	6	gamma	46.0	28.8	13.5	0.0	1.2	0.2	9.6	0.0	0.0	0.0	0.8	0.0	mid coat
G13/4-Y	7	alpha	4.6	85.5	2.2	0.0	0.8	0.0	1.4	0.3	0.0	0.0	5.2	0.0	mid coat
G13/4-Y	8	alpha	5.1	84.8	2.0	0.0	0.9	0.1	1.6	0.0	0.0	0.0	5.6	0.0	mid coat
G13/4-Y	9	alpha	4.9	85.0	2.2	0.0	0.7	0.1	1.5	0.0	0.0	0.0	5.6	0.0	mid coat
G13/4-Y	10	phase	15.6	57.9	14.1	0.0	1.4	0.0	2.4	0.0	0.0	0.0	8.7	0.0	mid coat
G13/4-Y	11	phase	15.8	57.3	14.5	0.0	1.6	0.1	2.6	0.0	0.0	0.0	8.2	0.0	mid coat
G13/4-Y	1	g prime	64.1	5.9	6.2	0.0	2.0	2.7	18.7	0.0	0.0	0.0	0.3	0.0	inter
G13/4-Y	2	g prime	65.0	5.1	6.0	0.0	2.0	3.3	18.0	0.0	0.0	0.0	0.5	0.0	inter
G13/4-Y	3	g prime	64.7	5.1	6.2	0.0	1.9	3.3	18.3	0.0	0.0	0.0	0.4	0.0	inter
G13/4-Y	4	alpha	5.3	87.7	2.0	0.3	1.5	0.1	1.0	0.0	0.0	0.0	2.1	0.0	inter
G13/4-Y	5	phase	44.4	36.1	4.9	0.5	2.1	1.9	9.6	0.0	0.0	0.0	0.4	0.0	inter
G13/4-Y	6	alpha	9.6	81.8	2.3	0.0	1.5	0.3	1.6	0.0	0.0	0.0	3.0	0.0	inter
G13/4-Y	7	Alpha	4.8	86.2	2.3	0.0	1.2	0.1	1.1	0.2	0.0	0.0	4.1	0.0	inter
G13/4-Y	8	Alpha	4.8	86.9	1.9	0.0	1.0	0.2	1.2	0.0	0.0	0.0	4.1	0.0	inter
G13/4-Y	9	Alpha	5.4	86.1	2.2	0.0	1.2	0.0	1.2	0.0	0.0	0.0	3.9	0.0	inter
G13/2-W	1	Beta	51.1	6.2	6.1	0.0	1.3	0.0	35.0	0.0	0.0	0.0	0.3	0.0	mid coat
G13/2-W	2	Beta	49.1	9.2	5.9	0.0	1.5	0.1	33.7	0.0	0.0	0.0	0.6	0.0	mid coat
G13/2-W	3	Beta	49.8	7.4	5.9	0.0	1.5	0.1	34.8	0.0	0.0	0.0	0.6	0.0	mid coat
G13/2-W	4	g prime	58.6	10.4	7.3	0.1	1.6	0.2	21.1	0.0	0.0	0.0	0.7	0.0	mid coat
G13/2-W	5	g prime	57.5	11.4	7.2	0.0	1.5	0.1	21.8	0.0	0.0	0.0	0.5	0.0	mid coat
G13/2-W	6	g prime	57.0	11.7	7.5	0.0	1.5	0.1	21.8	0.0	0.0	0.0	0.4	0.0	mid coat
G13/2-W	7	Sigma	17.1	57.8	19.9	0.0	0.7	0.0	1.7	0.0	0.0	0.0	2.8	0.0	mid coat
G13/2-W	8	Sigma	13.1	61.8	19.9	0.0	0.9	0.0	1.3	0.0	0.0	0.0	3.0	0.0	mid coat
G13/2-W	9	Sigma	13.2	61.1	20.2	0.0	0.9	0.0	1.7	0.0	0.0	0.0	2.9	0.0	mid coat
G13/2-W	10	Phase	23.3	56.2	5.1	0.0	1.0	0.0	11.8	0.0	0.0	0.0	2.6	0.0	mid coat
G13/2-W	11	Phase	43.3	18.9	5.5	0.0	1.3	0.0	30.2	0.0	0.0	0.0	0.7	0.0	mid coat
G13/2-W	12	Phase	49.2	9.4	6.1	0.0	1.5	0.1	32.8	0.0	0.0	0.0	0.5	0.5	mid coat
G13/2-W	1	g prime	58.5	10.6	8.1	0.1	1.7	1.8	18.7	0.0	0.0	0.0	0.3	0.0	inter
G13/2-W	2	g prime	59.7	10.2	6.8	0.0	1.8	2.8	18.3	0.0	0.0	0.0	0.4	0.0	inter
G13/2-W	3	g prime	62.8	5.5	7.0	0.0	2.2	2.4	19.9	0.0	0.0	0.0	0.3	0.0	inter
G13/2-W	4	phase	31.8	54.6	4.0	0.1	1.3	1.4	6.5	0.0	0.0	0.0	0.4	0.0	inter
G13/2-W	5	phase	20.0	69.9	3.1	0.0	0.9	0.6	5.1	0.0	0.0	0.0	0.3	0.0	inter
G13/2-W	6	phase	48.0	27.3	5.8	0.1	1.7	1.5	15.2	0.0	0.0	0.0	0.4	0.0	inter
G13/2-W	7	sigma E	16.9	58.5	20.2	0.4	1.3	0.3	1.6	0.0	0.0	0.0	0.9	0.0	inter
G13/2-W	8	sigma E	15.7	59.2	20.4	0.7	1.4	0.3	1.7	0.0	0.0	0.0	0.6	0.0	inter
G13/2-W	9	sigma E	39.0	35.2	15.2	1.0	2.0	2.1	5.2	0.0	0.0	0.0	0.2	0.0	inter
G13/2-W	10	sigma E	20.6	55.1	19.0	0.0	1.1	0.4	2.4	0.0	0.0	0.0	1.5	0.0	inter
G13/2-W	11	sigma E	25.1	48.8	18.1	0.2	1.2	0.4	4.7	0.0	0.0	0.0	1.5	0.0	inter
G13/2-W	12	sigma E	19.5	53.6	19.1	0.3	1.3	0.3	3.4	0.0	0.0	0.0	1.2	1.3	inter
G13/2-W	13	sigma N	30.8	41.2	16.3	2.2	2.0	1.8	5.7	0.0	0.0	0.0	0.0	0.0	inter
G13/2-W	14	sigma N	33.2	39.0	16.2	1.4	2.0	2.0	5.9	0.0	0.0	0.0	0.4	0.0	inter
G13/2-W	15	sigma N	34.9	36.6	15.3	1.7	2.0	2.2	7.2	0.0	0.0	0.0	0.1	0.0	inter
G13/2-W	1	sigma N	31.7	40.9	15.5	2.5	2.2	2.3	4.7	0.0	0.0	0.0	0.1	0.0	needle
G13/2-W	2	sigma N	41.3	30.2	12.4	2.0	2.0	3.1	9.0	0.0	0.0	0.0	0.1	0.0	needle
G13/2-W	3	sigma N	30.3	42.0	16.9	1.6	1.9	1.8	5.5	0.0	0.0	0.0	0.0	0.0	needle

Lab ID	Spot ID	phase	Ni K	Cr K	Co K	Mo L	W L	Ti K	Al K	Ta L	Nb L	Zr L	Re L	Y L	region
G13/2-W	1		29.7	44.6	4.9	0.0	0.5	0.0	18.4	0.0	0.0	0.0	1.7	0.0	inter
G13/2-W	2		35.6	33.0	5.3	0.0	0.0	0.0	24.9	0.0	0.0	0.0	1.2	0.0	inter
G13/2-W	3		29.6	46.1	5.6	0.0	0.0	0.0	16.2	0.2	0.0	0.0	2.3	0.0	inter
G13/2-W	4		27.7	50.9	5.1	0.0	0.0	0.0	14.3	0.0	0.0	0.0	2.1	0.0	inter
G13/2-W	5		17.0	65.7	4.4	0.0	0.0	0.0	9.7	0.1	0.0	0.0	2.9	0.0	inter
G13/2-W	6		31.8	43.3	5.0	0.0	0.3	0.0	17.4	0.0	0.0	0.0	2.2	0.0	inter
G13/2-W	7		22.2	57.1	4.6	0.0	0.5	0.1	12.8	0.1	0.0	0.0	2.6	0.0	inter
G13/2-W	8	sigma	14.6	60.4	20.3	0.0	0.0	0.3	1.6	0.0	0.0	0.0	2.8	0.0	inter
G13/2-W	9	sigma	16.9	57.5	20.4	0.0	0.0	0.0	2.5	0.0	0.0	0.0	2.6	0.0	inter
G13/2-W	10	g prime	61.8	8.1	7.6	0.0	0.6	0.2	21.5	0.0	0.0	0.0	0.1	0.0	inter
G13/2-W	11	g prime	56.0	15.0	7.0	0.0	2.7	0.3	20.8	0.0	0.0	0.0	0.6	0.0	inter
G13/2-X	1	sigma	15.5	59.6	20.0	0.0	0.3	0.2	1.7	0.0	0.0	0.0	2.6	0.0	coating
G13/2-X	2	sigma	14.2	60.6	20.2	0.0	0.5	0.0	1.2	0.0	0.0	0.0	3.1	0.0	coating
G13/2-X	3	sigma	14.1	61.0	20.0	0.0	0.0	0.0	1.6	0.0	0.0	0.0	3.3	0.0	coating
G13/2-X	4	g prime	65.4	8.0	7.8	0.2	0.2	0.6	17.9	0.0	0.0	0.0	0.0	0.0	coating
G13/2-X	5	g prime	64.4	7.8	8.0	0.0	0.6	0.6	18.0	0.0	0.0	0.0	0.6	0.0	coating
G13/2-X	6	g prime	64.7	8.0	7.7	0.0	0.2	0.3	18.8	0.0	0.0	0.0	0.3	0.0	coating
G13/2-X	7	beta	52.0	12.6	6.2	0.0	0.0	0.0	29.1	0.0	0.0	0.0	0.1	0.0	coating
G13/2-X	8	beta	55.6	6.4	6.4	0.1	0.6	0.2	30.2	0.2	0.0	0.0	0.3	0.1	coating
G13/2-X	9	beta	56.1	6.3	6.6	0.1	0.3	0.0	30.3	0.0	0.1	0.1	0.0	0.1	coating
G13/2-X	10	gamma	58.7	13.3	6.4	0.4	0.4	0.1	7.5	0.0	0.0	0.0	0.5	12.9	coating
G13/2-X	11	gamma	58.9	13.8	5.7	0.2	0.2	0.2	10.1	0.0	0.0	0.0	0.4	10.5	coating
G13/2-X	12	gamma	64.8	11.0	7.2	0.0	0.2	0.2	14.3	0.0	0.0	0.0	0.3	2.0	inter
G13/2-X	1	sigma E	15.3	60.0	21.0	1.4	1.2	0.3	0.9	0.0	0.0	0.0	0.0	0.0	inter
G13/2-X	2	sigma E	53.2	22.2	12.1	0.8	0.9	2.8	7.7	0.2	0.0	0.0	0.0	0.0	inter
G13/2-X	3	sigma E	27.5	47.6	17.7	2.5	1.6	1.3	1.2	0.2	0.0	0.0	0.2	0.0	inter
G13/2-X	4	sigma N	35.6	37.3	15.7	2.1	1.3	2.1	5.6	0.2	0.0	0.0	0.0	0.0	inter
G13/2-X	5	sigma N	55.2	20.8	11.5	1.3	0.8	4.4	6.0	0.1	0.0	0.0	0.0	0.0	inter
G13/2-X	6	g prime	63.1	4.0	6.6	0.0	1.1	4.6	15.0	0.3	0.0	0.0	0.3	0.0	inter
G13/2-X	7	g prime	68.3	4.0	6.8	0.1	1.2	5.0	13.9	0.1	0.0	0.0	0.5	0.0	inter
G13/2-X	8	g prime	67.3	4.6	7.1	0.0	1.3	3.9	15.0	0.4	0.0	0.0	0.3	0.0	inter
G13/5-W	1	gamma	48.1	28.1	14.2	0.2	0.6	0.3	7.8	0.0	0.0	0.0	0.7	0.0	coating
G13/5-W	2	gamma	47.5	28.5	14.2	0.2	0.6	0.3	7.8	0.0	0.0	0.0	0.8	0.0	coating
G13/5-W	3	gamma	47.5	27.9	14.1	0.2	0.8	0.2	8.3	0.0	0.0	0.0	0.9	0.0	coating
G13/5-W	4	beta	58.0	6.4	5.7	0.0	0.4	28.9	0.0	0.0	0.0	0.0	0.2	0.0	coating
G13/5-W	5	beta	58.2	6.5	5.9	0.0	0.4	0.3	28.6	0.0	0.0	0.0	0.1	0.0	coating
G13/5-W	6	beta	58.2	6.5	5.8	0.0	0.4	0.4	28.4	0.0	0.0	0.0	0.3	0.0	coating
G13/5-W	7	alpha	5.0	85.5	2.4	0.0	0.4	0.0	0.9	0.2	0.0	0.0	5.6	0.0	coating
G13/5-W	8	alpha	6.7	82.8	2.2	0.0	0.6	0.1	1.6	0.0	0.0	0.0	6.0	0.0	coating
G13/5-W	9	alpha	5.4	85.1	2.1	0.0	0.5	0.0	1.2	0.2	0.0	0.0	5.5	0.0	coating
G13/5-W	10	sigma	16.0	57.6	14.8	0.0	0.9	0.1	1.8	0.0	0.0	0.0	8.9	0.0	coating
G13/5-W	11	sigma	15.8	57.9	14.4	0.0	0.9	0.0	2.2	0.0	0.0	0.0	8.8	0.0	coating
G13/5-W	12	sigma	47.8	28.4	14.2	0.0	0.4	0.2	8.1	0.0	0.0	0.0	0.9	0.0	coating
G13/5-W	1	g prime	68.4	5.2	6.6	0.0	1.1	3.0	15.3	0.1	0.0	0.0	0.2	0.0	inter
G13/5-W	2	g prime	68.4	5.6	6.3	0.1	0.9	3.2	15.1	0.4	0.0	0.0	0.0	0.0	inter
G13/5-W	3	g prime	68.5	5.0	6.6	0.1	0.8	3.2	15.7	0.1	0.0	0.0	0.0	0.0	inter
G13/5-W	4	alpha	5.5	86.2	2.2	0.0	0.9	0.2	0.9	0.0	0.0	0.0	4.1	0.0	inter
G13/5-W	5	alpha	4.9	88.1	2.1	0.1	1.2	0.2	0.6	0.0	0.0	0.0	2.7	0.0	inter
G13/5-W	6	alpha	56.1	21.3	5.2	0.0	1.2	2.1	12.7	0.4	0.0	0.0	1.0	0.0	inter

Lab ID	Spot ID	phase	Ni K	Cr K	Co K	Mo L	W L	Ti K	Al K	Ta L	Nb L	Zr L	Re L	Y L	region
G13/5-W	7	alpha	5.6	86.3	2.2	2.5	2.0	0.4	0.5	0.0	0.0	0.0	0.3	0.0	inter
G13/5-W	8	alpha	5.7	85.6	2.2	3.0	2.4	0.4	0.5	0.1	0.0	0.0	0.1	0.0	inter
G13/5-W	9	alpha	5.9	85.0	1.9	3.2	2.7	0.5	0.4	0.1	0.0	0.0	0.2	0.0	inter
G13/5-W	10	alpha	5.4	87.6	2.4	0.0	1.0	0.1	0.9	0.0	0.0	0.0	3.2	0.0	inter
G13/5-W	11	alpha	5.3	86.9	2.3	0.0	1.1	0.1	1.2	0.0	0.0	0.0	3.2	0.0	inter
G13/5-X	1	sigma	17.3	54.7	14.5	0.0	1.2	0.0	2.3	0.0	0.0	0.0	10.0	0.0	coating
G13/5-X	2	sigma	17.5	55.4	14.1	0.0	1.0	0.1	2.8	0.0	0.0	0.0	9.2	0.0	coating
G13/5-X	3	alpha	5.2	85.9	2.0	0.0	0.2	0.1	0.8	0.0	0.0	0.0	5.9	0.0	coating
G13/5-X	4	alpha	4.7	85.3	2.4	0.0	0.4	0.0	1.5	0.1	0.0	0.0	5.6	0.0	coating
G13/5-X	5	alpha	5.1	84.5	2.1	0.0	0.1	0.0	1.8	0.0	0.0	0.0	6.4	0.0	coating
G13/5-X	6	gamma	47.9	27.2	13.9	0.2	0.6	0.2	9.3	0.1	0.0	0.0	0.8	0.0	coating
G13/5-X	7	gamma	48.6	26.5	14.0	0.2	0.5	0.5	8.8	0.0	0.0	0.0	0.9	0.0	coating
G13/5-X	8	gamma	48.1	27.1	14.3	0.1	0.3	0.2	9.1	0.0	0.0	0.0	0.9	0.0	coating
G13/5-X	9	beta	55.1	6.3	6.1	0.0	0.5	0.4	31.6	0.0	0.0	0.0	0.0	0.0	coating
G13/5-X	10	beta	54.8	6.0	5.9	0.1	0.4	0.1	32.3	0.0	0.0	0.3	0.3	0.1	coating
G13/5-X	1	alpha	5.5	86.4	1.5	3.1	2.5	0.2	0.7	0.0	0.0	0.0	0.0	0.0	coating
G13/5-X	2	alpha	6.5	84.3	2.6	2.8	2.1	0.6	1.2	0.0	0.0	0.0	0.0	0.0	inter
G13/5-X	3	g prime	63.4	8.0	6.1	0.2	0.3	2.7	19.0	0.0	0.0	0.0	0.0	0.3	inter
G13/5-X	4	g prime	64.4	6.9	6.5	0.0	0.3	2.0	19.8	0.0	0.0	0.0	0.0	0.0	inter
G13/5-X	5	alpha	5.1	87.9	1.9	0.0	1.0	0.0	0.4	0.4	0.0	0.0	3.4	0.0	inter
G13/5-X	6	alpha	4.8	86.9	2.1	0.0	1.0	0.1	1.1	0.1	0.0	0.0	3.9	0.0	inter
G13/5-X	7	alpha	5.0	85.4	2.3	0.0	1.3	0.0	1.2	0.0	0.0	0.0	4.9	0.0	inter
G13/2-W		alpha	8.1	87.4	1.9	0.1	0.3	0.2	1.6	0.0	0.0	0.0	0.3	0.0	inter
G13/2-W		alpha	9.7	81.2	5.7	0.3	0.3	0.4	2.0	0.1	0.0	0.0	0.3	0.0	inter
G13/2-W		alpha	6.4	86.3	5.2	0.3	0.5	0.2	0.8	0.1	0.0	0.0	0.3	0.0	inter
G13/2-W		sigma	21.3	67.2	3.1	2.6	1.4	1.9	2.3	0.0	0.0	0.0	0.0	0.0	inter
G13/2-W		sigma	19.2	67.5	3.4	3.7	2.0	1.6	2.2	0.0	0.0	0.0	0.5	0.0	inter
G13/2-W	1	gamma	58.0	13.7	6.3	0.0	0.9	0.2	8.6	0.0	0.0	0.0	0.6	11.7	coating
G13/2-W	2	gamma	71.4	6.8	6.6	0.2	1.0	0.1	5.3	0.0	0.0	0.1	0.2	8.2	coating
G13/2-W	3	gamma	61.4	6.4	4.7	0.0	0.5	0.0	9.4	0.0	0.0	0.0	0.7	17.0	coating
G13/2-W	4	gamma	55.2	17.5	9.3	0.0	1.1	0.2	7.7	0.0	0.0	0.0	1.2	7.9	coating
G13/2-W	5	gamma	62.6	6.1	5.8	0.1	0.8	0.0	9.8	0.0	0.0	0.0	0.5	14.2	coating
G13/2-W	6	gamma	61.9	9.0	7.6	0.2	0.8	0.4	19.4	0.0	0.0	0.0	0.7	0.0	coating
G13/2-X	1		66.9	8.0	5.3	0.0	1.1	0.0	6.4	0.0	0.0	0.0	0.4	11.8	inter
G13/2-X	2		22.0	65.7	3.9	2.4	1.8	1.3	2.5	0.3	0.0	0.0	0.1	0.0	inter
G13/2-X	3		16.5	73.7	3.2	1.4	2.2	0.8	1.6	0.2	0.0	0.0	0.4	0.0	inter
G13/2-X	4		47.9	27.0	8.6	0.1	0.3	1.6	14.3	0.0	0.0	0.0	0.2	0.0	inter
G13/2-X	5		13.6	80.0	2.2	0.0	0.4	0.5	2.8	0.2	0.0	0.0	0.4	0.0	inter
G13/2-X	6		14.6	60.3	20.9	0.6	0.6	0.2	1.5	0.0	0.0	0.0	1.3	0.0	inter
G13/2-X	7		15.0	60.2	21.3	0.3	0.6	0.3	1.0	0.0	0.0	0.0	1.3	0.0	inter

6 Modelling of Microstructural Transformation in IN738LC

6.1 Introduction

Research has established that transformation of MC carbide to $M_{23}C_6$ carbide is dependent on temperature and time. Within the temperature range where this transformation is active, the relative volume fraction of the two carbides should enable prediction of effective temperature for a given exposure time. This volume fraction will be dependent on the precipitation of $M_{23}C_6$. Predicting the volume fractions with respect to time and temperature will therefore entail modelling the kinetics of precipitation.

Kinetic modelling is discussed in the following sections, beginning with general models and then detailing modifications made by investigators to apply a model to carbide transformation in nickel base superalloys.

6.2 Johnson Mehl Avrami Kolmogorov (JMAK) Equation

The basis for many models predicting the kinetics of a solid state transformation is the classical Johnson-Mehl-Avrami-Kolmogorov theory^{77,78,79}. This is described briefly in the following paragraphs.

Consider a cellular transformation (A to B) in which B cells are continuously nucleated throughout the transformation at a constant rate of N .

The nucleation rate is therefore given by	Equation 6.2.1	$\frac{dn}{dt} = N$
Cells grow at a constant rate dr/dt r is radius of growing sphere v is velocity of growth of sphere	Equation 6.2.2	$\frac{dr}{dt} = v$
If the cells grow as spheres at a constant rate N the volume V of a cell nucleated at time zero is;	Equation 6.2.3	$V = \frac{4}{3}\pi r^3 = \frac{4}{3}\pi(vt)^3$

A cell that does not nucleate until time τ will have a volume V' ,	Equation 6.2.4	$V' = \frac{4}{3}\pi v^3 (t - \tau)^3$
The number of nuclei that are formed in a time increment of $d\tau$ will be $N.d\tau$ of untransformed A. Thus if the particles do not impinge on one another, for a unit of total volume	Equation 6.2.5	$f = \sum V' = \frac{4}{3}\pi N v^3 \int_0^t (t - \tau)^3 d\tau$
This is valid for $f \ll 1$ i.e. assumes no impingement. f becomes;	Equation 6.2.6	$f = \frac{\pi}{3} N v^3 t^4$
As time passes the B cells will eventually impinge on one another and the rate of transformation will decrease again. The equation valid for randomly distributed nuclei is	Equation 6.2.7	$f = 1 - \exp\left(-\frac{\pi}{3} N v^3 t^4\right)$
Approximations enable this equation to be valid for short and long times; at short times $1 - \exp(-z) \approx z$ when $z \ll 1$ at long times as $t \rightarrow \infty$ $f \rightarrow 1$ This is known as the <i>Johnson-Mehl-Avrami-Kolmogorov</i> equation.		
Depending on assumptions made about nucleation and growth, a variety of similar equations can be obtained with the form; n ; numerical exponent that can vary from 1 to 4, independent of temperature k ; dependent on nucleation and growth rate, sensitive to temperature	Equation 6.2.8	$f = 1 - \exp(-kt^n)$

6.2.1 Extended Volume Concept

Application of the Johnson-Mehl-Avrami-Kolmogorov equation requires an understanding of the relationship between the theoretical extended volume and the (calculated) actual volume.

Particles of B are considered to nucleate randomly throughout the volume of A. Two simplifications at this stage are;

- impingement is ignored
- particles are allowed to nucleate in region already transformed.

The volume under these conditions is theoretical and is termed extended volume, V_B . Only those parts of the change in extended volume which lie in the untransformed region of the parent phase A can contribute to the change in real volume of B. The probability that any change in extended volume lies in untransformed A is proportional to the volume fraction of untransformed A. Hence,

$$\text{Equation 6.2.9} \quad dV_B = \left(1 - \frac{V_B}{V}\right) dV_B^e$$

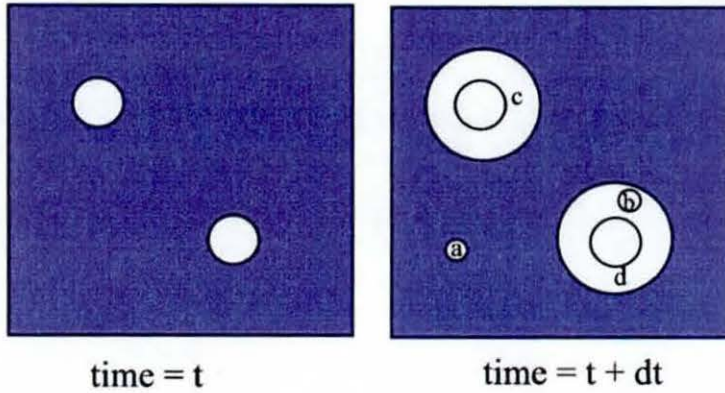
where

dV_B = change in real volume of B

dV_B^e = change in extended volume of B

The concept of extended volume is illustrated in Figure 6.1

Figure 6.1 Concept of extended volume



Two precipitate particles have nucleated and grown to finite size in the time t . New regions c and d are formed as the original particles grow, but a and b are new particles, of which b is unreal because it has formed in a region which is already transformed⁷⁹.

6.3 Models for Diffusion Controlled Precipitation Reactions

Starink⁸⁰ proposes modification to the JMAK model, specifically for a diffusion controlled precipitation reaction. Starink points out that for reactions such as recrystallisation, the boundary between the transformed and untransformed regions is sharp, resulting in an easily definable transformed volume V_B . However, for a diffusion controlled precipitation reaction the definition of V_B is less clear. In the diffusion zone there is gradual change from a transformed (fully depleted) matrix to an untransformed matrix that is not depleted. The transformed volume V_B for a diffusion controlled precipitation reaction is defined as the volume of an imaginary fully depleted area around a precipitate needed to give a precipitate size equal to the real case with a diffusion zone.

<p>According to Starink's version of the basic JMAK model, the transformed volume V_B around a single nucleus is given by;</p> <p>where</p> <p>G is the average growth rate</p> <p>A is a constant</p> <p>z is the time at which the nucleus is formed</p> <p>m is a constant related to the dimensionality of growth and the mode of transformation, termed the growth exponent.</p>	<p>Equation 6.3.1</p>	$V_B = A(G[t - z])^m$
<p>The term α is introduced which is the fraction transformed;</p>	<p>Equation 6.3.2</p>	$\alpha_{ext} = \frac{V_B^e}{V_0}$
<p>Impingement is taken into account by using η_i, the impingement exponent</p>	<p>Equation 6.3.3</p>	$\alpha = 1 - \left(\frac{\alpha_{ext}}{\eta_i} + 1 \right)^{-\eta_i}$
<p>To calculate extended transformed volume, for a constant nucleation rate:</p> <p>$k(T)$ is a temperature dependent factor determined by A, G, and I (nucleation rate).</p>	<p>Equation 6.3.4</p>	$\alpha_{ext} = [k(T)t]^n$
<p>An expression for $k(T)$ is given;</p> <p>Where</p> <p>E_{ISO} is effective isothermal activation energy</p> <p>k_0 is a constant</p>	<p>Equation 6.3.5</p>	$k(T) = k_0 \exp\left(-\frac{E_{iso}}{k_B T}\right)$

To derive the fraction transformed for a linear heating path it is assumed first that both the growth rate and nucleation rate can be described by Arrhenius type factors, with E_G and E_N and the activation energies for growth and nucleation respectively. An approximation for α_{ext} is given as;	Equation 6.3.6	$\alpha_{ext} \approx \left[\frac{\beta k_B}{E_G} \exp\left(\frac{-E_{eff}}{k_B T}\right) \left(\frac{T}{\beta}\right)^2 \right]^s$
E_{eff} is defined as	Equation 6.3.7	$E_{eff} = \frac{mE_G + E_N}{m+1}$
The exponent n is	Equation 6.3.8	$s = m + 1$
<p>Where</p> <p>E_G and E_N are activation energies for growth and nucleation</p> <p>β is the heating rate</p> <p>k_B is the Boltzman constant</p> <p>k_C is a constant</p> <p>If the assumptions for the derivation of the above equation are satisfied and the processes occurring for an isothermal and a linear heating path are the same, s equals n.</p>		

6.4 A Model for Precipitation of Carbides in Superalloys

The use of the ratio $M_{23}C_6 : MC$ (measurable by XRD) in a superalloy has already been investigated by Starink and Thomson⁷⁴. In their program of work a quantitative model was developed for $M_{23}C_6$ precipitation in a hafnium containing superalloy, MarM002. This predicts the kinetics of decomposition of Ti-rich MC and the subsequent precipitation of three other types of carbide, including Hf rich MC and allows for the presence of M_7C_3 at higher temperatures. Thermodynamic calculations using MTDATA were carried out for MarM002. In the simpler

IN738LC alloy, the following insights into thermodynamics and diffusion with respect to precipitation of $M_{23}C_6$ were used:

1. Nearly all carbon forms carbides and hence the total amount of carbon in carbides is fixed. The thermodynamic software (ThermoCalc with a nickel alloy database) predicts for IN738LC that 99.93 mass% of carbon is in carbides at 850°C (the rest being in Ni FCC) and 99.81% is in carbides at 950°C (with C solubility of about 0.19 mass% in Ni FCC)
2. Following ThermoCalc predictions, MC is assumed to be fixed at about 50 at% C, i.e. the possible presence of C deficient MC carbides is neglected
3. C diffusivity is several orders of magnitude higher than the metallic elements
4. $M_{23}C_6$ formation rate is determined by diffusion of one element (Cr) to the grain boundary.

In IN738LC there is generally only one carbide reaction:



At higher temperatures ($T > 1000^\circ\text{C}$) dissolution of $M_{23}C_6$ will occur. The predicted solvus is 1020°C , and in IN738LC no other lower carbides have been observed.

The kinetics and thermodynamics of the Starink and Thomson model can therefore be very much simplified. The following model is proposed,

Define the following symbols:

Main symbols:

$y_{M_{23}C_6}$ = amount of C present in $M_{23}C_6$

y_{TiC} = amount of C present in MC

y_X^{eq} = amount of C present in carbide X under equilibrium conditions

y_γ = amount of C present in γ

$r_{M_{23}C_6}$ = C to M ratio in $M_{23}C_6$ ($\cong 6/23$)

l_D = typical diffusion distance for precipitation / dissolution of carbides

D = the diffusion constant for a rate determining process (in dissolution of MC the rate determining process is thought to be Ta diffusion)

D_0 = pre-exponential factor for diffusion

n = exponential factor for diffusion

E = activation energy of diffusion

η = the impingement parameter

c = constants/ fittable parameters

Subscripts:

Ta, Cr = diffusion of elements

$M_{23}C_6$ = pertaining to $M_{23}C_6$ carbide (formation)

TiC = pertaining to MC carbide (dissolution)

Note assumption 1 above. For IN738 there are only two carbides, $M_{23}C_6$ and MC. Hence, while the relative proportions of carbon in these two carbides may change with time and temperature (t, T) the sum of the carbon always remains a constant. A suitable way of expressing the total carbon in carbide is the equilibrium value of $M_{23}C_6$, since at equilibrium (for a temperature where the transformation from MC to $M_{23}C_6$ is taking place) all carbide will be $M_{23}C_6$.

Equation 6.4.2
$$y_{TiC}(t, T) + y_{M_{23}C_6}(t, T) \cong y_{M_{23}C_6}^{eq}(T)$$

where $y_{M_{23}C_6}^{eq}(T)$ is a constant.

In line with the Starink and Thomson model and earlier work by Starink and Zahra^{80,81} on precipitation theory, the amount of $M_{23}C_6$ can be expressed as

Equation 6.4.3
$$y_{M_{23}C_6}(t, T) = [y_{M_{23}C_6}^{eq}(T) - y_{M_{23}C_6}(t = 0, T)] f \left(\left[C \frac{D_{Cr} t}{l_{M_{23}C_6}^2} \right]^n \right)$$

This states that the amount of carbon in $M_{23}C_6$ at time t and temperature T , is the amount at equilibrium minus the initial amount multiplied by a diffusion related factor.

Diffusivity is given by

Equation 6.4.4
$$D = D_0 \exp \left(- \frac{E_D}{k_B T} \right)$$

The function f is given by

Equation 6.4.5
$$f(\chi) = 1 - \left(\frac{\chi}{\eta} + 1 \right)^{-\eta}$$

where χ is a function (in this case the transformation $f(\chi)$ is applied to Equation 6.4.3)

A necessary assumption is that C diffusion is very fast and does not determine the reaction rate. Hence, the amount of $M_{23}C_6$ formed is determined by the rate at which it can form (i.e. limited by the supply of Cr) when C is supplied instantly.

$y_{M_{23}C_6}^{eq}(T)$ for IN738LC is expected to be dependent on the temperature and local composition of the alloy. Equilibrium proportions and compositions of $M_{23}C_6$ and MC can be predicted using thermodynamic predictions (see Thermodynamic Modelling – Chapter 3 and Equilibrium Predictions – Chapter 4). In fact, the conditions at equilibrium in IN738LC are very simple with respect to the carbides, predicting that all carbon partitions to $inM_{23}C_6$ in the temperature range under investigation (up to the solution temperature of $M_{23}C_6$, approximately 1010°C). The thermodynamic portion of the Starink and Thomson model does not, therefore, need to be adapted.

The model contains simplifications and assumptions that should be considered. These simplifications fall into four main categories: geometrical simplifications, kinetic simplifications, thermodynamic simplifications and phase structure simplifications;

1. Geometrical simplifications

This concerns mostly Equation 6.4.5 in which the entire diffusion symmetry is simplified down to 2 parameters, n and η_i . No account is taken of the different diffusivities in γ and γ' .

2. Kinetic simplifications

This concerns mostly Equation 6.4.4 in which diffusivity is described by a single Arrhenius type equation. The influence of alloying elements is neglected.

3. Phase structure simplifications

This is related to the structure assumed for the phases: $M_{23}C_6$ and MC are supposed to have a fixed stoichiometric C content.

4. Thermodynamic simplifications

These are related to the equilibrium predictions, and will be a function of the assumptions the various models used to predict phases using ThermoCalc and Ni-data.

6.5 A Model for IN738LC

1.1.1 Development of Model

The theory in the previous section can be used in conjunction with experimental data to model microstructural changes of carbides in IN738. Initially Equation 6.4.2 can be adapted to reflect measurable data.

Remembering that the total amount of carbon is equivalent to $y_{M_{23}C_6}^{eq}(T)$ and that the ratio of the two carbides is measurable, let us define two equations to include the data that are obtainable;

$$\text{Equation 6.5.1} \quad R = \frac{y_{M_{23}C_6}(t, T)}{y_{M_{23}C_6}^{eq}(T)}$$

$$\text{Equation 6.5.2} \quad R' = \frac{y_{M_{23}C_6}(t, T)}{y_{MC}(t, T)}$$

Note that R' is the parameter being measured experimentally (i.e. $M_{23}C_6$: MC ratio using XRD), and $y_{M_{23}C_6}^{eq}(T)$ can be obtained from thermodynamic predictions. We have an expression for $y_{M_{23}C_6}(t, T)$ that includes constants available from literature and an unknown constant. Hence, the equations can be solved to include parameters for obtainable data, available constants, and the unknown constant. These equations can be combined and solved for the constant. A value for this constant can then be obtained. The final equation can then be used to obtain temperature or time from carbide ratio data.

The steps to solve the equations are outlined below;

Divide Equation 6.4.2 by $y_{M_{23}C_6}(t, T)$ and we have

$$\text{Equation 6.5.3} \quad 1 + \frac{1}{R'} = \frac{1}{R}$$

from this

$$\text{Equation 6.5.4} \quad R' = \frac{R}{1 - R}$$

and

$$\text{Equation 6.5.5} \quad R = \frac{1}{1 + \frac{1}{R'}}$$

$$\text{Now look at Equation 6.4.3} \quad y_{M_{23}C_6}(t, T) = [y_{M_{23}C_6}^{eq}(T) - y_{M_{23}C_6}(t = 0, T)] f \left(\left[C_{M_{23}C_6} \frac{D_C t}{l_{M_{23}C_6}^2} \right]^n \right)$$

$y_{M_{23}C_6}(t = 0, T)$ is the initial amount of $M_{23}C_6$ in the material and can be considered to be zero.

Hence,

$$\text{Equation 6.5.6} \quad y_{M23C6}(t, T) = [y_{M236}^{eq}(T)] f \left(\left[C_{M23C6} \frac{D_{Cr} t}{l_{M23C6}^2} \right]^n \right)$$

Transpose, then substitute for R

$$\text{Equation 6.5.7} \quad R = f \left(\left[C_{M23C6} \frac{D_{Cr} t}{l_{M23C6}^2} \right]^n \right)$$

Noting that Equation 6.5.5 gives R' in terms of R, Equation 6.5.7 can be solved in two ways;

1. For C with respect to R' and constants for which values are available from literature. Remember that R' is a measurable parameter. The experimental values of R' and the constants can be entered, and values of C calculated and averaged.
2. The equation can be solved for R' . C can then be fitted by minimising the χ^2 values (square of difference between experimental and calculated values) of R' .

The solution for C is as follows;

$$\text{Equation 6.5.8} \quad C = \frac{\left(\left[\left[\frac{1}{1 - \frac{1}{1 + \frac{1}{R'}}} \right] - 1 \right] \eta \right)^{\frac{1}{n}}}{\frac{D_{M23C6} \cdot t}{l^2}}$$

The solution for R' is

Equation 6.5.9

$$R' = \frac{1 - \left(\frac{\left[\frac{C \cdot D_{M_{23}C_6} \cdot t}{l^2} \right]^n}{\eta} + 1 \right)^{-\eta}}{\left(\frac{\left[\frac{C \cdot D_{M_{23}C_6} \cdot t}{l^2} \right]^n}{\eta} + 1 \right)^{-\eta}}$$

1.1.2 Values for Parameters and Constants

For the diffusion constants, D , the literature values for diffusion in pure Ni as gathered in Appendix 5A are used. For the diffusion constant of Ta no data are available and instead the diffusion constant of Ti is used.

The dissolution of MC is governed by diffusion of Ta away from the orthorhombic MC carbides. A value of $n_{TaC} = 0.5$ was found to give a close fit of the model to experimental results.

$\eta_{M_{23}C_6}$ has relatively little influence on the results of the model. Hence a value of 2 is chosen for this parameter. This value is a typical one for diffusion controlled precipitation reactions (see Refs.^{80,81,81}).

The peak intensities of the MC and $M_{23}C_6$ carbides in unexposed IN738LC (which had undergone a typical pre-service heat treatment) indicate that $y_{TiC}(t=0, T) = 0.95$

A summary of the values for the constants is given in Table 6.1, below;

Table 6.1 Values for parameters and constants

Kinetics	E_d	D_0 (m ² /hr)	N	η	l_d (m)	$y(t=0, T)$
TiC / Ta	257	3.0E-01	0.5	2	0.0001	0.95
$M_{23}C_6$ / Cr	263	2.2E-01	0.5	2	0.0001	0.05

1.1.3 Solution

The solution for R' has been implemented in a spreadsheet, and C has been fitted as described above. The fitted value of C obtained with current data is 2.13.

Graphs for selected temperatures showing experimental and calculated results are shown in section 1.2.1.

1.2 Discussion

The model shows relatively good agreement with experimental results at the temperatures where the carbide transformation is most active, see Figure 6.2. At 850°C, the reaction is very slow and beyond 950°C the temperature for dissolution of $M_{23}C_6$ is relatively close. The accuracy of the temperature dependence in the model seems therefore to be lower at the extremes of the active temperature range. It should be noted that typical operating temperatures of industrial gas turbines are likely to be closest to 900°C.

Using the value for the fitted constant above, it is possible to see how the model projects long term microstructural change. Graphs have been created for times up to 40000 hours, shown in Figure 6.3 These graphs indicate an exponential increase in $M_{23}C_6$: MC ratio with time, at all temperatures. Since all the carbide is assumed to be in either MC or $M_{23}C_6$, the transformation of the former carbide to the latter would be expected to result in an increasing $M_{23}C_6$: MC ratio, with exposure time, in the temperature range 850°C to 950°C. However, the experimental $M_{23}C_6$: MC ratio appears to increase in a parabolic manner with respect to time, rather than exponentially. Hence, it is recommended that fitting of the model is performed within the temperature range of interest. The model does not take into account dissolution of $M_{23}C_6$, predicted by ThermoCalc and Ni-data (see Thermodynamic Modelling in Chapter 4) to be approximately 1010°C. The service temperature of the gas turbine blades to which the model is to be applied is expected to be less than 1010°C, thus the model is suitable for practical application.

1.2.1 Data for Carbide Ratios

Figure 6.2 Experimental data (averaged) and calculated curve for $M_{23}C_6 / MC$ ratio versus exposure time

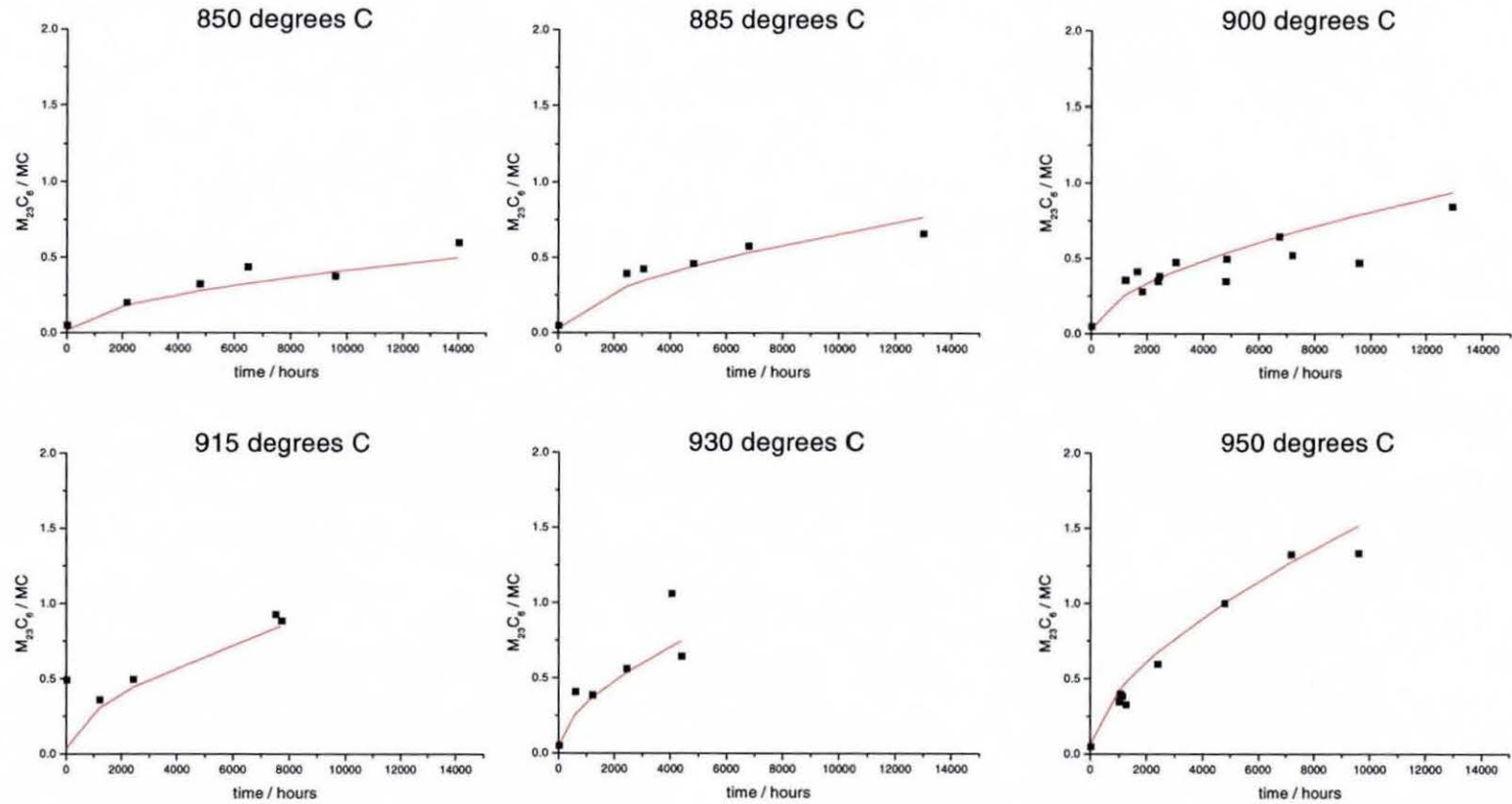
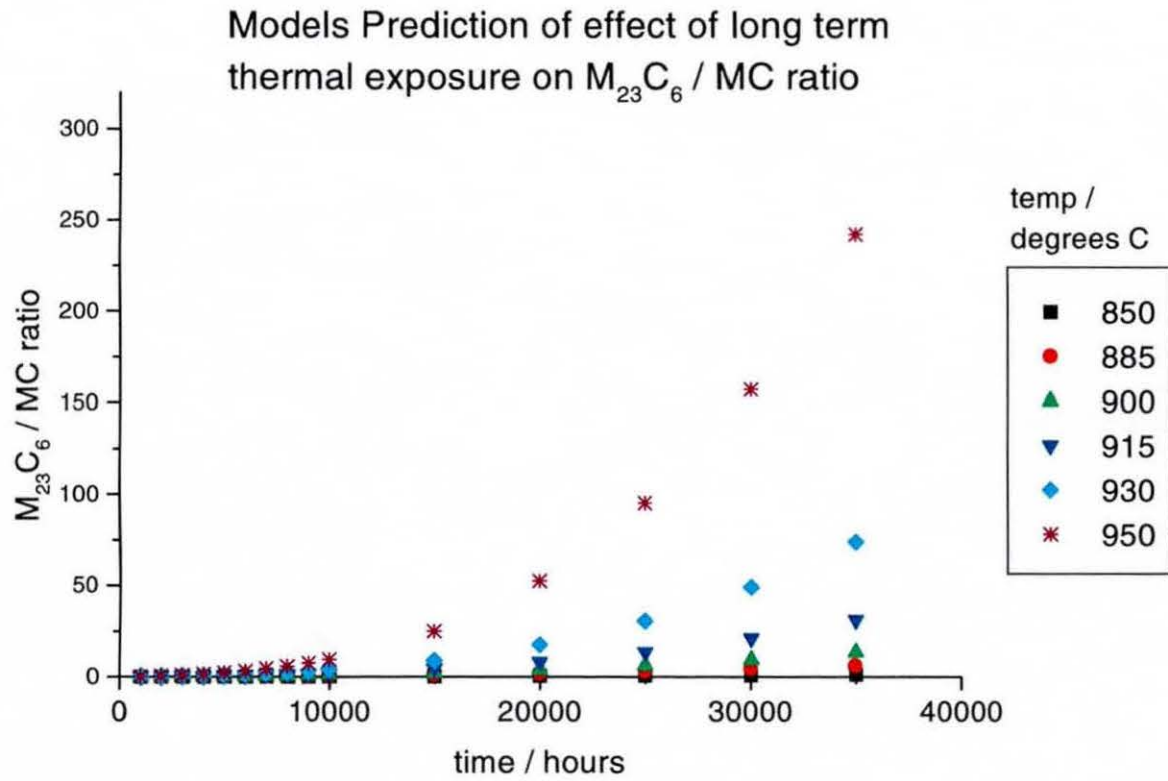


Figure 6.3 Long term calculated values of R'



Appendix 6A: Diffusion Coefficients of Some Elements in Ni and Ni-based Alloys

Table 6A.1 below contains diffusion data of some relevant elements in pure Ni, γ , Ni-based alloys and MC carbides. Data is from Refs.^{82,83,84}. The typical diffusion distances are compared graphically in Equation 6.4.2. Note that the typical diffusion distances of the various groups increase in the order: M in MC - C in MC - M in Ni - C in Ni. The differences between the groups are generally more than an order of magnitude.

Table 6A.1 Diffusion coefficients

Diffusant	alloy	Q (J/mol)	Do (cm ² /s)	x (mm) 250d/900°C	x (mm) 50d/1000°C	x (mm) 500d/1000°C	x (mm) 20h/1190°C
Hf	HfC	547	63	0.0005	0.002	0.006	0.007
Ta	TaC	509	26.4	0.0023	0.01	0.02	0.02
Ti	TiC	494	9000	0.0867	0.28	0.9	0.76
C	TaC	354	0.18	0.518	0.96	3.05	1.09
W	Ni	299	2	28.948	43.2	136	34.9
V	Ni	278	0.87	55.769	76.4	242	54.3
Ni	Ni	284	1.9	59.752	84	266	62
Ni	Ni-20at%Cr	259	0.15	61.638	78.2	247	49.5
Mo	Ni	213	0	66.352	70	221	33.5
Co	Ni	276	1.39	80.169	109	344	76.1
Cr	Ni	272	1.1	84.66	113	358	77.7
Fe	Ni	245	0.07	88.47	106	336	61.6
Cr	Ni-20at%Cr	263	0.61	101.25	131	413	84.6
Al	Ni	260	1	151.19	193	609	123
Ti	Ni	257	0.84	160.78	202	640	127
Hf	Ni	251	1.8	321.77	395	1250	238
C	Ni	142	0.01	6953.5	5513	17433	1703
C	TiC	94.6	0.01	56380	36905	1e5	8512
Ni	Ni-24at%Al*	345	132	37.259	46.6	147	44
Ni	Ni-25at%Al*	347	146	31.066	42.6	135	42.3
Ni	Ni-26at%Al*	342	105	34.498	45	142	43.3

* The diffusion of Ni in γ is the sum of two exponential functions⁸⁴. Only the one dominating at higher temperatures is given in the present table.

7 Conclusions and Further Work

7.1 Introduction

Most of the quantitative work has been carried out on the IN738LC alloy, for which a time temperature-recorder model has been successfully implemented. The conclusions that stem from the IN738LC analysis are given in separate sections. However, the coating systems have been studied in a more qualitative manner. The systematic investigation of the effect of thermal exposure on the coatings and their interaction with IN738LC substrate does provide an insight into the diffusion processes and phase transformations involved, and some potential parameters for time-temperature estimation.

7.2 Characterisation of IN738LC

The nature of the carbides in IN738LC have been characterised in some detail. The initial state of the carbides, the different types and relative quantities have been examined. The effect of long term thermal exposure at service temperatures, and short term exposure at very high temperatures was investigated. Additional investigations have been made of other microstructural features affected by thermal exposure, in particular, the development of a γ envelope associated with the grain boundary $M_{23}C_6$ carbide.

7.2.1 *As-received Material*

IN738LC that has undergone a standard heat treatment process (solution at 1120°C for 2 hours and age at 845°C for 24 hours) consists of a γ matrix with cuboidal γ' . There are additionally two types of MC carbide, probably as a result of the solidification sequence, but virtually no $M_{23}C_6$ carbide. The MC carbides appear predominantly at intercellular and intergranular positions, a result of these particles being amongst the first to solidify. The two types of MC carbide have the lattice structure of TiC but the compositions are different. These MC carbides have been termed Ti, Nb-rich and Ti, Nb-lean. The majority of the carbides are of the Ti, Nb-rich type.

Backscattered imaging in the SEM suggests that the Ti, Nb-lean carbide particles have a composition gradient. The focus of the EDX analyses was generally on the central region, and the composition was found to vary from particle to particle. In general the titanium content is higher and the niobium, tantalum and zirconium contents are lower than those of the Ti, Nb-rich carbide.

7.2.2 Effects of Thermal Exposure

Thermodynamic calculations predict $M_{23}C_6$ is the more stable carbide, up to its solvus temperature 1010°C. During thermal exposure, $M_{23}C_6$ forms at the expense of MC carbides. The quantity of $M_{23}C_6$ was found to increase with severity of thermal exposure, within the temperature range at which this phase is stable. Small amounts of $M_{23}C_6$ can form a continuous grain boundary network, and $M_{23}C_6$ is most apparent at grain boundaries.

The transformation of MC to $M_{23}C_6$ draws chromium from the surrounding matrix, which has the effect of stabilising γ (which has a lower solubility for chromium) in the form of envelope around the grain boundary carbide. This effect becomes more pronounced at higher temperatures and longer times.

The composition of the Ti, Nb-rich carbide remains relatively constant on long term exposure up to 950°C.

γ particles in IN738LC that had undergone short term thermal exposure were very blocky. Longer term thermal exposure results in distortion of primary γ , rounding of the corners, coalescence and spheroidisation can occur.

7.2.3 Very High Temperature Thermal Exposure

Short term exposure at very high temperatures, including the range 1120°C to 1235°C causes dissolution of $M_{23}C_6$. The composition of the Ti, Nb-rich carbide remains relatively constant on short term exposure up to 1235°C.

7.3 Coating Characterisation

The two coatings RT122 and SC2453 have different microstructures but exhibit some similar characteristics on thermal exposure. In particular, the extent of the interdiffusion zone increases with thermal exposure, due to continuing co-diffusion of elements between the coating and substrate.

7.3.1 RT122

At 850°C and 950°C, the bulk coating initially consists of γ and β , consistent with thermodynamic modelling predictions. Thermal exposure at 850°C and 950°C results in the formation of an outer β depletion layer, due to loss of aluminium to form an Al_2O_3 surface oxide. A β depletion zone at the inner layer of coating also occurs, caused by a difference in concentration of aluminium between coating and substrate.

The interdiffusion zone consists mainly of γ , with small amounts of β . The extent of the interdiffusion zone increases with thermal exposure.

Shot peening of the surface prior to coating is likely to have induced residual stresses, resulting in a marked recrystallised zone being visible in the substrate at the coating interface on thermal exposure. It is considered that these the grain boundaries present in this recrystallised region may have acted as fast diffusion paths for aluminium diffusing out of the coating, resulting in the absence of β at the interdiffusion zone, which has been previously observed in othre similar coating systems.

7.3.2 SC2453

This coating system was found to be more complex compared to RT122, and different microstructures were found to occur in the bulk coating at 850°C and 950°C.

7.3.2.1 850°C

The bulk coating consists of γ , β , rhenium containing equiaxed σ , and small amounts of γ . Thermodynamic modelling at this temperature predicts an equilibrium microstructure of γ , β , σ and α . Thermal exposure results in diffusion of aluminium at the outer layer of the coating to the protective Al_2O_3 oxide layer, resulting in a β depletion zone. A β depletion zone also occurs at the inner layer of the coating, due to the lower aluminium content of the substrate effecting diffusion of aluminium from the coating towards the substrate. A similar effect is considered to cause diffusion of chromium from the coating towards the substrate.

The diffusion of aluminium and chromium from the coating towards the substrate results in the presence of γ and TCP σ at the interdiffusion zone. Rhenium containing equiaxed σ is generated at the interface between the coating and the interdiffusion zone.

7.3.2.2 950°C

The bulk coating consists of γ , β , σ and α . The equilibrium microstructure is predicted by thermodynamic modelling to be γ , β and α . The aluminium diffusion effects are similar but more pronounced than those found at 850°C. At this, higher temperature, there is depletion of σ phase within the coating, considered to be a result of chromium diffusing from the coating toward the substrate.

The diffusion of aluminium and chromium from the coating towards the substrate generates γ and α , with no TCP σ evident as at 850°C. The solution temperature for TCP σ (at the

SC2453/IN738LC composition in the interdiffusion zone) is therefore below 950°C. A thin layer of rhenium containing α particles is present at the interface between the coating and interdiffusion zone. The rhenium content of α at the interdiffusion zone varies, generally reducing towards the substrate. This trend in the rhenium content of α in the interdiffusion zone implies diffusion of rhenium from coating to substrate, but at a slower rate than that of chromium.

7.4 Indicators of Remaining Service Life

In IN738LC alloy, the $M_{23}C_6$: MC ratio increases systematically with time and temperature, within the temperature range active for the transformation of MC to $M_{23}C_6$.

On long term exposed samples a γ envelope on the grain boundaries has been observed and limited investigation to date has shown the width of the grain boundary envelope to increase with prolonged service exposure.

For MCrAlY / IN738LC coated systems, possible parameters for use in a time temperature estimation model include depletion zone width and interdiffusion layer width, with the latter being more likely for the systems under consideration.

7.4.1 Time Temperature Recorder for IN738LC

A time-temperature recorder model, based on the $M_{23}C_6$: MC ratio, has been developed for IN738LC alloy using an extension of the Johnson-Mehl-Avrami-Kolmogorov type equation. The model is accurate in the temperature range 850°C to 950°C, when fitted with experimental data. The model does not take into account the dissolution temperature of $M_{23}C_6$ carbide (approximately 1010°C according to thermodynamic predictions), however service temperatures for the turbine blades under consideration are generally below this temperature and therefore the model will be suitable for practical situations.

7.5 Further Work

The model could be tested with data from samples of known exposure time and temperature. The exposure time and carbide ratio data would be input data for the model, and the predicted temperature would be compared with the known exposed temperature. The dissolution temperature of $M_{23}C_6$ should also be incorporated into the model.

Phase determination by optical techniques could be evaluated with a view to using it as a non-destructive method of indicating carbide ratios. The width of the γ envelope at the grain

boundary could be examined as an alternative parameter for use in time-temperature recorder model, however careful measuring methodologies with sound statistical analyses will have to be developed.

A generic time-temperature recorder model could be created for the coated systems, perhaps linking kinetic models involving diffusion directly to equilibrium thermodynamic predictions. Additionally, an examination of the effect of thermal cycling and in-service environment on coated and uncoated IN738LC material would be of particular benefit, in order to assess the wider applicability of the methodologies developed in this research.

Reference List

1. M. Durand-Charre, *The Microstructure of Superalloys*, Gordon and Breach Science Publishers, Amsterdam, 1997.
2. A. K. Jena and M. C. Chaturvedi, *Journal Of Materials Science* **19**, 3121-3139 (1984).
3. C. T. Sims, N. S. Stoloff, W. C. Hagel, *Superalloys II*, John Wiley & Sons, New York, 1987.
4. R. F. Decker, in *Steel Strengthening Mechanisms*, (Climax Molybdenum Company, Zurich, 1969).
5. O. H. Kriege and J. M. Baris, *Transactions of the ASM* **62**, (1969).
6. M. J. Starink, H. Cama, R. C. Thomson, *Scripta Materialia* **38**, 73-80 (1997).
7. M. J. Starink and R. C. Thomson, Carbide Reactions During High Temperature Exposure of the Ni-base Superalloy MarM002. 1999. Unpublished Work at Loughborough University, UK
8. K. M. Chang and E. L. Hall, *Journal Of Metals* **35**, 90 (1983).
9. R. H. Davies, A. T. Dinsdale, T. G. Chart, T. I. Barry, M. H. Rand, *High Temperature Science* **26**, 251-262 (1989).
10. R. R. Jensen and J. K. Tien, *Metallurgical Transactions A-Physical Metallurgy And Materials Science* **16**, 1049-1068 (1985).
11. R. A. Stevens and P. J. Flewitt, *Acta Metallurgica* **29**, 867-882 (1981).
12. M. Heilmaier and B. Reppich, *Metallurgical And Materials Transactions A-Physical Metallurgy And Materials Science* **27**, 3861-3870 (1996).
13. M. Y. Nazmy and C. Wuthrich, *Materials Science And Engineering* **61**, 119-125 (1983).
14. M. Y. Nazmy, *Metallurgical Transactions A-Physical Metallurgy And Materials Science* **14**, 449-461 (1983).
15. M. Y. Nazmy, *Materials Science And Engineering* **55**, 231-237 (1982).
16. H. Frenz et al., *Materials Science And Engineering A-Structural Materials Properties Microstructure And Processing* **230**, 49-57 (1997).
17. W. Hoffelner, E. Kny, R. Stickler, L. M. Mccaslin, *Zeitschrift Fur Metallkunde* **10**, 84-92 (1979).
18. J. Li and R. P. Wahi, *Acta Metallurgica Et Materialia* **43**, 507-517 (1995).

19. E. Balikci, A. Raman, R. A. Mirshams, *Metallurgical And Materials Transactions A-Physical Metallurgy And Materials Science* **28**, 1993-2003 (1997).
20. R. A. Stevens and P. E. J. Flewitt, *Materials Science And Engineering* **37**, 237-247 (1979).
21. R. A. Stevens and P. E. J. Flewitt, *Journal Of Materials Science* **13**, 367-376 (1978).
22. L. Liu, B. L. Zhen, A. Banerji, W. Reif, F. Sommer, *Scripta Metallurgica Et Materialia* **30**, 593-598 (1994).
23. L. Liu, F. Sommer, H. Z. Fu, *Scripta Metallurgica Et Materialia* **30**, 587-591 (1994).
24. V. P. Swaminathan, N. S. Cheruvu, J. M. Klein, Rocchini, *International gas turbine & aeroengine congress & exhibition, Stockholm* (1998).
25. D. Bettge, W. Osterle, J. Ziebs, *Zeitschrift Fur Metallkunde* **86**, 190-197 (1995).
26. D. Mukherji, F. Jiao, W. Chen, R. P. Wahi, *Acta Metallurgica Et Materialia* **39**, 1515-1524 (1991).
27. M. McLean and H. R. Tipler, Proceedings of 5th International Symposium on Superalloys, Champion, Pennsylvania, Oct 1984, 73-82
28. G. Van Drunen and J. Liburdi, *Proceedings of the Sixth Turbomachinery Symposium, Sponsored by, Gas Turbine Laboratories, Texas A&M University, December 1977* (1977).
29. G. Van Drunen and J. Liburdi, "Hot Isostatic Pressing of IN-738 Turbine Blades" *Report No. LTR-ST-999* (National Research Council Canada, National Aeronautical Establishment, Ottawa, Canada, 1978).
30. N. Birks and G. H. Meier, *Introduction to High Temperature Oxidation of Metals*, Butterworth-Heinemann, Oxford, 1983.
31. G. M. McColvin, *Metal Science* **October**, 447-453 (1977).
32. S. B. Newcomb and W. M. Stobbs, *Elevated Temperature Coatings Science And Technology II* 265-274 (1996).
33. Y. Niu et al., *Journal De Physique IV* **3**, 511-519 (1993).
34. E. Basuki, A. Crosky, B. Gleeson, *Materials Science And Engineering A-Structural Materials Properties Microstructure And Processing* **224**, 27-32 (1997).
35. P. Mazars, D. Manesse, C. Lopvet, *High Temperature Alloys For Gas Turbines And Other Applications 1986, Pts 1&2* 1183-1192 (1986).
36. A. R. Nicoll and G. Wahl, *Thin Solid Films* **95**, 21-34 (1982).
37. H. M. Tawancy, N. M. Abbas, A. Bennett, *Surface & Coatings Technology* **68**, 10-16 (1994).

38. N. Czech, F. Schmitz, W. Stamm, *Surface & Coatings Technology* **76**, 28-33 (1995).
39. N. S. Cheruvu, K. S. Chan, G. R. Leverant, *Journal Of Engineering For Gas Turbines And Power-Transactions Of The ASME* **122**, 50-54 (1998).
40. V. Srinivasan, N. S. Cheruvu, T. J. Carr, C. M. O'Brien, *Materials And Manufacturing Processes* **10**, 955-969 (1995).
41. N. S. Cheruvu, T. J. Carr, J. Dworak, J. Coyle, *Jom-Journal Of The Minerals Metals & Materials Society* **48**, 34-38 (1996).
42. N. S. Cheruvu and G. R. Leverant, Influence of metal temperature on base materials and coating degradation of GTD-111 buckets. 1998.
Unpublished Work at Southwest Research Institute, San Antonio
43. M. A. Dayananda, D. A. Behnke, L. M. Mccaslin, *Diffusion Analysis & Applications* 325-336 (1989).
44. N. Czech, F. Schmitz, W. Stamm, *Surface & Coatings Technology* **68**, 17-21 (1994).
45. F. Meisenkothen and J. E. Morral, *Elevated Temperature Coatings: Science And Technology III* 143-148 (1999).
46. M. M. Morra, R. D. Sisson, R. R. Biederman, *Surface Engineering .Surface Modification Of Materials* **85**, 482-495 (1984).
47. K. A. Ellison, J. A. Daleo, D. H. Boone, *Materials for Advanced Power Engineering 1998* 1523-1534 (1999).
48. J. E. Morral, C. Jin, W. D. Hopfe, *Elevated Temperature Coatings Science And Technology II* 245-253 (1996).
49. L. Peichl and G. Johner, *Journal Of Vacuum Science & Technology A-Vacuum Surfaces And Films ACUUM*, 2583-2592 (1986).
50. Y. Itoh and M. Tamura, *Journal Of Engineering For Gas Turbines And Power-Transactions Of The ASME* **121**, 476-483 (1999).
51. J. A. Nesbitt and J. F. Lei, *Elevated Temperature Coatings: Science And Technology III* 131-142 (1999).
52. A. Sanz, L. Llanes, J. P. Bernadou, M. Anglada, M. B. Lapaccini, *Elevated Temperature Coatings Science And Technology II* 373-388 (1996).
53. A. Sanz, L. Llanes, J. P. Bernadou, M. B. Lapaccini, *Elevated Temperature Coatings Science And Technology II* 219-232 (1996).
54. G. P. Degaudenzi, A. Colombo, G. Rocchini, F. Uberti, *Elevated Temperature Coatings Science And Technology II* 301-310 (1996).
55. K. S. Chan, *Metallurgical And Materials Transactions A-Physical Metallurgy And Materials Science* **28**, 411-422 (1997).

56. K. S. Chan, N. S. Cheruvu, G. R. Leverant, *Journal Of Engineering For Gas Turbines And Power-Transactions Of The ASME* **120**, 609-614 (1998).
57. K. S. Chan, N. S. Cheruvu, G. R. Leverant, *Journal Of Engineering For Gas Turbines And Power-Transactions Of The ASME* **121**, 484-488 (1998).
58. K. S. Chan, N. S. Cheruvu, and G. R. Leverant, Predicting Coating Performance Degradation under Variable Peak Temperatures. 1999.
Unpublished Work at Southwest Research Institute, San Antonio
59. E. S. Kartavova and P. G. Krukovsky, *Materials for Advanced Power Engineering 1998* 1689-1698 (1998).
60. E. Y. Lee, D. M. Chartier, R. R. Biederman, R. D. Sisson, *Surface & Coatings Technology* **32**, 19-39 (1987).
61. B. D. Cullity, *Elements of X-ray Diffraction*, Second Edition, Addison-Wesley, Harlow, UK, 1978.
62. W. Wong, M. Holomany, W. F. McClune, C. D. Hubbard, *Advances in X-Ray Analysis* **26**, 87-88 (1983).
63. K. W. Andrews and H. Hughes, *Iron and Steel* **30**, 43-50 (1958).
64. D. Vaughan, *Energy Dispersive X-ray Microanalysis, an introduction*, Kevex Corporation, Foster City, California, 1983.
65. J. M. Walls, "Auger electron microscopy" (Dept. Physics, Loughborough University, 1985).
66. N. Saunders and A. P. Miodownik, *Calphad, Calculation of Phase Diagrams*, Pergamon, Cambridge, 1998.
67. I. Ansara et al., *Calphad-Computer Coupling of Phase Diagrams and Thermochemistry* **18**, 177-222 (1994).
68. I. Ansara, *Thermochemical database for light metal alloys*, European Commission, Brussels, 1995.
69. B. Jansson, M. Schalin, M. Selleby, B. Sundman, *Computer Software in Chemical and Extractive Metallurgy* 57-71 (1993).
70. N. Saunders, Proceedings of 8th International Symposium on Superalloys-Champion, Pennsylvania, Sep 22-26, 1996, *Kissinger RD, Deye DJ Anton DL Cetel AD Nathal MV Pollock TM Woodford DA*, 101-110
71. N. Saunders, *Advanced Materials & Processes* **156**, 29-31 (1999).
72. N. Saunders, M. Fahrman, and C. J. Small, *The Application of Calphad Calculations to Ni-based Superalloys*. 2000.
Unpublished Work at Thermotech Ltd., Guildford, UK

73. M. J. Starink, M. Z. Omar, and R. C. Thomson, A Method for Analysis of EDX Data Containing Contributions from Several Phases using SEM. 1999. Unpublished Work at Loughborough University, UK
74. M. J. Starink and R. C. Thomson, *Modelling of Microstructural Evolution in Creep Resistant Materials* 357-371 (1999).
75. W. B. Pearson, Handbook of lattice Spacings and Structure of Metals and Alloys, Pergamon Press, London, 1958.
76. K. A. Ellison, J. A. Daleo, and D. H. Boone, Microstructural Evaluation of MCRAly / Superalloy Interdiffusion Zones. 1999. 5-10-0099. Unpublished Work at BWD Turbines Ltd., Ontario
77. D. A. Porter and K. E. Easterling, Phase Transformations in Metals and Alloys, Chapman and Hall, London, ed. second, 1992.
78. J. D. Robson and H. K. D. H. Bhadeshia, *Materials Science And Technology* **13**, 631-639 (1997).
79. H. K. D. H. Bhadeshia, Proceedings of Advanced Materials for 21st Century Turbines and Power Plant- Fifth International Charles Parsons Turbine Conference, Cambridge, July 2000, *Strang, A, Banks, W. M., Conroy, R. D., McColvin, G. M., Neal, J. C., and Simpson, S.*, 3-39
80. M. J. Starink and A. M. Zahra, *Philosophical Magazine A-Physics Of Condensed Matter Structure Defects And Mechanical Properties* **77**, 187-199 (1998).
81. M. J. Starink, C. Y. Zahra, A. M. Zahra, *Journal Of Thermal Analysis And Calorimetry* **51**, 933-942 (1998).
82. C. J. Smithells, Metals Reference Book, 7th ed., Butterworth-Heinemann, Oxford, 1992.
83. W. G. Moffat, Handbook of Binary Phase Diagrams, Genium Publ, New York, Schenectady, New York, NY, USA, 1998.
84. K. Hoshino, S. J. Rothman, R. S. Averbach, *Acta Metallurgica* **36**, 1271-1279 (1988).

The Novartis and The Daily Telegraph
Visions of Science
Photographic Competition

Dear Mr Shaheedullah,

Congratulations! The judges in the Visions of Science photographic competition have nominated you as a runner up of the Scientist/Healthcare Worker Category, for your photograph entitled "Carbide Particles". You have won a Kodak Advantix T550AF.

The prize camera will be presented to you by Lord Melvyn Bragg at the Visions of Science Awards Ceremony on 31 October 2000 at the Royal Society in London.

The Awards Ceremony will begin at 11.30am, with coffee and a chance to look at the Visions of Science exhibition, which will include your image. At 12.00pm the ceremony will take place and this will incorporate an overview of the competition from the sponsors and an outline on the winning entries by Dr Adam Hart-Davis, presenter of the popular Local Heroes series. There will be a light lunch at 12.45pm and guests will leave from 1.45pm onwards.

You are welcome to bring one colleague or family member with you. Novartis will subsidise travel for you personally, up to a limit of £70. Please bring receipts for your travel.

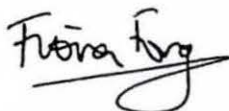
We very much hope you will be able to join us. Please could you complete the attached form advising us of your attendance and either post or fax it back to KSA at PO Box 29760, London E2 8TZ, Fax 020 7613 0007.

The Royal Society is situated at 6 Carlton House Terrace, London SW1 (Tel 020 7451 2612), near Piccadilly Circus tube station. (A map is attached).

As one of my colleagues has explained to you on the telephone, a number of finalist's photographs may be used in the Daily Telegraph before the awards as an example of the finalists. We will let you know if your image is used.

- We look forward to seeing you and congratulations.

Yours sincerely



FIONA FONG

Novartis/Daily Telegraph Visions of Science, PO Box 29670, London, E2 8TZ
Tel: 020 7613 5577 Fax: 020 7613 0007 Email: visions-of-science@ksaevents.com
Website: www.visions-of-science.co.uk

 NOVARTIS

The Daily Telegraph

